UNIVERSITY OF OKLAHOMA

GRADUATE COLLEGE

SEARCH FOR ELECTROWEAK PRODUCTION OF SUPERSYMMETRIC

STATES IN NON-UNIVERSAL HIGGS MASS MODEL WITH TWO EXTRA

PARAMETERS COMPRESSED SCENARIO WITH THE ATLAS DETECTOR

A DISSERTATION

SUBMITTED TO THE GRADUATE FACULTY

in partial fulfillment of the requirements for the

Degree of

DOCTOR OF PHILOSOPHY

By

YU-TING SHEN
Norman, Oklahoma
2018

SEARCH FOR ELECTROWEAK PRODUCTION OF SUPERSYMMETRIC
STATES IN NON-UNIVERSAL HIGGS MASS MODEL WITH TWO EXTRA
PARAMETERS COMPRESSED SCENARIO WITH THE ATLAS DETECTOR

A DISSERTATION APPROVED FOR THE
HOMER L. DODGE DEPARTMENT OF PHYSICS AND ASTRONOMY

BY

Dr. Patrick Skubic, Chair

Dr. Michael Strauss

Dr. Howie Baer

Dr. Deborah Watson

Dr. Zhisheng Shi

'Blood, sweat & respect. First two you give, last one you earn."

- Dwayne Johnson

Acknowledgements

I would like to thank everyone who has helped me. Especially, thanks to my advisor Patrick Skubic, SS/3L+jets analysis convenor Ximo Poveda Torres, and postdoc Judita Mamužić. Patrick gave me enough freedom and space to work on projects related to the analysis I was interesting in. He guided me and gave me a lot of useful feedback in the weekly meeting. He also helped me handle everything related to the university when I based at CERN for the past three years. Ximo is a very good mentor and friend while I was at CERN. He always taught me physics, helped me to solve the problems I encountered, and helped me to acclimate myself to my new life at CERN. Without Ximo's substantial help, I couldn't finish my dissertation smoothly and successfully. Judita kindly agreed to help me work on the NUHM2 interpretation in the Higgsino LSP search after I finished the study on the SS/3L+jets analysis. Because she had experience regarding the NUHM2 model, she provided me with assistance carrying out the analysis and writing documentation. Without her full support, I could not have finished the NUHM2 study in such a short period. Thanks to all my friends at CERN and OU for the good times we enjoyed together in exploring delicious food, traveling, hiking, bouldering, skiing, and boxing. Thanks to my ex-girlfriend to warm my heart, to encourage me, and to love me, making me feel happiness in the first half of my Ph.D. life. Thanks to my brother for taking care of my parents while I am far away from Taiwan. Finally, many thanks to my parents for everything they bestowed on me.

Table of Contents

List of Tables

List of Figures

xiii

Abstract

The ATLAS and CMS collaborations announced the discovery of the Higgs boson in July 2012, completing the particle content of the Standard Model. Although the Standard Model is a great triumph, it is not considered to be the complete theory of particle physics. Several new theories have been proposed which seek to move beyond the Standard Model. Among the newly-developed theories, Supersymmetry (SUSY) is one of the most promising ones. SUSY predicts the existence of supersymmetric partner particles and it is one of the best-motivated extensions of the space-time symmetry of particle interactions. There are supersymmetric partner particles associated with each SM particles in which the spin differs by 1/2. This dissertation focuses on a search for electroweak production of supersymmetric particles with compressed mass spectra in the final states with exactly two low-momentum leptons and missing transverse momentum. The proton-proton collision data is recorded by the ATLAS detector at the Large Hadron Collider in 2015 and 2016, corresponding to 36.1 fb^{-1} of integrated luminosity at $\sqrt{s} = 13$ TeV. Events with same-flavor and opposite electric charge lepton pairs are selected. The data are found to be consistent with the Standard Model prediction. Results are interpreted using the non-universal Higgs mass model with two extra parameters (NUHM2) with small mass differences between the masses of produced supersymmetric particles. Upper limits of the cross-section at 95% confidence level are set for the NUHM2 model as a function of the universal gaugino mass $m_{1/2}$.

CHAPTER 1

INTRODUCTION

The Standard Model of particle physics (SM) describes various phenomena of particle physics. The discovery of the Higgs boson (H) by the ATLAS and CMS collaborations at CERN completes the missing part of the SM predictions [6, 7]. However, there are several open challenges that cannot be explained by the SM, such as the hierarchy problem [21, 22, 23] and a dark matter candidate. In order to answer those questions, a new theory extending the SM is necessary. Supersymmetry (SUSY) [24, 25, 26, 9] is one of the most promising extensions of the SM. SUSY, which is a spacetime symmetry, introduces the superpartners of SM particles (sparticles) with spin differing by one-half unit with respect to the SM partners. The sparticles provide a potential solution to the hierarchy problem. If R-parity is conserved [27, 28, 29], the sparticles are produced in pairs and the lightest SUSY particle (LSP) is stable providing a candidate for dark matter.

The charginos $\widetilde{\chi}_{1,2}^{\pm}$ and neutralinos $\widetilde{\chi}_{1,2,3,4}^{0}$ are the mass eigenstates in the order of increasing masses and collectively referred to as electroweakinos. They are the mixture of the bino $\widetilde{B}$, winos $\widetilde{W}$, and Higgsinos $\widetilde{H}_{u,d}$ which are the superpartners of the $U(1)$, $SU(2)$ gauge bosons, and the Higgs bosons, respectively. The charginos and neutralinos can decay into leptons and LSPs via W, Z, H or sleptons $\widetilde{\ell}$. In many SUSY models, the lightest neutralino $\widetilde{\chi}_1^0$ is the LSP. The LSP would not be detected and results in significant missing transverse energy $E_{\mathrm{T}}^{\mathrm{miss}}$.

The compressed scenarios refer to the small mass differences between heavier

SUSY particles and the LSP. For example, the mass differences between the heavier electroweakino states $\widetilde{\chi}_2^0$, $\widetilde{\chi}_1^\pm$ and the wino- or Higgsino-dominated LSP $\widetilde{\chi}_1^0$ range from a few MeV to tens of GeV depending on the composition of the mixture. The $\widetilde{B}$, $\widetilde{W}$, and $\widetilde{H}$ composition of the $\widetilde{\chi}_1^0$ have an influence on the degree of compression. Figure 1.1 shows the composition of the lightest neutralino in a MSSM scan of the electroweakino sector [4]. Based on naturalness arguments [30, 31], the Higgsino mass parameter μ, the bino and wino mass parameters M_1 and M_2 satisfy $|\mu| \ll |M_1|, |M_2|$ leading to the three electroweakinos $\widetilde{\chi}_1^0$, $\widetilde{\chi}_1^\pm$, and $\widetilde{\chi}_2^0$ being dominated by the Higgsino.
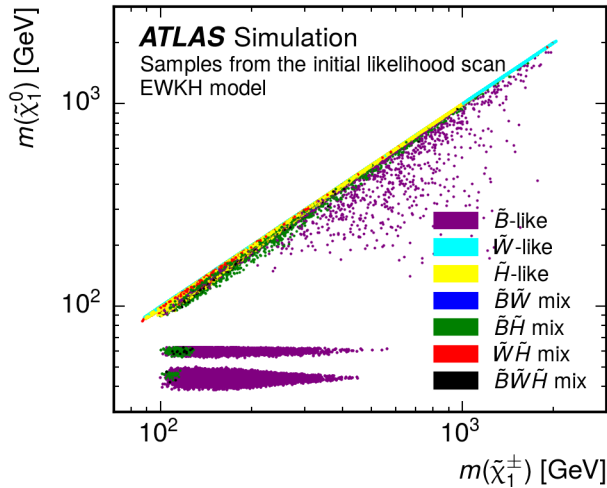
Figure 1.1: The scatter plot in the $m(\widetilde{\chi}_1^0)$ vs $m(\widetilde{\chi}_1^\pm)$ plane of the lightest neutralino in a MSSM scan [4]. The color encodes the $\widetilde{\chi}_1^0$ composition. The Higgsino-dominated LSPs are colored in yellow and along the $\widetilde{\chi}_1^0$-$\widetilde{\chi}_1^\pm$ diagonal.

This dissertation focuses on searching for electroweak production of SUSY particles in compressed scenarios with exactly two low-momentum same-flavor opposite-charged leptons (electron and muon) in final states and missing transverse momentum $\mathbf{p}_T^{\text{miss}}$. This search uses proton-proton collision data at $\sqrt{s} = 13$ TeV

recorded by the ATLAS detector at the Large Hadron Collider (LHC) [32] in 2015 and 2016, corresponding to a total integrated luminosity of 36.1 fb^{-1}. Figure 1.2 shows the Feynman diagrams representing the electroweakino productions with two leptons final state in association with an initial state radiated jet. Same-flavor opposite-charged leptons come from the $\widetilde{\chi}_2^0$ decays in the $\widetilde{\chi}_2^0\widetilde{\chi}_1^\pm$ and $\widetilde{\chi}_2^0\widetilde{\chi}_1^0$ productions, and from the $\widetilde{\chi}_1^\pm$ decays in the $\widetilde{\chi}_1^\pm\widetilde{\chi}_1^\mp$ production. The two leptons can be reconstructed in the detector and carry small transverse momentum p_{T}. However, the two LSPs are invisible and back-to-back in the rest frame of their parent electroweakinos. Because they carry large momentum, the missing transverse energy $E_{\mathrm{T}}^{\mathrm{miss}}$ is relatively large. Similar searches have been performed using $\sqrt{s} = 8$ TeV and $\sqrt{s} = 13$ TeV by the ATLAS [33, 34, 35, 4] and CMS [36, 37, 38] experiments. Combining with the results from the LEP experiments, the mass limits for sleptons and charginos are $m(\widetilde{e}_R) > 73$ GeV, $m(\widetilde{\mu}_R) > 94.6$ GeV, and $m(\widetilde{\chi}_1^\pm) > 103.5$ GeV or 92.4 GeV depending on the $\Delta m(\widetilde{\chi}_1^0, \widetilde{\chi}_1^\pm)$.
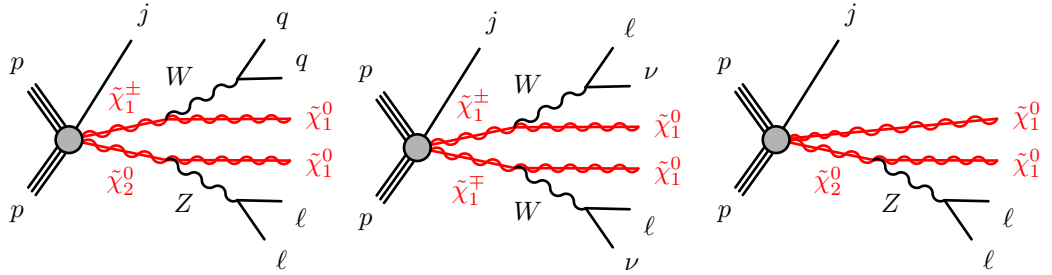
(a) The $\widetilde{\chi}_2^0\widetilde{\chi}_1^\pm$ production. (b) The $\widetilde{\chi}_1^\pm\widetilde{\chi}_1^\mp$ production. (c) The $\widetilde{\chi}_2^0\widetilde{\chi}_1^0$ production.

Figure 1.2: The Feynman diagrams representing the two leptons final state of (a) $\widetilde{\chi}_2^0\widetilde{\chi}_1^\pm$, (b) $\widetilde{\chi}_1^\pm\widetilde{\chi}_1^\mp$, (c) $\widetilde{\chi}_2^0\widetilde{\chi}_1^0$ productions.

This dissertation has the following structure. An introduction is given in Chapter 1 followed by theoretical foundations in Chapter 2 and 3. The experiment

facilities are described in Chapter 4. The data and Monte Carlo samples used are detailed in Chapter 5. Chapter 6 presents the event reconstruction and the signal region selection. The background estimation and the systematic uncertainties are discussed in Chapter 7. The results and interpretation are reported in Chapter 8. Finally, the conclusions are summarized in Chapter 9.

CHAPTER 2

THE STANDARD MODEL

This chapter outlines relevant theoretical and mathematical concepts of high energy particle physics. The Standard Model of particle physics (SM) [39, 40, 41, 42, 43] has been developed since the early 1970s and it has successfully explained almost all experimental results. The SM is well-tested and the most successful physics theory to describe the nature of the elementary particles and their interactions. An overview of the SM is given in Sect. 2.1. Then, some of the open questions are mentioned in Sect. 2.2.

2.1 The Standard Model of Particle Physics

The Standard Model of particle physics is known as the most accurate theory for describing elementary particles and the interactions between them. By combining quantum mechanics and special relativity, the SM is a relativistic *Quantum Field Theory* (QFT) based on a $SU(3)_C \otimes SU(2)_L \otimes U(1)_Y$ symmetry gauge group, where C denotes color, L represents left chirality, and Y stands for weak hypercharge, respectively. The $SU(3)_C$ group is the basis for *Quantum Chromodynamics* (QCD) which describes the strong interaction and the $SU(2)_L \otimes U(1)_Y$ group is the foundation of the electroweak interaction which unifies the electromagnetic and weak interactions. Therefore, the SM Lagrangian is invariant under the local gauge transformation. According to *Noether's Theorem* [44], the invariance of an action of a physical system undergoes a symmetry transformation corresponding

to a conservation law and vice versa. The gauge invariance of the SM Lagrangian corresponds to the conserved quantum numbers, or the charges, of each interaction. The conserved charges are the three color charge (red, blue, green) for the strong interaction, the third component of the weak isospin I_3 for the weak interaction, and the electric charge Q for the electromagnetic interaction.

2.1.1 Particle Content

According to the SM, all matter around us is made of elementary particles called *quarks* and *leptons*. The quarks and leptons are fermions which have half integral spin $s = \frac{1}{2}$, hence the fermions follow the Pauli exclusion principle which says no two fermions have the same quantum state at the same time. Each fermion has an anti-fermion with the equal mass but carries opposite electric charge, weak isospin and color charge. There are six quarks and six leptons, they are grouped into three pairs, or "*generations*", ordered by their mass. The lightest and most stable particles constitute the first generation and they are constituents of ordinary matter. The heavier and less stable particles form the second and third generations and the heavier particles quickly decay to the next most stable particles. The three generations of quarks are up (u) and down (d), charm (c) and strange (s), and top (t) and bottom (b) quarks. The up-type quarks (u, c, t) carry $+\frac{2}{3}|e|$ charge and with isospin $+\frac{1}{2}$ while the down-type quarks (d, s, b) carry $-\frac{1}{3}|e|$ charge with isospin $-\frac{1}{2}$. The quarks carry an additional color charge of either red, green, or blue, and hence they interact via the strong force. The strong force holds quarks together. Only non-integer charges of the quark combinations are experimentally allowed. The quark combinations are called *hadrons* which can

be categorized into *mesons* and *baryons*. A meson is composed by a quark and anti-quark pair ($q\bar{q}$) whereas a baryon is made up by three quarks (qqq or $\bar{q}\bar{q}\bar{q}$). Only colorless bound states of hadrons are allowed so the quark and anti-quark pair in a meson should contain color and anti-color and the three quarks in a baryon must carry different colors. The leptons are colorless and are therefore participating in the weak and electromagnetic force only. They do not participate in the strong interaction. The electron-type leptons (e, μ, τ) carry an elementary charge $|e|$ and their corresponding neutrinos (ν_e, ν_μ, ν_τ) are neutral. The neutrinos have very little mass and interact via the weak force only. A summary table of the properties of quarks and leptons is given in Table 2.1.

Generation	Fermion		particle	electric charge Q	weak isospin I_3	color charge C	mass [GeV]
I	Quark	u	up quark	$+\frac{2}{3}|e|$	$+\frac{1}{2}$	r,g,b	0.0023
		d	down quark	$-\frac{1}{3}|e|$	$-\frac{1}{2}$	r,g,b	0.0048
	Lepton	e	electron	$-1|e|$	$-\frac{1}{2}$	-	0.00051
		ν_e	electron neutrino	0	$+\frac{1}{2}$	-	$< 2 \times 10^{-9}$
II	Quark	c	charm quark	$+\frac{2}{3}|e|$	$+\frac{1}{2}$	r,g,b	1.275
		s	strange quark	$-\frac{1}{3}|e|$	$-\frac{1}{2}$	r,g,b	0.095
	Lepton	μ	muon	$-1|e|$	$-\frac{1}{2}$	-	0.106
		ν_μ	muon neutrino	0	$+\frac{1}{2}$	-	$< 1.9 \times 10^{-7}$
III	Quark	t	top quark	$+\frac{2}{3}|e|$	$+\frac{1}{2}$	r,g,b	173.2
		b	bottom quark	$-\frac{1}{3}|e|$	$-\frac{1}{2}$	r,g,b	4.18
	Lepton	τ	tau	$-1|e|$	$-\frac{1}{2}$	-	1.777
		ν_τ	tau neutrino	0	$+\frac{1}{2}$	-	$< 1.82 \times 10^{-5}$

Table 2.1: The Standard Model fermions with charges and masses [1]. The quark masses in the last column are approximate values.

There are four fundamental forces in the universe: the strong force, the weak force, the electromagnetic force, and the gravitational force. The first three forces

are described in the SM, however, the gravitational force is not yet be included in the SM. Because the effect of the gravitational force is very weak and can be negligible, the SM works well without considering the gravitational force. Each force has a force-carrier particle called a gauge boson with a quantum number associated to it. The gauge bosons of the strong force are eight massless *gluons*, g, which are associated to color charge C. The gauge bosons of the weak force are the $W^{\pm}$ and Z^0 bosons which are associated to weak isospin I_3. The gauge boson of the electromagnetic force is massless *photon*, γ, which is associated to electric charge Q. Although the gluons and photon are massless particles, the $W^{\pm}$ and Z^0 bosons are massive. The mass of the $W^{\pm}$ and Z^0 bosons are $m_W = 80.385 \pm 0.015$ GeV and $m_Z = 91.1876 \pm 0.0021$ GeV [1], respectively. Table 2.2 shows the four fundamental forces, the relative strength and range together with the theories and the mediators.

Force	Rel. Strength	Range [m]	Theory	Mediator	Mass [GeV]
Strong	10	10^{-15}	Chromodynamics	Gluon	0
Weak	10^{-13}	10^{-18}	Flavourdynamics	$W^{\pm}$ and Z^0 bosons	80.4/91.2
Electromagnetic	10^{-2}	∞	Electrodynamics	Photon	0
Gravitational	10^{-42}	∞	General relativity	Graviton	-

Table 2.2: The four fundamental forces with the relative strength, interaction range, describing theory, and the mediator with its mass. The gravitational force is not a part of the SM and the graviton is a theoretical particle.

2.1.2 Local Gauge Theory

The Lagrangian density of the SM for the free fields[1] listed in Eq. (2.1) is invariant under local gauge transformation[2]

$$\mathcal{L} = \bar{\psi}(i\gamma^\mu\partial_\mu - m)\psi + e\bar{\psi}\gamma^\mu\psi\boldsymbol{A}_\mu - \frac{1}{4}\boldsymbol{F}_{\mu\nu}\boldsymbol{F}^{\mu\nu} \tag{2.1}$$

where $\boldsymbol{F}_{\mu\nu} = \partial_\mu\boldsymbol{A}_\nu - \partial_\nu\boldsymbol{A}_\mu$. The local gauge transformation means the scalar field ψ and the vector field $\boldsymbol{A}_\mu$ transform as

$$\psi(x) \rightarrow \psi'(x) = e^{i\theta(x)}\psi(x) \tag{2.2}$$

$$\boldsymbol{A}_\mu(x) \rightarrow \boldsymbol{A}'_\mu(x) = \boldsymbol{A}_\mu(x) + \frac{1}{e}\partial_\mu\theta(x). \tag{2.3}$$

By introducing the gauge term, i.e. the vector field, the interacting force can be obtained by calculating the derivatives of the *Euler-Lagrange equations*. The gauge field can be associated to particular spin one gauge bosons which mediate the force. The number of the mediating gauge bosons is equal to the dimension of the symmetry group. From group theory, the dimension of an unitary group $U(n)$ is n^2. The special unitary group $SU(n)$ consists of $n \times n$ unitary matrices with determinant 1. Because the SM is based on a $SU(3)_C \otimes SU(2)_L \otimes U(1)_Y$ symmetry gauge group, the number of mediators are 8 for $SU(3)_C$, 3 for $SU(2)_L$, and 1 for $U(1)_Y$ corresponding to 8 gluons for the strong interaction, 3 gauge bosons ($W^\pm$ and Z^0) for weak interaction, and 1 photon for the electromagnetic interaction.

---

[1] This is the Lagrangian density of QED. The three terms are fermion kinematic term, photon kinematic term, and interaction, respectively.

[2] In Dirac representation, the four contravariant gamma matrices are $\gamma^0 = \begin{pmatrix} 1 & 0 & 0 & 0 \\ 0 & 1 & 0 & 0 \\ 0 & 0 & -1 & 0 \\ 0 & 0 & 0 & -1 \end{pmatrix}$,

$\gamma^1 = \begin{pmatrix} 0 & 0 & 0 & 1 \\ 0 & 0 & 1 & 0 \\ 0 & -1 & 0 & 0 \\ -1 & 0 & 0 & 0 \end{pmatrix}, \gamma^2 = \begin{pmatrix} 0 & 0 & 0 & -i \\ 0 & 0 & i & 0 \\ 0 & i & 0 & 0 \\ -i & 0 & 0 & 0 \end{pmatrix}, \gamma^3 = \begin{pmatrix} 0 & 0 & 1 & 0 \\ 0 & 0 & 0 & -1 \\ -1 & 0 & 0 & 0 \\ 0 & 1 & 0 & 0 \end{pmatrix}$

2.1.3 Strong interaction

Quantum Chromodynamics (QCD) is the theory that describes the strong interaction. The gauge bosons are the eight massless gluons which carry three different colors (and anti-colors), red, green, and blue. Quarks interact with gluons hence they also carry color charge C and can be represented in color triplets

$$\psi = \begin{pmatrix} \psi_r \\ \psi_g \\ \psi_b \end{pmatrix}. \tag{2.4}$$

QCD is based on the non-Abelian $SU(3)_C$ group which requires invariance under the local gauge transformation

$$\psi \to \psi' = e^{ig_s\alpha_a(x)T^a}\psi \tag{2.5}$$

where the g_s is the strong coupling constant, $\alpha_a(x)$ are arbitrary functions of space-time, and T^a are the generators of the non-Abelian $SU(3)_C$ group and the summation over a with $a = 1, \ldots, 8$ is implied. The Lagrangian density is invariant under the local gauge transformation by introducing the new form of the gauge fields and the covariant derivative

$$\boldsymbol{G}_\mu^a \to \boldsymbol{G}_\mu^a - \partial_\mu\alpha^a(x) - g_sf_{abc}\alpha^b(x)\boldsymbol{G}_\mu^c \tag{2.6}$$

$$\partial_\mu \to D_\mu = \partial_\mu + ig_sT_a\boldsymbol{G}_\mu^a \tag{2.7}$$

where f_{abc} is the structure constant. The Lagrangian density of QCD is given by

$$\mathcal{L}_{QCD} = \bar{\psi}(i\gamma^\mu\partial_\mu - m)\psi - g_s(\bar{\psi}\gamma^\mu T_a\psi)\boldsymbol{G}_\mu^a - \frac{1}{4}\boldsymbol{G}_{\mu\nu}^a\boldsymbol{G}_a^{\mu\nu} \tag{2.8}$$

where the field strength tensor $\boldsymbol{G}_{\mu\nu}^a = \partial_\mu\boldsymbol{G}_\nu^a - \partial_\nu\boldsymbol{G}_\mu^a - g_sf_{abc}\boldsymbol{G}_\mu^b\boldsymbol{G}_\nu^c$ causing self-interactions between the gluons. The strong force increases with distance between

quarks, therefore, the quarks exist only as color singlets such as mesons or baryons mentioned in Sect. 2.1.1. The production of a single quark is accompanied by the creation of an anti-quark from vacuum to form a quark and anti-quark pair as a color singlet. This is called *hadronisation.* The phenomena that confines quarks in the small interaction range is called *confinement.* But at small distance or high energy, the quarks can be considered as quasi-free particles. This is referred to as *asymptotic freedom.*

2.1.4 Electroweak interaction

Fermi formulated the first weak interaction theory in 1933 [45], however, the theory only holds for energies less than 100 GeV. Glashow, Salam, and Weinberg (GSW) proposed a new model [39, 41, 40] which unifies electromagnetic and weak forces to become the *electroweak* (EW) force and this new *GSW model* can apply to energies greater than 100 GeV. The electroweak theory is based on $SU(2)_L \otimes U(1)_Y$ gauge symmetry where the subscript L denotes left-handedness and Y denotes the weak hypercharge, a new quantum number, which relates to the electric charge Q and the weak isospin I_3 by the *Gell-Mann-Nishijima relation* [46, 47]

$$Y = 2(Q - I_3). \tag{2.9}$$

The left-handed and right-handed fermion field ψ can be decomposed into two components

$$\psi = P_L\psi + P_R\psi \tag{2.10}$$

$$= \psi_L + \psi_R \tag{2.11}$$

where the projection operators P_L and P_R are defined as[3]

$$P_L = \frac{1}{2}(1 - \gamma^5) \tag{2.12}$$

$$P_R = \frac{1}{2}(1 + \gamma^5). \tag{2.13}$$

The projection operators satisfy $P_L P_R = 0$ and $P_L + P_R = 1$. The local gauge transformations of $SU(2)_L \otimes U(1)_Y$ are

$$\psi_L \to \psi'_L = e^{i\alpha_a(x)T^a} e^{i\beta(x)Y} \psi_L \tag{2.14}$$

$$\psi_R \to \psi'_R = e^{i\beta(x)Y} \psi_R \tag{2.15}$$

where $T^a = \frac{\sigma^a}{2}$ are the generators of $SU(2)_L$ with Pauli matrix σ^a[4] and Y is the generator of $U(1)_Y$. The $\alpha_a(x)$ and $\beta(x)$ depend on space-time. The covariant derivative with respect to the $SU(2)_L \otimes U(1)_Y$ is

$$D_\mu = \partial_\mu + ig_W T_a \boldsymbol{W}^a_\mu + ig_Y Y \boldsymbol{B}_\mu \tag{2.16}$$

where g_W and g_Y are coupling constants and $\boldsymbol{W}^a_\mu$ ($a = 1, 2, 3$) and $\boldsymbol{B}_\mu$ are the gauge fields. The gauge fields $\boldsymbol{W}^a_\mu$ and $\boldsymbol{B}_\mu$ transform under the $SU(2)_L \otimes U(1)_Y$ symmetry as

$$\boldsymbol{W}^a_\mu \to \boldsymbol{W}^a_\mu - \frac{1}{g_W}\partial_\mu\alpha^a(x) - \epsilon^{abc}\alpha^b(x)\boldsymbol{W}^c_\mu \tag{2.17}$$

$$\boldsymbol{B}_\mu \to \boldsymbol{B}_\mu - \frac{1}{g_Y}\partial_\mu\beta(x) \tag{2.18}$$

where ϵ^{abc} is the Levi-Civita tensor. The electroweak Lagrangian density is given by

$$\mathcal{L}_{EW} = \bar{\psi}_L(i\gamma^\mu D_\mu - m)\psi_L + \bar{\psi}_R(i\gamma^\mu D_\mu - m)\psi_R - \frac{1}{4}\boldsymbol{W}^a_{\mu\nu}\boldsymbol{W}^{\mu\nu}_a - \frac{1}{4}\boldsymbol{B}_{\mu\nu}\boldsymbol{B}^{\mu\nu} \tag{2.19}$$

---

[3]γ^5 is the product of the four gamma matrices. $\gamma^5 = i\gamma^0\gamma^1\gamma^2\gamma^3 = \begin{pmatrix} 0 & 0 & 1 & 0 \\ 0 & 0 & 0 & 1 \\ 1 & 0 & 0 & 0 \\ 0 & 1 & 0 & 0 \end{pmatrix}$

[4]The Pauli matrices are $\sigma_1 = \begin{pmatrix} 0 & 1 \\ 1 & 0 \end{pmatrix}$, $\sigma_2 = \begin{pmatrix} 0 & -i \\ i & 0 \end{pmatrix}$, and $\sigma_3 = \begin{pmatrix} 1 & 0 \\ 0 & -1 \end{pmatrix}$

where $\boldsymbol{W}_{\mu\nu}^a$ and $\boldsymbol{B}_{\mu\nu}$ are the field strength tensors

$$\boldsymbol{W}_{\mu\nu}^a = \partial_\mu \boldsymbol{W}_\nu^a - \partial_\nu \boldsymbol{W}_\mu^a - g_W \epsilon^{abc} \boldsymbol{W}_\mu^b \boldsymbol{W}_\nu^c \tag{2.20}$$

$$\boldsymbol{B}_{\mu\nu} = \partial_\mu \boldsymbol{B}_\nu - \partial_\nu \boldsymbol{B}_\mu \tag{2.21}$$

and $\bar{\psi} \equiv \psi^\dagger \gamma^0$ is the adjoint spinor of ψ[5]. Therefore, the mass eigenstates are the mixture of the gauge fields

$$\boldsymbol{W}_\mu^\pm = \frac{1}{\sqrt{2}}(\boldsymbol{W}_\mu^1 \mp i\boldsymbol{W}_\mu^2) \tag{2.22}$$

$$\begin{pmatrix} \boldsymbol{A}_\mu \\ \boldsymbol{Z}_\mu \end{pmatrix} = \begin{pmatrix} \cos\theta_W & \sin\theta_W \\ -\sin\theta_W & \cos\theta_W \end{pmatrix} \begin{pmatrix} \boldsymbol{B}_\mu \\ \boldsymbol{W}_\mu^3 \end{pmatrix}. \tag{2.23}$$

Thus, the mass eigenstates $\boldsymbol{A}_\mu$, $\boldsymbol{W}_\mu^\pm$, and $\boldsymbol{Z}_\mu$ are identified as the photon, γ, $W^\pm$ and Z^0 bosons experimentally. The *Weinberg weak mixing angle* θ_W is defined as

$$\tan\theta_W = \frac{g_Y}{g_W}. \tag{2.24}$$

The coupling constants g_W and g_Y are related to the electric charge by

$$e = g_W \sin\theta_W = g_Y \cos\theta_Y. \tag{2.25}$$

And the weak eigenstates of quark, q', are the linear combinations of the mass eigenstates of quark, q, by the *Cabbibo-Kobayashi-Maskawa* (CKM) matrix [48]

$$\begin{pmatrix} d' \\ s' \\ b' \end{pmatrix} = \begin{pmatrix} V_{ud} & V_{us} & V_{ub} \\ V_{cd} & V_{cs} & V_{cb} \\ V_{td} & V_{ts} & V_{tb} \end{pmatrix} \begin{pmatrix} d \\ s \\ b \end{pmatrix}. \tag{2.26}$$

The CKM matrix allows the quarks to change their flavor and generation as observed in experiments. Similarly, the *Pontecorvo-Maki-Nakagawa-Sakata* (PMNS) matrix [49] is responsible for the flavor changing of the neutrinos.

---

[5]$\psi^\dagger$ is the hermitian conjugate of ψ

Spontaneous symmetry breaking and the Higgs mechanism

The gauge bosons of the weak interaction, $W^\pm$ and Z^0, are massive particles[6]. However, the existence of the mass terms violate the gauge invariance of the $\mathcal{L}_{EW}$. In order to explain the mass of gauge bosons, the Englert-Brout-Higgs mechanism [50, 51, 52, 53, 54] was proposed in 1964. A new scalar complex $SU(2)_L$ doublet field Φ is introduced in the Higgs mechanism

$$\Phi = \begin{pmatrix} \Phi^+ \\ \Phi^0 \end{pmatrix} = \begin{pmatrix} \Phi_1 & i\Phi_2 \\ \Phi_3 & i\Phi_4 \end{pmatrix} \tag{2.27}$$

with hypercharge $Y = 1$ and four degrees of freedom, Φ_i, which are scalar fields and called the *Goldstone modes*. The Lagrangian density for this new field, the Higgs field, is

$$\mathcal{L}_\Phi = (D^\mu \Phi)^\dagger (D_\mu \Phi) - V(\Phi) \tag{2.28}$$

where the Higgs potential is defined as

$$V(\Phi) = \mu^2 |\Phi|^2 + \lambda |\Phi|^4 \tag{2.29}$$

where μ and λ are free parameters. The Higgs potential is shown in Fig. 2.1. The Higgs potential is invariant under the rotation $U(1)$ symmetry. Choosing any of the points at the bottom of the Higgs potential breaks the symmetry spontaneously. The *spontaneously symmetry breaking* (SSB) means the Lagrangian remains invariant under certain symmetry but no longer invariant at the ground state.

Because the Higgs potential is invariant under $SU(2)_L \otimes U(1)_Y$, the parameters μ and λ must satisfy $\mu^2 < 0$ and $\lambda > 0$ resulting in a set of degenerate ground

---

[6]$m_W = 80.385 \pm 0.015$ GeV and $m_Z = 91.1876 \pm 0.0021$ GeV
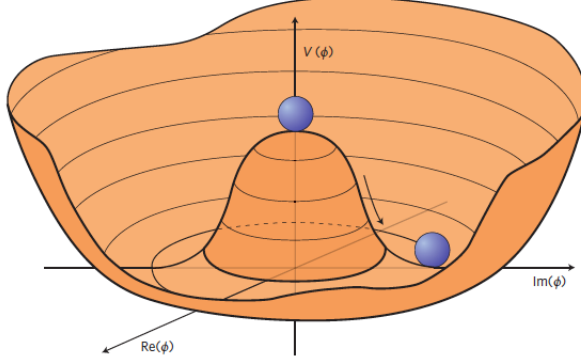
Figure 2.1: An illustration of the Higgs potential which has the form of a "Mexican hat" [5].

states where $\langle 0|\Phi|0 \rangle \neq 0$. Among the degenerate ground states, the ground state is often chosen to have the form

$$\Phi = \frac{1}{\sqrt{2}} \begin{pmatrix} 0 \\ v \end{pmatrix} \tag{2.30}$$

where $v = \sqrt{-\mu^2/\lambda}$ is the *the vacuum expectation value* (VEV). This particular choice of the ground state breaks the $SU(2)_L \otimes U(1)_Y$ symmetries spontaneously and ensures the unbroken electromagnetic interaction under $U(1)_{EM}$ symmetry and photon being massless. By introducing a massive particle, Higgs boson H, the Higgs field can be re-written as

$$\Phi = \frac{1}{\sqrt{2}} \begin{pmatrix} 0 \\ v + H \end{pmatrix} \tag{2.31}$$

and the kinematic term of the Lagrangian density becomes

$$\mathcal{L}_\Phi^{\text{kinematic}} = (D^\mu \Phi)^\dagger (D_\mu \Phi) \tag{2.32}$$

$$= \frac{1}{2} \partial_\mu H \partial^\mu H + (v + H)^2 \left\{ \frac{g_W^2}{4} \boldsymbol{W}_\mu^\dagger \boldsymbol{W}^\mu + \frac{g_W^2}{8 \cos^2 \theta_W} \boldsymbol{Z}_\mu^\dagger \boldsymbol{Z}^\mu \right\} \tag{2.33}$$

and the Higgs potential is now

$$V(\Phi) = -\frac{v^2 \lambda}{2} (v + H)^2 + \frac{\lambda}{4} (v + H)^4. \tag{2.34}$$

15

Thus the masses of the $W^{\pm}$ and Z^0 are obtained by the interaction between the gauge bosons and Higgs boson. The masses are defined as

$$m_H = v\sqrt{2\lambda}, \quad m_W = \frac{v}{2}g_W, \quad m_Z = \frac{v}{2}\sqrt{g_W^2 + g_Y^2}, \quad m_\gamma = 0. \qquad (2.35)$$

However, the masses of fermions are obtained by the *Yukawa interaction*

$$\mathcal{L}_{\text{Yukawa}} = y_f \bar{L}_L \Phi f_R + y_f \bar{Q}_L \Phi f_R + \text{h.c.} \qquad (2.36)$$

where the y_f is *Yukawa coupling*, f stands for $\{\ell^i, u^i, d'^i\}$ and h.c. represents the hermitian conjugate, respectively. The $\bar{L}_L$ and $\bar{Q}_L$ are the left-handed lepton and quark doublet and f_R is the lepton or quark singlet. The mass of fermions is defined as

$$m_f = \frac{v}{\sqrt{2}} y_f \qquad (2.37)$$

where y_f is a free parameter which causes the fermion mass not to be predictable. Finally, the non-zero VEV, v, can be related to *Fermi constant*, G_F, by

$$v = \frac{1}{\sqrt{\sqrt{2}G_F}} \approx 246 \text{ GeV}. \qquad (2.38)$$

2.1.5 The discovery of the Higgs boson

The SM predictions are successfully confirmed by experimental observations besides the existence of the theoretical Higgs boson. The search for the Higgs boson has become a major goal of experimental particle physicists. A Higgs-like resonance was discovered and announced on July 4th 2012 by the ATLAS[7] and CMS[8] collaborations [6, 7]. By combining the data with integrated luminosities of 4.8 fb^{-1} collected at $\sqrt{s} = 7$ TeV in 2011 and 5.8 fb^{-1} at $\sqrt{s} = 8$ TeV

---

[7]A Toroidal LHC ApparatuS
[8]Compact Muon Solenoid

in 2012, the ATLAS experiment measured the mass of the Higgs boson to be 126.0 ± 0.4 (stat.) ± 0.4 (syst.) GeV with significance of 5.9σ corresponding to a background fluctuation probability of 1.7×10^{-9} [6]. In the meantime, the CMS experiment announced the mass of the Higgs boson to be 125.3 ± 0.4 (stat) ± 0.5 (syst.) GeV with significance 5.0σ using integrated luminosities of up to 5.1 fb^{-1} at 7 TeV and 5.3 fb^{-1} at 8 TeV [7]. The $H \rightarrow ZZ^{(*)} \rightarrow 4\ell$, $H \rightarrow \gamma\gamma$, and $H \rightarrow WW^{(*)} \rightarrow e\nu\mu\nu$ channels were studied by the ATLAS collaboration and the $H \rightarrow \gamma\gamma, ZZ, W^+W^-, \tau^+\tau^-$, and $b\bar{b}$ channels were studied by the CMS collaboration. Figure 2.2 shows the local p-value as a function of the Higgs mass for ATLAS and CMS results, respectively.

(a) ATLAS results   **(b)** CMS results
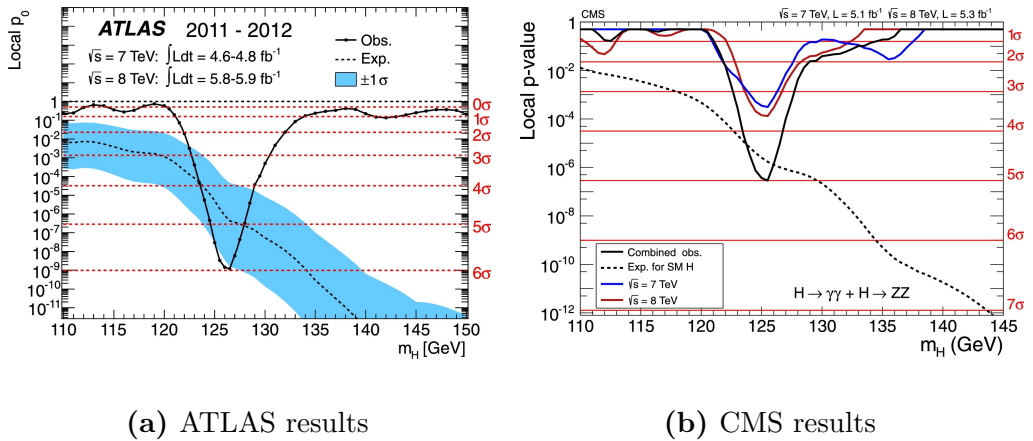
Figure 2.2: The observed local p-value as a function of m_H for the ATLAS [6] and CMS [7] experiments, respectively. The dashed line shows the expected local p_0 for a SM Higgs boson. The horizontal lines denotes the p-values corresponding to significances of 1 to 6σ.

2.2 Beyond the Standard Model

Although the SM is an incredible successful theory for explaining the phenomenon in particle physics, it leaves some questions which cannot be answered. Some of the unanswered questions are introduced in the rest part of this section.

2.2.1 Hierarchy problem

The weakest force in the SM is the weak force but the strength of the weak force is 10^{24} times as strong as the gravitational force which isn't incorporated into the SM. The large discrepancy between the weak force and the gravitational force is called the hierarchy problem [9, 55, 56]. The classical potential of the SM Higgs field Φ is

$$V(\Phi) = \mu^2 |\Phi|^2 + \lambda |\Phi|^4. \tag{2.39}$$

Since the SM requires the VEV for Φ, $\langle \Phi \rangle$, at the minimum of the potential to be non-vanishing, this is only satisfied if $\mu^2 < 0$ and $\lambda > 0$. However, the parameter μ^2 receives enormous radiative corrections causing it to be ultraviolet divergent as shown in Eq. (2.40).

$$\mu^2 = \mu_{bare}^2 - \frac{|\lambda_f|^2}{8\pi} \Lambda_{UV}^2 + \mathcal{O}(\Lambda_{UV}^2) \tag{2.40}$$

where μ_{bare} is the Higgs mass, $-\frac{|\lambda_f|^2}{8\pi} \Lambda_{UV}^2$ is the one-loop correction, and Λ_{UV} is an ultraviolet momentum cutoff which is valid up to the Plank scale 10^{19} GeV. The electroweak gauge bosons $W^{\pm}$ and Z^0 obtain their finite masses from $\langle \Phi \rangle$ so μ^2 cannot be divergent. There must some unknown mechanism to protect it from diverging.

2.2.2 Dark matter and dark energy

The matter we know today composes only 5% [57, 58] of the content of the universe and the remaining part is something we don't know. This unknown matter is called *Dark Matter* (DM) [59] which makes up about 27% of the universe and the other 68% is called *Dark Energy* (DE) [57, 58]. Because DM interacts weakly and doesn't interact with the electromagnetic force, it doesn't absorb, emit, or reflect light causing it to be hard to detect directly. The name DM comes because it is invisible. Dark energy is distributed evenly in both space and time throughout the universe so it doesn't dilute as the universe expands. The observed scientific data hints that the presence of DE is necessary to explain the accelerated expansion of the universe.

2.2.3 Grand Unification

Maxwell unified electricity and magnetism into electromagnetism in the 1860s. About a century later, physicists successfully developed an electroweak theory which links the electromagnetic and the weak force. Because of the triumph of the electroweak theory, theorists have raised the question of the possibility of unifying all forces. The *Grand Unified Theory* (GUT) [60], which tries to link three of the four known forces together, was developed in the mid-1970s by theorists. The GUT proposes that the electromagnetic force, weak force, and strong force unify to one force at the GUT scale, $\Lambda_{GUT} \approx 10^{16}$ GeV. So the three running coupling constants [61] are expected to converge at the GUT scale. However, the current experimental results show the coupling constants are still different at the GUT scale as shown in Fig. 2.3.
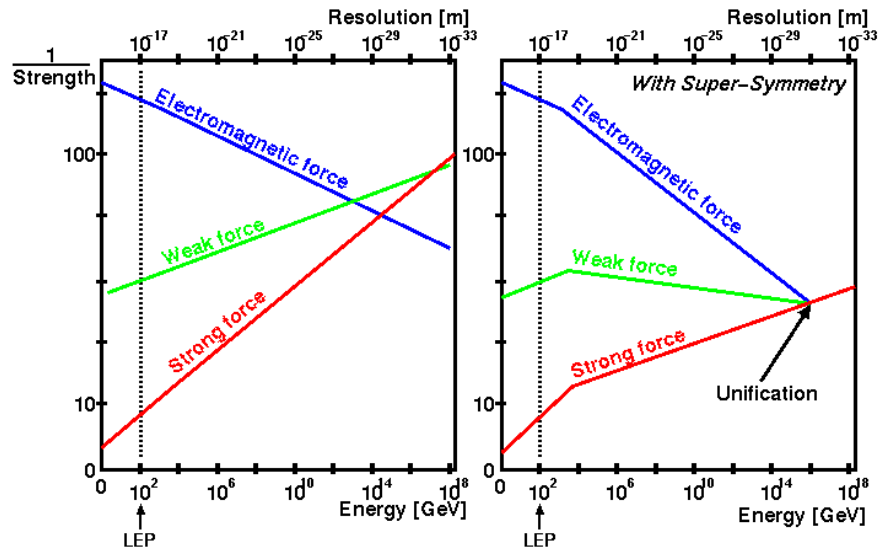
Figure 2.3: The measured running coupling constants in the SM (left) and prediction in the GUT (right) [8]. The three lines show the inverse value of the coupling constant for the three fundamental forces.

2.2.4   More questions

There are some more interesting questions for which we don't know the answers. For example, we don't know the reason why there are 61 elementary particles and more than 20 arbitrary parameters in the SM. Also, the SM doesn't explain why there are only three generations. The amount of matter and anti-matter were equal at the beginning of the universe based on the prediction of the SM but matter dominates in the current universe which the SM does not explain.

In order to answer these questions, there are many theories being developed beyond the SM but none of them have yet been observed. One of the most probable candidates for answering these question is supersymmetry which will be introduced in the next chapter.

CHAPTER 3

SUPERSYMMETRY

The SM [39, 40, 41, 42, 43] has been a stupendous success in predicting and explaining the physics phenomena of the elementary particles. However, the SM leaves several open questions unanswered as mentioned in Sect. 2.2. Many different models of new physics were proposed to explain those unanswered questions. Among these new models, *supersymmetry* (SUSY) [25, 62, 63, 9, 64, 65, 66, 67, 68] is favored by most physicists. SUSY proposed by Wess and Zumino [25] in the early 1970s is a symmetry that relates bosonic and fermionic degrees of freedom. It extends the SM by requiring that every SM boson/fermion has a fermonic/bosonic supersymmetric partner and vice versa. The reason why physicists favor SUSY is described in Sect. 3.1 and the introduction of SUSY as well as the formalism are given in Sect. 3.2. The *Radiative Natural SUSY* (RNS) and the *Non-Universal Higgs Mass model* with two extra parameters (NUHM2) are described in Sect. 3.3 and 3.4, respectively.

3.1 Why supersymmetry

The SM leaves several unanswered questions; for example, the hierarchy problem (Sect. 2.2.1), and what are the candidates of dark matter (Sect. 2.2.2), and why don't the running coupling constants unify at the GUT level (Sect. 2.2.3). SUSY provides good explanations for these questions.
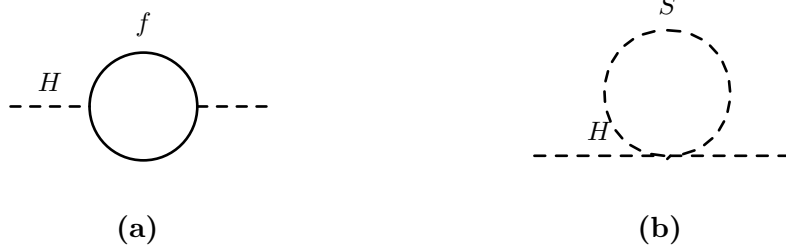
Figure 3.1: The Feynman diagram for the one loop correction to the Higgs squared mass due to (a) a fermion f and (b) a scalar S [9].

The hierarchy problem

The SM predicts the Higgs squared mass diverges at the Plank scale $\sim 10^{19}$ GeV. However, the fact that $W^{\pm}$ and Z^0 gauge bosons obtain their finite mass through the Higgs mechanism indicates the Higgs squared mass must be finite. Figure 3.1 shows the Feynman diagram for the one loop correction to the Higgs squared mass due to a fermion f and a scalar S. The corrections are

$$\Delta m_H^2 = -\frac{|\lambda_f^2|}{8\pi^2}\Lambda_{UV}^2 + \cdots, \quad \text{fermion} \tag{3.1}$$

$$\Delta m_H^2 = \frac{\lambda_S}{16\pi^2}\Lambda_{UV}^2 + \cdots, \quad \text{boson} \tag{3.2}$$

where the Λ_{UV} is an ultraviolet momentum cutoff which is valid up to the Plank scale 10^{19} GeV. The corrections diverge when Λ_{UV} becomes very large. Because the contributions from the fermion and scalar loops have opposite sign, the divergent contributions can be canceled out if there is a scalar loop for each fermonic loop. SUSY predicts the existence of the bosonic/fermonic sparticles. Therefore, if $\lambda_S = 2|\lambda_f^2|$ then SUSY maintain the finiteness of the Higgs squared mass in a natural way.

Dark matter

Dark matter (DM) makes up about 27% of the universe and might originate from neutral relics from the early universe. The cosmologic observations of DM indicate that the dark matter should be electrically neutral, cold, massive, and participates only in weak and gravitational interactions. Therefore, the DM candidate should be a new particle that is a *weakly interacting massive particle* (WIMP). SUSY requires that all the sparticles are produced in pairs that decay into stable the *lightest SUSY particles* (LSP) with odd number. If there are a lot of sparticles produced in the early Universe, they will have to decay to LSPs and remain until the present day because the LSP is stable. The LSP is a weakly interacting massive particle. LSPs do not interact electromagnetically so they cannot be scattered by photons and thus are dark. There are three kinds of LSP that could be a possible DM candidate: the lightest *neutralino*, the lightest *sneutrino* and the *gravitino*.

Grand Unification

Grand Unified Theories (GUT) try to unify the strong and electroweak interactions. There will be only one interaction and one coupling constant at the GUT scale ($\approx 10^{16}$ GeV). However, the current coupling constants for electromagnetic, weak, and strong interactions do not unify at the GUT scale as shown in the left hand side of Fig. 2.3. This problem can be solved by introducing SUSY which modifies the renormalization group equations and makes the running gauge couplings converge at the GUT scale. The right hand side of Fig. 2.3 shows the running gauge couplings in SUSY.

3.2 Introduction to supersymmetry

A brief overview of SUSY is introduced in this section. The mathematical foundation of the SUSY, superalgebra, is described in Sect. 3.2.1 followed by the superspace and superfields in Sect. 3.2.2.

3.2.1 Superalgebra

Poincaré algebra

SUSY is based on superalgebra which is an extension of space-time Poincaré algebra. The Poincaré group is a product of the Lorentz group and the group of translations in space-time. A Lorentz group must satisfies the commutation relations

$$[J_i^+, J_j^+] = i\epsilon_{ijk}J_k^+, \quad [J_i^-, J_j^-] = i\epsilon_{ijk}J_k^-, \quad [J_i^+, J_j^-] = 0 \quad , \tag{3.3}$$

where $i, j, k = 1, 2, 3$. If the six Lorentz group generators are combined into an antisymmetric second rank tensor generator $M_{\mu\nu}$ where $M_{ij} = \epsilon_{ijk}J_k$ and $M_{0i} = -M_{i0} = -K_i$[1] and the generator of the translation groups is P_μ, the energy-momentum operator, then the commutation relations of the Poincaré group are

$$[P_\mu, P_\nu] = 0 \quad , \tag{3.4}$$

$$[M_{\mu\nu}, P_\lambda] = i(g_{\nu\lambda}P_\mu - g_{\mu\lambda}P_\nu) \quad , \tag{3.5}$$

$$[M_{\mu\nu}, M_{\rho\sigma}] = -i(g_{\mu\rho}M_{\nu\sigma} - g_{\mu\sigma}M_{\nu\rho} - g_{\nu\rho}M_{\mu\sigma} + g_{\nu\sigma}M_{\mu\rho}) \quad , \tag{3.6}$$

---

[1] The J_i and K_i with $i = 1, 2, 3$ are rotation and boost generators in 3-dimensions, respectively. And the ladder operators are defined as $J_i^\pm = \frac{1}{2}(J_i \pm iK_i)$.

where the metric is

$$g_{\mu\nu} = \begin{pmatrix} 1 & 0 & 0 & 0 \\ 0 & -1 & 0 & 0 \\ 0 & 0 & -1 & 0 \\ 0 & 0 & 0 & -1 \end{pmatrix} \quad . \tag{3.7}$$

Spinors

A general spin $\frac{1}{2}$ particle state, χ, can be expressed as a *spinor* in SUSY using the two-component spin up χ_+ and spin down χ_- column matrices

$$\chi = c_+\chi_+ + c_-\chi_- = c_+ \begin{pmatrix} 1 \\ 0 \end{pmatrix} + c_- \begin{pmatrix} 0 \\ 1 \end{pmatrix} = \begin{pmatrix} c_+ \\ c_- \end{pmatrix} \quad . \tag{3.8}$$

The solution of the Dirac equation[2], ψ_D[3], can be expressed using the left-handed and right-handed *Weyl spinors* ψ_L and ψ_R

$$\psi_D = \begin{pmatrix} \psi_1 \\ \psi_2 \\ \psi_3 \\ \psi_4 \end{pmatrix} = \left(\begin{Bmatrix} \psi_1 \\ \psi_2 \\ \psi_3 \\ \psi_4 \end{Bmatrix} \right) = \begin{pmatrix} \psi_L \\ \psi_R \end{pmatrix} \quad . \tag{3.9}$$

It is convenient to use the Weyl spinors to represent the building blocks for any fermion field. The Majorana spinor $\tilde{\psi}_M$ is a real solution of Dirac equation. It is its own charge conjugate and satisfies the Majorana condition

$$\tilde{\psi}_M = \tilde{\psi}_M^* \quad . \tag{3.10}$$

The Majorana spinor can be expressed in terms of the Weyl spinors

$$\psi_M = \begin{pmatrix} \xi_\alpha \\ \bar{\xi}^{\dot{\alpha}} \end{pmatrix} \quad , \tag{3.11}$$

---

[2]The Dirac equation is $(i\gamma^\mu\partial_\mu - m)\psi = 0$.
[3]The Dirac spinor ψ_D is a four-component field which can be expressed using a four-component matrix.

where the left-handed Weyl spinor ξ_α and the right-handed Weyl spinor $\bar{\xi}^{\dot{\alpha}}$ are the Hermitian conjugate of each other.

Helicity

A particle with momentum $\vec{p}$ and angular momentum $\vec{J}$ has *helicity* defined as

$$h = \vec{J} \cdot \hat{p} = (\vec{L} + \vec{S}) \cdot \hat{p} = \vec{S} \cdot \hat{p}, \quad \hat{p} = \frac{\vec{p}}{|\vec{p}|} \quad . \tag{3.12}$$

The eigenvalues of h are $+1$ and -1 corresponding to right-handed and and left-handed eigenstates. Although helicity is rotational invariant but not boost invariant, the helicity of a massless particle moving at the speed of light is Lorentz invariant.

3.2.2 Superspace and superfields

Superspace is composed of ordinary space-time coordinates and four anticommuting fermionic coordinates θ_α and $\bar{\theta}_{\dot{\alpha}}$ where the spinor indices α and $\dot{\alpha}$ can be 1 or 2. A superfield $S(x^\mu, \theta_\alpha, \bar{\theta}_{\dot{\alpha}})$ is a function in superspace. The general form of a superfield can be expressed in terms of θ and $\bar{\theta}$

$$S(x, \theta, \bar{\theta}) = a + \theta\xi + \bar{\theta}\bar{\chi} + \theta\theta b + \bar{\theta}\bar{\theta}c + \bar{\theta}\bar{\sigma}^\mu\theta v_\nu + \theta\theta\bar{\theta}\bar{\zeta} + \bar{\theta}\bar{\theta}\theta\eta + \theta\theta\bar{\theta}\bar{\theta}d \quad , \tag{3.13}$$

where all spinor indices are suppressed. The a, b, c, d, and v_μ are bosonic fields and $\xi, \bar{\chi}, \bar{\zeta}, \eta$ are fermionic fields which are complex functions of x^μ. The SUSY generators Q_α and $\bar{Q}_{\dot{\alpha}}$ can be expressed as

$$Q_\alpha = -i\frac{\partial}{\partial\theta^\alpha} - \sigma^\mu_{\alpha\dot{\beta}}\bar{\theta}^{\dot{\beta}}\partial_\mu, \quad \bar{Q}_{\dot{\alpha}} = i\frac{\partial}{\partial\bar{\theta}^{\dot{\alpha}}} + \theta^\beta\sigma^\mu_{\beta\dot{\alpha}}\partial_\mu \quad , \tag{3.14}$$

and the commutation relations are

$$\{Q_\alpha, \bar{Q}_{\dot{\beta}}\} = -2i\sigma^\mu_{\alpha\dot{\beta}}\partial_\mu, \quad \{Q_\alpha, Q_\beta\} = \{\bar{Q}_{\dot{\alpha}}, \bar{Q}_{\dot{\beta}}\} = 0 \quad . \tag{3.15}$$

The SUSY covariant derivatives are defined as

$$D_\alpha = \frac{\partial}{\partial\theta^\alpha} + i\sigma^\mu_{\alpha\dot\beta}\bar\theta^{\dot\beta}\partial_\mu, \quad \bar D_{\dot\alpha} = (D_\alpha)^\dagger = \frac{\partial}{\partial\bar\theta^{\dot\alpha}} + i\theta^\beta\sigma^\mu_{\beta\dot\alpha}\partial_\mu \qquad (3.16)$$

and the commutation relations are

$$\{D_\alpha, \bar D_{\dot\beta}\} = 2i\sigma^\mu_{\alpha\dot\beta}\partial_\mu, \quad \{D_\alpha, D_\beta\} = \{\bar D_{\dot\alpha}, \bar D_{\dot\beta}\} = 0 \quad . \qquad (3.17)$$

The SUSY covariant derivatives anticommute with the SUSY generators[4].

Chiral superfields and vector superfields

The spin 0 bosons and spin 1/2 fermions are described using the *chiral superfield*
and the spin 1 gauge bosons are described using the *vector superfields.* $V(x,\theta,\bar\theta)$.
The chiral superfield, $\Phi(x,\theta,\bar\theta)$, satisfies the condition[5]

$$\bar D_{\dot\alpha}\Phi = 0 \quad . \qquad (3.18)$$

If we redefine the new coordinates (y^μ,θ) and $(\bar y^\mu,\bar\theta)$ in the superspace[6],

$$y^\mu = x^\mu + i\theta\sigma^\mu\bar\theta, \quad \bar y^\mu = x^\mu - i\theta\sigma^\mu\bar\theta \quad , \qquad (3.19)$$

then the covariant derivatives become

$$D_\alpha = \frac{\partial}{\partial\theta^\alpha} + 2i\sigma^\mu_{\alpha\dot\beta}\bar\theta^{\dot\beta}\frac{\partial}{\partial y^\mu}, \quad \bar D_{\dot\alpha} = \frac{\partial}{\partial\bar\theta^{\dot\alpha}} \quad . \qquad (3.20)$$

And the general form of a chiral superfield can be expressed in terms of the chiral
coordinate (y^μ,θ) only

$$\Phi(y,\theta) = \phi(y) + \sqrt{2}\theta\psi(y) + \theta\theta F(y) \quad . \qquad (3.21)$$

---

[4] $\{D_\alpha, Q_\beta\} = \{D_\alpha, \bar Q_{\dot\beta}\} = \{\bar D_{\dot\alpha}, Q_\beta\} = \{\bar D_{\dot\alpha}, \bar Q_{\dot\beta}\} = 0$.
[5] The antichiral superfield satisfies $D_\alpha\Phi^* = 0$ where Φ^* is the complex conjugate of Φ.
[6] The chiral coordinate is (y^μ,θ) and the antichiral coordinate is $(\bar y^\mu,\bar\theta)$.

The vector superfield, V, is a real field[7] and the general form is

$$V(x, \theta, \bar{\theta}) = C + i\theta\chi - i\bar{\theta}\bar{\chi} + \theta\sigma^\mu\bar{\theta}v_\mu + \frac{i}{2}\theta\theta(M + iN) - \frac{i}{2}\bar{\theta}\bar{\theta}(M - iN)$$

$$+ i\theta\theta\bar{\theta}(\bar{\lambda} + \frac{i}{2}\bar{\sigma}^\mu\partial_\mu\chi) - i\bar{\theta}\bar{\theta}\theta(\lambda - \frac{i}{2}\sigma^\mu\partial_\mu\bar{\chi}) + \frac{1}{2}\theta\theta\bar{\theta}\bar{\theta}(D - \frac{1}{2}\partial^2 C) \quad , \tag{3.22}$$

where the C, M, N, D are real scalars, the χ, λ are Weyl spinors, and the v_μ is a vector field. By applying the Wess-Zumino gauge, the general form can be reduced into

$$V_{WZ} = \theta\sigma^\mu\bar{\theta}v_\mu + i\theta\theta\bar{\theta}\bar{\lambda} - i\bar{\theta}\bar{\theta}\theta\lambda + \frac{1}{2}\theta\theta\bar{\theta}\bar{\theta}D \tag{3.23}$$

The non-vanishing power of V_{WZ} is $V_{WZ}^2 = \frac{1}{2}\theta\theta\bar{\theta}\bar{\theta}v_\mu v^\mu$. The higher power of V_{WZ} all vanish $V_{WZ}^n = 0, n \geq 3$.

3.2.3 R-parity

The baryon number B and lepton number L are conserved in the SM but violated in SUSY. Therefore, a new symmetry called R-parity is introduced to eliminate the B and L violating term. R-parity is defined as

$$R \equiv (-1)^{3(B-L)+2s} \quad , \tag{3.24}$$

where s is the spin of the particle. All of the SM particles have even R-parity ($R = +1$), while all of the sparticles have odd R-parity ($R = 1$). If the R-parity is conserved, SUSY predicts that sparticles are produced in pairs in collider experiments.

---

[7]The vector superfield satisfies $V(x, \theta, \bar{\theta}) = V^\dagger(x, \theta, \bar{\theta})$.

3.2.4 Supersymmetry breaking

The supermultiplets are single particle states in SUSY theory and correspond to the irreducible representations of the super-Poincaré algebra. A supermultiplet contains boson and fermion with the same degrees of freedom and the same mass. However, no sparticles have been observed from the experiments. Therefore, SUSY must be spontaneously broken and the sparticles must be heavier than their SM partners. The scalar superpotential V can be represented by the auxiliary fields F_i and D_a

$$V = F^{*i} F_i + \frac{1}{2} \sum_a D^a D_a \quad . \tag{3.25}$$

A state $|\Omega\rangle$ is called a vacuum state if $E_\Omega = \langle \Omega | H | \Omega \rangle = 0$. This happens when the potential V has a minimum. There are two kinds of vacuums, the true vacuum and the false vacuum which correspond to the global minimum and the local minimum of the scalar potential V, respectively. For example, when $F_i = D_a = 0$, then $V = 0$ is a global minimum. The $\langle F \rangle = 0$ is called F-term breaking and the $\langle D \rangle = 0$ is called D-term breaking.

3.2.5 The Minimal Supersymmetry Standard Model

The Minimal Supersymmetry Standard Model (MSSM) is the minimal extension of the Standard Model. The MSSM contains only the smallest number of superfields and interactions such that the SM particles can keep their current forms.

Particle content

All the super particles, *sparticles*[8], have exactly the same quantum number as their SM particles except the spins differ by $\frac{1}{2}$. The super partners of the leptons and quarks are called *sleptons* and *squarks*. The sleptons and squarks are scalar particles with spin $s = 0$. The left-handed and right-handed states are treated as different particles such that SM particles and SUSY **s**particles have the same number of degrees of freedom. The super partners of gluons are *gluinos*. There are eight gluinos with spin $s = \frac{1}{2}$. The super partners of the gauge bosons $W^{\pm}, Z^0$, and γ, are *gauginos*. The gauginos have spin $s = \frac{1}{2}$. The super partners of the Higgs bosons[9] are *Higgsinos*. The Higgsino and gaugino mixing states are two *charginos* $\tilde{\chi}_1^{\pm}, \tilde{\chi}_2^{\pm}$ and four *neutralinos* $\tilde{\chi}_1^0, \tilde{\chi}_2^0, \tilde{\chi}_3^0, \tilde{\chi}_4^0$, each with spin $s = \frac{1}{2}$. Table 3.1 shows the particle contents in the MSSM.

3.3 Radiative natural SUSY

Radiative natural SUSY (RNS) [69, 70, 71, 72] is a framework based on MSSM and may be vaild all the way up to the GUT scale[10]. RNS maintains the Higgs mass $m_H \sim 125$ GeV and Z boson mass $m_Z = 91.2$ GeV and requires no large cancellations at the electroweak scale. It also expects the light Higgsino masses to be $100 \sim 300$ GeV, the electroweak gaugino masses $300 \sim 1200$ GeV, the masses of $\tilde{g}$, $\tilde{t}$, and $\tilde{b}$ to be $1 \sim 4$ TeV, and the masses of $\tilde{u}$, $\tilde{d}$, $\tilde{s}$, $\tilde{c}$ exist in the $5 \sim 30$ TeV range.

---

[8]The super particles of the SM fermions have prefix a "*s*" and the super particles of the SM bosons have suffix an "*ino*". A tilde is added on the symbol of the SM particle to denote its super partner.

[9]The Higgs sector contains two charged states $H^{\pm}$ and three neutral states h^0, H^0, and A^0. The $h^0 and H^0$ are CP even states and A^0 is a CP odd state.

[10]The GUT scale is about $m_{\mathrm{GUT}} \approx 2 \times 10^{16}$ GeV.

Supermultiplet	Names	Symbol	spin 0	spin 1/2	spin 1	$SU(3)_C \otimes SU(2)_L \otimes U(1)_Y$
Chiral	squarks, quarks ($\times$3 families)	Q	$(\widetilde{u}_L, \quad \widetilde{d}_L)$	$(u_L, \quad d_L)$	-	$\mathbf{3} \otimes \mathbf{2} \otimes \frac{1}{6}$
		$\overline{u}$	$\widetilde{u}_R^*$	$u_R^\dagger$	-	$\overline{\mathbf{3}} \otimes \mathbf{1} \otimes -\frac{2}{3}$
		$\overline{d}$	$\widetilde{d}_R^*$	$d_R^\dagger$	-	$\overline{\mathbf{3}} \otimes \mathbf{1} \otimes \frac{1}{3}$
Chiral	sleptons, leptons ($\times$3 families)	L	$(\widetilde{\nu}, \quad \widetilde{e}_L)$	$(\nu, \quad e_L)$	-	$\mathbf{1} \otimes \mathbf{2} \otimes -\frac{1}{2}$
		$\overline{e}$	$\widetilde{e}_R^*$	$e_R^\dagger$	-	$\mathbf{1} \otimes \mathbf{1} \otimes 1$
Chiral	Higgs, Higgsinos	H_u	$(H_u^+, \quad H_u^0)$	$(\widetilde{H}_u^+, \quad \widetilde{H}_u^0)$	-	$\mathbf{1} \otimes \mathbf{2} \otimes +\frac{1}{2}$
		H_d	$(H_d^0, \quad H_d^-)$	$(\widetilde{H}_d^0, \quad \widetilde{H}_d^-)$	-	$\mathbf{1} \otimes \mathbf{2} \otimes -\frac{1}{2}$
Gauge	gluino, gluon	-	-	$\widetilde{g}$	g	$\mathbf{8} \otimes \mathbf{1} \otimes 0$
	winos, W bosons	-	-	$\widetilde{W}^\pm, \widetilde{W}^0$	$W^\pm, W^0$	$\mathbf{1} \otimes \mathbf{3} \otimes 0$
	bino, B boson	-	-	$\widetilde{B}^0$	B^0	$\mathbf{1} \otimes \mathbf{1} \otimes 0$

Table 3.1: Chiral supermultiplets and gauge supermultiplets in the MSSM. In the chiral supermultiplets, the spin 0 fields are complex scalars and the spin 1/2 fields are left-handed two-component Weyl spinors.

In SUSY models, the Z boson mass can be obtained from the minimization condition on the Higgs sector scalar potential

$$\frac{m_Z^2}{2} = \frac{m_{H_d}^2 + \Sigma_d^d - (m_{H_u}^2 + \Sigma_u^u)\tan^2\beta}{\tan^2\beta - 1} - \mu^2 \quad , \quad (3.26)$$

where Σ_d^d and Σ_u^u are radiative corrections including the contributions from various particle and sparticle Yukawa and gauge couplings to the Higgs sector. Requiring no large cancellations means each term on the right-hand-side of Eq. (3.26) are individually comparable to the left-hand-side, $m_Z^2/2$. Therefore, no large electroweak fine-tuning (EWFT) is required to obtain $m_Z = 91.2$ GeV and leads to a model with electroweak naturalness. The EWFT parameter is defined as

$$\Delta_{EW} = max_i \frac{|C_i|}{(m_Z^2/2)} \quad , \quad (3.27)$$

which depends only on the weak scale parameters of the theory. Low Δ_{EW} value means less fine-tuning. For example, $\Delta_{EW} = 10 \sim 30$ correspond to $3 \sim 10\%$

fine-tuning. The C_i represents C_{H_d}, C_{H_u}, C_μ, $C_{\Sigma_d^d(k)}$, and $C_{\Sigma_u^u(k)}$

$$C_{H_d} = \frac{m_{H_d}^2}{\tan^2\beta - 1} \quad , \tag{3.28}$$

$$C_{H_u} = \frac{-m_{H_u}^2 \tan^2\beta}{\tan^2\beta - 1} \quad , \tag{3.29}$$

$$C_\mu = -\mu^2 \quad , \tag{3.30}$$

$$C_{\Sigma_d^d(k)} = \frac{\Sigma_d^d}{\tan^2\beta - 1} \quad , \tag{3.31}$$

$$C_{\Sigma_u^u(k)} = \frac{-\Sigma_u^u \tan^2\beta}{\tan^2\beta - 1} \quad , \tag{3.32}$$

where k denotes the various loop contributions included in Eq. (3.26). In order to get a small EWFT value, $\Delta_{EW} \leq 30$, the RNS has to satisfy

- The light Higgsino mass $100 < |\mu| < 300$ GeV.

- $m_{H_u}(m_{\text{GUT}}) \sim (1.3 \sim 2)m_0$. This leads to $m_{H_u}^2 \sim -\frac{m_Z^2}{2}$ at the weak scale.

- $A_0 \sim \pm 1.6 m_0$. This results in large radiative corrections of $\widetilde{t}_i$ while maintaining m_H to $\sim$125 GeV.

In the RNS framework, which allows fine-tuning at $5 \sim 10\%$ level, the masses of the Higgsino-like gauginos $\widetilde{\chi}_1^\pm$, $\widetilde{\chi}_1^0$, and $\widetilde{\chi}_2^0$ lie in the range 100 to 300 GeV and the mass gap between $\widetilde{\chi}_2^0$ and $\widetilde{\chi}_1^0$ is $10 \sim 30$ GeV. The masses of third generation squarks are $m_{\widetilde{t}_1} \sim 1$ to 2 TeV and $m_{\widetilde{t}_2}$, $m_{\widetilde{b}_1} \sim 2$ to 4 TeV. The gluino mass, $m_{\widetilde{g}}$, is about 1 to 5 TeV and the masses of first and second generation sferminos, $m_{\widetilde{q}}, m_{\widetilde{\ell}}$, are about 5 to 10 TeV. The light Higgs scalar mass is kept at 125 GeV. The typical mass spectra of RNS is shown in Fig. 3.2. The $m_{\widetilde{t}_{1,2}}$ and $m_{\widetilde{b}_{1,2}}$ are typically beyond 1 TeV in the RNS, so it is very difficult to detect at the LHC. The light Higgsino-like charginos $\widetilde{\chi}_1^\pm$ and neutralinos $\widetilde{\chi}_{1,2}^0$ have substantial production cross-section in the RNS, and are produced at large rates at the LHC.

Because of the small mass splittings $\Delta m(\widetilde{\chi}_1^\pm, \widetilde{\chi}_1^0)$ and $\Delta m(\widetilde{\chi}_2^0, \widetilde{\chi}_1^0)$, the visible decay products tend to be at very low energies and will be hard to detect above the SM background, resulting in large $E_{\mathrm{T}}^{\mathrm{miss}}$.
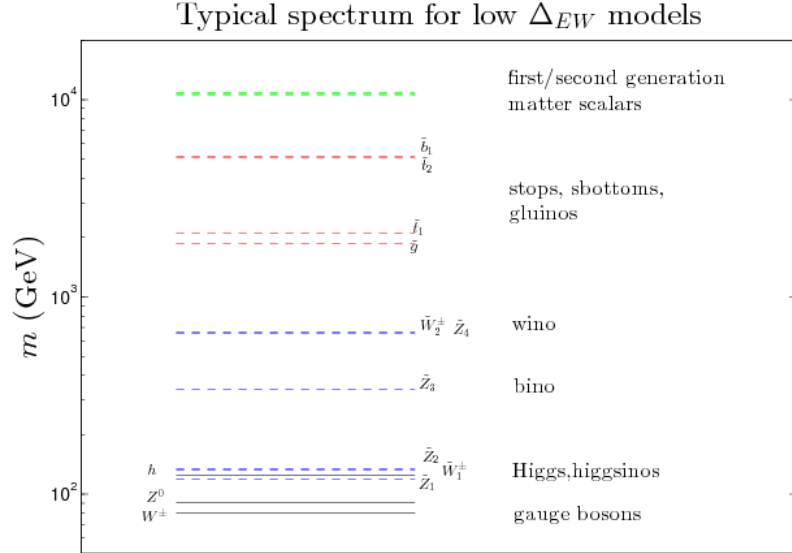
Figure 3.2: Typical sparticle mass spectra of RNS [10].

3.4 The non-universal Higgs mass model with two extra parameters

The RNS can be generated from SUSY GUT type models using the non-universal Higgs masses model with two extra parameters (NUHM2) [73, 74, 75, 76] leading to a low fine-tuning Δ_{EW} value at the electroweak scale and keeping electroweak naturalness. The NUHM2 decouples the Higgs mass doublet parameters $m_{H_u}^2$ and $m_{H_d}^2$ at the GUT scale such that

$$m_{H_u}^2 \neq m_{H_d}^2 \neq m_0^2(m_{\mathrm{GUT}}) \quad , \tag{3.33}$$

and usually uses the weak scale parameters μ and m_A to replace the $m^2_{H_u}$ and $m^2_{H_d}$.

$$\mu^2 = \frac{m^2_{H_d} - m^2_{H_u} \tan^2 \beta}{\tan^2 \beta - 1} - \frac{m^2_Z}{2} \quad , \tag{3.34}$$

$$m^2_A = m^2_{H_d} + m^2_{H_u} + 2\mu^2 \quad , \tag{3.35}$$

If the value of NUHM2 free parameters are chosen as the following ranges

- The matter scalar mass $m_0 \sim 1$ to 7 TeV,

- The soft SUSY breaking gaugino mass $m_{1/2} \sim 0.3$ to 1.5 TeV,

- The trilinear SUSY breaking parameter $A_0 \sim \pm(1 \text{ to } 2)m_0$,

- The ratio of the Higgs field vacuum expectation value $\tan \beta \sim 5$ to 50,

- The superpotential Higgs mass $\mu \sim 100$ to 300 GeV,

- The pseudoscalar Higgs boson mass m_A is varied,

then the low EWFT can be achieved while maintaining the SUSY spectrum in the range $123 < m_H < 127$ GeV. Compared with the well-known mSUGRA/CMSSM models which have the lowest $\Delta_{EW} \sim 200$, the Δ_{EW} in the NUHM2 model is only ~ 10. The NUHM2 is expected to form the effective theory for energies lower than m_{GUT} resulting from $SU(5)$ or general $SO(10)$ grand unified theories. Detailed scans for the NUHM2 parameter space with low EWFT have been performed in [69]. The NUHM2 parameter values used in this analysis were set to $m_0 = 5$ TeV, $A_0 = -1.6m_0$, $\tan \beta = 15$, $m_A = 1$ TeV, $\mu = 150$ such that $\text{sign}(\mu) > 0$, and $m_{1/2}$ are varied from 350 to 800 GeV. These parameter choices lead to low EWFT (electroweak naturalness) and predict final state signatures that

allow large background rejection while retaining high signal efficiency. Although the kinematics of NUHM2 are very similar to the simplified Higgsino model in compressed scenarios, the primary differences between the two models exist in the mass spectra, cross-sections, and branching ratios.

NUHM2: m_0=5 TeV, tanβ=15, A_0 =-1.6m_0, m_A=1TeV, m_t =173.2 GeV
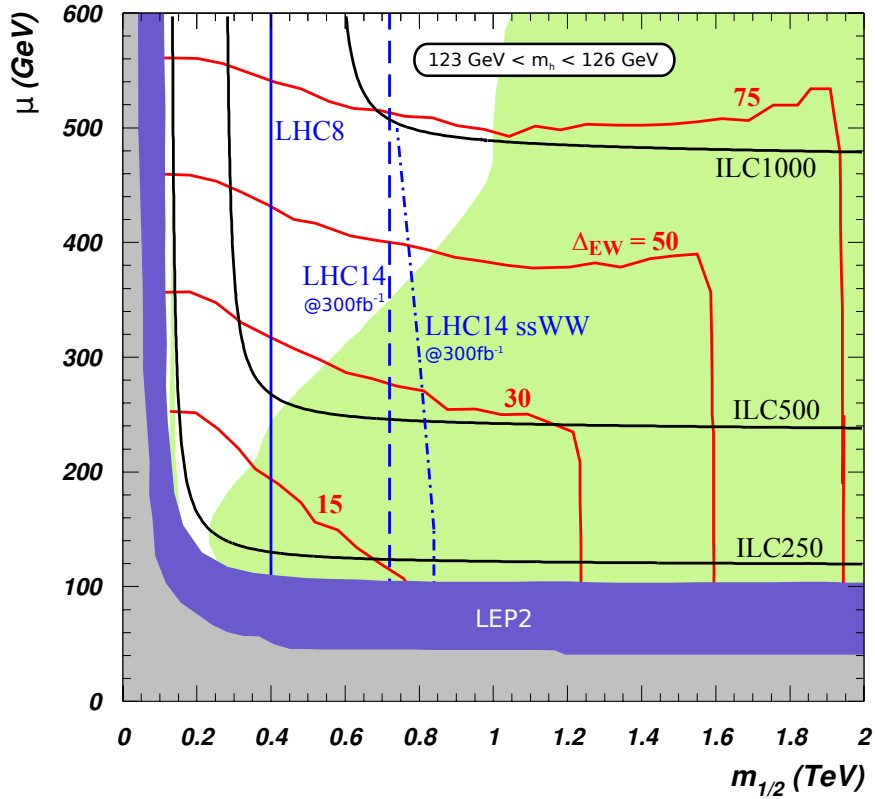
Figure 3.3: The Δ_{EW} contours in the $m_{1/2}$ vs μ plane of NUHM2 model for $m_0 = 5$ GeV, $\tan\beta = 15$, $A_0 = -1.6m_0$, and $m_A = 1$ TeV [11]. The gray and blue shaded regions are excluded by the LEP1 and LEP2 searches for chargino pair production. The region on the left hand side of the blue solid line is excluded by LHC $\sqrt{s} = 8$ TeV gluino pair searches.

Figure 3.3 shows the $m_{1/2}$ vs μ plane of NUHM2 model for $m_0 = 5$ GeV, $\tan\beta = 15$, $A_0 = -1.6m_0$, and $m_A = 1$ TeV. The gray and blue regions are excluded by searches for chargino pair production at LEP1 and LEP2. The area

to the left of the blue solid line is excluded by the $\widetilde{g}\widetilde{g}$ production at the LHC with $\sqrt{s} = 8$ TeV. The contours for $\Delta_{EW} = 15, 30, 50, 70$ are shown. The $\widetilde{\chi}_2^0\widetilde{\chi}_1^0$ with one ISR jet production where $\widetilde{\chi}_2^0 \to \ell^+\ell^-\widetilde{\chi}_1^0$ is labeled by two horizontal dashed contours at 300 fb^{-1} and 3000 fb^{-1}, respectively[11]. The $\widetilde{\chi}_2^0\widetilde{\chi}_1^0$ with one ISR jet is accessible in nearly the entire $\Delta_{EW} < 30$ region. For comparison, the reach of the International Linear Collider (ILC) with $\sqrt{s} = 0.5$ and 1 TeV are shown. Thus, the RNS, which accommodates the electroweak naturalness, can be either discovered or ruled out by the LHC plus ILC searches.

---

[11]The $\widetilde{\chi}_1^0$ is indicated by $\widetilde{Z}_1$ and the $\widetilde{\chi}_2^0$ is indicated by $\widetilde{Z}_2$ in the plot.

CHAPTER 4

THE ATLAS EXPERIMENT AT THE LHC

The European Organization for Nuclear Research (CERN[1]) was founded in 1954 and is based in a suburb of Geneva on the Franco–Swiss border. The main function of CERN is to provide particle accelerators and detectors for high-energy physics research. The physicists and engineers at CERN are probing the fundamental structure of the universe using the world's largest and most complex scientific facility — the *Large Hadron Collider* (LHC) [32]. In the LHC, the particles are boosted to high energies and collide at close to the speed of light. The results of the collisions are recorded by the various detectors. There are seven experiments at the LHC. The biggest of these experiments are *ATLAS* (A Toroidal LHC ApparatuS) [2] and *CMS* (Compact Muon Solenoid) [77] which use general-purpose detectors to investigate a broad physics program ranging from the search for the Higgs boson to extra dimensions and particles that could make up dark matter. The *ALICE* (A Large Ion Collider Experiment) [78] experiment is designed to study the physics of quark-gluon plasma and the *LHCb* (Large Hadron Collider beauty) [79] experiment specializes in investigating CP violation[2] by studying the *b*-quark. These four detectors sit underground in huge caverns of the LHC ring. The other three experiments, *TOTEM* [80], *LHCf* [81], and *MoEDAL* [82], are smaller. The TOTEM (TOTal Elastic and

---

[1]The name CERN is derived from the acronym for the French Conseil Européen pour la Recherch Nucléaire.

[2]CP violation is violation of the charge conjugate and parity symmetry which says if a particle is interchanged with its anti-particle and its spatial coordinates are inverted, then the physics laws should be the same.

diffractive cross-section Measurement) [80] experiment aims at the measurement of total cross-section, elastic scattering, and diffractive dissociation. The LHCf (Large Hadron Collider forward) [81] experiment is intended to measure the neutral particle produced by the collider using the forward particles. The prime motivation of the MoEDAL (Monopole and Exotics Detector at the LHC) [82] experiment is to search directly for the magnetic monopole. An overview of the LHC is described in Sect. 4.1 and the detector apparatus of the ATLAS experiment is outlined in Sect. 4.2.

4.1   The Large Hadron Collider

The LHC [32] is the world's largest and most powerful accelerator which accelerates and collides protons in a 26.7 km circumference tunnel crossing the Franco–Swiss border 100 m underground. Built in the tunnel of the former *LEP* (Large Electron–Positron), the LHC is capable of colliding protons as well as heavy ions. Compared with LEP which collides electrons and positrons, the advantage of the LHC is the lower energy loss[3] through synchrotron radiation, so higher energies can be reached by the LHC. The LHC is designed for collisions at a center-of-mass energy $\sqrt{s} = 14$ TeV and an instantaneous luminosity of $\mathcal{L} = 10^{34}$ cm^{-2}s^{-1}. Figure 4.1 shows the infrastructure of the LHC and the pre-accelerator system.

The protons are extracted by ionization from a hydrogen source and are accelerated to 50 MeV by the linear accelerator *LINAC2*. Then they are injected into the *Proton Synchrotron Booster* (PSB) where the proton energies are increased to 1.4 GeV before they enter the *Proton Synchrotron* (PS) which accelerates the

---

[3]The energy loss for protons is about eleven orders of magnitude smaller than the electrons.
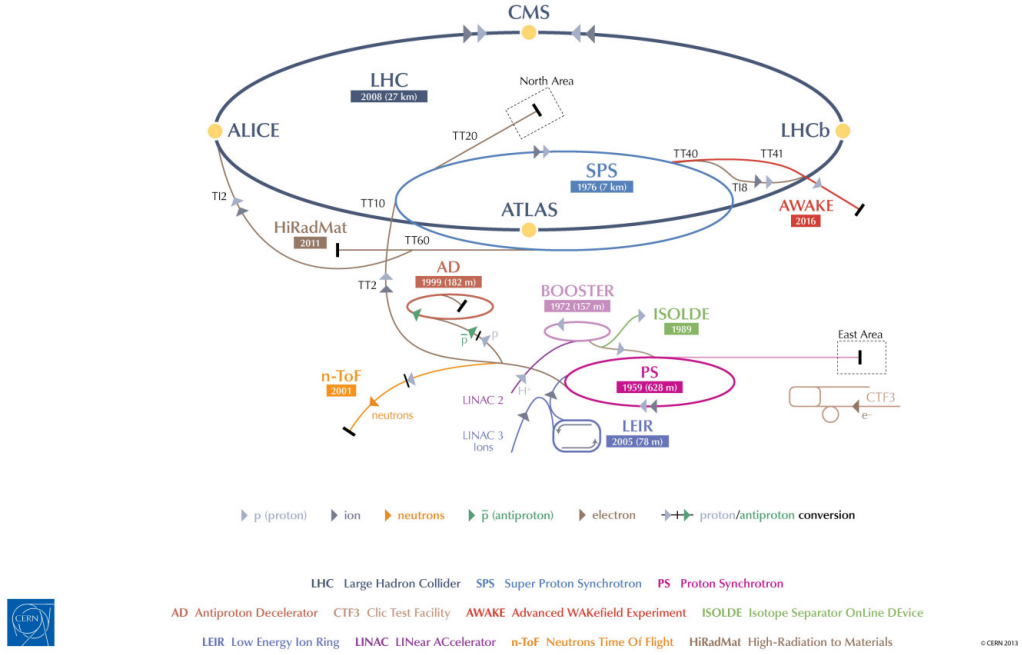
Figure 4.1: The accelerator complex at CERN [12].

protons to 25 GeV. Next, the proton energies are increased to 450 GeV in the *Super Proton Synchrotron* (SPS). Finally, the protons are split into two beams and enter the LHC where the two beams run in opposite directions. In order to keep the protons on a circular trajectory in the LHC, 1232 superconducting dipole magnets [83] generate a magnetic field strength of 8.33 T to bend the proton beams in eight arcs. Additionally, 392 quadrupole magnets [83] are installed to focus the beam. A cryogenic system running with super-fluid helium-4 is used to cool down the superconducting magnets to a temperature of 1.7 K.

For a given physics process, the event rate is proportional to the cross-section σ of this process

$$\frac{dN}{dt} = \mathcal{L} \cdot \sigma \tag{4.1}$$

where N is the number of events and $\mathcal{L}$ denotes the luminosity of the beam. The

luminosity of the beam, $\mathcal{L}$, can be calculated by

$$\mathcal{L} = \frac{N^2 f}{4\pi\sigma_x\sigma_y} \cdot F \tag{4.2}$$

where N is the number of protons, f is the bunches crossing frequency, and σ_x and σ_y are the x and y components of the cross-section σ. The geometric luminosity reduction factor, F, is related to the crossing angle at the *interaction point* (IP). A beam consisting of 1.15×10^{11} protons with bunching spacing of 25 ns, and a transverse bunch size at the IP of 16×10^{-4} cm, with the geometric luminosity reduction factor as 1, will reach the design luminosity of 10^{34} cm^{-2}s^{-1}.

The first beam was circulated through the collider on the morning of September 10, 2008 [84]. However, a magnet quench incident occurred on September 19 and caused extensive damage to over 50 superconducting magnets, their mountings, and the vacuum pipe. Most of 2009 was spent on repairing the damage caused by the magnet quench incident and operations resumed on November 20, 2009. The first phase of data-taking (Run 1) started at the end of 2009 and the beam energy was increased to a center-of-mass $\sqrt{s} = 7$ TeV in 2011 and $\sqrt{s} = 8$ TeV in 2012. A total integrated luminosity of 5.46 fb^{-1} was collected in 2011 and 22.8 fb^{-1} was collected in 2012. Since February 13, 2013 the LHC was in the Long Shutdown 1 (LS1) phase for maintenance and upgrades. On April 5, 2015, the LHC restarted and was operating at a center-of-mass energy $\sqrt{s} = 13$ TeV throughout the Run 2 phase[4].

---

[4]The Run 2 data-taking started in 2015.

4.2 The ATLAS experiment

The ATLAS[5] detector [2] is a multi-purpose detector housed in its cavern at point 1 at the LHC [32]. It is the largest experiment at the LHC with a length of 44 m, a diameter of 25 m, and a weight of approximately 7000 tones. It consists of three high precision sub-detector systems which are arranged concentrically around the interaction point with forward and backward symmetry. Related to this symmetry, the ATLAS detector is sectioned into the central barrel region with one end-cap region perpendicular to the beam pipe on either side. Figure 4.2 shows an overview of the ATLAS detector with its major components.

The ATLAS detector is designed to record the proton-proton interactions delivered by the LHC. It can identify particles and measure their tracks and energies with very high precision. Therefore, it is sensitive to large areas of particle physics phenomena from the precision measurement of the Standard Model to beyond the Standard Model (BSM). The detector is composed of three sub-detector systems and the magnet system. The innermost part of the detector is called the *inner detector* which identifies and reconstructs the charged particles as well as the primary and secondary vertices. Around it, the *calorimeter* system is built as a cylindrical barrel with caps at each end to measure the particle energies. The detector is completed by the *muon spectrometer* which performs identification and measurement of the momenta of muons. The magnetic system produces a field of $B = 0.5$ T and $B = 1$ T at the barrel and two end-caps, respectively. The detector has to withstand large collision rates with approximately 1000 particles per collision Therefore, a fast readout and a three-level trigger system

---

[5]A Toroidal LHC Apparatus

41
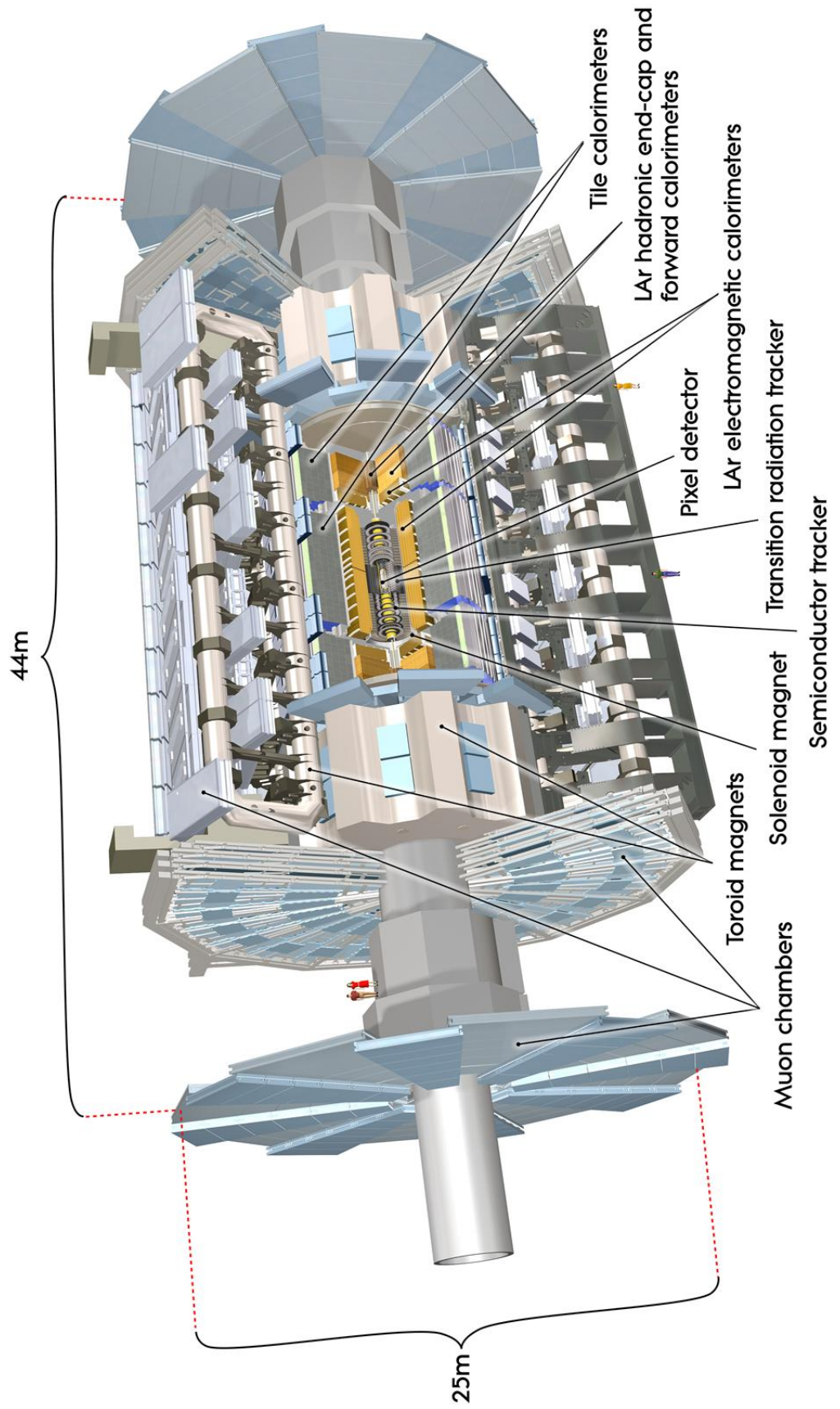
Figure 4.2: Overview of the ATLAS detector [2].

Tile calorimeters

LAr hadronic end-cap and forward calorimeters

LAr electromagnetic calorimeters

Pixel detector

Transition radiation tracker

Semiconductor tracker

Solenoid magnet

Toroid magnets

Muon chambers

44m

25m

are implemented to reduce the event rate from 40 MHz to 200 Hz. The ATLAS coordinate system and the detail of each sub-detector systems are described in the following sections.

4.2.1 The ATLAS coordinate system

ATLAS uses a *right-handed coordinate system* with its origin at the nominal proton-proton interaction point (IP) in the center of the detector and the z-axis along the beam pipe. Along the z-axis the detector is divided into side-A (positive z) and side-C (negative z). The positive x-axis is defined by the direction pointing from the interaction point to the center of the LHC ring, and the positive y-axis points upward. The azimuthal angle ϕ is measured around the beam pipe and the polar angle θ is the angle from the z-axis. The transverse momentum p_{T}, the transverse energy E_{T} and the missing transverse energy $E_{\mathrm{T}}^{\mathrm{miss}}$ are defined in the transverse plane[6]. For example, p_{T} is defined as

$$p_{\mathrm{T}} = \sqrt{p_x^2 + p_y^2} \quad . \tag{4.3}$$

An important quantity in hadron collider physics is the *rapidity*, y, because it is invariant under Lorentz boosts in the longitudinal direction. The rapidity is defined as

$$y = \frac{1}{2} \ln \left[\frac{E + p_z}{E - p_z} \right] \tag{4.4}$$

where E denotes the particle energy and p_z is the component of the momentum along the beam direction. Since mainly leptons can be considered massless in respect to the nominal center-of-mass energy, the pseudorapidity, η, is used instead of using y. For a massless particle, the *pseudorapidity*, η, depends on the

---

[6]$x - y$ plane

polar angle θ through

$$\eta = -\ln\tan\frac{\theta}{2} \quad . \tag{4.5}$$

For a particle with the energy E much larger than its mass, the approximation $E \approx |\vec{p}|$ is valid. The distance, ΔR, between two objects in the $\eta - \phi$ plane is given by

$$\Delta R = \sqrt{\Delta\eta^2 + \Delta\phi^2} \tag{4.6}$$

where $\Delta\eta$ and $\Delta\phi$ are the difference in pseudorapidity and azimuthal angle, respectively.

4.2.2 The inner detector and tracking system

The *inner detector* (ID) consists of three sub-detectors: the *pixel* detector, the *semiconductor tracker* (SCT), and the *transition radiation tracker* (TRT). The main purpose of the inner detector is to provide high precision measurements of the tracks of charged particles and to reconstruct the primary and secondary vertices. Each sub-detector is composed of several layers of material which interact with the charged particles when the charged particles penetrate the layers. A 2 T magnetic field generated by the central solenoid parallel to the beam axis is applied to bend the charged particles using the Lorentz force. By using the radius r of the curvature of the tracks, the magnetic field strength B, and the charge of the particle q, we can calculate the magnitude of the transverse momentum p_{T}

$$p_{\mathrm{T}} = |q|Br \tag{4.7}$$

The layout of the inner detector is illustrated in Fig. 4.3 and the detail of sub-detectors are described in the following paragraphs.
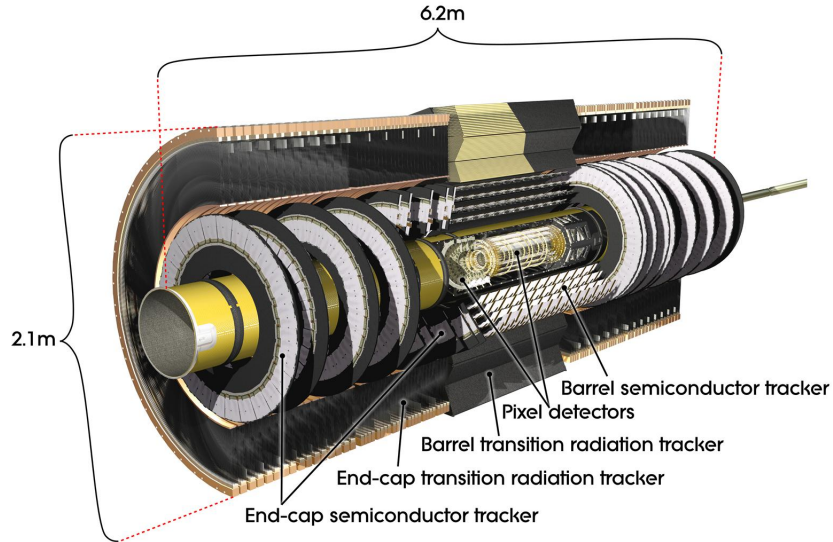
Figure 4.3: Cut-away view of the ATLAS inner detector [2].

Pixel detector

The innermost part of the entire ATLAS detector components is the *pixel* detector which is composed of three barrel layers and three end-cap disks on each side. The three cylindrical barrel layers around the beam axis have radial positions of 50.5 mm, 88.5 mm, and 122.5 mm respectively and are made of 22, 38, and 52 identical staves respectively. Each stave is inclined with an azimuthal angle of 20 degrees and is composed of 13 pixel modules with 46,080 readout channel per module. The size of each pixel is $50 \times 400 \ \mu\text{m}^2$ in $R - \phi \times z$. In the forward region, three disks on each side equip modules identical to the barrel modules, except the connecting cables. The total 1,744 modules in the pixel detector lead to nearly 80 million channel readout and provide an intrinsic accuracy of 10 μm in the $R - \phi$ plane and 115 μm in the z direction covering the region $|\eta| < 2.5$.

An additional pixel layer called the Insertible b-Layer (IBL) was installed during the long shutdown period between Run 1 and Run 2. The IBL is located

at $\langle R \rangle = 33$ mm with granularity $\Delta\phi \times \Delta z = 50 \times 250$ μm. This new IBL module was designed to improve tracking efficiency, flavour tagging performance and primary vertex finding. A spatial resolution of 4 μm along the radial direction and 115 μm along the z direction is achieved.

Semiconductor tracker

Outside of the pixel detector is the *semiconductor tracker* (SCT) which is a silicon strip detector. There are about 6.3 million readout channels which are arranged in 4088 microstrips. The intrinsic accuracy per sensor is 17 μm in $R - \phi$ and 580 μm in z direction for the barrel and in R for the disks, respectively. Similar to the pixel detector, the SCT covers the region $|\eta| < 2.5$ and consists of 8 strip layers in the barrel and a total of 9 discs in the end-cap region on each side. No track reconstruction is possible beyond the covered pseudorapidity range. Therefore, the electrons cannot be distinguished from photons above the $|\eta| > 2.5$ region.

Transition radiation tracker

The outermost component of the inner detector is the *transition radiation tracker* (TRT) which consists of 4 mm diameter straw tubes filled with a xenon-based gas mixture. The gas mixture is ionized by charged particles when they penetrate the straws. The ionized electrons drift to the cathode because a high voltage is applied on the tungsten wire in the center of the straw tube. Therefore, the TRT allows enhanced electron identification, momentum measurement, and vertex measurement. In the barrel region, the straws are surrounded by polypropylene fibers and are divided into two halves at $|\eta| = 0$. In the end-caps, the straws are arranged radially and surrounded by foils as a transition radiation element. They

are read out at two sides and at the center of the TRT so the total number of the readout channels of TRT is approximately 350,000. The TRT only provides information in the $R - \phi$ plane with an intrinsic accuracy of 130 μm per straw and covers a range up to $|\eta| < 2.0$.

Solenoid magnet

A superconducting solenoid magnet encloses the inner detector and produces a 2 T magnetic field to bend the trajectories of the charged particles. A cooling system is used and shared with the *electromagnetic calorimeter* (Sect. 4.2.3) to reduce the deterioration of the energy measurement.

4.2.3 The calorimeters

The calorimeters are used to measure the energy of particles, such as electrons, photons, and jets. Besides muons and neutrinos, all other particles interacting electromagnetically or hadronically are stopped in the calorimeters by absorbing their energy. Not only charged particles but also neutral particles such as photons and neutral hadrons can be detected in the calorimeters. By requiring high hermiticity of the calorimeters, the missing energy $E_{\mathrm{T}}^{\mathrm{miss}}$ can be reconstructed precisely as a negative vectorial sum of all energy deposits. The ATLAS calorimeter system is placed between the inner detector (Sect. 4.2.2) and the muon spectrometer (Sect. 4.2.4). The ATLAS calorimeter system consists of an inner *electromagnetic calorimeter* and an outer *hadronic calorimeter* together with the *forward calorimeter*. The electromagnetic calorimeter and hadronic calorimeter are *sampling calorimeters* which consist of two different materials alternately.

An absorber material is used to enhance the particle showers[7] and a highly ionizable active medium is used to measure the deposited energy. Because only the energies deposited in the active medium can be observed, the total energy of the shower can be estimated from the deposited energy by clustering algorithms. The electromagnetic calorimeter focuses on measuring electrons and photons, and the hadronic calorimeter is dedicated to hadronically interacting particles. The whole ATLAS calorimeter system covers a range $|\eta| < 4.9$. A layout view of the ATLAS calorimeter system is shown in Fig. 4.4 and the details of the three calorimeters are described in the following paragraphs.
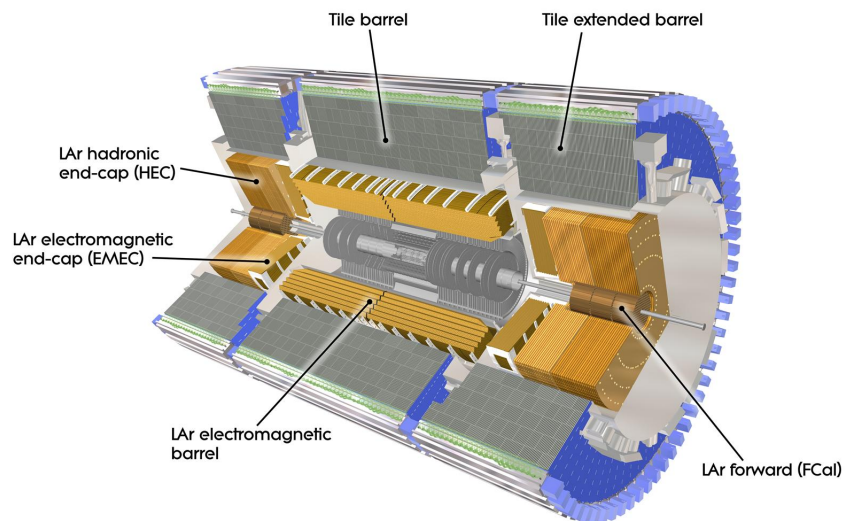
Figure 4.4: Cut-away view of the calorimeter system [2].

Electromagnetic calorimeter

The *electromagnetic calorimeter* (ECAL) measures the energy of electrons and photons as they interact with matter. The ECAL consists of accordion shaped

---

[7]The shower is the cascade of secondary particles produced by the high-energy particle interacting with dense material.

cells of alternating layers of lead as absorber material and liquid argon (LAr) as active medium. The accordion shape provides the full coverage in the azimuthal angle ϕ. The LAr is chosen as an active medium because it withstands radiation, it has a stable response time and linear behavior [2]. The electrons or photons lose their energy by alternating bremsstrahlung and pair production when they interact with lead, which results in electromagnetic particle showers which ionize the LAr creating the ionization currents which are collected by the copper electrodes. The ECAL is divided into barrel (EMB) and end-cap (EMEC) components, which cover $|\eta| < 1.475$ and $1.375 < |\eta| < 3.2$[8], respectively. The EMB is made up of three longitudinal layers with different granularity and are sensitive in the region $|\eta| < 2.5$. The first strip layer has the highest granularity where the size of cells correspond to $\Delta\eta \times \Delta\phi = 0.0031 \times 0.1$ for $|\eta| < 1.8$ and are coarser for larger $|\eta|$. The smallest granularity allows separation of the showers coming from electrons, photons and neutral pions. The second layer is the largest part of the EMB with the size of cells corresponding to $\Delta\eta \times \Delta\phi = 0.025 \times 0.0245$ so most of the energy is deposited in this layer. The third layer has the granularity $\Delta\eta \times \Delta\phi = 0.05 \times 0.0245$. The total thickness are 22 X_0[9] and 24 X_0 for EMB and EMECs, respectively. This special thickness is sufficient to prevent the punch through of high energy showers into the muon spectrometer. Figure 4.5 shows the cut-away view of the the accordion shaped EMB module with the dimensions for three layers.

---

[8]There are two EMECs and each of them consists of two wheels. The inner wheel covers $1.375 < |\eta| < 2.5$ and the outer wheel covers $2.5 < |\eta| < 3.2$.

[9]The X_0 stands for radiation lengths which is a characteristic of material. It is related to the energy loss of the particle when it interacts with the material electromagnetically.
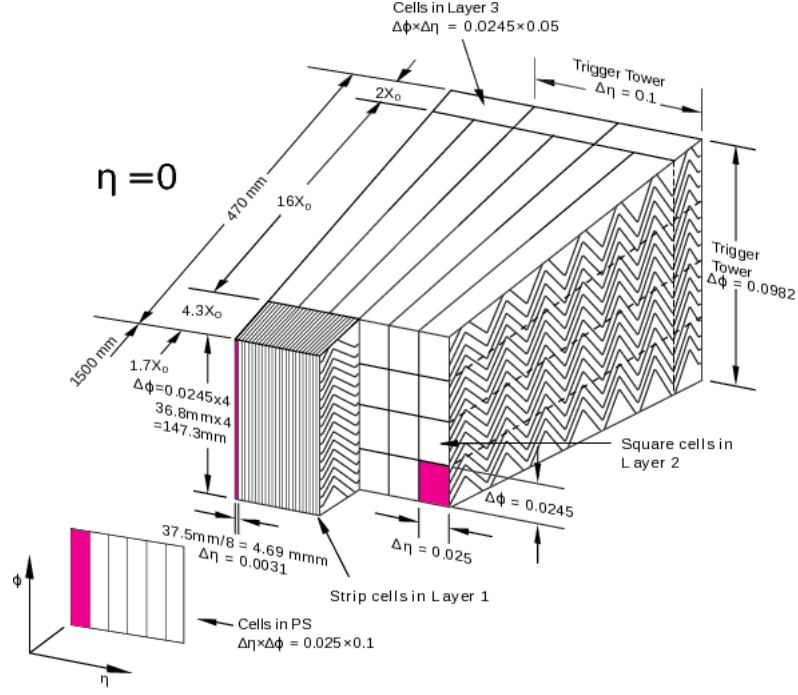
Figure 4.5: Cut-away view of the accordion shaped EMB module with the dimensions for three layers [13].

Hadronic calorimeter

The electromagnetic interacting particles produce narrow showers, however, the hadrons, which are heavier and penetrate medium further, produce more widespread hadronic showers. The *hadronic calorimeter* (HCAL) surrounds the ECAL and is made up by a barrel and two end-caps (HEC). The barrel covers $|\eta| < 1.7$ and it uses plastic scintillator tiles as active medium and steel as absorber material. The hadronic showers stimulate the scintillator and emit light which is collected by *photo multiplier tubes* (PMTs) and then read-out via wavelength shifting optical fibers. The HEC covers $1.5 < |\eta| < 3.2$ which overlap with the pseudorapidity coverage region of barrel. The HEC is composed of two copper plate wheels as absorber material on each side with LAr in between. The designed thickness in the

barrel region is 9.7 λ[10]. Therefore, the punch-through to the muon spectrometer is suppressed. The granularity of the HCAL is coarser than the ECAL but it is sufficient for measuring $E_\mathrm{T}^\mathrm{miss}$ and jet reconstruction.

Forward calorimeter

The *forward calorimeter* (FCAL) uses LAr as an active medium and one copper and two tungsten layers as absorber materials. The copper layer (FCAL1) is used to measure the electromagnetic interactions whereas the two tungsten layers (FCAL2 and FCAL3) are used to measure the hadronically interactions. The FCAL provides the very forward region coverage $3.1 < |\eta| < 4.9$ and can contribute to the $E_\mathrm{T}^\mathrm{miss}$ measurement.

Energy resolution

The energy resolution is the ability of the calorimeter to distinguish between two adjacent energies. The number of ionized particles N is proportion to the energy E of the incoming particle. Therefore, the higher the energy of the incoming particle the more ionized particles are produced in the shower. Based on the Poisson statistics we know

$$\frac{\sigma_E}{E} \propto \frac{\sigma_N}{N} = \frac{\sqrt{N}}{N} = \frac{1}{\sqrt{N}} \propto \frac{1}{\sqrt{E}} \tag{4.8}$$

where σ_E is the energy resolution at FWHM[11] in a Gaussian distribution and $\sigma_N = \sqrt{N}$ is the Poisson standard deviation. Taking the effects of calibration

---

[10]The λ represents the hadronic interaction lengths which is the mean free path of a strongly interacting particle between two inelastic scatterings.
[11]The FWHM means full width at half maximum.

and electronics noise into account, the relative energy resolution becomes

$$\frac{\sigma_E}{E} = \frac{a}{E} \oplus \frac{b}{\sqrt{E}} \oplus c \qquad (4.9)$$

where a, b, c are noise, sampling, and constant terms, respectively. The relative energy resolutions for ECAL, HCAL, and FCAL are summarized in Table 4.1.

Calorimeter	Required resolution
Electromagnetic calorimeter	$\sigma_E/E = 10\%/\sqrt{E(\text{GeV})} \oplus 0.7\%$
Hadronic calorimeter	$\sigma_E/E = 50\%/\sqrt{E \ (\text{GeV})} \oplus 3\%$
Forward calorimeter	$\sigma_E/E = 100\%/\sqrt{E \ (\text{GeV})} \oplus 10\%$

Table 4.1: Resolution requirements for the different calorimeters of the ATLAS detector [2].

4.2.4 The muon spectrometer

The outermost part of the ATLAS detector is the *muon spectrometer* [2, 85, 86]. Muons have the same properties as electrons but are 200 times heavier than electrons. Because muons don't interact predominately by bremsstrahlung, most of the muons escape the inner detector and calorimeters without being stopped. Only the muons with an energy less than 5 GeV are stopped before the muon spectrometer. Therefore, a detector that concentrates on a precision measurement of the momentum and trajectory of high momentum muons is necessary.

The muon spectrometer is designed to measure the transverse momentum (p_{T}) of muons with $p_{\text{T}} > 3$ GeV with a resolution of 3% for $p_{\text{T}} < 250$ GeV increasing to 10% at 1 TeV. It consists of large toroid magnets and high precision tracking chambers allowing a precise measurement of the muon momentum over

nearly the full solid angle. The barrel toroid magnet system is composed of eight superconducting coils which are installed radial symmetrically around the beam pipe. It covers the range $|\eta| < 1.4$ and bends the trajectories of muons with the bending power 1.5 to 5.5 Tm. The magnetic field produced by the barrel toroid magnets provides an approximately 1 T field at the center of each of the coils, but is rather non-uniform, especially in the barrel-endcap transition region. In the endcap toroid magnets system, the magnetic field is provided by eight superconducting coils, closed in an insulation vessel extending to about 10 m in diameter, located between the first and the second station of tracking chambers. The endcap toroid magnets cover $1.6 < |\eta| < 2.4$ and provide a magnetic field in the range of 1 to 2 T with bending power 1 to 7.5 Tm.

The *monitored drift tubes* (MDT) consist of cylindrical drift tubes, filled with a gas mixture of Ar and CO_2. A tungsten-rhenium alloyed aluminum wire in the center of each tube collects the electrons freed by ionization of the gas volume by traversing muons. The MDT covers a full range of $|\eta| < 2.7$, while the inner layer only covers $|\eta| < 2.0$. The *cathode strip chambers* (CSC) provide a coverage range $2.0 < |\eta| < 2.7$, where the MDTs would have occupancy problems. The CSC is made up by two discs and filled with Ar and CO_2 gas mixture. Both MDT and CSC are slow in triggering but they provide high precision tracking in the spectrometer bending plane and end-cap inner layer, respectively. The *resistive plate chambers* (RPC) and *thin gap chambers* (TGC) are used for triggering in the barrel and end-cap, because they have sufficient intrinsic time resolution of 1.5 ns and 4 ns, respectively. A sketch of the muon spectrometer and its four components are depicted in Fig. 4.6 and Table 4.2 gives a summary of the muon

spectrometer components.
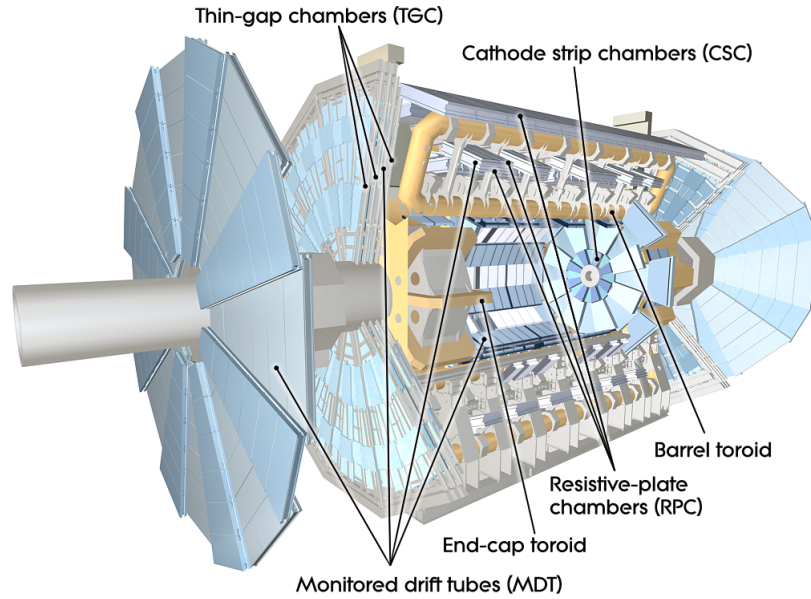
Figure 4.6: Sketch of the muon system of the ATLAS detector [2].

Type	Purpose	Location	η coverage	Channel
MDT	Tracking	barrel + end-cap	$0.0 < \eta < 2.7$	354k
CSC	Tracking	end-cap layer 1	$2.0 < \eta < 2.7$	30.7k
RPC	Trigger	barrel	$0.0 < \eta < 1.0$	373k
TGC	Trigger	end-cap	$1.0 < \eta < 2.4$	318k

Table 4.2: A summary of the muon spectrometer components.

4.2.5   The trigger system and data acquisition

The LHC pp collision rate is 40 MHz corresponding to 50 TB/s data[12] generated

by the ATLAS detector [87]. However, the limited rate for writing the events into

disk is about 1 kHz[13]. The majority of the products of the pp collision are low p_T

---

[12]Assuming the typical event size is 1.3 MB.
[13]The data storage rate is 200 Hz in Run-1 but it is increased to about 1 kHz in Run-2.

QCD processes which are not the interesting events for the analysis. Hence, the three-level ATLAS trigger and data acquisition (DAQ) system is designed to pick the interesting events and reduce the data size. Figure 4.7 shows the functional view of the ATLAS trigger/DAQ system and brief descriptions are given in the following paragraph.
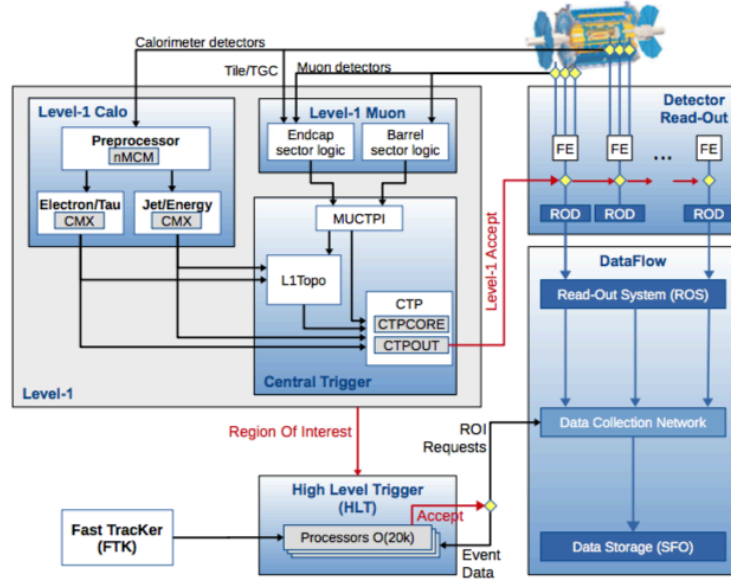
Figure 4.7: The schematic view of the ATLAS trigger/DAQ system in Run-2 [14].

The level-1 trigger

The initial selection is made by the hardware-based *level-1* (LVL1) trigger based on reduced-granularity information from calorimeters and the muon spectrometer. The latency[14] of the level-1 trigger is required to be less than 2.5 μs[15]. The high p_T muons are identified using only RPC and TGC. The high p_T e/γ, jets, hadronically decaying τ-leptons, large E_T^{miss} and total E_T objects are selected

---

[14]The latency is the time interval from the *pp* collision until trigger decision is available to the front-end electronics.

[15]The target latency for the level-1 trigger is 2.0 μs.

by calorimeter triggers using a number of sets of p_T thresholds[16] and energy isolation cuts can be applied. The selected events are read out from the front-end electronics into *readout drivers* (RODs) and written into *readout buffers* (ROBs). The information such as the p_T, η, and ϕ of the candidate objects and $E_\mathrm{T}^\mathrm{miss}$ and total E_T are saved into *region-of-interest* (ROI) buffers and send to the high level trigger. The level-1 trigger reduces the event rate from the high LHC bunch crossing rate to 100 kHz.

The high level trigger

The *level-2* trigger and *event filter* (EF) computer clusters used in Run-1 are merged into a single event professing *high level trigger* (HLT) farm in Run-2. This combination reduces the complexity, allows resource sharing between algorithms, and results in a more flexible HLT. The HLT is a completely software based trigger system that uses the ROI information from the level-1 trigger and the tracking information from the inner detector. The full-event track reconstruction information is performed by the *fast tracker* (FTK) system after each level-1 trigger and provided to the HLT. The trigger reconstruction algorithms for HLT were re-optimized to minimize the differences between the HLT and the offline analysis selections. The output rate of the HLT is approximately 1 kHz within a processing time about 200 μs.

---

[16]Typically, there are 6 to 8 sets of thresholds per object type.

CHAPTER 5

DATA SET AND SIMULATED EVENTS

This chapter describes the collision data and simulated event samples used for searching for electroweak production of SUSY states in compressed scenarios. The collision data are presented in Sect. 5.1 and the Monte Carlo (MC) simulated event samples are detailed in Sect. 5.2.

5.1 Collision data

The LHC pp collision data used in this analysis were collected by the ATLAS detector at $\sqrt{s} = 13$ TeV during 2015 and 2016. The data corresponds to an integrated luminosity of 36.1 fb^{-1} (3.2 fb^{-1} in 2015 and 32.9 fb^{-1} in 2016) with a combined uncertainty of 2.1% after applying beam, detector, and data-quality requirements. The combined uncertainty is derived following the methodology similar to those described in Ref. [88]. The average number of pp interactions per bunch crossing (pileup) is 13.5 in the 2015 data set and is 25 in the 2016 data set. The data samples are required to satisfy the following good runs list (GRLs) as recommended by the ATLAS collaboration

- `data15_13TeV.periodAllYear_DetStatus-v79-repro20-02_DQDefects`
  `-00-02-02_PHYS_StandardGRL_All_Good_25ns.xml`

- `data16_13TeV.periodAllYear_DetStatus-v88-pro20-21_DQDefects`
  `-00-02-04_PHYS_StandardGRL_All_Good_25ns.xml`

Events are selected using different inclusive E_T^{miss} triggers depending on the run period as listed in Table. 5.1. Two new triggers, HLT_mu4_j125_xe90_mht and HLT_2mu4_j85_xe50_mht[1], are developed for compressed scenarios starting from run number 308084. However, these new triggers only contribute a small gain compared to the inclusive E_T^{miss} triggers. This analysis uses inclusive E_T^{miss} triggers only.

Run period	E_T^{miss} trigger
2015	HLT_xe70_mht
A-D3	HLT_xe90_mht_L1XE50
D4-F1	HLT_xe100_mht_L1XE50
F1-	HLT_xe110_mht_L1XE50

Table 5.1: The inclusive E_T^{miss} triggers used in this analysis. The E_T^{miss} threshold varies from 70 (xe70) to 110 (xe110) GeV depending on the run period. The trigger naming convention and definition can be found at [3].

5.2 Monte Carlo simulated event samples

MC samples are used to model the SUSY signals and to estimate the SM background. All SM background MC samples were processed through a detailed ATLAS detector simulation based on GEANT4 [89] and the SUSY signal samples were simulated by a fast simulation (AF2) that parameterizes the calorimeter response [90]. To simulate the effects of additional pp collisions (pileup) in the same and nearby bunch crossings, inelastic interactions were generated using the soft

---

[1]HLT_mu4_j125_xe90_mht means high level trigger with $p_T(\mu) > 4$, $p_T(\text{jets}) > 125$, and $E_T^{miss} > 90$ GeV and HLT_2mu4_j85_xe50_mht means high level trigger requiring two muons with $p_T > 4$, $p_T(\text{jets}) > 85$, and $E_T^{miss} > 50$ GeV.

QCD processes of PYTHIA v8.186 [91] with A2 tune [92] and the MSTW2008LO PDF set [93]. These MC events were overlaid onto each simulated hard-scatter event and reweighted to match the pileup conditions observed in the data.

5.2.1 The SM background samples

Table 5.2 summarizes the event generator configurations of the ME, parton shower (PS), PDF set, and the cross-section normalization. SHERPA 2.1.1, 2.2.1, and 2.2.2 [94] were used to produce the $Z^{(*)}/\gamma^*$ + jets, diboson, and triboson events. The matrix elements (ME) were calculated for up to two partons at next-to-leading order (NLO) and up to four partons at leading order (LO) depending on the process. The $Z^{(*)}/\gamma^*$ + jets and diboson samples cover the dilepton invariant masses from 0.5 GeV for $Z^{(*)}/\gamma^* \to e^+e^-/\mu^+\mu^-$ and from 3.8 GeV for $Z^{(*)}/\gamma^* \to \tau^+\tau^-$. POWHEG-Box v1 and v2 interfaced to PYTHIA 6.428 were used to simulate $t\bar{t}$ and single-top production at NLO in the ME. The Higgs boson production was generated using POWHEG-Box v2 interfaced to PYTHIA 8.186. A Higgs boson in association with a W or Z boson production was simulated using MG5_AMC@NLO 2.2.2 with PYTHIA 8.186 and the ATLAS A14 tune. The processes containing $t\bar{t}$ and at least one electroweak boson were produced using MG5_AMC@NLO 2.2.1, 2.2.2, 2.3.2, 2.3.3 with PYTHIA 6.4.28 or 8.186. These processes were generated at NLO in the ME except for $t + Z$ and $t + t\bar{t}$ which were produced at LO. Except those produced by the SHERPA event generator, the EVTGEN v1.2.0 [95] was used to model the decay of bottom and charm hadrons in all MC samples.

Process	Matrix element	Parton shower	PDF set	Cross-section
$Z^{(*)}/\gamma^* +$ jets	Sherpa 2.2.1		NNPDF 3.0 NNLO	NNLO
Diboson	Sherpa 2.1.1 / 2.2.1 / 2.2.2		NNPDF 3.0 NNLO	Generator NLO
Triboson	Sherpa 2.2.1		NNPDF 3.0 NNLO	Generator LO, NLO
$t\bar{t}$	Powheg-Box v2	Pythia 6.428	NLO CT10	NNLO + NNLL
t (s-channel)	Powheg-Box v1	Pythia 6.428	NLO CT10	NNLO + NNLL
t (t-channel)	Powheg-Box v1	Pythia 6.428	NLO CT10f4	NNLO + NNLL
$t + W$	Powheg-Box v1	Pythia 6.428	NLO CT10	NNLO + NNLL
$h(\to \ell\ell, WW)$	Powheg-Box v2	Pythia 8.186	NLO CTEQ6L1	NLO
$h + W/Z$	MG5_AMC@NLO 2.2.2	Pythia 8.186	NNPDF 2.3 LO	NLO
$t\bar{t} + W/Z/\gamma^*$	MG5_AMC@NLO 2.3.3	Pythia 8.186	NNPDF 3.0 LO	NLO
$t\bar{t} + WW/t\bar{t}$	MG5_AMC@NLO 2.2.2	Pythia 8.186	NNPDF 2.3 LO	NLO
$t + Z$	MG5_AMC@NLO 2.2.1	Pythia 6.428	NNPDF 2.3 LO	LO
$t + WZ$	MG5_AMC@NLO 2.3.2	Pythia 8.186	NNPDF 2.3 LO	NLO
$t + t\bar{t}$	MG5_AMC@NLO 2.2.2	Pythia 8.186	NNPDF 2.3 LO	LO

Table 5.2: The MC simulated samples of SM background process.

5.2.2   The SUSY signal samples

The NUHM2 model allows the masses of the Higgs doublets m_{H_u} and m_{H_d} to differ from the universal scalar mass m_0 at the GUT scale for the signal sample generation. The parameters of the NUHM2 model are fixed to $m_0 = 5$ TeV, $m_A = 1$ TeV, $A_0 = -1.6m_0$, $\tan\beta = 15$, $\mu = 150$ GeV, and the $m_{1/2}$ is varied from 350 to 800 GeV as suggested in Ref. [69]. These parameter settings lead to RNS with low EWFT which keeps the Higgs boson mass about 125 GeV, the masses of $\tilde{g}$ and $\tilde{q}$ about the TeV scale, and the light Higgsino mass about μ. The mass spectra and decay branching ratios were calculated using Isajet v7.84 [96] and the cross-sections and the theoretical uncertainties were calculated to NLO using Prospino v2.1 [97].

The NUHM2 mass spectra

Figure 5.1 shows the mass spectra of the charginos $\widetilde{\chi}^{\pm}_{1,2}$ and neutralinos $\widetilde{\chi}^{0}_{1,2,3,4}$ as a function of $m_{1/2}$ in the NUHM2 model and the mass splitting spectra between electroweakinos as a function of $m_{1/2}$ are shown in Fig. 5.2. The masses of lower mass electroweakinos $\widetilde{\chi}^{0}_{1,2}$ and $\widetilde{\chi}^{\pm}_{1}$ are roughly flat when $m_{1/2} > 500$ GeV. However, the masses of higher mass electroweakinos $\widetilde{\chi}^{0}_{3,4}$ and $\widetilde{\chi}^{\pm}_{2}$ increased with $m_{1/2}$. The mass splittings between the lower mass electroweakinos decrease with $m_{1/2}$ and the mass splittings between $\widetilde{\chi}^{0}_{3}$ and the lower mass chargino $\widetilde{\chi}^{\pm}_{1}$ or neutralinos $\widetilde{\chi}^{0}_{1,2}$ increase with $m_{1/2}$. In the NUHM2 model, the $m_{\widetilde{\chi}^{\pm}_{1}}$ is not exactly in the middle between $m_{\widetilde{\chi}^{0}_{1}}$ and $m_{\widetilde{\chi}^{0}_{2}}$ but it varied such that the mass ratio varies from 1.61 to 1.21 as shown in Table 5.3.
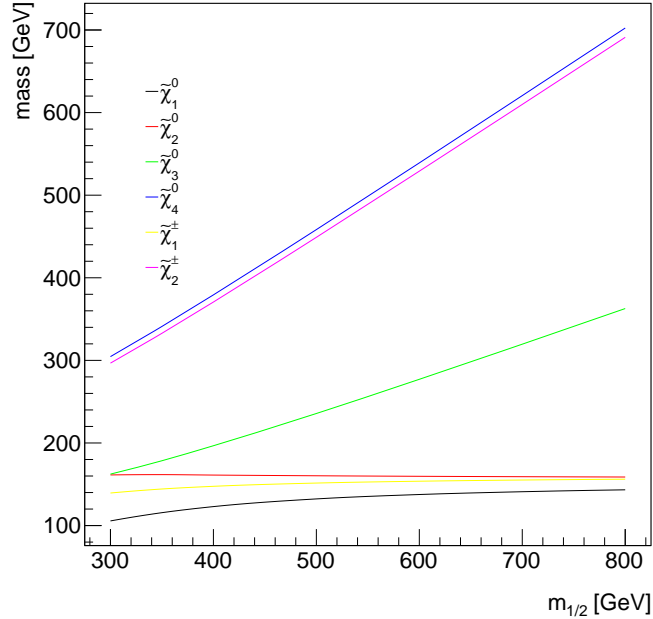
Figure 5.1: The mass spectra of the charginos $\widetilde{\chi}^{\pm}_{1,2}$ and neutralinos $\widetilde{\chi}^{0}_{1,2,3,4}$ as a function of $m_{1/2}$ in the NUHM2 model. The $m_{\widetilde{\chi}^{0}_{1}}$, $m_{\widetilde{\chi}^{0}_{2}}$, and $m_{\widetilde{\chi}^{\pm}_{1}}$ are roughly flat when $m_{1/2} > 500$ GeV. The $m_{\widetilde{\chi}^{0}_{3}}$, $m_{\widetilde{\chi}^{0}_{4}}$, and $m_{\widetilde{\chi}^{\pm}_{2}}$ are heavier and increase with $m_{1/2}$.
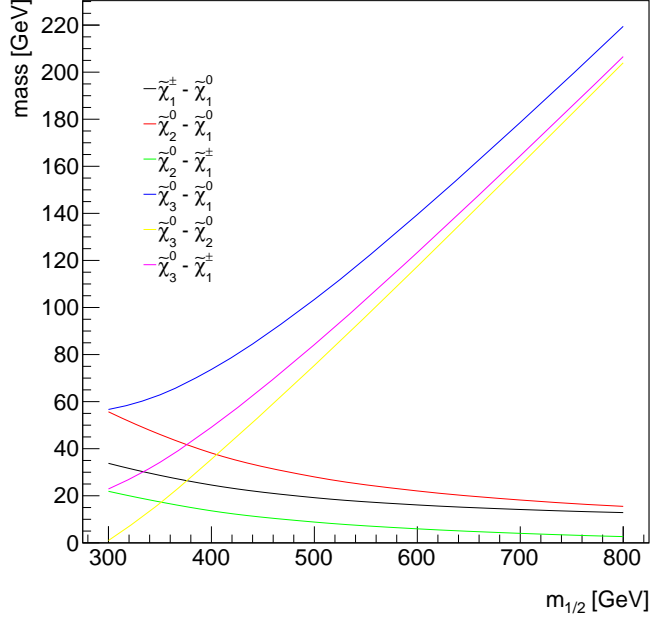
Figure 5.2: The mass splitting spectra between charginos and neutralinos in the NUHM2 model. The mass differences $\Delta m(\widetilde{\chi}_3^0, \widetilde{\chi}_{1,2}^0)$ and $\Delta m(\widetilde{\chi}_3^0, \widetilde{\chi}_1^\pm)$ increase with $m_{1/2}$. The mass differences $\Delta m(\widetilde{\chi}_1^\pm, \widetilde{\chi}_1^0)$, $\Delta m(\widetilde{\chi}_2^0, \widetilde{\chi}_1^0)$, and $\Delta m(\widetilde{\chi}_2^0, \widetilde{\chi}_1^\pm)$ decrease with $m_{1/2}$.

The NUHM2 cross-sections

The electroweakinos are divided into two categories, compressed and accessible, in the NUHM2 model. The compressed category contains the lower mass charginos $\widetilde{\chi}_1^\pm$ and neutralinos $\widetilde{\chi}_{1,2}^0$ and the accessible category contains the higher mass charginos $\widetilde{\chi}_2^\pm$ and neutralinos $\widetilde{\chi}_{3,4}^0$. Figure 5.3 shows the cross-sections for different combinations of electroweakino production and the detailed values can be found in App. A. The largest cross-section is the compressed + compressed production[2]

---

[2]Compressed + compressed means two particles belong to the compressed category.

$m_{1/2}$ [GeV]	$m_{\widetilde{\chi}_2^0}$ [GeV]	$m_{\widetilde{\chi}_1^\pm}$ [GeV]	$m_{\widetilde{\chi}_1^0}$ [GeV]	$(m_{\widetilde{\chi}_2^0} - m_{\widetilde{\chi}_1^\pm})/(m_{\widetilde{\chi}_1^\pm} - m_{\widetilde{\chi}_1^0})$
350	161.68	144.29	115.62	1.61
400	161.14	147.54	122.97	1.55
500	160.30	151.47	132.28	1.46
600	159.66	153.71	137.61	1.37
700	159.17	155.14	140.98	1.28
800	158.78	156.14	143.29	1.21

Table 5.3: The masses of $\widetilde{\chi}_1^0$, $\widetilde{\chi}_2^0$, and $\widetilde{\chi}_1^\pm$ and the ratios of the mass difference between $(m_{\widetilde{\chi}_2^0} - m_{\widetilde{\chi}_1^\pm})$ and $(m_{\widetilde{\chi}_1^\pm} - m_{\widetilde{\chi}_1^0})$. The $m_{\widetilde{\chi}_1^\pm}$ is not in the middle between $m_{\widetilde{\chi}_1^0}$ and $m_{\widetilde{\chi}_2^0}$.

and is almost independent of $m_{1/2}$. The cross-section of compressed + accessible[3] and accessible + accessible[4] productions are much smaller than the compressed + compressed production and they decrease quickly when $m_{1/2}$ increases. Therefore, only the different combinations of compressed production are considered in this analysis. The compressed + compressed production has cross-sections about the pb scale at 13 TeV, hence the Higgsino analysis is expected to have good sensitivity for the NUHM2 model.

The NUHM2 production channels and relevant decays

The compressed category contains $\widetilde{\chi}_1^\pm$, $\widetilde{\chi}_1^0$, and $\widetilde{\chi}_2^0$. Therefore, the compressed + compressed productions can be specified by $\widetilde{\chi}_1^0\widetilde{\chi}_1^0$, $\widetilde{\chi}_1^0\widetilde{\chi}_2^0$, $\widetilde{\chi}_1^0\widetilde{\chi}_1^\pm$, $\widetilde{\chi}_2^0\widetilde{\chi}_2^0$, $\widetilde{\chi}_2^0\widetilde{\chi}_1^\pm$, and $\widetilde{\chi}_1^\pm\widetilde{\chi}_1^\mp$. Because the highest sensitivity of this analysis is expected using two leptons, only the productions which can lead to events with two leptons

---

[3]Compressed + accessible means one particle belongs to the compressed category and another particle belongs to the accessible.

[4]Accessible + accessible means two particles belong to the accessible category.
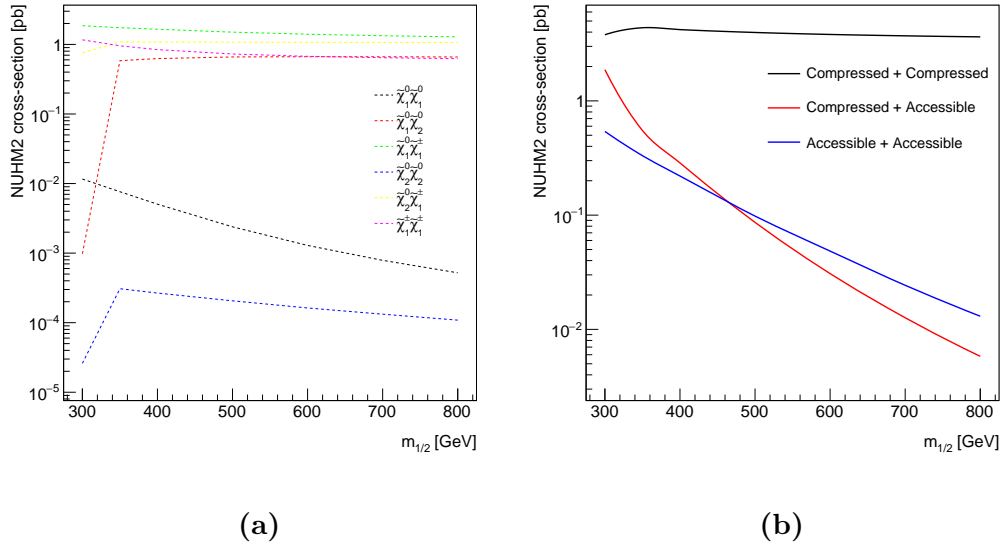
Figure 5.3: The NUHM2 cross-sections for (a) different combinations of compressed + compressed production and (b) all compressed + compressed, compressed + accessible, and accessible + accessible productions.

are considered. The R-parity conservation requires $\widetilde{\chi}_1^0$, which is the LSP, to be stable. Therefore, the $\widetilde{\chi}_1^0\widetilde{\chi}_1^0$ production cannot lead to events with the two leptons requirement. The cross-section of $\widetilde{\chi}_2^0\widetilde{\chi}_2^0$ production is very small so it can be neglected. The $\widetilde{\chi}_1^\pm$ decays into a $W^\pm$ and a $\widetilde{\chi}_1^0$, therefore, the $\widetilde{\chi}_1^0\widetilde{\chi}_1^\pm$ production does not lead to two leptons in the final state. Only the $\widetilde{\chi}_2^0\widetilde{\chi}_1^0$, $\widetilde{\chi}_2^0\widetilde{\chi}_1^\pm$, and $\widetilde{\chi}_1^\pm\widetilde{\chi}_1^\mp$ productions are considered in this analysis.

The neutralino $\widetilde{\chi}_2^0$ can decay into $\gamma\widetilde{\chi}_1^0$, $W^\pm\widetilde{\chi}_1^\mp$, $q\bar{q}\widetilde{\chi}_1^0$, $\ell^+\ell^-\widetilde{\chi}_1^0$, and $\nu\bar{\nu}\widetilde{\chi}_1^0$. Table 5.4 lists the branching ratios for all possible $\widetilde{\chi}_2^0$ decays for $m_{1/2} = 600$ GeV. Since the $\widetilde{\chi}_2^0 \to \gamma\widetilde{\chi}_1^0$ has very small branching ratio, this decay can be neglected.

The MC samples for the $\widetilde{\chi}_2^0\widetilde{\chi}_1^\pm$ generated by pp collisions are produced where four kinds of $\widetilde{\chi}_2^0$ decay are specified to determine the dominant one and the $\widetilde{\chi}_1^\pm$ decay is assumed to be $\widetilde{\chi}_1^\pm \to W^\pm\widetilde{\chi}_1^0 \to f\bar{f}\widetilde{\chi}_1^0$ where f and $\bar{f}$ stand for fermion

Decay	Branching Ratio	type
$\widetilde{\chi}_2^0 \to \gamma \widetilde{\chi}_1^0$	3.917×10^{-3}	-
$\widetilde{\chi}_2^0 \to \widetilde{\chi}_1^- u\bar{d}$	7.456×10^{-4}	
$\widetilde{\chi}_2^0 \to \widetilde{\chi}_1^- \nu_e e^+$	2.485×10^{-4}	
$\widetilde{\chi}_2^0 \to \widetilde{\chi}_1^- \nu_\nu \mu^+$	2.485×10^{-4}	
$\widetilde{\chi}_2^0 \to \widetilde{\chi}_1^+ d\bar{u}$	7.456×10^{-4}	
$\widetilde{\chi}_2^0 \to \widetilde{\chi}_1^+ e^- \bar{\nu}_e$	2.485×10^{-4}	$\widetilde{\chi}_2^0 \to W^\pm \widetilde{\chi}_1^\mp$
$\widetilde{\chi}_2^0 \to \widetilde{\chi}_1^+ \mu^- \bar{\nu}_\mu$	2.485×10^{-4}	
$\widetilde{\chi}_2^0 \to \widetilde{\chi}_1^- c\bar{s}$	7.456×10^{-4}	
$\widetilde{\chi}_2^0 \to \widetilde{\chi}_1^- \nu_\tau \tau^+$	2.485×10^{-4}	
$\widetilde{\chi}_2^0 \to \widetilde{\chi}_1^+ s\bar{c}$	7.456×10^{-4}	
$\widetilde{\chi}_2^0 \to \widetilde{\chi}_1^+ \tau^- \bar{\nu}_\tau$	2.485×10^{-4}	
$\widetilde{\chi}_2^0 \to \widetilde{\chi}_1^0 u\bar{u}$	0.126	
$\widetilde{\chi}_2^0 \to \widetilde{\chi}_1^0 d\bar{d}$	0.162	
$\widetilde{\chi}_2^0 \to \widetilde{\chi}_1^0 s\bar{s}$	0.162	$\widetilde{\chi}_2^0 \to q\bar{q}\widetilde{\chi}_1^0$
$\widetilde{\chi}_2^0 \to \widetilde{\chi}_1^0 c\bar{c}$	0.126	
$\widetilde{\chi}_2^0 \to \widetilde{\chi}_1^0 b\bar{b}$	0.091	
$\widetilde{\chi}_2^0 \to \widetilde{\chi}_1^0 e^- e^+$	3.672×10^{-2}	
$\widetilde{\chi}_2^0 \to \widetilde{\chi}_1^0 \mu^- \mu^+$	3.672×10^{-2}	$\widetilde{\chi}_2^0 \to \ell^+ \ell^- \widetilde{\chi}_1^0$
$\widetilde{\chi}_2^0 \to \widetilde{\chi}_1^0 \tau^- \tau^+$	3.354×10^{-2}	
$\widetilde{\chi}_2^0 \to \widetilde{\chi}_1^0 \nu_e \bar{\nu}_e$	7.307×10^{-2}	
$\widetilde{\chi}_2^0 \to \widetilde{\chi}_1^0 \nu_\mu \bar{\nu}_\mu$	7.307×10^{-2}	$\widetilde{\chi}_2^0 \to \nu\bar{\nu}\widetilde{\chi}_1^0$
$\widetilde{\chi}_2^0 \to \widetilde{\chi}_1^0 \nu_\tau \bar{\nu}_\tau$	7.307×10^{-2}	

Table 5.4: The possible $\widetilde{\chi}_2^0$ decays in NUHM2 model with $m_{1/2} = 600$ GeV. The $\widetilde{\chi}_2^0 \to \gamma \widetilde{\chi}_1^0$ has the lowest branching ratio hence it is not considered in our study. The rest of the decays are categorized into 4 types as shown in the third column.

and anti-fermion. Since $\tilde{\chi}_2^0 \to q\bar{q}\tilde{\chi}_1^0$ and $\tilde{\chi}_2^0 \to \nu\bar{\nu}\tilde{\chi}_1^0$ do not satisfy the two leptons requirement, the $\tilde{\chi}_2^0$ decay should be dominated by $\tilde{\chi}_2^0 \to W^{\pm}\tilde{\chi}_1^{\mp}$ and $\tilde{\chi}_2^0 \to \ell^+\ell^-\tilde{\chi}_1^0$. Table 5.5 shows the two leptons filter efficiency for the $\tilde{\chi}_2^0$ decays considered, the number of events in each decay type, and the contributions to the whole $\tilde{\chi}_2^0$ decay. Because the $\tilde{\chi}_2^0 \to \ell^+\ell^-\tilde{\chi}_1^0$ contributes more than 99%, the other three decays can be neglected. Although $\tilde{\chi}_2^0 \to q\bar{q}\tilde{\chi}_1^0$ and $\tilde{\chi}_2^0 \to \nu\bar{\nu}\tilde{\chi}_1^0$ are expected to have no contribution, due to the presence of the fake leptons, there are some contributions. This is expected, as no requirement on the truth matching was used in the selection.

		Filter efficiency			
Decay type	Branching Ratio	$pp \to \tilde{\chi}_2^0\tilde{\chi}_1^+$	$pp \to \tilde{\chi}_2^0\tilde{\chi}_1^-$	N_{event}	$N_{\mathrm{event}}/N_{\mathrm{total}}$
		$\tilde{\chi}_1^+ \to f\bar{f}\tilde{\chi}_1^0$	$\tilde{\chi}_1^- \to f\bar{f}\tilde{\chi}_1^0$		
$\tilde{\chi}_2^0 \to W^{\pm}\tilde{\chi}_1^{\mp}$	0.005	0.117	0.123	1.032	0.377%
$\tilde{\chi}_2^0 \to q\bar{q}\tilde{\chi}_1^0$	0.666	0.029	0.029	0.386	0.141%
$\tilde{\chi}_2^0 \to \ell^+\ell^-\tilde{\chi}_1^0$	0.108	0.606	0.620	272.463	99.482%
$\tilde{\chi}_2^0 \to \nu\bar{\nu}\tilde{\chi}_1^0$	0.220	0.010	0.010	0	0.0%
All $\tilde{\chi}_2^0$ decays	1	-	-	273.881	100%

Table 5.5: The two leptons filter efficiency for 4 kinds of $\tilde{\chi}_2^0$ decay, the number of events for each decay in $0 < m_{\ell\ell} < 50$ GeV, and the contributions to the whole $\tilde{\chi}_2^0$ decay. The transverse momentum of two leptons are required to be greater than 2 GeV and no $E_{\mathrm{T}}^{\mathrm{miss}}$ requirement is applied in the filter.

Figure 5.4 shows the $m_{\ell\ell}$ distributions in the NUHM2 model with $m_{1/2} = 600$ GeV and in the simplified Higgsino model with $m_{\tilde{\chi}_2^0} = 170$ GeV and $m_{\tilde{\chi}_1^0} = 150$ GeV. In this plot, only the $\tilde{\chi}_2^0\tilde{\chi}_1^{\pm}$ production is considered and the different

$\widetilde{\chi}_2^0$ decay contributions are stacked.

The NUHM2 generation

The ISAJET 7.84 SUSY mass spectrum generator is used to calculate the NUHM2 mass spectrum. The NUHM2 signal events were generated using MG5_AMC@NLO v2.2.3 with NNPDF23LO PDF set up to two extra partons in the ME. The MAD-SPIN [98] was used to decay the electroweakinos which were required to produce at least two leptons in the final state. Then the results were interfaced with PYTHIA v8.186 using the A14 tune to model the parton shower and hadronization. The PROSPINO v2.1 [99] is used to calculate the cross-section and theoretical uncertainties to the next-to-leading-logarithm (NLL) level. A filter required two leptons of at least 3 GeV and $E_{\mathrm{T}}^{\mathrm{miss}} \geq 50$ GeV was added at the generator level. Table 5.6 lists the NUHM2 MC production samples used in this analysis. The $\widetilde{\chi}_2^0\widetilde{\chi}_1^\pm$, $\widetilde{\chi}_2^0\widetilde{\chi}_1^0$, and $\widetilde{\chi}_1^\pm\widetilde{\chi}_1^\pm$ productions are considered in each $m_{1/2}$ mass point. The relative branching ratios were calculated using SUSY-HIT v1.5b [100] and were used in the event weighting. Table 5.7 compares the branching ratios for $\widetilde{\chi}_2^0 \to \ell^+\ell^-\widetilde{\chi}_1^0$ and $\widetilde{\chi}_1^\pm \to \ell\bar{\nu}\widetilde{\chi}_1^0$ calculated by ISAJET and SUSY-HIT. Good agreement can be seen using two different branching ratio calculators. In the $\widetilde{\chi}_2^0\widetilde{\chi}_1^\pm$, $\widetilde{\chi}_2^0\widetilde{\chi}_1^0$ productions, the $\widetilde{\chi}_2^0$ decays via $\widetilde{\chi}_2^0 \to \ell^+\ell^-\widetilde{\chi}_1^0$ and the $\widetilde{\chi}_1^\pm$ decays via $\widetilde{\chi}_1^\pm \to f\bar{f}\widetilde{\chi}_1^0$. But in the $\widetilde{\chi}_1^\pm\widetilde{\chi}_1^\mp$ production, the $\widetilde{\chi}_1^\pm$ decays via $\widetilde{\chi}_1^\pm \to \ell\bar{\nu}\widetilde{\chi}_1^0$.
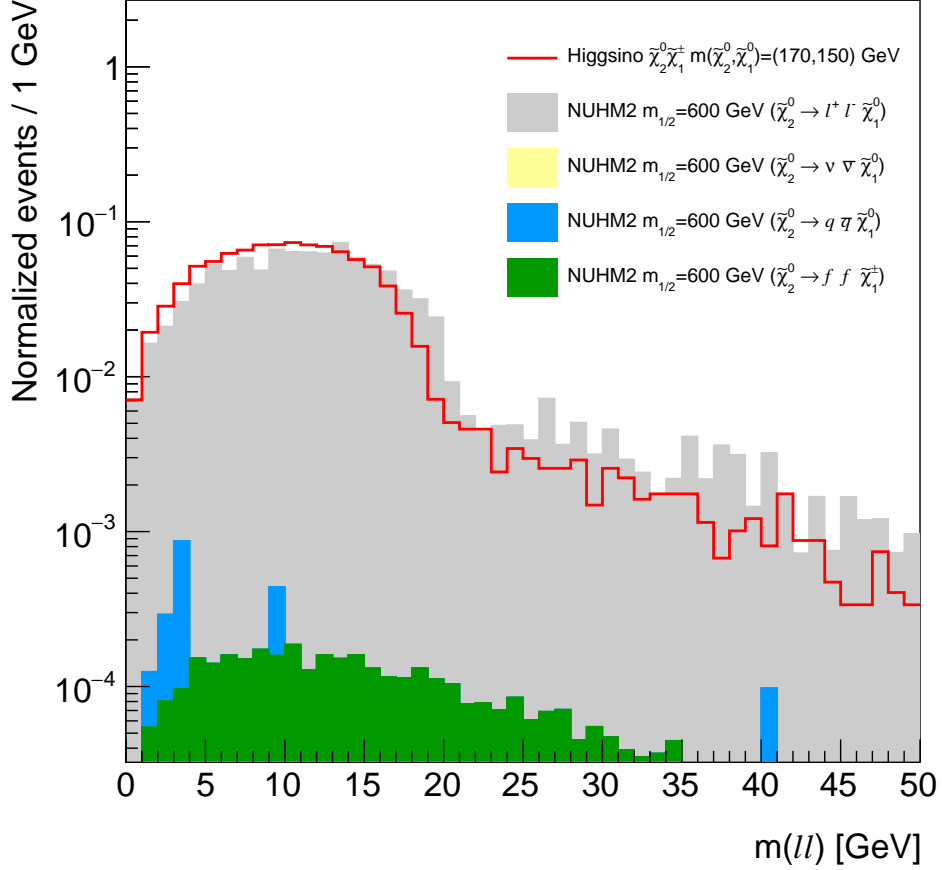
Figure 5.4: The $m_{\ell\ell}$ distributions for NUHM2 and simplified Higgsino models. The four possible $\widetilde{\chi}_2^0$ decay contributions for the NUHM2 model are stacked and $\widetilde{\chi}_2^0 \to \ell\ell\widetilde{\chi}_1^0$ is the dominant decay (shown in grey area). The difference between the two models come from the mass splitting $\Delta m = m_{\widetilde{\chi}_2^0} - m_{\widetilde{\chi}_1^0}$ where $\Delta m = 22$ GeV for NUHM2 and $\Delta m = 20$ GeV for simplified Higgsino model.

$m_{1/2}$ [GeV]	DSID	Production	Cross-section [pb]	Process	BF	Filter Efficiency	Relative uncertainty
350	394305	$\widetilde{\chi}_1^+\widetilde{\chi}_1^-$	0.9549	$\widetilde{\chi}_1^\pm \to l\nu\widetilde{\chi}_1^0$	0.3333	0.1299	0.0728
350	394306	$\widetilde{\chi}_2^0\widetilde{\chi}_1^-$	0.3984	$\widetilde{\chi}_2^0 \to ll\widetilde{\chi}_1^0$	0.1014	0.2529	0.0860
350	394307	$\widetilde{\chi}_2^0\widetilde{\chi}_1^+$	0.6833	$\widetilde{\chi}_2^0 \to ll\widetilde{\chi}_1^0$	0.1014	0.2558	0.0644
350	394308	$\widetilde{\chi}_2^0\widetilde{\chi}_1^0$	0.5835	$\widetilde{\chi}_2^0 \to ll\widetilde{\chi}_1^0$	0.1014	0.2277	0.0719
400	394309	$\widetilde{\chi}_1^+\widetilde{\chi}_1^-$	0.8416	$\widetilde{\chi}_1^\pm \to l\nu\widetilde{\chi}_1^0$	0.3332	0.1220	0.0740
400	394310	$\widetilde{\chi}_2^0\widetilde{\chi}_1^-$	0.3977	$\widetilde{\chi}_2^0 \to ll\widetilde{\chi}_1^0$	0.1029	0.2206	0.0852
400	394311	$\widetilde{\chi}_2^0\widetilde{\chi}_1^+$	0.6845	$\widetilde{\chi}_2^0 \to ll\widetilde{\chi}_1^0$	0.1029	0.2239.	0.0648
400	394312	$\widetilde{\chi}_2^0\widetilde{\chi}_1^0$	0.6256	$\widetilde{\chi}_2^0 \to ll\widetilde{\chi}_1^0$	0.1029	0.2042	0.0716
500	394313	$\widetilde{\chi}_1^+\widetilde{\chi}_1^-$	0.7281	$\widetilde{\chi}_1^\pm \to l\nu\widetilde{\chi}_1^0$	0.3332	0.1082	0.0733
500	394314	$\widetilde{\chi}_2^0\widetilde{\chi}_1^-$	0.3956	$\widetilde{\chi}_2^0 \to ll\widetilde{\chi}_1^0$	0.1054	0.1892	0.0842
500	394315	$\widetilde{\chi}_2^0\widetilde{\chi}_1^+$	0.6819	$\widetilde{\chi}_2^0 \to ll\widetilde{\chi}_1^0$	0.1054	0.1881	0.0636
500	394316	$\widetilde{\chi}_2^0\widetilde{\chi}_1^0$	0.6603	$\widetilde{\chi}_2^0 \to ll\widetilde{\chi}_1^0$	0.1054	0.1760	0.0701
600	394317	$\widetilde{\chi}_1^+\widetilde{\chi}_1^-$	0.6745	$\widetilde{\chi}_1^\pm \to l\nu\widetilde{\chi}_1^0$	0.3332	0.1000	0.0740
600	394318	$\widetilde{\chi}_2^0\widetilde{\chi}_1^-$	0.3930	$\widetilde{\chi}_2^0 \to ll\widetilde{\chi}_1^0$	0.1076	0.1687	0.0834
600	394319	$\widetilde{\chi}_2^0\widetilde{\chi}_1^+$	0.6791	$\widetilde{\chi}_2^0 \to ll\widetilde{\chi}_1^0$	0.1076	0.1693	0.0638
600	394320	$\widetilde{\chi}_2^0\widetilde{\chi}_1^0$	0.6657	$\widetilde{\chi}_2^0 \to ll\widetilde{\chi}_1^0$	0.1076	0.1535	0.0705
700	394321	$\widetilde{\chi}_1^+\widetilde{\chi}_1^-$	0.6439	$\widetilde{\chi}_1^\pm \to l\nu\widetilde{\chi}_1^0$	0.3331	0.0935	0.0730
700	394322	$\widetilde{\chi}_2^0\widetilde{\chi}_1^-$	0.3913	$\widetilde{\chi}_2^0 \to ll\widetilde{\chi}_1^0$	0.1097	0.1580	0.0858
700	394323	$\widetilde{\chi}_2^0\widetilde{\chi}_1^+$	0.6766	$\widetilde{\chi}_2^0 \to ll\widetilde{\chi}_1^0$	0.1097	0.1587	0.0643
700	394324	$\widetilde{\chi}_2^0\widetilde{\chi}_1^0$	0.6643	$\widetilde{\chi}_2^0 \to ll\widetilde{\chi}_1^0$	0.1097	0.1379	0.0702
800	394325	$\widetilde{\chi}_1^+\widetilde{\chi}_1^-$	0.6240	$\widetilde{\chi}_1^\pm \to l\nu\widetilde{\chi}_1^0$	0.3331	0.0872	0.0724
800	394326	$\widetilde{\chi}_2^0\widetilde{\chi}_1^-$	0.3906	$\widetilde{\chi}_2^0 \to ll\widetilde{\chi}_1^0$	0.1116	0.1392	0.0824
800	394327	$\widetilde{\chi}_2^0\widetilde{\chi}_1^+$	0.6749	$\widetilde{\chi}_2^0 \to ll\widetilde{\chi}_1^0$	0.1116	0.1463	0.0628
800	394328	$\widetilde{\chi}_2^0\widetilde{\chi}_1^0$	0.6598	$\widetilde{\chi}_2^0 \to ll\widetilde{\chi}_1^0$	0.1116	0.1283	0.0694

Table 5.6: The NUHM2 MC sample dataset ID (DSID), productions, cross-sections, and decay processes and its relevant branching ratios, the filter efficiencies, and the uncertainties are given.

$m_{1/2}$ [GeV]	Process	Branching ratio		Difference (%)
		ISAJET	SUSY-HIT	
350	$\widetilde{\chi}_1^\pm \to \ell\bar{\nu}\widetilde{\chi}_1^0$	0.33333	0.33326	0.02
	$\widetilde{\chi}_2^0 \to \ell\ell\widetilde{\chi}_1^0$	0.10133	0.10138	0.05
400	$\widetilde{\chi}_1^\pm \to \ell\bar{\nu}\widetilde{\chi}_1^0$	0.33334	0.33324	0.03
	$\widetilde{\chi}_2^0 \to \ell\ell\widetilde{\chi}_1^0$	0.10288	0.10293	0.05
500	$\widetilde{\chi}_1^\pm \to \ell\bar{\nu}\widetilde{\chi}_1^0$	0.33334	0.33320	0.04
	$\widetilde{\chi}_2^0 \to \ell\ell\widetilde{\chi}_1^0$	0.10517	0.10538	0.20
600	$\widetilde{\chi}_1^\pm \to \ell\bar{\nu}\widetilde{\chi}_1^0$	0.33334	0.33316	0.05
	$\widetilde{\chi}_2^0 \to \ell\ell\widetilde{\chi}_1^0$	0.10883	0.10760	1.13
700	$\widetilde{\chi}_1^\pm \to \ell\bar{\nu}\widetilde{\chi}_1^0$	0.33334	0.33313	0.06
	$\widetilde{\chi}_2^0 \to \ell\ell\widetilde{\chi}_1^0$	0.10843	0.10970	1.16
800	$\widetilde{\chi}_1^\pm \to \ell\bar{\nu}\widetilde{\chi}_1^0$	0.33333	0.33311	0.07
	$\widetilde{\chi}_2^0 \to \ell\ell\widetilde{\chi}_1^0$	0.10947	0.11164	1.95

Table 5.7: The branching ratios calculated by ISAJET and SUSY-HIT. The differences are calculated with respect to the SUSY-HIT branching ratio results. Good agreement between the results from the two branching ratio calculators can be seen. The largest difference between the results calculated by ISAJET and SUSY-HIT is less than 2%.

CHAPTER 6

EVENT RECONSTRUCTION AND SELECTION

Candidate events are required to have a reconstructed pp interaction vertex with at least two $p_\mathrm{T} > 400$ MeV associated tracks. The vertex with the largest $\sum p_\mathrm{T}^2$ of the associated tracks is selected as the primary vertex of the event. In this chapter, the various object reconstruction and identification criteria in the ATLAS experiment are presented. The electron, muon, and tau objects are presented in Sect. 6.1.1, 6.1.2, and 6.1.3, respectively, followed by the photons in Sect. 6.1.4, jets in Sect. 6.1.5, and $E_\mathrm{T}^\mathrm{miss}$ in Sect. 6.1.6. Finally, the signal region (SR) selection is described in Sect. 6.2.

6.1   Object selections

This section presents the object definition and selection in the analysis. The general object selections for ATLAS are described followed by the specific selections used for this analysis. The definition of objects used in this analysis are based on the recommendations by Combined Performance groups and are summarized in Table 6.1. The objects are divided into two categories: preselected and signal objects where signal objects are a subset of preselected objects. Unless otherwise stated, the recommendations implemented in `SUSYTools-00-08-69` [101] and `AnalysisBase 2.4.37` [102] are used for all the objects.

Property	Preselected object	Signal object
Electrons		
Kinematic	$p_T > 4.5$ GeV	$p_T > 4.5$ GeV, $|\eta| < 2.47$ (include crack)
Identification	`VeryLooseLLH`	`TightLLH`
Isolation	-	`GradientLoose`
Impact parameter	$|z_0 \sin\theta| < 0.5$ mm	$|d_0/\sigma(d_0)| < 5$, $|z_0 \sin\theta| < 0.5$ mm
Reco algorithm	Veto `author==16`	Veto `author==16`
Muons		
Kinematic	$p_T > 4$ GeV	$p_T > 4$ GeV, $|\eta| < 2.5$
Identification	`Medium`	`Medium`
Isolation	-	`FixedCutTightTrackOnly`
Impact parameter	$|z_0 \sin\theta| < 0.5$ mm	$|d_0/\sigma(d_0)| < 3$, $|z_0 \sin\theta| < 0.5$ mm
Jets		
Kinematic	$p_T > 20$ GeV, $|\eta| < 4.5$	$p_T > 30$ GeV, $|\eta| < 2.8$
Clustering	Anti-k_t $R = 0.4$ `EMTopo`	Anti-k_t $R = 0.4$ `EMTopo`
Pileup mitigation	-	JVT `Medium` for $p_T < 60$ GeV, $|\eta| < 2.4$
b-tagging	-	$p_T > 20$ GeV, $|\eta| < 2.5$, MV2c10 `FixedCutBeff` 85%

Table 6.1: Summary of object definitions used in this analysis.

6.1.1 Electrons

General electron reconstruction and identification

In the ATLAS experiment, electron[1] objects are reconstructed and identified using the information from the ID tracks matched to energy clusters in the ECAL. Three likelihood based electron identification algorithms, `Loose`, `Medium`, and `Tight` are applied to determine the signal-like reconstructed electron candidates. These three identifications use the same variables to define the likelihood discriminant but with different selection criteria. Depending on the electron identification

---

[1]Electrons and positrons are collectively referred to as electrons.

used, the reconstruction efficiency varies from 78 to 90% and increases with E_T^{miss}. The electron isolation efficiency varies between 90% and 99% depending on the isolation selection criteria. More details about the electron reconstruction performance can be found in Ref. [17] and a detailed description about the electron isolation, which is my ATLAS authorship project, can be found in the App. C.

Specific to this analysis

The preselected electrons used in this analysis have to satisfy $p_T > 4.5$ GeV and $|\eta| < 2.47$ and pass the likelihood-based `VeryLooseLLH` identification. The electron tracks are required to satisfy the longitudinal impact parameter $|z_0 \sin \theta| < 0.5$ mm. The electrons coming from the photon conversion are rejected by an algorithm. The signal electrons have a tighter selection criteria. Besides all the requirements for the preselected electrons, the signal electrons are also required to pass `TightLLH` identification, `GradientLoose` isolation, and the transverse impact parameter $|d_0/\sigma(d_0)| < 5$ requirements.

6.1.2 Muons

General muon reconstruction and identification

In the ATLAS experiment, muon objects are reconstructed and identified using the information from ID and muon spectrometer in the $p_T > 4$ GeV and $|\eta| < 2.7$ region. Muon candidates are identified by applying quality requirements to suppress background which mainly come from pion and kaon decays. Four categories of muon identification, `Medium`, `Loose`, `Tight`, and `High-`p_T are provided

for different physics analyses. The `Medium` identification minimizes the systematic uncertainties and is provided as the default selection for muons in ATLAS. The `Loose` identification maximizes the reconstruction efficiency and is used for analyses with multilepton final states. The `Tight` identification maximizes the purity of muons and the `High-`p_T identification maximizes the momentum resolution for $p_\mathrm{T} > 100$ GeV. The muon reconstruction efficiency is about 99% in the $5 < p_\mathrm{T} < 100$ GeV and $|\eta| < 2.5$ phase space. The muon isolation efficiency varies between 93% and 100% depending on the isolation selection criteria. More details about the muon reconstruction performance can be found in Ref. [103].

Specific to this analysis

The preselected muons used in this analysis have to satisfy $p_\mathrm{T} > 4$ GeV and $|\eta| < 2.5$, pass the `Medium` identification, and require $|z_0 \sin\theta| < 0.5$ mm on the longitudinal impact parameter. A tighter requirement is applied on the signal muons which in addition pass the `FixedCutTightTrackOnly` isolation together with $|d_0/\sigma(d_0)| < 3$ on the transverse impact parameter.

6.1.3 Taus

General τ reconstruction and identification

The mass of τ lepton is 1.77 GeV and the decay length is 80 μm which is too short for the τ to reach the active region of the ATLAS detector. The τ can decay either leptonically ($\tau \to \ell\nu_\ell$, $\ell = e, \mu$) or hadronically ($\tau \to \mathrm{hadrons} + \nu_\tau$). The hadronic tau decays are about 65% of all possible decay modes and the decay products contain one charged pion (22%) or three charged pions (72%). Tau

candidates are seeded by jets using the method described in Ref. [104] and they are required to have $p_\mathrm{T} > 10$ GeV and $|\eta| < 2.5$ but vetoing the candidates in the crack region $1.37 < |\eta| < 1.52$. A boosted decision tree (BDT) based algorithm is used to identify the τ candidate and to reject backgrounds from quark- and gluon-initiated jets. Three identification criteria, `Loose`, `Medium`, and `Tight` are provided with the efficiency 60%, 55%, and 45% for 1-track and 50%, 40%, and 30% for 3-tracks, respectively. More details about the τ lepton reconstruction and identification performance can be found in Ref. [104].

Specific to this analysis

The di-tau invariant mass $m_{\tau\tau}$ is used in this analysis and addressed in Sect. 6.2.1.

6.1.4   Photons

General photons reconstruction and identification

In the ATLAS experiment, photons are reconstructed using the tracking information in the ID and the energy deposits in the CAL. To distinguish prompt photons[2] from background photons, the photon identification is based on a set of rectangular cuts on several discriminating variables computed from the energy deposited in the ECAL and from the shower leakage to the HCAL. The photon identification is separately applied to the converted and unconverted photons with $25 \leq E_\mathrm{T} \leq 1500$ GeV and four $|\eta|$ intervals. Two identification criteria, `Loose` and `Tight`, are provided. The `Loose` identification provides high efficiency with low jet rejection and the `Tight` identification, which is recommended for

---

[2]Prompt photons are photons not originating from hadron decays

the analyses by the Combined Performance groups, provides high fake photon rejection and good efficiency. The `Tight` identification efficiency starts from 84% at low E_T and reaches around 98% in the $1.37 < |\eta| < 1.81$ region for unconverted photons. Similar to the unconverted photons, the efficiency for converted photons increases with energy and reaches up to 98%. More details about the photon reconstruction and identification can be found in Ref. [105].

Specific to this analysis

Photons are required to pass `Tight` identification and have $p_T > 25$ GeV.

6.1.5 Jets

General jets reconstruction

In the ATLAS experiment, jets are reconstructed using the anti-k_t algorithm with radius parameter $R = 0.4$. The reconstruction algorithm uses calorimeter topological clusters in $|\eta| < 4.5$ as input. Four jet cleaning selections, `Looser`, `Loose`, `Medium`, and `Tight`, are provided. The `Looser` has the highest efficiency, $\sim$99.8%, and the `Tight` has the highest background rejection with efficiency 85% at $p_T = 25$ GeV and 98% at $p_T > 50$ GeV. More details about the jets reconstruction using anti-k_t algorithm can be found in Ref. [106].

b-tagging

In the ATLAS experiment, it is very important to identify jets containing b hadrons and discriminate them from light flavor jets[3]. Many b-tagging algorithms were developed to maintain a high b-tagging efficiency for real b-jets and to

---

[3]The light flavor jets mean jets containing u, d, s, c, or gluons.

retain very low misidentification efficiency of the light flavor jets. The newly developed multivariable algorithm, MV2, improving the c-jet rejection $\sim$40% at 77% b-tagging efficiency and the rejection power at high b-jet p_{T} is also improved. More details about the b-tagging can be found in Ref. [107, 108].

Specific to this analysis

The preselected jets are reconstructed with the anti-k_t algorithm with radius parameter $R = 0.4$ and required $p_{\mathrm{T}} > 20$ GeV and $|\eta| < 4.5$. Jets with $p_{\mathrm{T}} < 60$ GeV and $|\eta| < 2.4$ are required to satisfy `Medium` jet vertex tagger requirement which can suppress pileup jets [109]. The MV2c10 b-tagging algorithm with an 85% efficiency is applied on the preselected jets with $|\eta| < 2.5$. The signal jets are required to satisfy $p_{\mathrm{T}} > 30$ GeV and $|\eta| < 2.8$.

6.1.6 Missing transverse energy

The missing transverse energy $E_{\mathrm{T}}^{\mathrm{miss}}$ is defined as the negative vector sum of p_{T} of all reconstructed objects including leptons, jets, and soft term as show in Eq. (6.1).

$$E_{\mathrm{T}}^{\mathrm{miss}} = -(\sum \mathbf{p}_{\mathrm{T}}^{\mathrm{hard}} + \mathbf{p}_{\mathrm{T}}^{\mathrm{soft}}) \tag{6.1}$$

The soft term is constructed from all tracks associated to the primary vertex but not associated with any physics object. Two kinds of soft term, calorimeter based soft term (CST) and track based soft term (TST) can be used in $E_{\mathrm{T}}^{\mathrm{miss}}$ calculation. The CST $E_{\mathrm{T}}^{\mathrm{miss}}$ is constructed from the energy deposits in the calorimeters not associated with hard objects and the TST $E_{\mathrm{T}}^{\mathrm{miss}}$ is built from ID tracks which do not match to any reconstructed object. More details about the

$E_{\mathrm{T}}^{\mathrm{miss}}$ reconstruction performance can be found in Ref. [110].

6.1.7 Overlap removal

After preselected objects are reconstructed, an overlap removal procedure is applied to resolve ambiguities between the reconstructed jets and leptons. The distance ΔR between two objects is used for overlap removal and ΔR is defined as

$$\Delta R = \sqrt{(\Delta y)^2 + (\Delta \phi)^2} \tag{6.2}$$

where y and ϕ are rapidity and azimuthal angle, respectively. The overlap removal procedure has to follow the steps listed below. In order to avoid the bremsstrahlung from muons followed by a photon conversion into electron pairs, the electron candidate is removed if it shares the same ID track with a muon object. The jet is removed if $\Delta R(\mathrm{jets}, e) < 0.2$ from the remaining electrons unless it is a b-jet. If there are less than 3 tracks with $p_{\mathrm{T}} > 500$ MeV in a jet and the distance between jets and a muon candidate is less than 0.4, i.e. $\Delta R(\mathrm{jets}, \mu) < 0.4$, then the jet is removed. This step can suppress muon bremsstrahlung. Finally, the electrons and muons are removed if the e or μ lie in a distance $\Delta R(\mathrm{jets}, e/\mu) < 0.4$ of the surviving jets so that charm and bottom hadron decays are suppressed.

6.2 Signal region selection

6.2.1 Discriminating variables

This section provides the explanations for various variables used to discriminate signals and background.

- **Same flavor opposite sign (SFOS) lepton pair**: This analysis requires exactly two preselected and two signal leptons in the final state. These two leptons have to carry the same flavor and with opposite electric charge such as $e^{\pm}e^{\mp}$ and $\mu^{\pm}\mu^{\mp}$.

- $\mathbf{p_T^{\ell_1}}$ and $\mathbf{p_T^{\ell_2}}$: The momentum of the leading lepton $p_T^{\ell_1} > 5$ GeV is required to suppressed fake/non-prompt leptons background and the threshold of the momentum of the subleading lepton $p_T^{\ell_2} > 4.5(4)$ GeV for electron (muon) is used to retain signal acceptance.

- $\mathbf{\Delta R_{\ell\ell}}$: The dilepton distance is defined by Eq. (6.3). The $\Delta R_{\ell\ell}$ variable, which is required to be greater than 0.05, suppresses muons causing fake pairs of tracks or the lepton pairs originating from photon conversions.

$$\Delta R_{\ell\ell} = \sqrt{(\eta_{\ell_1} - \eta_{\ell_2})^2 + (\phi_{\ell_1} - \phi_{\ell_2})^2} \tag{6.3}$$

- $\mathbf{m_{\ell\ell}}$: The dilepton invariant mass $m_{\ell\ell}$ is bounded by the mass splitting $m(\widetilde{\chi}_2^0) - m(\widetilde{\chi}_1^0)$ for signal events providing the background suppression power. Background originating from on-shell Z decay can be suppressed if the upper bound of $m_{\ell\ell}$ is set to 60 GeV and the contributions from J/ψ are vetoed by required a $3 < m_{\ell\ell} < 3.2$ GeV window.

- $\mathbf{E_T^{miss}}$: In order to keep the E_T^{miss} trigger efficiency exceeding 95%, E_T^{miss} is required to be greater than 200 GeV.

- N_{jet}: The presence of at least one jet is required because of the initial state radiation (ISR) jets.

- $\mathbf{p_T^{j_1}}$: The momentum of the leading jet is required to be greater than 100 GeV.

- $\mathbf{\Delta\phi(j_1, p_T^{miss})}$: The azimuthal separation between j_1 and $\mathbf{p_T^{miss}}$ is required to be greater than 2 to suppress the QCD and Z+jets background.

- $\mathbf{min(\Delta\phi(any\ jet, p_T^{miss}))}$: By requiring $\Delta\phi(\text{any jet}, p_T^{miss}) > 0.4$, the effect of jet-energy mismeasurement on E_T^{miss} can be reduced.

- $\mathbf{N_{b\text{-}jet}}$: By vetoing the presence of b-jets ($N_{b\text{-}jet} = 0$), the $t\bar{t}$ and single-top backgrounds can be reduced significantly.
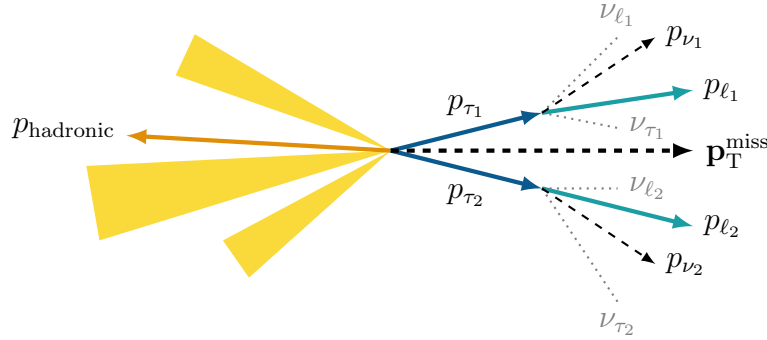
Figure 6.1: The illustration of the $Z \to \tau\tau$ + jets decay where τ decays leptonically $\tau \to \ell\nu_\ell\nu_\tau$.

- $\mathbf{m_{\tau\tau}}$: The di-tau invariant $m_{\tau\tau}(p_{\ell_1}, p_{\ell_2}, \mathbf{p_T^{miss}})$ variable is defined as the signed square root of $m_{\tau\tau}^2$. The $m_{\tau\tau}$ is used to reconstructed the $Z \to \tau\tau$ process where τ decays leptonically $\tau \to \ell\nu_\ell\nu_\tau$. Figure 6.1 shows the Z boson leptonic decay process. The $m_{\tau\tau}^2$ is defined in Eq. (6.4)

$$m_{\tau\tau}^2 \equiv 2p_{\ell_1} \cdot p_{\ell_2}(1 + \xi_1)(1 + \xi_2) \tag{6.4}$$

where p_{ℓ_1} and p_{ℓ_2} are the momenta of the leptons and the ξ_1 and ξ_1 are the scale factor which can be determined by solving $\mathbf{p_T^{miss}} = \xi_1\mathbf{p_T^{\ell_1}} + \xi_2\mathbf{p_T^{\ell_2}}$. From

Eq. (6.4), the $m_{\tau\tau}^2$ can be negative when either $1 + \xi_1 < 0$ or $1 + \xi_2 < 0$. This situation occurs when only one lepton moves in the same direction as $\mathbf{p}_{hadronic}$ and $|\mathbf{p}_\ell|$ is small. This rarely happens for highly boosted $Z \to \tau\tau$ decays but it happens with larger frequency for less boosted heavy particles which decay back-to-back. The $m_{\tau\tau}$ is calculated using Eq. (6.6).

$$m_{\tau\tau} = \text{sign}(m_{\tau\tau}^2)\sqrt{|m_{\tau\tau}^2|} \tag{6.5}$$

$$= \begin{cases} \sqrt{m_{\tau\tau}^2} & m_{\tau\tau}^2 \geq 0, \\ -\sqrt{|m_{\tau\tau}^2|} & m_{\tau\tau}^2 < 0. \end{cases} \tag{6.6}$$

Despite a discontinuity at $m_{\tau\tau} = 0$, this variable can be used to discriminate the leptons originating from $Z \to \tau\tau$.

- $\mathbf{m_T^{\ell_1}}$: The transverse mass of E_T^{miss} and the leading lepton is defined in Eq. (6.7). The $t\bar{t}$, WW/WZ, and W+jets background can be reduced by requiring $m_T^{\ell_1} < 70$ GeV.

$$m_T^{\ell_1} = \sqrt{2(E_T^{\ell_1} E_T^{\text{miss}} - \mathbf{p}_T^{\ell_1} \cdot \mathbf{p}_T^{\text{miss}})} \tag{6.7}$$

- $\mathbf{E_T^{\text{miss}}/H_T^{\text{lep}}}$: The scalar sum of the lepton transverse momentum, H_T^{lep}, is defined in Eq. (6.8). The H_T^{lep} variable has smaller value in the compressed SUSY signal and larger value in the SM background such as WW or WZ.

$$H_T^{\text{lep}} = p_T^{\ell_1} + p_T^{\ell_2} \tag{6.8}$$

The leptons coming from SM background, for example, $t\bar{t}$ and diboson are harder but they are softer in the compressed SUSY signal events. Therefore, for a given value of E_T^{miss}, the $E_T^{\text{miss}}/H_T^{\text{lep}}$ variable is larger in the compressed signals but is smaller for the background. The minimal requirement of this

variable is defined in Eq. (6.9) which is adjusted event by event depending on the mass splitting.

$$E_{\mathrm{T}}^{\mathrm{miss}}/H_{\mathrm{T}}^{\mathrm{lep}} > \max[5, 15 - 2m_{\ell\ell}/(1 \ \mathrm{GeV})] \tag{6.9}$$

Figure 6.2 shows the $E_{\mathrm{T}}^{\mathrm{miss}}/H_{\mathrm{T}}^{\mathrm{lep}}$ requirement for the electroweakino SR after applying all the SR common requirements and the $\Delta R_{\ell\ell} < 2$.

6.2.2 Signal region

Events with 2 lepton final state are selected if the lepton pair satisfies the same flavor and opposite charge (SFOS) requirement. To optimize the signal selection criteria, a number of scans over the cut values of discriminating variables listed in Sect. 6.2.1 are performed and the significance Z_n [111] is calculated. In order to maximize the Z_n, an integrated luminosity of 36 fb^{-1}and a systematic uncertainty of 20% on the background are assumed and at least one background event remaining is required after optimized cuts. A set of binned dilepton invariant mass $m_{\ell\ell}$ are defined in the SR and the kinematic distribution of $m_{\ell\ell}$ is used in a fit to extract the number of signal events. The event selection criteria for the SR are summarized in Table 6.2.

The $m_{\ell\ell}$ binnings are listed in Table 6.3. There are 14 exclusive regions and 7 inclusive regions defined. The exclusive regions are used to set model-dependent limits while the inclusive regions are used to set the model-independent upper limits. To derive the exclusion limits on the signal model, the SRee-$m_{\ell\ell}$ and SR$\mu\mu$-$m_{\ell\ell}$ regions are combined and fit simultaneously. The tightest inclusive region allowing the mass splitting up to 3 GeV is the most compressed scenario while the looser regions allow large mass splittings up to 60 GeV.
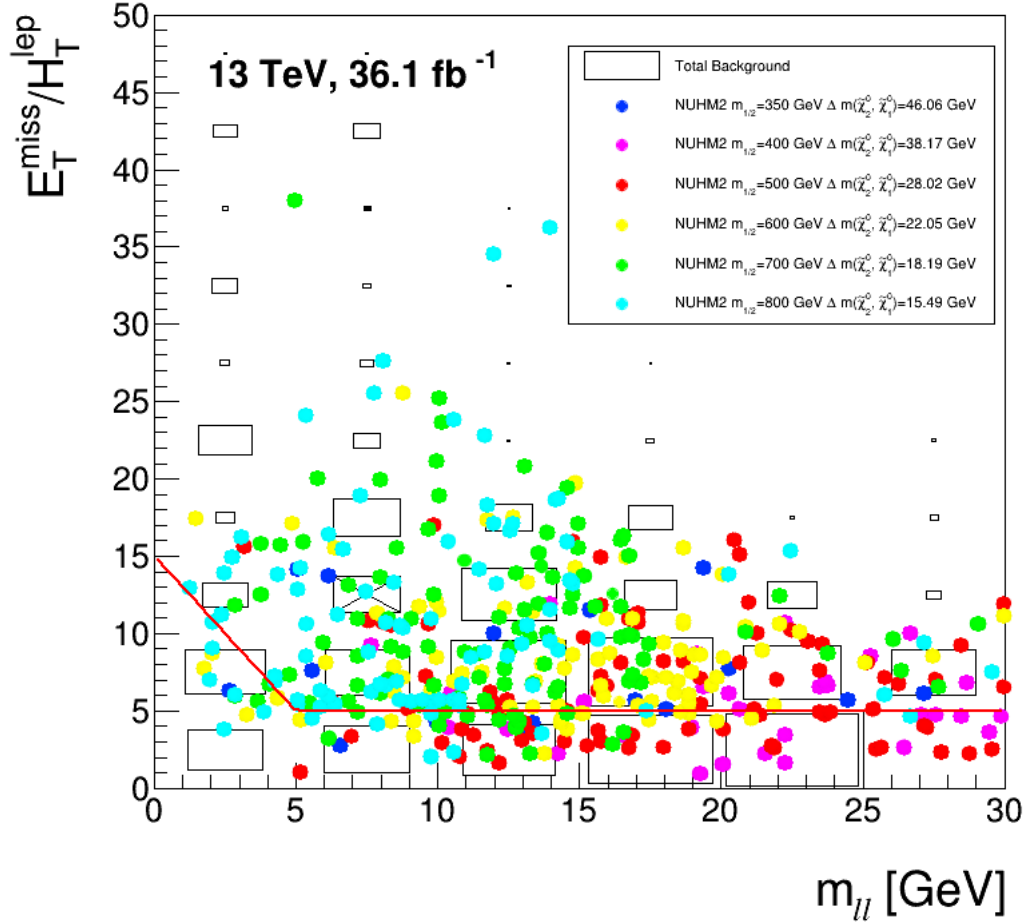
Figure 6.2: The distribution of $E_T^{\mathrm{miss}}/H_T^{\mathrm{lep}}$ as function of $m_{\ell\ell}$ for the electroweakino after applying all the SR common requirements and the $\Delta R_{\ell\ell} < 2$. The red line indicates the SR selection. Events in the region below this line are rejected. The signal events are labeled in colored circles for different mass splitting.

Variable	Common requirement
Number of leptons	$= 2$
Lepton charge and flavor	e^+e^- or $\mu^+\mu^-$
Leading lepton $p_T^{\ell 1}$	> 5 GeV for electron and muon
Subleading lepton $p_T^{\ell 2}$	> 4.5 (4) GeV for electron (muon)
$\Delta R_{\ell\ell}$	> 0.05
$m_{\ell\ell}$	$\in [1, 60]$ GeV excluding $[3.0, 3.2]$ GeV
E_T^{miss}	> 200 GeV
Number of jets	≥ 1
Leading jet p_T	> 100 GeV
$\Delta\phi(j_1, \mathbf{p}_T^{miss})$	> 2.0
$\min(\Delta\phi(\text{any jet}, \mathbf{p}_T^{miss}))$	> 0.4
Number of b-tagged jets	$= 0$
$m_{\tau\tau}$	< 0 or > 160 GeV
	Electroweakino SRs
$\Delta R_{\ell\ell}$	< 2
$m_T^{\ell 1}$	< 70 GeV
E_T^{miss}/H_T^{lep}	$> \max(5, 15 - 2\ \frac{m_{\ell\ell}}{1\ \text{GeV}})$
Binned in	$m_{\ell\ell}$

Table 6.2: Summary of event selection criteria. The upper part lists the common selection criteria and the lower part lists the SR requirement for this analysis searching electroweakinos. Signal leptons and signal jets are used when applying all requirements. The SR binning is listed in Table 6.3.

	Electroweakino SRs							
Exclusive	SRee-$m_{\ell\ell}$, SR$\mu\mu$-$m_{\ell\ell}$	[1, 3]	[3.2, 5]	[5, 10]	[10, 20]	[20, 30]	[30, 40]	[40, 60]
Inclusive	SR$\ell\ell$-$m_{\ell\ell}$	[1, 3]	[1, 5]	[1, 10]	[1, 20]	[1, 30]	[1, 40]	[1, 60]

Table 6.3: The SR binnings for the electroweakino SRs. The SR is defined by a $m_{\ell\ell}$ range in GeV. The exclusive bins are used to set the exclusion limits on the model and the inclusive bins are used to set the model-independent limits.

6.2.3 Expected yields in SR

The expected yields in SR for the NUHM2 are estimated using the signal MC samples. Four kind of production channels, $\widetilde{\chi}_2^0\widetilde{\chi}_1^0$, $\widetilde{\chi}_2^0\widetilde{\chi}_1^+$, $\widetilde{\chi}_2^0\widetilde{\chi}_1^-$, and $\widetilde{\chi}_1^\pm\widetilde{\chi}_1^\mp$, and 6 different $m_{1/2}$, 350, 400, 500, 600, 700, and 800 GeV, are generated. The $\widetilde{\chi}_2^0$ decays to $\ell^+\ell^-\widetilde{\chi}_1^0$ only and $\widetilde{\chi}_1^\pm$ decays to $f\bar{f}\widetilde{\chi}_1^0$ for the $\widetilde{\chi}_2^0\widetilde{\chi}_1^\pm$ channel and to $\ell\nu_\ell\widetilde{\chi}_1^0$ for $\widetilde{\chi}_1^\pm\widetilde{\chi}_1^\mp$ channel.

Truth level study

The truth level information in the signal MC samples are used to calculate the acceptance of the SR selection criteria. The expected yields after SR selection in the truth level can be obtained by taking the product of luminosity (36.1 fb^{-1}), acceptance, filter efficiency, cross-section, and the branching ratio. Table 6.4 shows the acceptance, the cross-section, the branchings for different production channels, the 2LMET50 filter efficiency, and the expected yields in SR using the truth level information.

NUHM2 $m_{1/2}$ [GeV]		$\tilde{\chi}_2^0 \tilde{\chi}_1^0$	$\tilde{\chi}_1^{\pm} \tilde{\chi}_1^{\mp}$	$\tilde{\chi}_2^0 \tilde{\chi}_1^+$	$\tilde{\chi}_2^0 \tilde{\chi}_1^-$
	acceptance	0.030534	0.020215	0.017051	0.013404
	cross-section	0.583519	0.954870	0.683346	0.398366
350	branching ratio	0.101385	0.111060	0.101385	0.101385
	filter efficiency	0.22768	0.12992	0.25578	0.25287
	expected events in SR	14.85	10.05	10.91	4.94
	acceptance	0.032875	0.021152	0.017745	0.017960
	cross-section	0.625560	0.841584	0.684520	0.397684
400	branching ratio	0.102935	0.111047	0.102935	0.102935
	filter efficiency	0.20416	0.12201	0.22389	0.22064
	expected events in SR	15.60	8.71	10.11	5.85
	acceptance	0.036173	0.024281	0.023709	0.022937
	cross-section	0.660309	0.728079	0.681917	0.395590
500	branching ratio	0.105385	0.111019	0.105385	0.105385
	filter efficiency	0.17602	0.10822	0.18806	0.18924
	expected events in SR	15.99	7.66	11.57	6.53
	acceptance	0.042456	0.024326	0.027313	0.027153
	cross-section	0.665650	0.674514	0.679145	0.393040
600	branching ratio	0.107604	0.110995	0.107604	0.107604
	filter efficiency	0.15353	0.10002	0.16926	0.16871
	expected events in SR	16.85	6.57	12.19	6.99
	acceptance	0.044454	0.025197	0.031214	0.028996
	cross-section	0.664327	0.643884	0.676607	0.391328
700	branching ratio	0.109701	0.110976	0.109701	0.109701
	filter efficiency	0.13788	0.093538	0.15874	0.15801
	expected events in SR	16.12	6.08	13.27	7.10
	acceptance	0.043270	0.024337	0.030427	0.026019
	cross-section	0.659812	0.624032	0.674869	0.390607
800	branching ratio	0.111643	0.110964	0.111643	0.111643
	filter efficiency	0.12825	0.087180	0.14631	0.13915
	expected events in SR	14.75	5.30	12.11	5.68

Table 6.4: The acceptance, the cross-section, the branchings for different production channels, the 2LMET50 filter efficiency, and the expected yields in SR common to 2ℓ channel for four different production channels of NUHM2 signal MC samples are given. The expected yields in the SR are obtained by taking the product of luminosity (36.1 fb^{-1}), acceptance, filter efficiency, cross-section, and the branching ratio.

Kinematic distributions

Figure 6.3, 6.4, and 6.5 show the kinematic variable distributions for the NUHM2 model with $m_{1/2} = 500$ GeV in $1 < \text{SR}\ell\ell\text{-}m_{\ell\ell} < 60$ GeV. The distributions for the other $m_{1/2}$ mass points can be found in the App. B. In order to compare the signal with background distributions, the NUHM2 distributions are multiplied by 10 but the number of events listed in the legends are actual values. When making these so called '$N-1$' plots, all the selections listed in Table 6.2 are applied, except the variable plotted. The bigger arrows in the upper pad present the selection criteria of the plotting variable as listed in Table 6.2 and the hatched uncertainty bands in the lower pad are the quadratic sum of the statistical uncertainty and a flat 20% systematic uncertainty on the backgrounds.

Cutflows

The cutflows is a sequential cumulative yields after the event selections. Table 6.5 and Table 6.6 show the signal selection cutflows yield table for the NUHM2 signal with $m_{1/2}$ ranging from 350 to 800 GeV. The weighted number of events are normalized to 36.1 fb^{-1}and the raw number of events is also shown.

(a) N_{jets}^{30}

(b) $N_{\mathrm{b-jets}}^{20}$

(c) $p_{\mathrm{T}}^{\ell_1}$
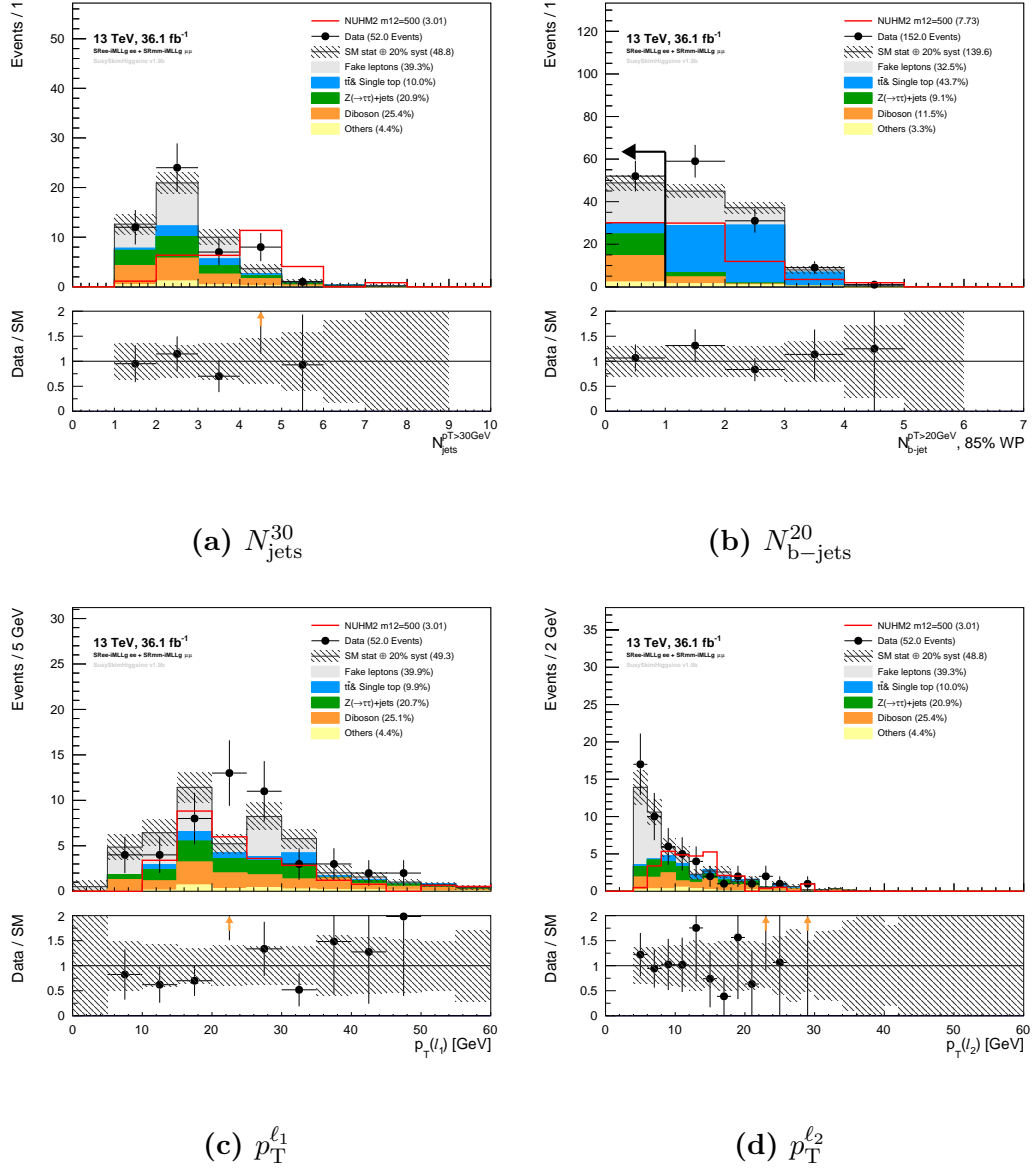
(d) $p_{\mathrm{T}}^{\ell_2}$

Figure 6.3: The '$N-1$' distributions for NUHM2 model with $m_{1/2} = 500$ GeV in SR region 1 <SR$\ell\ell$-$m_{\ell\ell} < 60$ GeV. The NUHM2 distributions are multiplied by 10 but the number of events in the legend use its actual values. The distributions of N_{jets}^{30}, $N_{\mathrm{b-jets}}^{20}$, $p_{\mathrm{T}}^{\ell_1}$, and $p_{\mathrm{T}}^{\ell_2}$ are shown. The uncertainties combine the SM statistical uncertainty and assuming 20% of the systematic uncertainty in quadrature.

(a) E_T^{miss}

(b) $E_T^{\mathrm{miss}}/H_T^{\mathrm{leptons}}$

(c) $m_{\ell\ell}$

(d) $m_{\tau\tau}$
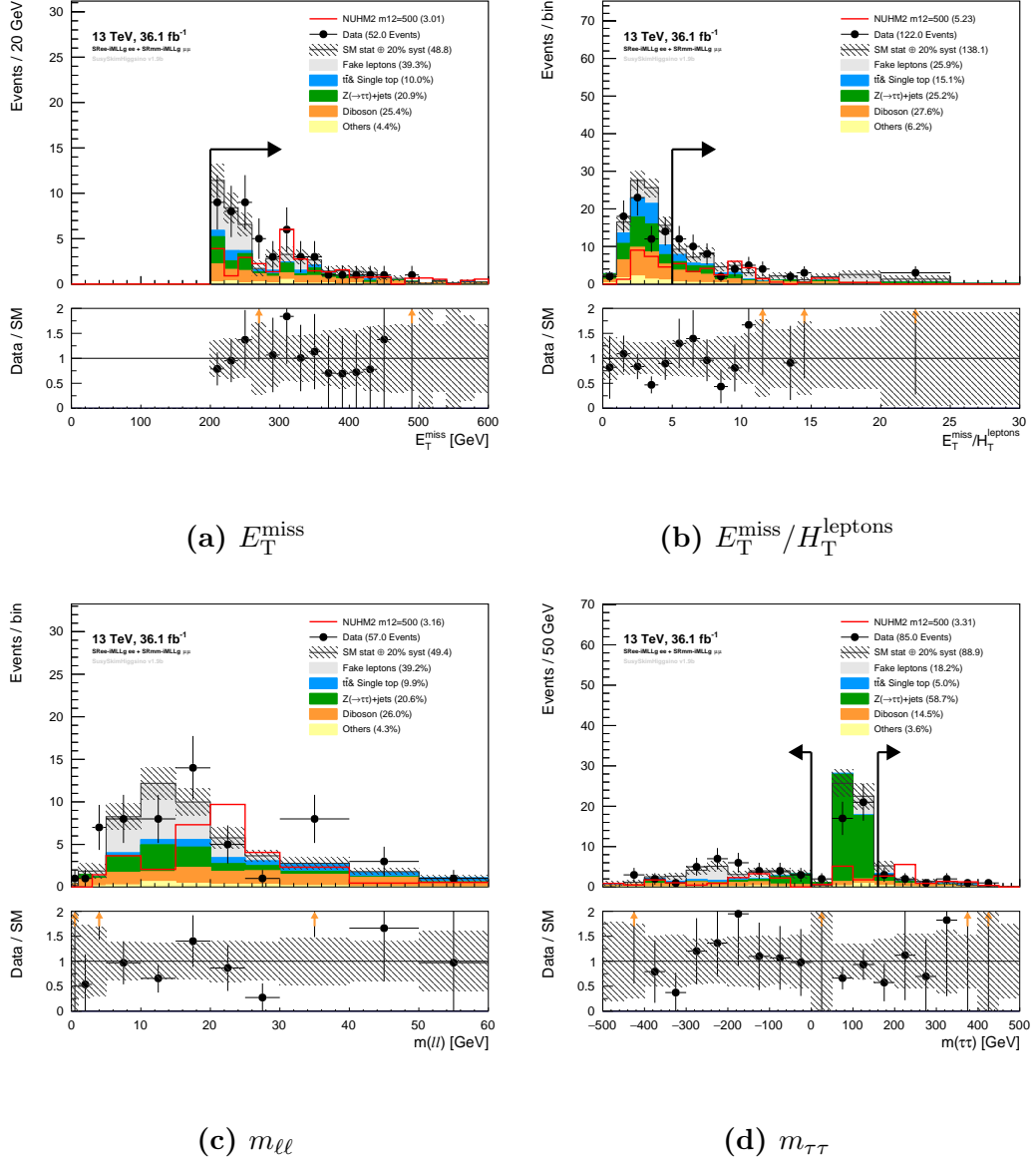
Figure 6.4: The 'N − 1' distributions for NUHM2 model with $m_{1/2} = 500$ GeV in SR region 1 <SR$\ell\ell$-$m_{\ell\ell}$ < 60 GeV. The NUHM2 distributions are multiplied by 10 but the number of events in the legend use its actual values. The distributions of E_T^{miss}, $E_T^{\mathrm{miss}}/H_T^{\mathrm{leptons}}$, $m_{\ell\ell}$, and $m_{\tau\tau}$ are shown. The uncertainties combine the SM statistical uncertainty and assuming 20% of the systematic uncertainty in quadrature.

(a) $m_T(\ell_1)$

(b) $\Delta R_{\ell\ell}$

(c) $|\Delta\phi(\mathbf{p}_T^{j_1}, \mathbf{p}_T^{\mathrm{miss}})|$
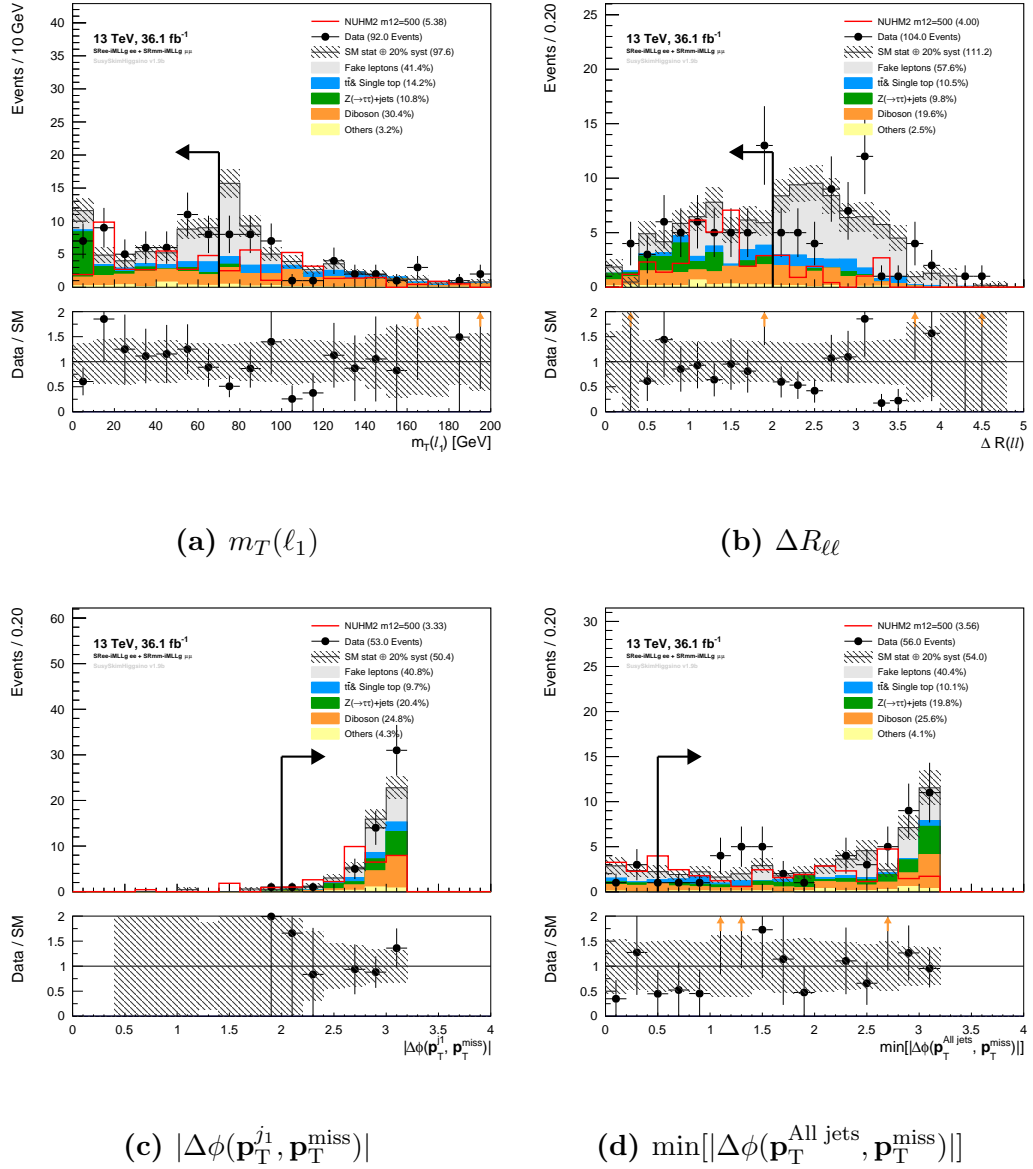
(d) $\min[|\Delta\phi(\mathbf{p}_T^{\mathrm{All\ jets}}, \mathbf{p}_T^{\mathrm{miss}})|]$

Figure 6.5: The '$N-1$' distributions for NUHM2 model with $m_{1/2} = 500$ GeV in SR region 1 $<$SR$\ell\ell$-$m_{\ell\ell} < 60$ GeV. The NUHM2 distributions are multiplied by 10 but the number of events in the legend use its actual values. The distributions of $m_T(\ell_1)$, $\Delta R_{\ell\ell}$, $|\Delta\phi(\mathbf{p}_T^{j_1}, \mathbf{p}_T^{\mathrm{miss}})|$, and $\min[|\Delta\phi(\mathbf{p}_T^{\mathrm{All\ jets}}, \mathbf{p}_T^{\mathrm{miss}})|]$ are shown. The uncertainties combine the SM statistical uncertainty and assuming 20% of the systematic uncertainty in quadrature.

Selection common to all SRs	NUHM2 m12=350		NUHM2 m12=400		NUHM2 m12=500	
	Weighted	Raw	Weighted	Raw	Weighted	Raw
$E_{\mathrm{T}}^{\mathrm{miss}}$ triggers, $E_{\mathrm{T}}^{\mathrm{miss}} > 150$ GeV, $N_{\mathrm{baseline}}^{\ell} \geq 2$	205	968	196	1262	122.7	1882
Stau veto	205	968	196	1262	122.7	1882
$N_{\mathrm{baseline}}^{\ell} = 2$	158	741	156	975	96.5	1501
$N_{\mathrm{signal}}^{\ell} = 2$	158	741	156	975	96.5	1501
Same flavor	94	445	100	598	64.1	1010
Opposite charge	78	369	79	503	55.1	868
Lepton truth matching	78	366	78	493	54.0	851
Lepton author 16 veto	77	364	77	487	53.8	848
$E_{\mathrm{T}}^{\mathrm{miss}} > 200$ GeV	77	364	77	487	53.8	848
$N_{\mathrm{b\text{-}jets}} = 0$	38.0	194	31.5	234	22.2	394
$p_{\mathrm{T}}(j_1) > 100$ GeV	38.0	194	31.5	234	22.2	394
$\Delta\phi\left(j_1, \mathbf{p}_{\mathrm{T}}^{\mathrm{miss}}\right) > 2.0$	37.3	190	30.3	223	21.0	372
$\min(\Delta\phi\left(\text{any jet}, \mathbf{p}_{\mathrm{T}}^{\mathrm{miss}}\right)) > 0.4$	30.7	153	25.9	188	17.4	316
Veto $m_{\tau\tau} \in [0, 160]$ GeV	26.2	128	21.6	161	15.8	287
$p_{\mathrm{T}}^{\ell_1} > 5$ GeV	26.2	128	21.6	161	15.8	287
$m_{\ell\ell} > 1$ GeV	26.2	128	21.6	161	15.8	287
Veto $m_{\ell\ell} \in [3, 3.2]$ GeV	26.2	128	21.6	161	15.7	286
$m_{\ell\ell} < 60$ GeV	26.2	128	21.6	161	15.7	286
$\Delta R_{\ell\ell} > 0.05$ GeV	26.2	128	21.5	160	15.7	286
SR$\ell\ell$-$m_{\ell\ell}$ selection						
$E_{\mathrm{T}}^{\mathrm{miss}}/H_{\mathrm{T}}^{\mathrm{lep}} > \max(5, 15 - 2 \cdot m_{\ell\ell}/\mathrm{GeV})$	12.4	60	9.9	71	7.9	150
$\Delta R_{\ell\ell} < 2.0$ GeV	6.5	34	6.7	51	5.6	105
$m_{\mathrm{T}}^{\ell_1} < 70$ GeV	2.7	14	2.5	21	3.0	52

Table 6.5: The yields after the initial preselection and the sequential selections (cutflows) for the SR. The weighted number of events are normalized to 36.1 fb^{-1} and the raw number of events are also shown. This table only shows $m_{1/2} = 350, 400, 500$ GeV.

Selection common to all SRs	NUHM2 m12=600		NUHM2 m12=700		NUHM2 m12=800	
	Weighted	Raw	Weighted	Raw	Weighted	Raw
$E_{\mathrm{T}}^{\mathrm{miss}}$ triggers, $E_{\mathrm{T}}^{\mathrm{miss}} > 150$ GeV, $N_{\mathrm{baseline}}^{\ell} \geq 2$	76.1	2321	41.2	2471	22.2	2500
Stau veto	76.1	2321	41.2	2471	22.2	2500
$N_{\mathrm{baseline}}^{\ell} = 2$	63.0	1904	33.1	1993	18.1	2029
$N_{\mathrm{signal}}^{\ell} = 2$	63.0	1904	33.1	1993	18.1	2029
Same flavor	42.1	1288	22.7	1383	12.6	1392
Opposite charge	35.9	1101	19.4	1194	10.9	1205
Lepton truth matching	35.2	1079	19.1	1174	10.8	1192
Lepton author 16 veto	35.2	1078	19.0	1168	10.8	1189
$E_{\mathrm{T}}^{\mathrm{miss}} > 200$ GeV	35.2	1078	19.0	1168	10.8	1189
$N_{\mathrm{b\text{-}jets}} = 0$	13.3	453	6.8	470	3.75	477
$p_{\mathrm{T}}(j_1) > 100$ GeV	13.3	453	6.8	470	3.75	477
$\Delta\phi\left(j_1, \mathbf{p}_{\mathrm{T}}^{\mathrm{miss}}\right) > 2.0$	12.4	428	6.5	453	3.59	455
$\min(\Delta\phi\left(\text{any jet}, \mathbf{p}_{\mathrm{T}}^{\mathrm{miss}}\right)) > 0.4$	10.6	360	5.47	379	3.07	383
Veto $m_{\tau\tau} \in [0, 160]$ GeV	9.3	315	4.77	333	2.73	340
$p_{\mathrm{T}}^{\ell_1} > 5$ GeV	9.3	315	4.77	333	2.73	340
$m_{\ell\ell} > 1$ GeV	9.3	315	4.76	332	2.72	339
Veto $m_{\ell\ell} \in [3, 3.2]$ GeV	9.3	315	4.76	332	2.71	337
$m_{\ell\ell} < 60$ GeV	9.3	315	4.76	332	2.71	337
$\Delta R_{\ell\ell} > 0.05$ GeV	9.3	315	4.76	332	2.71	337
SR$\ell\ell$-$m_{\ell\ell}$ selection						
$E_{\mathrm{T}}^{\mathrm{miss}}/H_{\mathrm{T}}^{\mathrm{lep}} > \max(5, 15 - 2 \cdot m_{\ell\ell}/\mathrm{GeV})$	5.5	188	3.05	226	1.85	235
$\Delta R_{\ell\ell} < 2.0$ GeV	4.5	153	2.55	192	1.47	194
$m_{\mathrm{T}}^{\ell_1} < 70$ GeV	2.06	78	1.21	95	0.64	85

Table 6.6: The yields after the initial preselection and the sequential selections (cutflows) for the SR. The weighted number of events are normalized to 36.1 fb^{-1}and the raw number of events are also shown. This table only shows $m_{1/2} = 600, 700, 800$ GeV.

CHAPTER 7

BACKGROUND ESTIMATION

The SM background can be categorized into the irreducible and reducible background. The irreducible background includes events containing two prompt leptons, $E_{\mathrm{T}}^{\mathrm{miss}}$, and jets. The reducible background includes events containing fake/non-prompt leptons. Since the background estimations rely on the choice of the control regions (CRs) and validation regions (VRs) heavily, the concepts of the CRs and VRs are introduced in Sect. 7.1. A detailed discussion of the irreducible background is presented in Sect. 7.2 and of the reducible background in Sect. 7.3. Finally, a systematic uncertainty study for this analysis is given in Sect. 7.4.

7.1 Control and validation regions

7.1.1 The concepts

Three different data regions are usually considered in any physics analysis: signal region (SR), control region (CR), and validation region (VR). The SR is a signal-enriched region, the CR is a background-enriched region, and the VR is a region used to validate the robustness of the signal and background predictions. The SR is a particular region of phase space where a set of selection criteria are applied on kinematic observables. In the SR, the number of predicted signal events have a significant excess over the number of predicted background events. The CR is

enriched in a particular background process with low expected contamination from the signals considered, designed to be similar to SR in the kinematic properties, and kept statistically independent from the SR. The background contamination in the SR can be estimated by extrapolating from the CR. The VR, usually placed in between the SR and CR, is used to validate the predicted number of background events in the SR. Figure 7.1 shows the concepts of multiple SRs, CRs, and VRs.
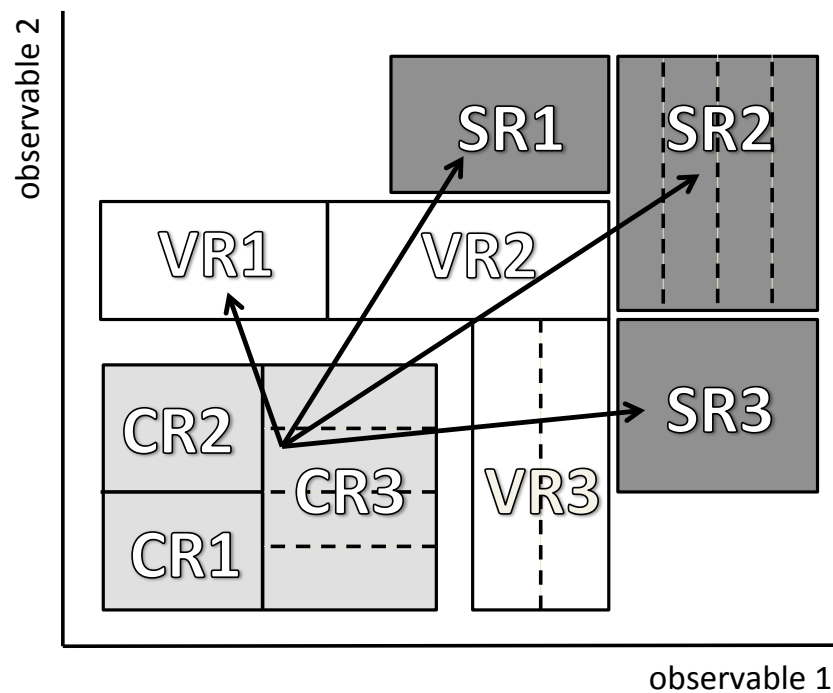
Figure 7.1: A illustration of multiple signal, control, and validation regions [15]. The background contamination in the SRs can be estimated by extrapolating from the CRs and is verified in the VRs which lie in between the SRs and CRs. All regions can be single bin or multiple bins which are indicated by the dashed lines.

7.1.2 Specific to this analysis

Table 7.1 lists the SM background processes for this analysis, the origins in the SR, and the estimation strategies. In order to estimate and validate the background contaminations in SR, two CRs and three VRs are defined. Table 7.2 lists the definitions of CRs and VRs where the common selection criteria listed in Table 6.2 have been applied. The CR-top is used to estimate the $t\bar{t}$ and tW contaminations in SR. The CR-tau is used to estimate the $Z^{(*)}/\gamma^*(\to \tau\tau)$+jets contamination in SR. The VR-VV is used for validating diboson background, the VR-SS is used for validating same-sign dilepton background, and VRDF-$m_{\ell\ell}$ is used for validating the background come from different flavor leptons, which include both $e\mu$ and μe.

Background process	Origin in SR	Estimation strategy
$t\bar{t}$, tW ($\to 2\ell$)	irreducible, b-jet fails identification	CR using b-tagging
$Z^{(*)}/\gamma^*(\to \tau\tau)$+jets	irreducible fully leptonic τ	CR using $m_{\tau\tau}$
$Z^{(*)}/\gamma^*(\to ee, \mu\mu)$+jets	instrumental $E_\mathrm{T}^\mathrm{miss}$	MC
loss mass Drell-Yen	instrumental $E_\mathrm{T}^\mathrm{miss}$	MC, data-driven cross check
fakes (W+jets, $VV(1\ell)$, $t\bar{t}$ (1ℓ))	jet fakes 2nd lepton	fake factor, SS VR
VV	irreducible dileptonic and missed 3rd lepton	MC, VR using $E_\mathrm{T}^\mathrm{miss}/H_\mathrm{T}^\mathrm{leptons}$
other rare processes	irreducible leptonic decays	MC

Table 7.1: The background processes for the 2ℓ analysis and the strategy for estimating the background contamination in the SR.

7.2 Irreducible background

The irreducible backgrounds for this analysis are the SM processes containing two prompt leptons, $E_\mathrm{T}^\mathrm{miss}$, and jets. Therefore, they can enter the SR and mimic the signal events. The dominant sources are the $t\bar{t}$, tW, and $Z^{(*)}/\gamma^*(\to \tau\tau)$+jets

Region	Leptons	$E_{\mathrm{T}}^{\mathrm{miss}}/H_{\mathrm{T}}^{\mathrm{lep}}$	Additional requirements
CR-top	$e^{\pm}e^{\mp}, \mu^{\pm}\mu^{\mp}, e^{\pm}\mu^{\mp}, \mu^{\pm}e^{\mp}$	> 5	$\geq 1b$-tagged jet(s)
CR-tau	$e^{\pm}e^{\mp}, \mu^{\pm}\mu^{\mp}, e^{\pm}\mu^{\mp}, \mu^{\pm}e^{\mp}$	$\in [4, 8]$	$m_{\tau\tau} \in [60, 120]$ GeV
VR-VV	$e^{\pm}e^{\mp}, \mu^{\pm}\mu^{\mp}, e^{\pm}\mu^{\mp}, \mu^{\pm}e^{\mp}$	< 3	-
VR-SS	$e^{\pm}e^{\pm}, \mu^{\pm}\mu^{\pm}, e^{\pm}\mu^{\pm}, \mu^{\pm}e^{\pm}$	> 5	-
VRDF-$m_{\ell\ell}$	$e^{\pm}\mu^{\mp}, \mu^{\pm}e^{\mp}$	$> \max(5, 15 - 2\ m_{\ell\ell}/1\ \mathrm{GeV})$	$\Delta R_{\ell\ell} < 2, m_{\mathrm{T}}^{\ell_1} < 70$ GeV

Table 7.2: Definition of control regions and validation regions.

processes. These processes decay to same flavor lepton pairs (ee and $\mu\mu$) and different flavor lepton pairs ($e\mu$ and μe) at the same rates. When defining the CR-top and CR-tau, all possible flavor $e^{\pm}e^{\mp}$, $\mu^{\pm}\mu^{\mp}$, $e^{\pm}\mu^{\pm}$, $\mu^{\pm}e^{\mp}$ are considered to enhance the statistics. By requiring the events with at least one b-tagged jet, the CR-top defined a top quarks enriched region with $\sim 72\%$ purity. The CR-top is used to estimate the $t\bar{t}$ and tW decaying to 2ℓ final states in the SR. By requiring that the events satisfying $60 < m_{\tau\tau} < 120$ GeV and $E_{\mathrm{T}}^{\mathrm{miss}}/H_{\mathrm{T}}^{\mathrm{lep}}$ between 4 and 8 to reduce the signal contaminations, the CR-tau defines a $Z^{(*)}/\gamma^*(\to \tau\tau)$+jets enriched region with $\sim 80\%$ purity. The CR-tau is used to estimate the leptonic τ contaminations in the SR. The kinematic distributions of $E_{\mathrm{T}}^{\mathrm{miss}}/H_{\mathrm{T}}^{\mathrm{lep}}$ and $m_{\tau\tau}$ in the CR-top and CR-tau after performing background-only fits are shown in Fig 7.2. All the event selection criteria are applied except the variable being plotted. The expected background contributions from different processes are stacked and compared with the data.

The VV diboson events and the rare processes also contribute to the irreducible background. But it is difficult to have pure diboson or rare samples that can be used to estimate the contaminations in SR. Therefore, the background
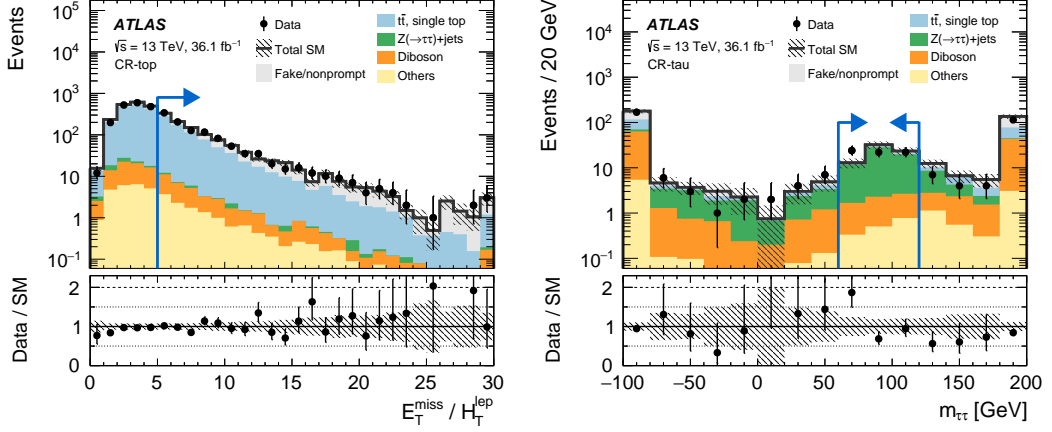
(a) The $E_{\mathrm{T}}^{\mathrm{miss}}/H_{\mathrm{T}}^{\mathrm{lep}}$ distribution in CR-top. **(b)** The $m_{\tau\tau}$ distribution in CR-tau.

Figure 7.2: The kinematic distributions of $E_{\mathrm{T}}^{\mathrm{miss}}/H_{\mathrm{T}}^{\mathrm{lep}}$ and $m_{\tau\tau}$ in the CR-top and CR-tau, respectively [16]. All the event selection criteria are applied except the variable being plotted and the background-only fits are performed. The selection requirement of the plotting variable is indicated by the blue arrows. The first and last bins include the underflow and overflow, respectively. The expected background contributions from different processes are stacked and compared with the data.

contaminations are estimated using MC simulation and validated by the VR-VV. By requiring $E_{\mathrm{T}}^{\mathrm{miss}}/H_{\mathrm{T}}^{\mathrm{lep}} < 3$, the signal contamination in the VR-VV is at most 8% in the samples, the diboson events contribute $\sim$40%, fake lepton events contribute $\sim$25%, $t\bar{t}$ and single top events contribute $\sim$23%, and the remaining parts are smaller and contributed by the other processes.

The VRDF-$m_{\ell\ell}$ validation region is constructed using different flavor ($e\mu$ and μe) leptons. This VR has the same selection criteria as the SR, except the leptons have different flavor. Since the irreducible backgrounds are symmetric in $ee + \mu\mu$ and $e\mu + \mu e$, the VRDF-$m_{\ell\ell}$ is used to check the eventual extrapolation in the fitting procedure within the same kinematics as the SR. The signal contamination

in this VR is less than 8%.

7.3   Reducible background

The main contributions of the reducible background come from the non-prompt leptons and the processes associated with miss-reconstruction of $E_\mathrm{T}^\mathrm{miss}$.

7.3.1   Fake/non-prompt lepton background

The background of non-prompt leptons, called fake leptons, mainly come from the W+jets, VV, $t\bar{t}$ processes. In these processes, a jet is misidentified as a lepton and form a dilepton final state in the SR. Because the MC simulation could not model fake leptons well, a data-driven Fake Factor method [112] is used to estimate the fake lepton contamination in the SR.

Fake factor method

The Fake Factor method defines a tight set and a loose set of lepton identification criteria. The tight set referred as the ID leptons and the loose set as anti-ID leptons. The ID leptons correspond to requirements applied to signal leptons used in the analysis. The anti-ID leptons define a fake lepton enriched sample by releasing or inverting one or more of the identification, isolation, or impact parameter $|d_0|/\sigma(d_0)$ requirements relative to the signal leptons. Therefore, the ID and anti-ID lepton sets are orthogonal. The fake factor F is defined then as the ratio between the number of ID and the number of anti-ID leptons as shown in Eq. 7.1.

$$F = \frac{N_\mathrm{ID}}{N_\mathrm{anti-ID}} \quad . \tag{7.1}$$

$N_\text{anti-ID}$ is the number of fake leptons in the anti-ID measurement region where the contributions from prompt leptons are subtracted using the MC simulation results. The fake factors for electrons and muons are measured in a fake leptons enriched region as a function of reconstructed lepton p_T and are used to estimate the reducible background in the SR. These ratios F are applied to events in the anti-ID control region, which has the same selection criteria as the SR, except an ID lepton is replaced by an anti-ID lepton. The total reducible background in the SR can be estimated by

$$N_\text{est}^\text{SR} = F \cdot N_\text{fake}^\text{CR} \quad . \tag{7.2}$$

The schematic illustration of the fake factor method is shown in Fig. 7.3.
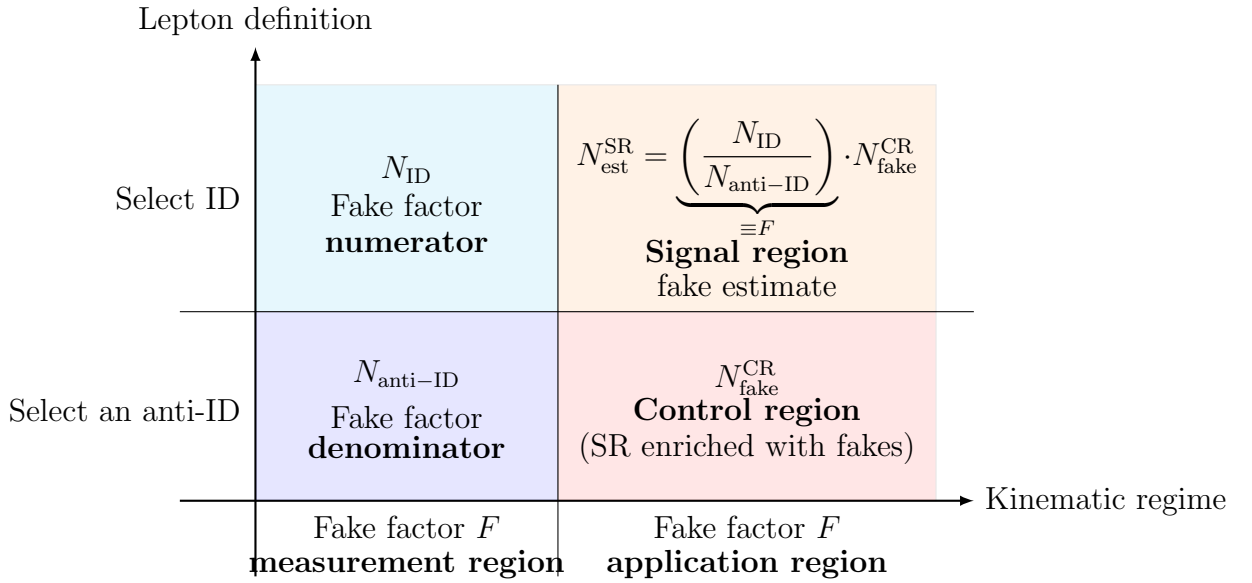
Figure 7.3: The schematic illustration of the fake factor method used to estimate the fake lepton contribution in the SR.

Specific to this analysis

The ID electrons are the signal electrons as shown in Table 6.1 and the anti-ID electrons are baseline electrons passing `LooseAndBLayer` identification but failing at least one of the following requirements: `Tight` identification, `GradientLoose` isolation, or $|d_0/\sigma(d_0)| < 5$. The ID muons are the signal muons as shown in Table 6.1 and the anti-ID muons are baseline muons failing either `FixedCutTightTrackOnly` isolation or $|d_0/\sigma(d_0)| < 3$. Both ID and anti-ID leptons are required to satisfy $|z_0 \sin\theta| < 0.5$ mm to reduce the impact of pileup. Table 7.3 summarizes the ID and anti-ID selection criteria for electrons and muons.

	Electrons	Muons
Kinematic	$p_{\mathrm{T}} > 4.5$ GeV, $|\eta| < 2.47$	$p_{\mathrm{T}} > 4$ GeV, $|\eta| < 2.5$
Identification	pass `LooseAndBLayerLLH`	pass `Medium`
Impact parameter	$|z_0 \sin\theta| < 0.5$ mm	$|z_0 \sin\theta| < 0.5$ mm
anti-ID have to fail at least one of the requirements		
Identification	`TightLLH`	-
Isolation	`GradientLooseLLH`	`FixedCutTightTrackOnlyLLH`
Impact parameter	$|d_0/\sigma(d_0)| < 5$	$|d_0/\sigma(d_0)| < 3$

Table 7.3: The ID and anti-ID selection criteria for electrons and muons.

The electron and muon fake factors depend on the lepton p_{T} largely and on the leading jet p_{T}. Therefore, the leading jet p_{T} for the events used for fake factor measurements are required to be greater than 100 GeV, making the fake factor measurement region similar to SR. The muon fake factor also depends on the $N_{b-\mathrm{jet}}$ in the events because the estimated number of fake lepton in CR-top is

calculated using events with at least one b-jet while the estimated number of fake lepton in the other regions are computed using zero b-jet events. The electron and muon fake factors are computed using events with $m_T < 40$ GeV in different p_T bins. Figure 7.4 shows the electrons fake factors as a function of p_T and leading jet p_T and Fig 7.5 shows the muons fake factor as a function of p_T with 0 b-jets and at least one b-jet.

(a) Electron p_T dependence   **(b)** Leading jet p_T dependence
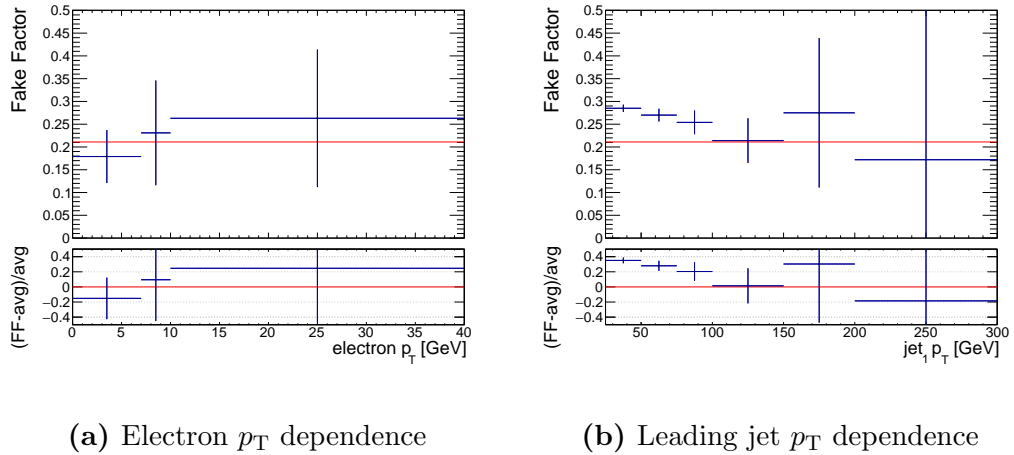
Figure 7.4: The electron fake factor as a function of p_T and leading jet p_T. The red line is the average electron fake factor.

7.3.2 Instrumental E_T^{miss} background

Detector mismeasurement of leptons or jets in background processes that do not contain invisible particles might satisfy the $E_T^{\mathrm{miss}} > 200$ GeV requirement. For example, $Z^{(*)}/\gamma^*(\rightarrow ee, \mu\mu)$+jets Drell-Yan dilepton production can enter the SR due to the instrumental E_T^{miss}. By requiring $E_T^{\mathrm{miss}} > 200$ GeV, the contributions from these background processes are expected to be very small. Using the MC simulation, these process are found to be negligible. The small mass splitting between $\widetilde{\chi}_2^0$ and $\widetilde{\chi}_1^0$ causes the low invariant dilepton mass where the dilepton
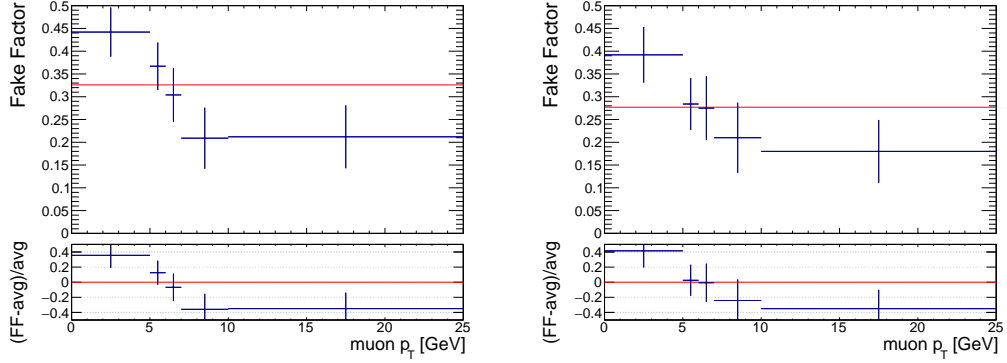
(a) Muon p_T dependence with 0 b-jet   **(b)** Muon p_T dependence with $\geq 1b$-jet

Figure 7.5: The muon fake factor as a function of p_T with 0 b-jet and at least one b-jet. The red line is the average muon fake factor.

events are the decay product of $\widetilde{\chi}_2^0$. The $e^\pm e^\mp$ and $\mu^\pm \mu^\mp$ invariant masses for data events passing E_T^{miss} trigger and $|\Delta\phi(j_1, \mathbf{p}_T^{miss})| < 1.5$ are shown in Fig. 7.6 where a J/ψ peak $3.0 < m_{\ell\ell} < 3.2$ GeV can be seen.

By vetoing $3.0 < m_{\ell\ell} < 3.2$ GeV, the contributions from J/ψ resonance can be removed efficiently. By requiring $\min|\Delta\phi(\text{any jet}, \mathbf{p}_T^{miss})| > 0.4$, the events containing mismeasured jets causing large E_T^{miss} can be suppressed. After applying these requirements, the instrumental E_T^{miss} background are found to be negligible.

A validation region VR-SS, which has similar kinematics as the SR, is constructed by requiring same sign leptons in the events. This VR is fake/non-prompt lepton enriched and can be used as a cross-check of the fake prediction. Typically, the leading lepton is the real lepton and the subleading lepton is the fake/non-prompt lepton. By considering the rate of the anti-ID leptons in data, the probability of both leptons being fake/non-prompt is found to be very small. Therefore, the VR-SS are divided into $ee + \mu e$ and $\mu\mu + e\mu$ final states where the left lepton and right lepton in the pairs denote the leading and subleading

(a) *ee* invariant mass   **(b)** $\mu\mu$ invariant mass
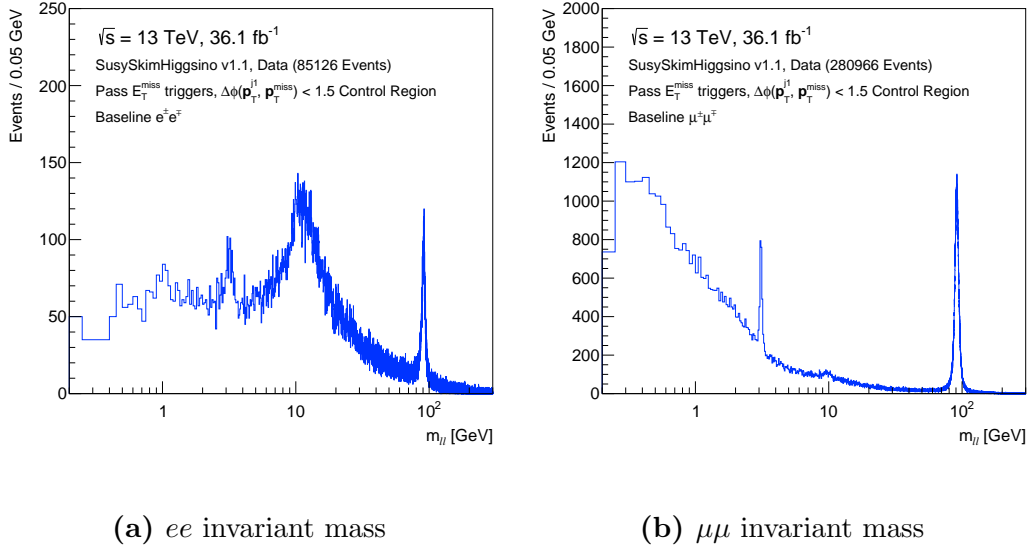
Figure 7.6: The opposite sign baseline dilepton mass $m_{\ell\ell}$ spectrum. All data events are required to pass $E_{\mathrm{T}}^{\mathrm{miss}}$ trigger and satisfies $|\Delta\phi(j_1, \mathbf{p}_{\mathrm{T}}^{\mathrm{miss}})| < 1.5$ requirement. A low mass J/ψ peak can be seen in *ee* and $\mu\mu$ invariant mass.

leptons, respectively. The electroweakino signal contamination in VR-SS is very small and can be neglected. Figure 7.7 shows the data and fake/non-prompt leptons $E_{\mathrm{T}}^{\mathrm{miss}}$ distributions for $ee + \mu e$ and $\mu\mu + e\mu$ final states in the VR-SS.

7.4   Systematic uncertainties

The systematic uncertainty includes the uncertainties due to theoretical modeling and experiment sources. The theoretical uncertainty arises from the MC simulation such as cross-section calculation, the parton distribution function (PDF), and renormalization and factorization scales. The experimental uncertainty arises from the object reconstruction, pileup measurement, and estimation using data-driven method.
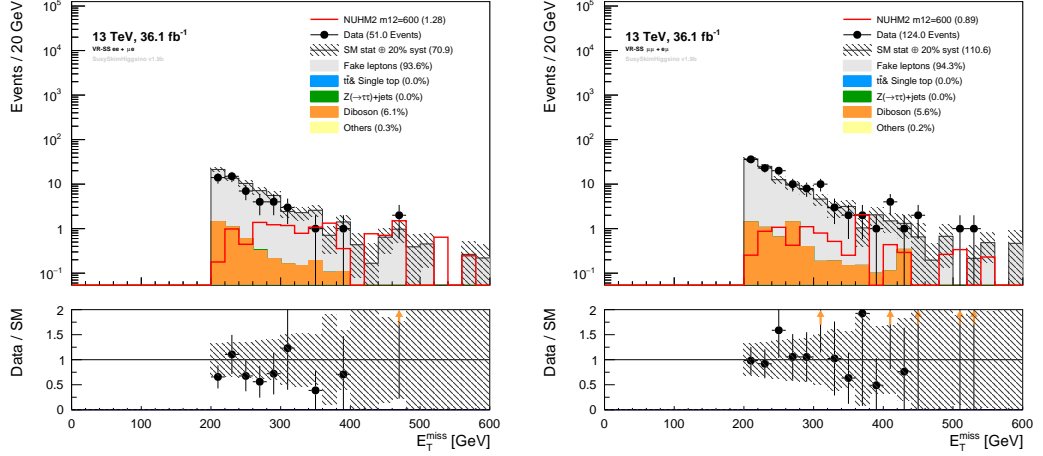
(a) $ee + \mu e$ **(b)** $\mu\mu + e\mu$

Figure 7.7: The data and fake/non-prompt leptons E_T^{miss} distributions in the VR-SS.

7.4.1 Theoretical uncertainty

SUSY signal uncertainty

The theoretical uncertainty in the SUSY signal is measured by varying the renormalization, factorization parameters and CKKW-L matching scales in the MG5_aMC@NLO generator and the shower tune parameters in the PYTHIA. The uncertainties are found to range from 20% to 40% in the signal acceptance depending on the mass splitting of the SUSY particles and the production process. The uncertainties due to PDF uncertainties are studied and amount to 15% at most for large $\tilde{\chi}_2^0$ mass.

SM background uncertainty

Three major factors affect the dominant SM backgrounds $t\bar{t}$, tW, $Z^{(*)}/\gamma^*(\rightarrow \tau\tau)$+jets, and diboson processes. The envelope is assigned to the theoretical

uncertainty. The uncertainties due to the QCD renormalization and factorization scales are evaluated by varying the generator parameters up and down by a factor of 2. The uncertainties due to the strong coupling constant α_S are evaluated by varying the α_S. The impact on the acceptance is assigned to the theoretical uncertainty. The uncertainties due to the PDF are evaluated by PDF sets CT14, MMHT2014, and NNPDF. The variations in acceptance are summarized and the envelope is assigned to the theoretical uncertainty. Events with all lepton flavors are used and the uncertainties are evaluated in all SRs and CRs. The final uncertainty is evaluated by adding all components in quadrature.

7.4.2   Experimental uncertainty

Combined performance uncertainty

The uncertainties of lepton reconstruction, identification, and isolation as well as the uncertainties of energy and momentum scale and resolution are considered, but they are found to be small. The pileup in the MC samples is not the same as the one observed in data. The $\langle\mu\rangle$ profile is the average number of interactions per bunch crossing and the $\langle\mu\rangle$ in data is scaled by 1/1.16 to obtain a better data/MC agreement. The uncertainty of the pileup reweighting is obtained by varying the scaling factor between 1.00 and 1.23. The uncertainties from the jet energy scale (JES) and resolution (JER) are considered. Five up and down variations are used to obtain the JES uncertainty and a up variation is used to obtain the JER uncertainty. Finally, the luminosity uncertainty is 3.2% for 2015+2016 combined datasets.

Fake factor uncertainty

The major experimental uncertainty is the fake/non-prompt lepton prediction from the fake factor method. The fake factor uncertainty arises from the sample size used to measure the fake factors, the prompt lepton contamination in anti-ID region, the kinematic differences between the measurement region and the SRs, and the differences between the fake factor estimation and observed data in the VR-SS.

Figure 7.8 shows the relative size of various uncertainties in the background predictions in the exclusive electroweakino SRs. The fake factor uncertainty is shown separately from the other experimental uncertainties due to the relatively large contribution.
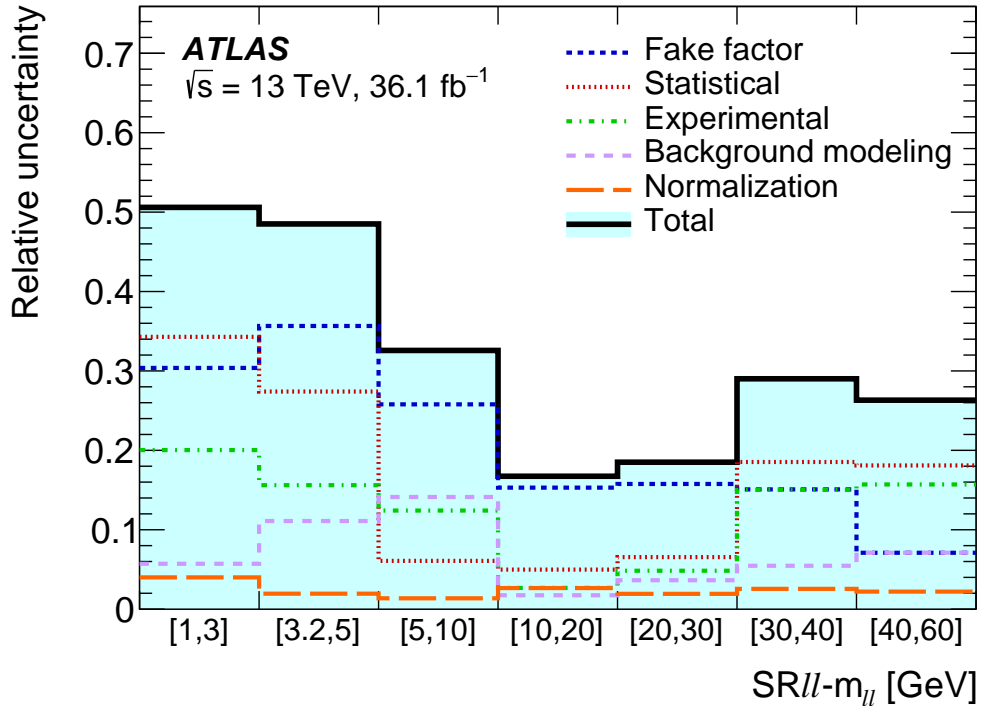
Figure 7.8: The relative systematic uncertainties in the background prediction in the exclusive electroweakino SRs [16].

CHAPTER 8

THE NUHM2 INTERPRETATION

This chapter presents the results of the search for electroweak production of supersymmetric states in the NUHM2 compressed scenario. The kinematic distributions of the NUHM2 are shown in Sect. 8.1. The $m_{\ell\ell}$ reweighting method is described in Sect. 8.2. The results of the NUHM2 interpretation using the $m_{\ell\ell}$ reweighting method is given in Sect. 8.2.3 and the interpretation using MC is detailed in Sect. 8.3.

8.1 Kinematic distributions

The realistic NUHM2 model and the simplified Higgsino model are similar except in NUHM2 the $m_{\widetilde{\chi}_1^\pm}$ is not exactly half way between $m_{\widetilde{\chi}_2^0}$ and $m_{\widetilde{\chi}_1^0}$. The ratio of the $\Delta m(\widetilde{\chi}_2^0, \widetilde{\chi}_1^0)$ to $\Delta m(\widetilde{\chi}_1^\pm, \widetilde{\chi}_1^0)$ varies from 1.61 to 1.21 as shown in Table 5.3. The sensitivity of the NUHM2 model used for the two leptons final state Higgsino analysis is examined by comparing the kinematic distributions of the NUHM2 signal samples and the simplified Higgsino model grid mass points. Figure 8.1 shows some of the kinematic distribution comparisons in truth level[1] using the NUHM2 samples with $m_{1/2} = 600$ GeV and the simplified Higgsino samples with $m_{\widetilde{\chi}_2^0} = 170$ GeV, $m_{\widetilde{\chi}_1^0} = 150$ GeV. The distributions for the other kinematic variable comparison can be found in the App. B. All events are selected after applying the event cleaning pre-selections and satisfying the ≥ 2 leptons with

---

[1]Truth level means using the truth matched event information in MC samples.

$p_T > 3$ GeV and $E_T^{\mathrm{miss}} > 50$ GeV requirements. All kinematic distributions in the truth level are very similar between two models. The largest difference is in the $m_{\ell\ell}$ distribution due to the mass splinting $\Delta m = m_{\widetilde{\chi}_2^0} - m_{\widetilde{\chi}_1^0}$ where $\Delta m \sim 22$ GeV for NUHM2 and 20 GeV for the simplified Higgsino model. This distinguishing feature motivates the NUHM2 interpretation.

8.2 NUHM2 interpretation using the $m_{\ell\ell}$ reweighting method

The mass eigenstates of the electroweakinos are composed of different mixtures of Bino, Wino, and Higgsino in the compressed scenario. The simplified Higgsino model signal samples are generated using a mixture of Higgsinos and the cross-sections are calculated accordingly. Since the main difference between NUHM2 and the simplified Higgsino model is the invariant mass distribution of the two leptons due to the mass splittings of $\Delta m(\widetilde{\chi}_2^0, \widetilde{\chi}_1^0)$ and $\Delta m(\widetilde{\chi}_1^\pm, \widetilde{\chi}_1^0)$, the simplified Higgsino model signal samples could be used for the NUHM2 interpretation by scaling the $m_{\ell\ell}$ distribution and cross-sections.

The invariant mass distribution can be calculated by

$$\frac{d\Gamma}{2mdm} \propto \frac{\sqrt{m^4 - m^2(m_{\widetilde{\chi}_2^0}^2 + m_{\widetilde{\chi}_1^0}^2) + (m_{\widetilde{\chi}_2^0}^2 - m_{\widetilde{\chi}_1^0}^2)^2}}{(m^2 - m_Z^2)^2} \tag{8.1}$$

$$\times \left[-2m^4 + m^2(m_{\widetilde{\chi}_1^0}^2 \pm 6m_{\widetilde{\chi}_1^0}m_{\widetilde{\chi}_1^0} + m_{\widetilde{\chi}_2^0}^2) + (m_{\widetilde{\chi}_1^0}^2 - m_{\widetilde{\chi}_2^0}^2)^2 \right] \tag{8.2}$$

where the $\pm$ depends on the assumption of the mixture of the eigenstates. The "+" is for the NUHM2 and "$-$" is for the simplified Higgsino model. The detail of the reweighted $m_{\ell\ell}$ distributions are shown in Sect. 8.2.1, the validations of the $m_{\ell\ell}$ reweighting method are shown in Sect. 8.2.2, and the results are shown in Sect. 8.2.3.
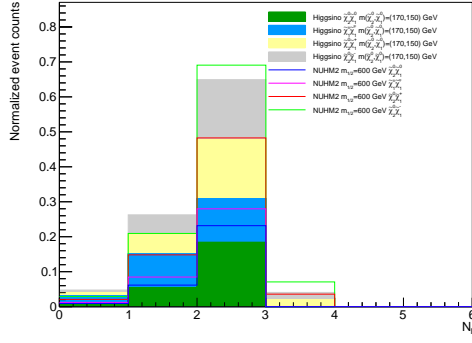
(a) Signal leptons multiplicities
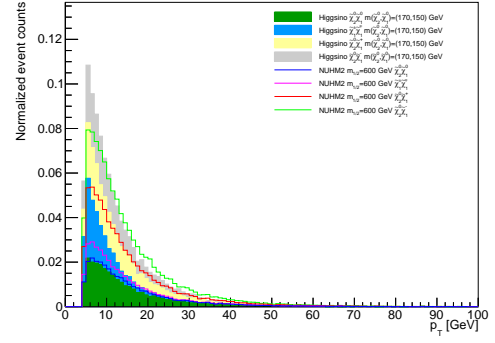
(b) Signal electrons p_{T}
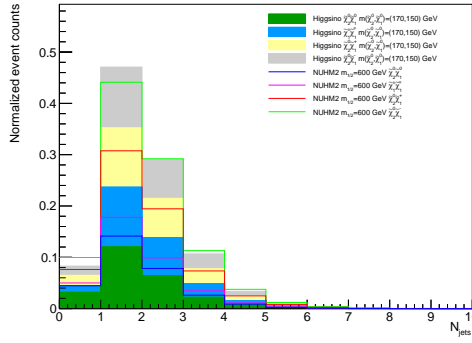
(c) Jets multiplicity
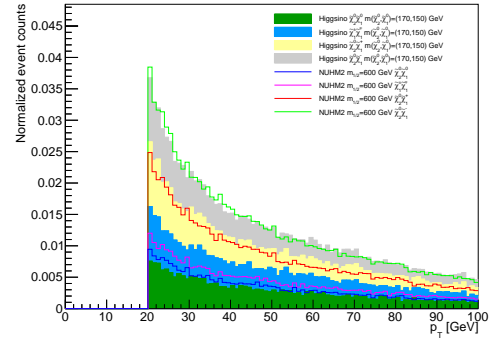
(d) Signal jets p_{T}.
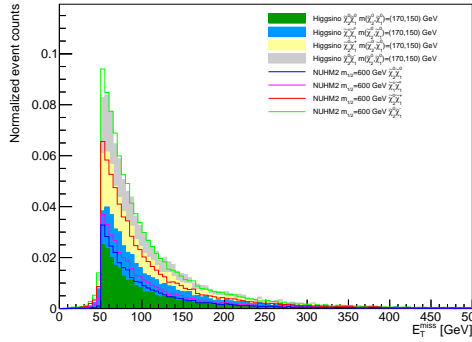
(e) $E_{\mathrm{T}}^{\mathrm{miss}}$
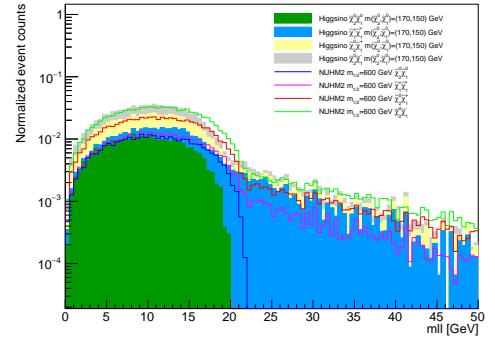
(f) $m_{\ell\ell}$

Figure 8.1: The kinematic distribution comparisons in truth level using the NUHM2 samples with $m_{1/2} = 600$ GeV and the simplified Higgsino samples with $m_{\widetilde{\chi}_2^0} = 170$ GeV, $m_{\widetilde{\chi}_1^0} = 150$ GeV. Four different production channels, $\widetilde{\chi}_2^0\widetilde{\chi}_1^0$, $\widetilde{\chi}_2^0\widetilde{\chi}_1^+$, $\widetilde{\chi}_2^0\widetilde{\chi}_1^-$, and $\widetilde{\chi}_1^\pm\widetilde{\chi}_1^\mp$, for the NUHM2 and the simplified Higgsino model are considered. The distributions of four productions are combined and normalized to equal area.

109

8.2.1 The reweighted $m_{\ell\ell}$ distributions

Using the $m_{\ell\ell}$ reweighting method, the simplified Higgsino samples can reproduce the NUHM2 distributions at the reconstruction level. The $m_{\ell\ell}$ distributions for the NUHM2 and the simplified Higgsino samples can be calculated by the $m_{\widetilde{\chi}_1^0}$ and $m_{\widetilde{\chi}_1^0}$ using Eq. 8.2. From the ratio of the $m_{\ell\ell}$ distributions between two models and the cross-section weight, the event weighting is performed. The event-by-event reweighting of the $m_{\ell\ell}$ distributions between two models is examined at the truth level.

A number of details have to be considered in the $m_{\ell\ell}$ reweighting procedure. The reweighting method only considers the $\widetilde{\chi}_2^0\widetilde{\chi}_1^0$ and $\widetilde{\chi}_2^0\widetilde{\chi}_1^\pm$ productions because the $\widetilde{\chi}_1^\pm\widetilde{\chi}_1^\mp$ contributes mainly to the tail region of the $m_{\ell\ell}$ distribution which is not sensitive in this analysis. The grid points have to be selected with similar $m_{\widetilde{\chi}_2^0}$, $m_{\widetilde{\chi}_1^0}$, and $\Delta m = m_{\widetilde{\chi}_1^2} - m_{\widetilde{\chi}_1^0}$. Table 8.1 shows the grid points used for the $m_{\ell\ell}$ reweighting. Table 8.2 shows the cross-section weights used for the $m_{\ell\ell}$ reweighting.

Figure 8.2 shows the $m_{\ell\ell}$ distributions before and after reweighting for NUHM2 and the simplified Higgsino model. The blue and green solid lines are the TRUTH $m_{\ell\ell}$ distributions for NUHM2 and simplified Higgsino models, respectively. The blue and green dashed lines are the theoretical distribution predicted by Eq. 8.2. Good agreement can be seen between the TRUTH (solid line) and the predicted (dashed line) distributions. The distribution of the reweighted Higgsino sample is shown in red line which matches well with the NUHM2 (blue solid line).

$m_{1/2}$ [GeV]	NUHM2			Simplified Higgsino			δ
	$m_{\widetilde{\chi}_2^0}$	$m_{\widetilde{\chi}_1^0}$	Δm	$m_{\widetilde{\chi}_2^0}$	$m_{\widetilde{\chi}_1^0}$	Δm	
350	161.68	115.62	46.06	160	100	60	13.94
400	161.14	122.97	38.17	190	150	40	1.8
500	160.30	132.28	28.02	190	150	40	11.98
600	159.66	137.61	22.05	190	150	40	17.95
700	159.17	140.98	18.19	170	150	20	1.81
800	158.78	143.29	15.49	170	150	20	4.51

Table 8.1: The grid points of NUHM2 and simplified Higgsino samples used for the $m_{\ell\ell}$ reweighting. The smaller $\delta = \Delta m_{Higgsino} - \Delta m_{NUHM2}$ the better reweighting results.

$m_{1/2}$ [GeV]	$\widetilde{\chi}_2^0\widetilde{\chi}_1^0$	$\widetilde{\chi}_1^\pm\widetilde{\chi}_1^\mp$	$\widetilde{\chi}_2^0\widetilde{\chi}_1^+$	$\widetilde{\chi}_2^0\widetilde{\chi}_1^-$
350	0.5004	0.8093	0.7533	0.7517
400	1.4061	1.8576	1.6181	1.6892
500	1.4842	1.6071	1.6120	1.6803
600	1.4962	1.4889	1.6054	1.6694
700	1.1811	1.1428	1.1703	1.1918
800	1.1731	1.1076	1.1673	1.1896

Table 8.2: The cross-section weight used for the $m_{\ell\ell}$ reweighting. The weights are obtained by calculating the ratio between σ(NUHM2) and σ(Higgsino).
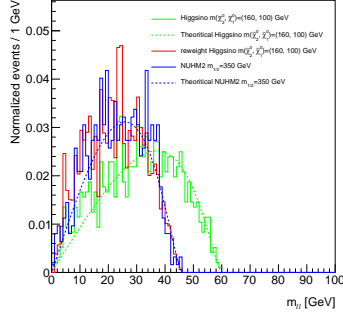
(a) NUHM2 $m_{1/2} = 350$ GeV
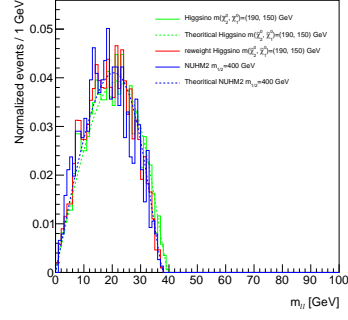
(b) NUHM2 $m_{1/2} = 400$ GeV
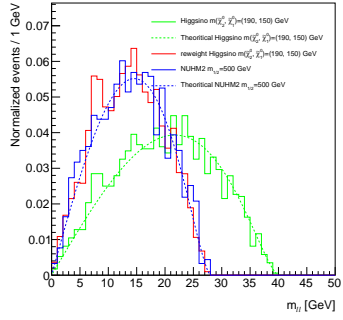
(c) NUHM2 $m_{1/2} = 500$ GeV

(d) NUHM2 $m_{1/2} = 600$ GeV
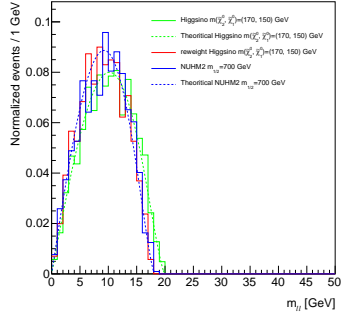
(e) NUHM2 $m_{1/2} = 700$ GeV
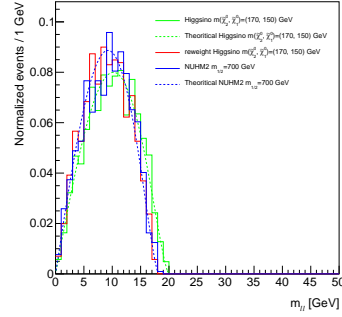
(f) NUHM2 $m_{1/2} = 800$ GeV

Figure 8.2: The $m_{\ell\ell}$ distributions before and after reweighting for NUHM2 and the simplified Higgsino model. The blue and green solid lines are the TRUTH $m_{\ell\ell}$ distributions and the dashed lines are the distributions obtained from the Eq. 8.2. The good agreement between solid and dashed lines indicate the robustness of the formula. The red line is the event-by-event reweighting of the simplified Higgsino to the NUHM2 $m_{\ell\ell}$ which agrees with the prediction (blue dashed line).

112

8.2.2 The validation of $m_{\ell\ell}$ reweighting method

The $m_{\ell\ell}$ reweighting method is validated by examining all kinematic variable distributions of NUHM2, simplified Higgsino, and reweighted Higgsino samples in truth level for all NUHM2 mass points. Figures 8.3 to 8.7 show the kinematic variable distributions for NUHM2 with $m_{1/2} = 700$ GeV, simplified Higgsino with $m_{\widetilde{\chi}_2^0} = 170$ and $m_{\widetilde{\chi}_1^0} = 150$ GeV, and reweighted Higgsino samples. The distributions for the other $m_{1/2}$ mass points can be found in the App. B. Good agreement between the NUHM2 and reweighted Higgsino samples can be found for all NUHM2 mass points. The agreement is better if the $\delta = \Delta m_{Higgsino} - \Delta m_{NUHM2}$ is smaller. Therefore, the reweighted Higgsino samples are used for the NUHM2 interpretation.

8.2.3 NUHM2 interpretation using the $m_{\ell\ell}$ reweighting

The NUHM2 interpretation is performed using the reweighted Higgsino samples to obtain the NUHM2 distributions at the reconstruction level. All systematic uncertainties are considered in the calculation. The upper limits of the cross-section combining $\widetilde{\chi}_2^0 \widetilde{\chi}_1^0$, $\widetilde{\chi}_2^0 \widetilde{\chi}_1^\pm$, and $\widetilde{\chi}_1^\pm \widetilde{\chi}_1^\mp$ productions are shown in Fig. 8.8. The upper limits of cross-section are labeled by the gray number on each $m_{1/2}$ and the lower axis shows the $\Delta m = m_{\widetilde{\chi}_2^0} - m_{\widetilde{\chi}_1^0}$. None of the NUHM2 $m_{1/2}$ points are excluded at the 95% CL.

8.3 NUHM2 interpretation using the MC production

Although the NUHM2 interpretation using the $m_{\ell\ell}$ reweighting Higgsino samples is shown in Sect. 8.2.3, the final results must be determined using the MC
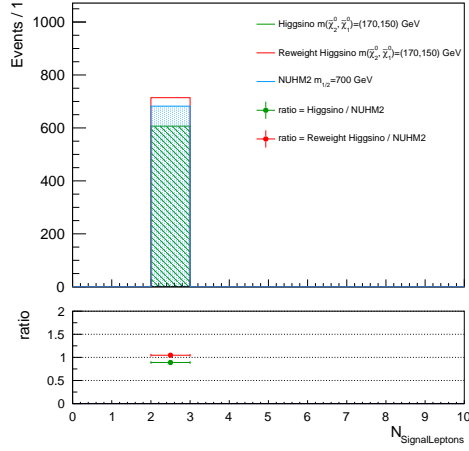
(a) Signal lepton multiplicity
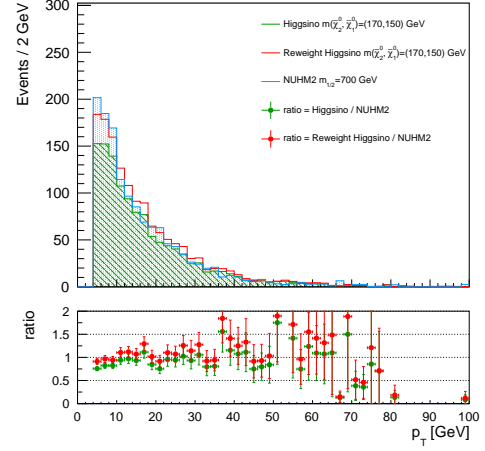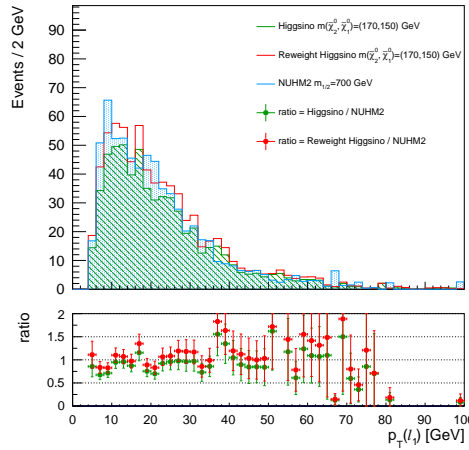
(b) Signal lepton p_T
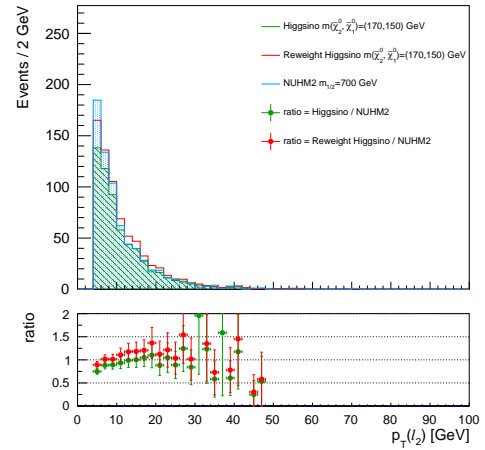
(c) Leading lepton p_T

(d) Subleading lepton p_T

Figure 8.3: The distributions for signal lepton multiplicity, all signal leptons p_T, the leading lepton p_T, and the subleading lepton p_T. The NUHM2 signal sample uses $m_{1/2} = 700$ GeV and the Higgsino signal sample uses $m_{\tilde{\chi}_2^0} = 170$ and $m_{\tilde{\chi}_1^0} = 150$ GeV. The reweighted Higgsino sample is shown in red line. The lower pad shows the ratio between NUHM2 and Higgsino (or reweighted Higgsino) distributions.

114
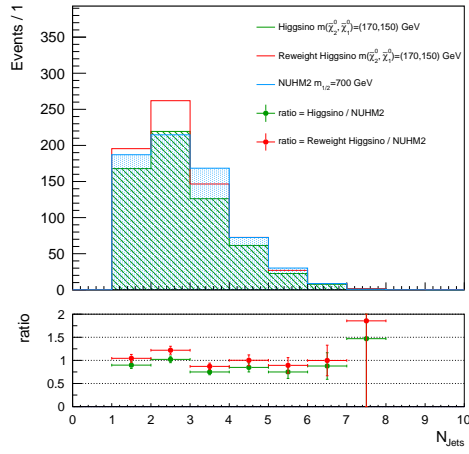
(a) Jet multiplicity
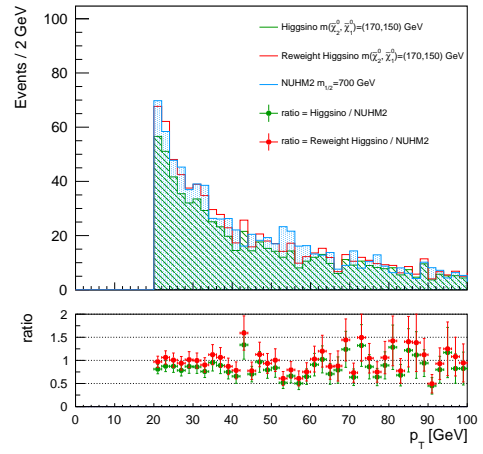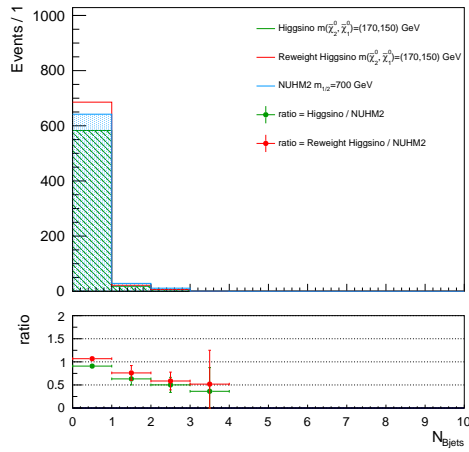
(b) Jet p_T

(c) b-jets multiplicity
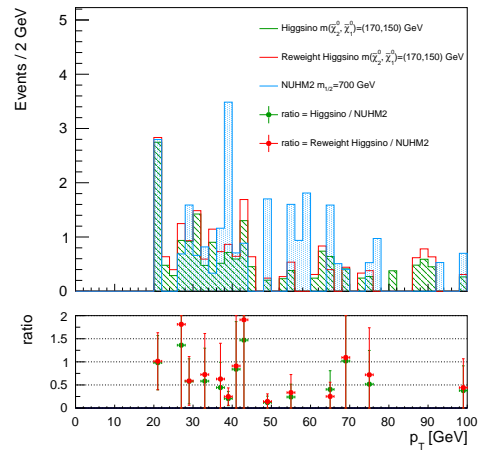
(d) b-jets p_T

Figure 8.4: The distributions for jet multiplicity, jet p_T, b-jets multiplicity, and b-jet p_T. The NUHM2 signal sample uses $m_{1/2} = 700$ GeV and the Higgsino signal sample uses $m_{\widetilde{\chi}_2^0} = 170$ and $m_{\widetilde{\chi}_1^0} = 150$ GeV. The reweighted Higgsino sample is shown in red line. The lower pad shows the ratio between NUHM2 and Higgsino (or reweighted Higgsino) distributions.

(a) E_T^{miss}

(b) $E_T^{miss}/H_T^{leptons}$

(c) $m_{\ell\ell}$

(d) $m_{\tau\tau}$
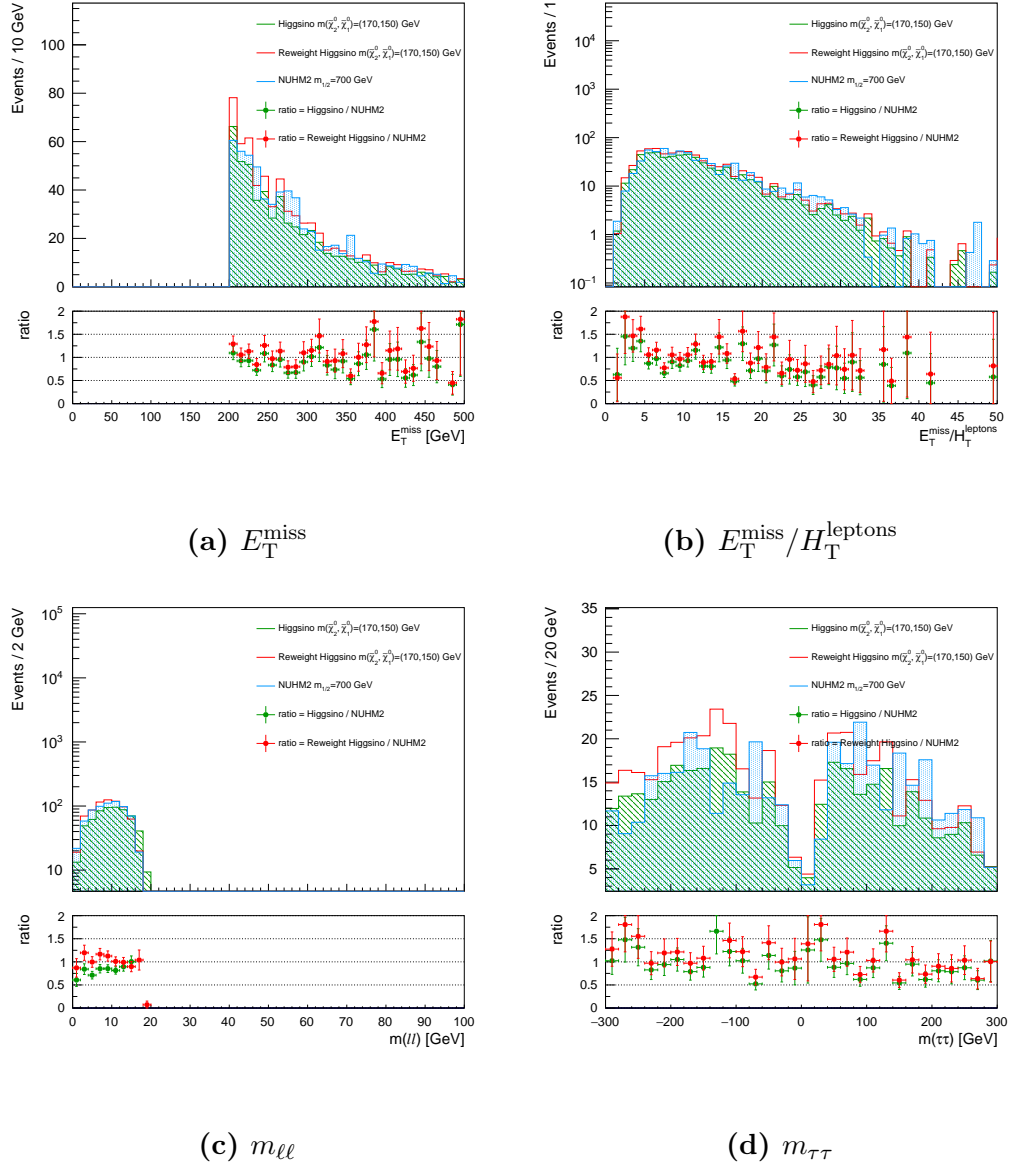
Figure 8.5: The distributions for E_T^{miss}, $E_T^{miss}/H_T^{leptons}$, $m_{\ell\ell}$, and $m_{\tau\tau}$. The NUHM2 signal sample uses $m_{1/2} = 700$ GeV and the Higgsino signal sample uses $m_{\tilde{\chi}_2^0} = 170$ and $m_{\tilde{\chi}_1^0} = 150$ GeV. The reweighted Higgsino sample is shown in red line. The lower pad shows the ratio between NUHM2 and Higgsino (or reweighted Higgsino) distributions.

116
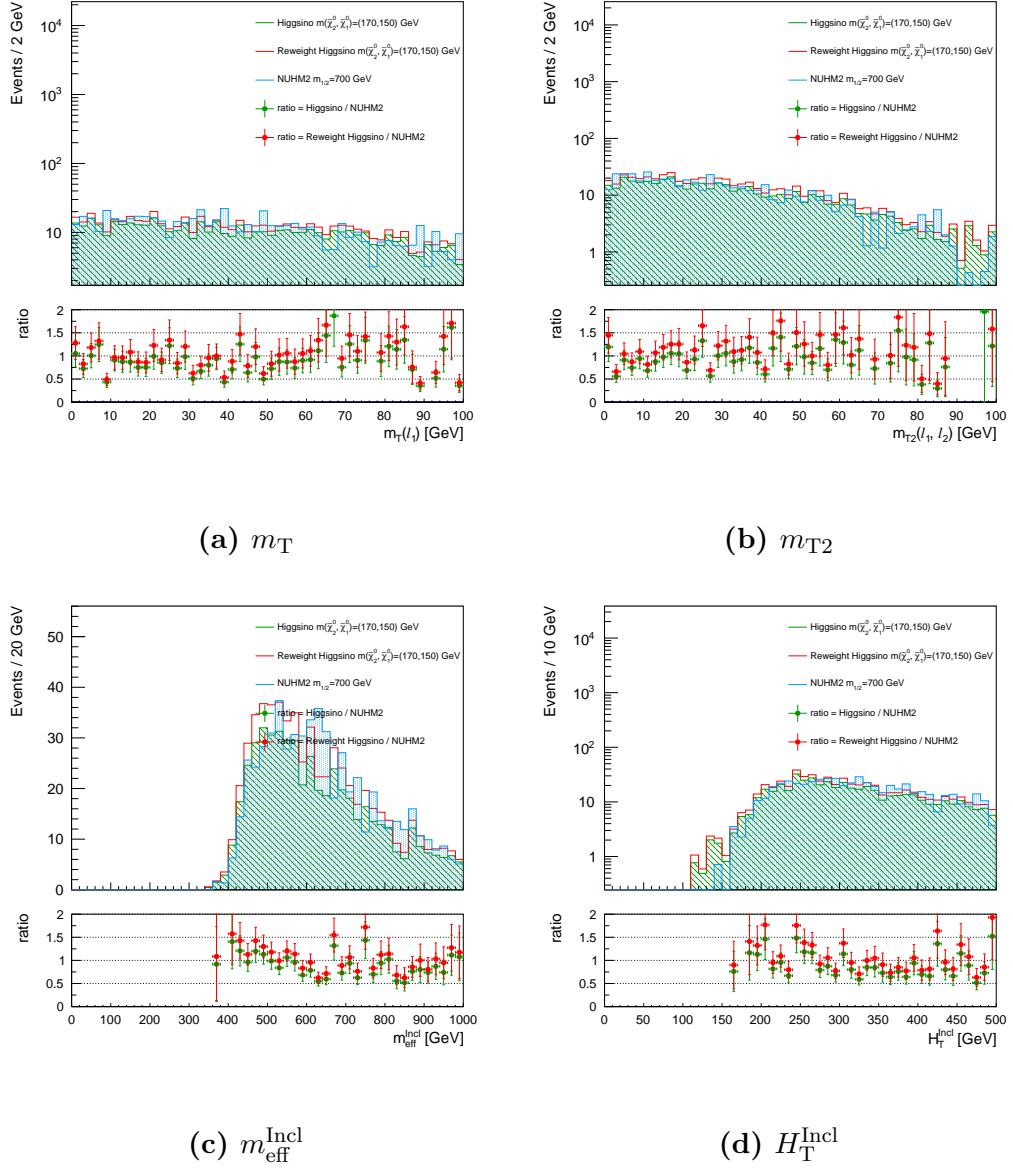
Figure 8.6: The distributions for m_T, m_{T2}, $m_{\text{eff}}^{\text{Incl}}$, H_T^{Incl}. The NUHM2 signal sample uses $m_{1/2} = 700$ GeV and the Higgsino signal sample uses $m_{\widetilde{\chi}_2^0} = 170$ and $m_{\widetilde{\chi}_1^0} = 150$ GeV. The reweighted Higgsino sample is shown in red line. The lower pad shows the ratio between NUHM2 and Higgsino (or reweighted Higgsino) distributions.
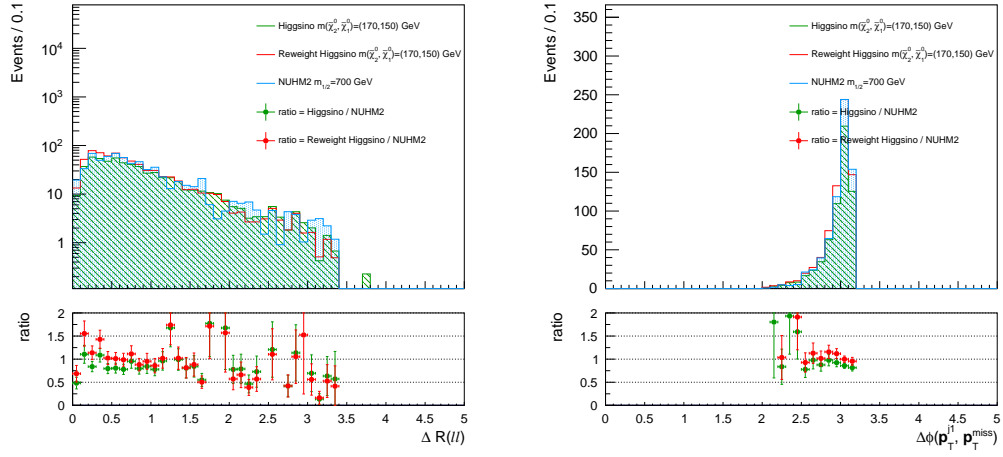
(a) $\Delta R_{\ell\ell}$ **(b)** $\Delta\phi(\mathbf{p}_T^{j1}, \mathbf{p}_T^{miss})$

Figure 8.7: The distributions for $\Delta R_{\ell\ell}$ and $\Delta\phi(\mathbf{p}_T^{j1}, \mathbf{p}_T^{miss})$. The NUHM2 signal sample uses $m_{1/2} = 700$ GeV and the Higgsino signal sample uses $m_{\widetilde{\chi}_2^0} = 170$ and $m_{\widetilde{\chi}_1^0} = 150$ GeV. The reweighted Higgsino sample is shown in red line. The lower pad shows the ratio between NUHM2 and Higgsino (or reweighted Higgsino) distributions.
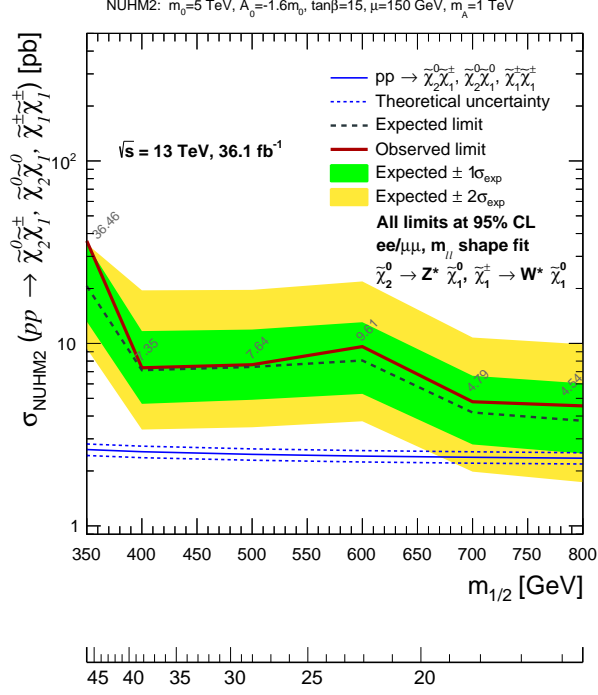
Figure 8.8: The upper limits of the cross-section for NUHM2 using the $m_{\ell\ell}$ reweighting method.

production samples. The NUHM2 signal MC production has been mentioned in Sect. 5.2.2 and the signal region selection is described in Sect. 6.2.2. The kinematic distributions in the SR$\ell\ell$-$m_{\ell\ell}$ are shown in Figs. 6.3, 6.4, and 6.5 and the yields are provided in Tables 6.5 and 6.6. The statistical interpretation is performed using the HiggsinoFitter which wraps the HistFitter [15]. Table 8.3 shows the calculated CLs values for NUHM2 with and without systematic uncertainties.

In both cases with and without systematics, the CLs_{obs} should be worse (higher) than the CLs_{exp} due to a small excess observed in some $m_{\ell\ell}$ bins. Two exceptions in NUHM2 $m_{1/2} = 400$ and 500 GeV with all systematics are observed. The CLs_{exp} are slightly higher than CLs_{obs} for these two mass points. Since this situation is not seen in the without systematics case, this situation happens when

$m_{1/2}$ [GeV]	No systematics		All systematics	
	CLs_{obs}	CLs_{exp}	CLs_{obs}	CLs_{exp}
350	0.6199	0.5434	0.6458	0.6007
400	0.5549	0.5233	0.5567	0.5844
500	0.3811	0.3556	0.4021	0.4494
600	0.3417	0.2305	0.3808	0.3133
700	0.2457	0.0879	0.2929	0.1362
800	0.2037	0.0916	0.2265	0.1307

Table 8.3: The calculated CLs values for NUHM2 with and without systematic uncertainties in the statistical interpretation.

there are increasing systematic uncertainties for these two $m_{1/2}$. Although the exceptions exist, the CLs_{obs} and CLs_{exp} with and without systematics have good agreement. Figure 8.9 shows the signal strength μ_{sig} for all NUHM2 points, all plots are consistent.

The upper limit of the cross-section is calculated by

$$\sigma_{UL} = \mu_{\text{sig}} \times \left[\sigma_{prod}(\widetilde{\chi}_2^0 \widetilde{\chi}_1^0) + \sigma_{prod}(\widetilde{\chi}_2^0 \widetilde{\chi}_1^+) + \sigma_{prod}(\widetilde{\chi}_2^0 \widetilde{\chi}_1^-) + \sigma_{prod}(\widetilde{\chi}_1^\pm \widetilde{\chi}_1^\mp) \right] \quad , \quad (8.3)$$

where μ_{sig} is the signal strength, and the four σ_{prod} are the cross-sections for different productions at next-to-leading-logarithm (NLL) accuracy. The upper limits of the cross-section with and without systematics are plotted in Fig. 8.10. The gray numbers are the upper limits of the cross-section in pb. The all systematics case has higher upper limits than the one without systematics as expected. None of the NUHM2 $m_{1/2}$ points are excluded at the 95% CL and the observed upper limits are higher then the theoretical prediction.
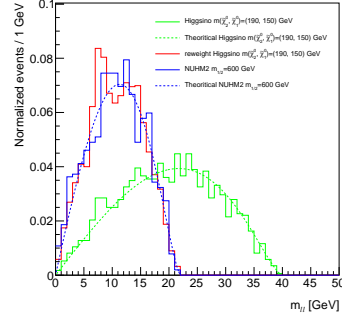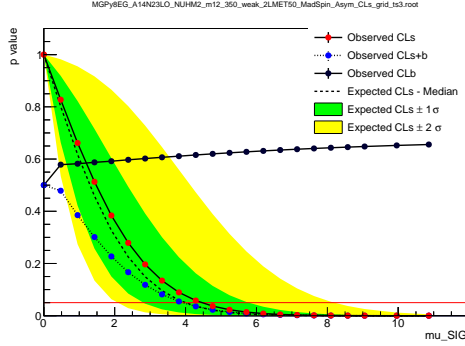
(a) NUHM2 $m_{1/2} = 350$ GeV
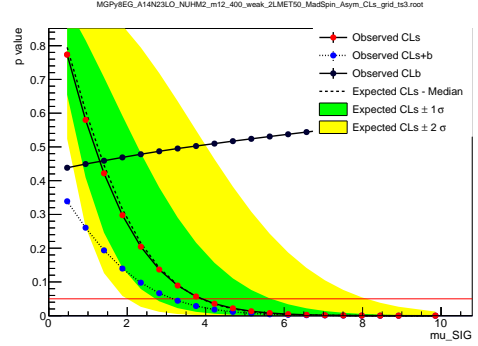
(b) NUHM2 $m_{1/2} = 400$ GeV
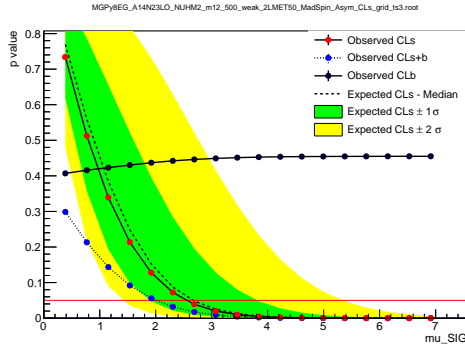
(c) NUHM2 $m_{1/2} = 500$ GeV
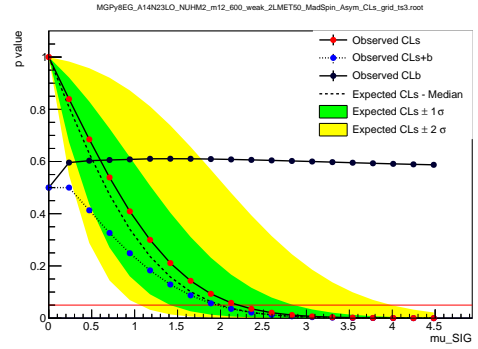
(d) NUHM2 $m_{1/2} = 600$ GeV
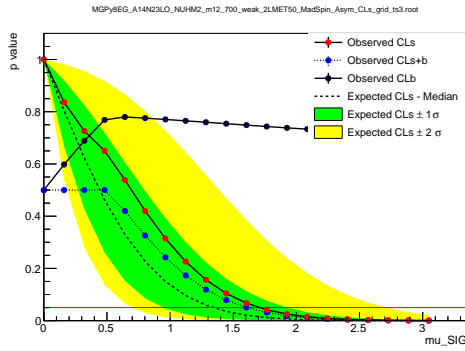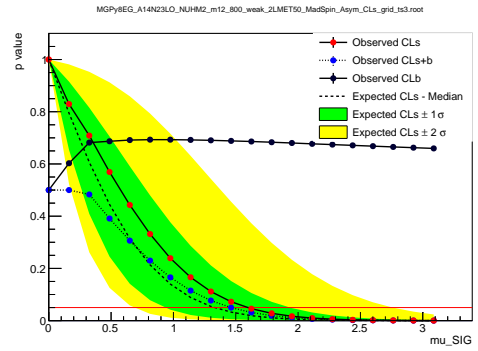
(e) NUHM2 $m_{1/2} = 700$ GeV

(f) NUHM2 $m_{1/2} = 800$ GeV

Figure 8.9: The signal strength μ_{sig} for the NUHM2 mass points.
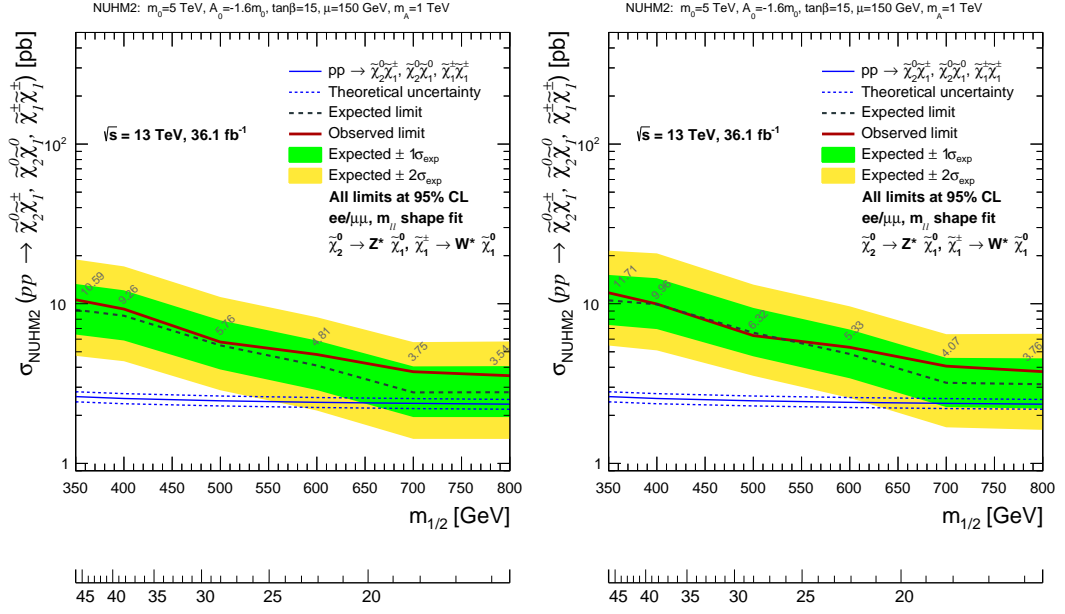
(a) No systematics

(b) All systematics

Figure 8.10: The upper limit of the cross-section of NUHM2 for with and without systematics. The gray numbers are the upper limits in pb.

CHAPTER 9

CONCLUSION

A search for the electroweak production of supersymmetric states with low p_T visible decay products is presented. Events with significant $E_\mathrm{T}^\mathrm{miss}$ and same flavor opposite charged lepton pairs are selected. The minimum p_T of the lepton is 4.5 GeV for the electrons and 4 GeV for the muons. The dilepton invariant mass is the main discriminating variable used to construct signal regions. This analysis is performed using LHC proton-proton collision data at $\sqrt{s} = 13$ TeV collected by the ATLAS detector corresponding to an integrated luminosity of 36.1 fb^{-1}. Since there is no observed excess over the Standard Model expectation, the results are interpreted using R-parity-conserving supersymmetry, where the produced states have small mass splitting with the lightest neutralino $\widetilde{\chi}_1^0$. For the NUHM2 scenario, 95% CL cross-section upper limits ranging between 11.5 and 3.8 pb for $m_{1/2}$ values of 350 to 800 GeV are provided.

References

[1] C. Patrignani et al. Review of Particle Physics. *Chin. Phys.*, C40(10):100001, 2016. (document), 2.1, 2.1.1

[2] G. Aad et al. The ATLAS Experiment at the CERN Large Hadron Collider. *JINST*, 3:S08003, 2008. (document), 4, 4.2, 4.2, 4.3, 4.4, 4.2.3, 4.1, 4.2.4, 4.6

[3] Atlas twiki: Trigger naming run 2. https://twiki.cern.ch/twiki/bin/viewauth/Atlas/TriggerNamingRun2. (document), 5.1

[4] Morad Aaboud et al. Dark matter interpretations of ATLAS searches for the electroweak production of supersymmetric particles in $\sqrt{s} = 8$ TeV proton-proton collisions. *JHEP*, 09:175, 2016. (document), 1, 1.1, 1

[5] John Ellis. Higgs Physics. In *Proceedings, 2013 European School of High-Energy Physics (ESHEP 2013): Paradfurdo, Hungary, June 5-18, 2013*, pages 117–168, 2015. (document), 2.1

[6] Georges Aad et al. Observation of a new particle in the search for the Standard Model Higgs boson with the ATLAS detector at the LHC. *Phys. Lett.*, B716:1–29, 2012. (document), 1, 2.1.5, 2.2

[7] Serguei Chatrchyan et al. Observation of a new boson at a mass of 125 GeV with the CMS experiment at the LHC. *Phys. Lett.*, B716:30–61, 2012. (document), 1, 2.1.5, 2.2

[8] The accelerator complex at cern. https://i.stack.imgur.com/Ur0ol.gif. (document), 2.3

[9] Stephen P. Martin. A Supersymmetry primer. 1997. [Adv. Ser. Direct. High Energy Phys.18,1(1998)]. (document), 1, 2.2.1, 3, 3.1

[10] Howard Baer, Vernon Barger, and Dan Mickelson. How conventional measures overestimate electroweak fine-tuning in supersymmetric theory. *Phys. Rev.*, D88(9):095013, 2013. (document), 3.2

[11] Howard Baer, Vernon Barger, Michael Savoy, and Xerxes Tata. Multichannel assault on natural supersymmetry at the high luminosity LHC. *Phys. Rev.*, D94(3):035025, 2016. (document), 3.3

[12] Fabienne Marcastel. CERN's Accelerator Complex. La chane des acclrateurs du CERN. Oct 2013. General Photo. (document), 4.1

[13] P. Strizenec. Performance of the ATLAS Liquid Argon Calorimeter after three years of LHC operation and plans for a future upgrade. *JINST*, 9:C09007, 2014. (document), 4.5

[14] A. Ruiz Martnez. The Run-2 ATLAS Trigger System. *J. Phys. Conf. Ser.*, 762(1):012003, 2016. (document), 4.7

[15] M. Baak, G. J. Besjes, D. Cte, A. Koutsman, J. Lorenz, and D. Short. HistFitter software framework for statistical data analysis. *Eur. Phys. J.*, C75:153, 2015. (document), 7.1, 8.3

[16] Morad Aaboud et al. Search for electroweak production of supersymmetric states in scenarios with compressed mass spectra at $\sqrt{s} = 13$ TeV with the ATLAS detector. *Submitted to: Phys. Rev. D*, 2017. (document), 7.2, 7.8

[17] The ATLAS collaboration. Electron efficiency measurements with the ATLAS detector using the 2015 LHC proton-proton collision data. 2016. (document), 6.1.1, C.1, C.3, C.5, C.6

[18] Morad Aaboud et al. Electron efficiency measurements with the ATLAS detector using 2012 LHC protonproton collision data. *Eur. Phys. J.*, C77(3):195, 2017. (document), C.2

[19] Electron reconstruction and identification efficiency measurements in 2016 data. https://atlas.web.cern.ch/Atlas/GROUPS/PHYSICS/PLOTS/EGAM-2017-003/index.html. (document), C.4

[20] Atlas electron/photon identification and calibration performance as a function of pile-up during the 2016 lhc data taking. https://atlas.web.cern.ch/Atlas/GROUPS/PHYSICS/PLOTS/EGAM-2016-005/index.html. (document), C.4

[21] Steven Weinberg. Implications of Dynamical Symmetry Breaking. *Phys. Rev.*, D13:974–996, 1976. [Addendum: Phys. Rev.D19,1277(1979)]. 1

[22] Eldad Gildener. Gauge Symmetry Hierarchies. *Phys. Rev.*, D14:1667, 1976. 1

[23] Leonard Susskind. Dynamics of Spontaneous Symmetry Breaking in the Weinberg-Salam Theory. *Phys. Rev.*, D20:2619–2625, 1979. 1

[24] J. Wess and B. Zumino. A Lagrangian Model Invariant Under Supergauge Transformations. *Phys. Lett.*, 49B:52, 1974. 1

[25] J. Wess and B. Zumino. Supergauge Transformations in Four-Dimensions. *Nucl. Phys.*, B70:39–50, 1974. 1, 3

[26] Yu. A. Golfand and E. P. Likhtman. Extension of the Algebra of Poincare Group Generators and Violation of p Invariance. *JETP Lett.*, 13:323–326, 1971. [Pisma Zh. Eksp. Teor. Fiz.13,452(1971)]. 1

[27] Pierre Fayet. Supersymmetry and Weak, Electromagnetic and Strong Interactions. *Phys. Lett.*, 64B:159, 1976. 1

[28] Pierre Fayet. Spontaneously Broken Supersymmetric Theories of Weak, Electromagnetic and Strong Interactions. *Phys. Lett.*, 69B:489, 1977. 1

[29] Glennys R. Farrar and Pierre Fayet. Phenomenology of the Production, Decay, and Detection of New Hadronic States Associated with Supersymmetry. *Phys. Lett.*, 76B:575–579, 1978. 1

[30] Riccardo Barbieri and G. F. Giudice. Upper Bounds on Supersymmetric Particle Masses. *Nucl. Phys.*, B306:63–76, 1988. 1

[31] B. de Carlos and J. A. Casas. One loop analysis of the electroweak breaking in supersymmetric models and the fine tuning problem. *Phys. Lett.*, B309:320–328, 1993. 1

[32] Lyndon Evans and Philip Bryant. LHC Machine. *JINST*, 3:S08001, 2008. 1, 4, 4.1, 4.2

[33] Georges Aad et al. Search for direct production of charginos, neutralinos and sleptons in final states with two leptons and missing transverse momentum in pp collisions at $\sqrt{s} = 8$ TeV with the ATLAS detector. *JHEP*, 05:071, 2014. 1

[34] Georges Aad et al. Search for direct production of charginos and neutralinos in events with three leptons and missing transverse momentum in $\sqrt{s} = 8$TeV pp collisions with the ATLAS detector. *JHEP*, 04:169, 2014. 1

[35] Georges Aad et al. Search for the electroweak production of supersymmetric particles in $\sqrt{s}$=8 TeV pp collisions with the ATLAS detector. *Phys. Rev.*, D93(5):052002, 2016. 1

[36] Vardan Khachatryan et al. Searches for electroweak production of charginos, neutralinos, and sleptons decaying to leptons and W, Z, and Higgs bosons in pp collisions at 8 TeV. *Eur. Phys. J.*, C74(9):3036, 2014. 1

[37] Vardan Khachatryan et al. Search for supersymmetry in events with soft leptons, low jet multiplicity, and missing transverse energy in protonproton collisions at $\sqrt{s}$=8 TeV. *Phys. Lett.*, B759:9–35, 2016. 1

[38] Albert M Sirunyan et al. Search for electroweak production of charginos and neutralinos in multilepton final states in proton-proton collisions at $\sqrt{s} = 13$ TeV. 2017. 1

[39] Abdus Salam. Weak and Electromagnetic Interactions. *Conf. Proc.*, C680519:367–377, 1968. 2, 2.1.4, 3

[40] S. L. Glashow. Partial Symmetries of Weak Interactions. *Nucl. Phys.*, 22:579–588, 1961. 2, 2.1.4, 3

[41] Steven Weinberg. A Model of Leptons. *Phys. Rev. Lett.*, 19:1264–1266, 1967. 2, 2.1.4, 3

[42] M. Herrero. The Standard model. *NATO Sci. Ser. C*, 534:1–59, 1999. 2, 3

[43] W. N. Cottingham and D. A. Greenwood. *An introduction to the standard model of particle physics.* Cambridge University Press, 2007. 2, 3

[44] Emmy Noether. Invariant Variation Problems. *Gott. Nachr.*, 1918:235–257, 1918. [Transp. Theory Statist. Phys.1,186(1971)]. 2.1

[45] E. Fermi. An attempt of a theory of beta radiation. 1. *Z. Phys.*, 88:161–177, 1934. 2.1.4

[46] T. Nakano and K. Nishijima. Charge Independence for V-particles. *Prog. Theor. Phys.*, 10:581–582, 1953. 2.1.4

[47] M. Gell-Mann. The interpretation of the new particles as displaced charge multiplets. *Nuovo Cim.*, 4(S2):848–866, 1956. 2.1.4

[48] Makoto Kobayashi and Toshihide Maskawa. CP Violation in the Renormalizable Theory of Weak Interaction. *Prog. Theor. Phys.*, 49:652–657, 1973. 2.1.4

[49] Ziro Maki, Masami Nakagawa, and Shoichi Sakata. Remarks on the unified model of elementary particles. *Prog. Theor. Phys.*, 28:870–880, 1962. 2.1.4

[50] Peter W. Higgs. Spontaneous Symmetry Breakdown without Massless Bosons. *Phys. Rev.*, 145:1156–1163, 1966. 2.1.4

[51] Peter W. Higgs. Broken Symmetries and the Masses of Gauge Bosons. *Phys. Rev. Lett.*, 13:508–509, 1964. 2.1.4

[52] Peter W. Higgs. Broken symmetries, massless particles and gauge fields. *Phys. Lett.*, 12:132–133, 1964. 2.1.4

[53] F. Englert and R. Brout. Broken Symmetry and the Mass of Gauge Vector Mesons. *Phys. Rev. Lett.*, 13:321–323, 1964. 2.1.4

[54] G. S. Guralnik, C. R. Hagen, and T. W. B. Kibble. Global Conservation Laws and Massless Particles. *Phys. Rev. Lett.*, 13:585–587, 1964. 2.1.4

[55] Piotr H. Chankowski, John R. Ellis, Keith A. Olive, and Stefan Pokorski. Cosmological fine tuning, supersymmetry, and the gauge hierarchy problem. *Phys. Lett.*, B452:28–38, 1999. 2.2.1

[56] Maarten C. Brak. The hierarchy problem in the standard model and little higgs theories. Oct 2004. 2.2.1

[57] C. L. Bennett et al. Nine-Year Wilkinson Microwave Anisotropy Probe (WMAP) Observations: Final Maps and Results. *Astrophys. J. Suppl.*, 208:20, 2013. 2.2.2

[58] P. A. R. Ade et al. Planck 2013 results. I. Overview of products and scientific results. *Astron. Astrophys.*, 571:A1, 2014. 2.2.2

[59] Gianfranco Bertone, Dan Hooper, and Joseph Silk. Particle dark matter: Evidence, candidates and constraints. *Phys. Rept.*, 405:279–390, 2005. 2.2.2

[60] Graham G. Ross. *GRAND UNIFIED THEORIES*. 1985. 2.2.3

[61] Peter J. Mohr, David B. Newell, and Barry N. Taylor. CODATA Recommended Values of the Fundamental Physical Constants: 2014. *Rev. Mod. Phys.*, 88(3):035009, 2016. 2.2.3

[62] Joseph D. Lykken. Introduction to supersymmetry. In *Fields, strings and duality. Proceedings, Summer School, Theoretical Advanced Study Institute in Elementary Particle Physics, TASI'96, Boulder, USA, June 2-28, 1996*, pages 85–153, 1996. 3

[63] Manuel Drees. An Introduction to supersymmetry. In *Current topics in physics. Proceedings, Inauguration Conference of the Asia-Pacific Center for Theoretical Physics (APCTP), Seoul, Korea, June 4-10, 1996. Vol. 1, 2*, 1996. 3

[64] Adel Bilal. Introduction to supersymmetry. 2001. 3

[65] Philip C. Argyres. An Introduction to Global Supersymmetry. 2001. 3

[66] Michael E. Peskin. Supersymmetry in Elementary Particle Physics. In *Proceedings of Theoretical Advanced Study Institute in Elementary Particle Physics : Exploring New Frontiers Using Colliders and Neutrinos (TASI 2006): Boulder, Colorado, June 4-30, 2006*, pages 609–704, 2008. 3

[67] Ian J. R. Aitchison. Supersymmetry and the MSSM: An Elementary introduction. 2005. 3

[68] Y. Shadmi. Introduction to Supersymmetry. In *Proceedings, 2014 European School of High-Energy Physics (ESHEP 2014): Garderen, The Netherlands, June 18 - July 01 2014*, pages 95–123, 2016. 3

[69] Howard Baer, Vernon Barger, Peisi Huang, Dan Mickelson, Azar Mustafayev, Warintorn Sreethawong, and Xerxes Tata. Radiatively-driven natural supersymmetry at the LHC. *JHEP*, 12:013, 2013. [Erratum: JHEP06,053(2015)]. 3.3, 3.4, 5.2.2

[70] Howard Baer, Vernon Barger, Peisi Huang, Azar Mustafayev, and Xerxes Tata. Radiative natural SUSY with a 125 GeV Higgs boson. *Phys. Rev. Lett.*, 109:161802, 2012. 3.3

[71] Howard Baer. Radiative natural supersymmetry with mixed axion/higgsino cold dark matter. 2012. [AIP Conf. Proc.1534,39(2012)]. 3.3

[72] Howard Baer, Vernon Barger, Peisi Huang, Dan Mickelson, Azar Mustafayev, and Xerxes Tata. Radiative natural supersymmetry: Reconciling electroweak fine-tuning and the Higgs boson mass. *Phys. Rev.*, D87(11):115028, 2013. 3.3

[73] John R. Ellis, Keith A. Olive, and Yudi Santoso. The MSSM parameter space with nonuniversal Higgs masses. *Phys. Lett.*, B539:107–118, 2002. 3.4

[74] John R. Ellis, Toby Falk, Keith A. Olive, and Yudi Santoso. Exploration of the MSSM with nonuniversal Higgs masses. *Nucl. Phys.*, B652:259–347, 2003. 3.4

[75] Howard Baer, Azar Mustafayev, Stefano Profumo, Alexander Belyaev, and Xerxes Tata. Neutralino cold dark matter in a one parameter extension of the minimal supergravity model. *Phys. Rev.*, D71:095008, 2005. 3.4

[76] Howard Baer, Azar Mustafayev, Stefano Profumo, Alexander Belyaev, and Xerxes Tata. Direct, indirect and collider detection of neutralino dark matter in SUSY models with non-universal Higgs masses. *JHEP*, 07:065, 2005. 3.4

[77] S. Chatrchyan et al. The CMS Experiment at the CERN LHC. *JINST*, 3:S08004, 2008. 4

[78] K. Aamodt et al. The ALICE experiment at the CERN LHC. *JINST*, 3:S08002, 2008. 4

[79] A. Augusto Alves, Jr. et al. The LHCb Detector at the LHC. *JINST*, 3:S08005, 2008. 4

[80] G. Anelli et al. The TOTEM experiment at the CERN Large Hadron Collider. *JINST*, 3:S08007, 2008. 4

[81] O. Adriani et al. The LHCf detector at the CERN Large Hadron Collider. *JINST*, 3:S08006, 2008. 4

[82] James Pinfold et al. Technical Design Report of the MoEDAL Experiment. 2009. 4

[83] L. Rossi. The LHC superconducting magnets. *Conf. Proc.*, C030512:141, 2003. 4.1

[84] Cern courier. http://cerncourier.com/cws/article/cern/35864. 4.1

[85] S. Palestini. The muon spectrometer of the ATLAS experiment. *Nucl. Phys. Proc. Suppl.*, 125:337–345, 2003. [,337(2003)]. 4.2.4

[86] E. Diehl. ATLAS Muon Detector Commissioning. In *Particles and fields. Proceedings, Meeting of the Division of the American Physical Society, DPF 2009, Detroit, USA, July 26-31, 2009*, 2009. 4.2.4

[87] K. Kordas et al. The ATLAS Data Acquisition and Trigger: Concept, design and status. *Nucl. Phys. Proc. Suppl.*, 172:178–182, 2007. 4.2.5

[88] Morad Aaboud et al. Luminosity determination in pp collisions at $\sqrt{s} = 8$ TeV using the ATLAS detector at the LHC. *Eur. Phys. J.*, C76(12):653, 2016. 5.1

[89] S. Agostinelli et al. GEANT4: A Simulation toolkit. *Nucl. Instrum. Meth.*, A506:250–303, 2003. 5.2, D.1

[90] ATLAS Collaboration. The simulation principle and performance of the ATLAS fast calorimeter simulation FastCaloSim. 2010. 5.2

[91] Torbjorn Sjostrand, Stephen Mrenna, and Peter Z. Skands. A Brief Introduction to PYTHIA 8.1. *Comput. Phys. Commun.*, 178:852–867, 2008. 5.2

[92] Summary of ATLAS Pythia 8 tunes. 2012. 5.2

[93] A. D. Martin, W. J. Stirling, R. S. Thorne, and G. Watt. Parton distributions for the LHC. *Eur. Phys. J.*, C63:189–285, 2009. 5.2, D.1

[94] T. Gleisberg, Stefan. Hoeche, F. Krauss, M. Schonherr, S. Schumann, F. Siegert, and J. Winter. Event generation with SHERPA 1.1. *JHEP*, 02:007, 2009. 5.2.1

[95] D. J. Lange. The EvtGen particle decay simulation package. *Nucl. Instrum. Meth.*, A462:152–155, 2001. 5.2.1, D.1

[96] Howard Baer, Frank E. Paige, Serban D. Protopopescu, and Xerxes Tata. ISAJET 7.48: A Monte Carlo event generator for p p, anti-p, p, and e+ e- reactions. 1999. 5.2.2

[97] W. Beenakker, M. Klasen, M. Kramer, T. Plehn, M. Spira, and P. M. Zerwas. The Production of charginos / neutralinos and sleptons at hadron colliders. *Phys. Rev. Lett.*, 83:3780–3783, 1999. [Erratum: Phys. Rev. Lett.100,029901(2008)]. 5.2.2

[98] Pierre Artoisenet, Rikkert Frederix, Olivier Mattelaer, and Robbert Rietkerk. Automatic spin-entangled decays of heavy resonances in Monte Carlo simulations. *JHEP*, 03:015, 2013. 5.2.2

[99] W. Beenakker, R. Hopker, and M. Spira. PROSPINO: A Program for the production of supersymmetric particles in next-to-leading order QCD. 1996. 5.2.2

[100] A. Djouadi, M. M. Muhlleitner, and M. Spira. Decays of supersymmetric particles: The Program SUSY-HIT (SUspect-SdecaY-Hdecay-InTerface). *Acta Phys. Polon.*, B38:635–644, 2007. 5.2.2

[101] The susytoolsv8 twiki. https://twiki.cern.ch/twiki/bin/view/AtlasProtected/SUSYToolsV8. 6.1

[102] The analysis release twiki. https://twiki.cern.ch/twiki/bin/viewauth/AtlasProtected/AnalysisRelease. 6.1

[103] Georges Aad et al. Muon reconstruction performance of the ATLAS detector in protonproton collision data at $\sqrt{s}$ =13 TeV. *Eur. Phys. J.*, C76(5):292, 2016. 6.1.2

[104] The ATLAS collaboration. Measurement of the tau lepton reconstruction and identification performance in the ATLAS experiment using *pp* collisions at $\sqrt{s}$ = 13 TeV. 2017. 6.1.3

[105] Expected photon performance in the ATLAS experiment. 2011. 6.1.4

[106] Matteo Cacciari, Gavin P. Salam, and Gregory Soyez. The Anti-k(t) jet clustering algorithm. *JHEP*, 04:063, 2008. 6.1.5

[107] Expected performance of the ATLAS *b*-tagging algorithms in Run-2. Technical Report ATL-PHYS-PUB-2015-022, CERN, Geneva, Jul 2015. 6.1.5

[108] Optimisation of the ATLAS *b*-tagging performance for the 2016 LHC Run. Technical Report ATL-PHYS-PUB-2016-012, CERN, Geneva, Jun 2016. 6.1.5

[109] Georges Aad et al. Performance of pile-up mitigation techniques for jets in *pp* collisions at $\sqrt{s}$ = 8 TeV using the ATLAS detector. *Eur. Phys. J.*, C76(11):581, 2016. 6.1.5

[110] Expected performance of missing transverse momentum reconstruction for the ATLAS detector at $\sqrt{s} = 13$ TeV. Technical Report ATL-PHYS-PUB-2015-023, CERN, Geneva, Jul 2015. 6.1.6

[111] Numbercountingutils. https://root.cern.ch/doc/v606/NumberCountingUtils_8cxx_source.html. 6.2.2

[112] Georges Aad et al. Observation and measurement of Higgs boson decays to WW* with the ATLAS detector. *Phys. Rev.*, D92(1):012006, 2015. 7.3.1

[113] Georges Aad et al. Topological cell clustering in the ATLAS calorimeters and its performance in LHC Run 1. *Eur. Phys. J.*, C77:490, 2017. C.3

[114] Morad Aaboud et al. Search for supersymmetry in final states with two same-sign or three leptons and jets using 36 fb^{-1} of $\sqrt{s} = 13$ TeV pp collision data with the ATLAS detector. *JHEP*, 09:084, 2017. D

[115] Georges Aad et al. Search for supersymmetry at $\sqrt{s}$=8 TeV in final states with jets and two same-sign leptons or three leptons with the ATLAS detector. *JHEP*, 06:035, 2014. D.3

[116] Search for supersymmetry using events with three leptons, multiple jets, and missing transverse momentum in 13.0 fb^{-1} of pp collisions with the ATLAS detector at $\sqrt{s} = 8$ TeV. Technical Report ATLAS-CONF-2012-151, CERN, Geneva, Nov 2012. D.3

[117] Tagging and suppression of pileup jets with the ATLAS detector. Technical Report ATLAS-CONF-2014-018, CERN, Geneva, May 2014. E.1

Appendix

APPENDIX A

CROSS-SECTIONS OF THE NUHM2 MODEL

The cross-sections, branching fraction, and filter efficiency for the NUHM2 signal samples are shown in Tables A.1, A.2, A.3, A.4, A.5, A.6 and A.7. The various final states are listed in Table A.8

DSID	Final state	Cross-section [pb]	K-factor/BF	Filter efficiency	Relative uncertainty
370617	111	0.0116116904	1.00000000	1.00000000	0.07950234
370617	112	0.0009775530	1.00000000	1.00000000	0.08535312
370617	113	0.5163867234	1.00000000	1.00000000	0.07315089
370617	114	0.0000593483	1.00000000	1.00000000	0.08483826
370617	115	1.1555478731	1.00000000	1.00000000	0.06803190
370617	116	0.0056717958	1.00000000	1.00000000	0.05803524
370617	117	0.7027932124	1.00000000	1.00000000	0.08979719
370617	118	0.0030806972	1.00000000	1.00000000	0.07709474
370617	122	0.0000260248	1.00000000	1.00000000	0.13101757
370617	123	0.1709342503	1.00000000	1.00000000	0.06993300
370617	124	0.0002175469	1.00000000	1.00000000	0.08148442
370617	125	0.4768609298	1.00000000	1.00000000	0.06541649
370617	126	0.0228714654	1.00000000	1.00000000	0.05697991
370617	127	0.2784795051	1.00000000	1.00000000	0.08434059
370617	128	0.0120807622	1.00000000	1.00000000	0.07942795
370617	133	0.0003583977	1.00000000	1.00000000	0.06910802
370617	134	0.0191236271	1.00000000	1.00000000	0.06575101
370617	135	0.6773400626	1.00000000	1.00000000	0.06477621
370617	136	0.0262277631	1.00000000	1.00000000	0.05716003
370617	137	0.3954923581	1.00000000	1.00000000	0.08483868
370617	138	0.0137758494	1.00000000	1.00000000	0.08211888
370617	144	0.0000568127	1.00000000	1.00000000	0.07453184
370617	145	0.0213534960	1.00000000	1.00000000	0.05398319
370617	146	0.2119219378	1.00000000	1.00000000	0.05665419
370617	147	0.0113003976	1.00000000	1.00000000	0.07780129
370617	148	0.1028839844	1.00000000	1.00000000	0.07544194
370617	157	1.1640104660	1.00000000	1.00000000	0.07733674
370617	158	0.0187939524	1.00000000	1.00000000	0.06417211
370617	167	0.0188413722	1.00000000	1.00000000	0.06767782
370617	168	0.1655520687	1.00000000	1.00000000	0.06249944
394301	157	1.1640104660	0.1110699593	1.4334E-01	0.07733674
394302	127	0.2784795051	0.0365485123	2.5440E-01	0.08434059
394303	125	0.4768609298	0.0365485123	2.5135E-01	0.06541649
394304	112	0.0009775530	0.0365485123	3.0251E-01	0.08535312

Table A.1: The cross-sections, branching fraction, and filter efficiency for the NUHM2 signal samples $m_{1/2} = 300$ GeV.

DSID	Final state	Cross-section [pb]	K-factor/BF	Filter efficiency	Relative uncertainty
370618	111	0.0076283799	1.00000000	1.00000000	0.07739107
370618	112	0.5835187445	1.00000000	1.00000000	0.07193879
370618	113	0.0000894312	1.00000000	1.00000000	0.09912250
370618	114	0.0001023491	1.00000000	1.00000000	0.07825966
370618	115	1.0850849571	1.00000000	1.00000000	0.07591545
370618	116	0.0049251988	1.00000000	1.00000000	0.05689268
370618	117	0.6538672654	1.00000000	1.00000000	0.08886870
370618	118	0.0025928251	1.00000000	1.00000000	0.07604635
370618	122	0.0003076705	1.00000000	1.00000000	0.06756051
370618	123	0.1082826561	1.00000000	1.00000000	0.06926016
370618	124	0.0094622361	1.00000000	1.00000000	0.06300188
370618	125	0.6833463531	1.00000000	1.00000000	0.06443308
370618	126	0.0129259483	1.00000000	1.00000000	0.05402434
370618	127	0.3983657446	1.00000000	1.00000000	0.08599203
370618	128	0.0066391822	1.00000000	1.00000000	0.07534667
370618	133	0.0000649975	1.00000000	1.00000000	0.10705877
370618	134	0.0001247362	1.00000000	1.00000000	0.07583934
370618	135	0.2353276570	1.00000000	1.00000000	0.06552596
370618	136	0.0091529911	1.00000000	1.00000000	0.05672728
370618	137	0.1357101599	1.00000000	1.00000000	0.08410482
370618	138	0.0046580255	1.00000000	1.00000000	0.07466805
370618	144	0.0000282761	1.00000000	1.00000000	0.07380597
370618	145	0.0104731869	1.00000000	1.00000000	0.05738262
370618	146	0.1421425400	1.00000000	1.00000000	0.06087756
370618	147	0.0054325991	1.00000000	1.00000000	0.07452907
370618	148	0.0669626098	1.00000000	1.00000000	0.07470349
370618	157	0.9548695995	1.00000000	1.00000000	0.07280905
370618	158	0.0093028684	1.00000000	1.00000000	0.06338077
370618	167	0.0092973351	1.00000000	1.00000000	0.06299140
370618	168	0.1082938946	1.00000000	1.00000000	0.05684157
394305	157	0.9548695995	0.111060393	1.2990E-01	0.07280905
394306	127	0.3983657446	0.101384714	2.5255E-01	0.08599203
394307	125	0.6833463531	0.101384714	2.5574E-01	0.06443308
394308	112	0.5835187445	0.101384714	2.2766E-01	0.07193879

Table A.2: The cross-sections, branching fraction, and filter efficiency for the NUHM2 signal samples $m_{1/2} = 350$ GeV.

DSID	Final state	Cross-section [pb]	K-factor/BF	Filter efficiency	Relative uncertainty
370619	111	0.0050511346	1.00000000	1.00000000	0.07579917
370619	112	0.6255603991	1.00000000	1.00000000	0.07158509
370619	113	0.0000109243	1.00000000	1.00000000	0.09579487
370619	114	0.0001052946	1.00000000	1.00000000	0.07766307
370619	115	1.0342689914	1.00000000	1.00000000	0.06820123
370619	116	0.0035382215	1.00000000	1.00000000	0.05558890
370619	117	0.6163842668	1.00000000	1.00000000	0.08756721
370619	118	0.0018044868	1.00000000	1.00000000	0.07509790
370619	122	0.0002664650	1.00000000	1.00000000	0.07041738
370619	123	0.0628066056	1.00000000	1.00000000	0.06735393
370619	124	0.0048696810	1.00000000	1.00000000	0.06286865
370619	125	0.6845201512	1.00000000	1.00000000	0.06476776
370619	126	0.0067063042	1.00000000	1.00000000	0.05627793
370619	127	0.3976839861	1.00000000	1.00000000	0.08518583
370619	128	0.0033679821	1.00000000	1.00000000	0.07318125
370619	133	0.0000557211	1.00000000	1.00000000	0.10394707
370619	134	0.0000636446	1.00000000	1.00000000	0.07539568
370619	135	0.1183185424	1.00000000	1.00000000	0.05812791
370619	136	0.0036848994	1.00000000	1.00000000	0.05773533
370619	137	0.0670198462	1.00000000	1.00000000	0.08128406
370619	138	0.0018161476	1.00000000	1.00000000	0.07634830
370619	144	0.0000158930	1.00000000	1.00000000	0.07992644
370619	145	0.0054376416	1.00000000	1.00000000	0.05587952
370619	146	0.0976478188	1.00000000	1.00000000	0.06106615
370619	147	0.0027346724	1.00000000	1.00000000	0.07262348
370619	148	0.0442265190	1.00000000	1.00000000	0.07409153
370619	157	0.8415837349	1.00000000	1.00000000	0.07397928
370619	158	0.0047908009	1.00000000	1.00000000	0.06312184
370619	167	0.0047973169	1.00000000	1.00000000	0.06465433
370619	168	0.0724744359	1.00000000	1.00000000	0.06197995
394309	157	0.8415837349	0.111047482	1.2199E-01	0.07397928
394310	127	0.3976839861	0.102934938	2.2044E-01	0.08518583
394311	125	0.6845201512	0.102934938	2.2387E-01	0.06476776
394312	112	0.6255603991	0.102934938	2.0415E-01	0.07158509

Table A.3: The cross-sections, branching fraction, and filter efficiency for the NUHM2 signal samples $m_{1/2} = 400$ GeV.

DSID	Final state	Cross-section [pb]	K-factor/BF	Filter efficiency	Relative uncertainty
370620	111	0.0023867653	1.00000000	1.00000000	0.07209579
370620	112	0.6603094819	1.00000000	1.00000000	0.07005129
370620	113	0.0001325585	1.00000000	1.00000000	0.07482547
370620	114	0.0000688236	1.00000000	1.00000000	0.07197169
370620	115	0.9426500411	1.00000000	1.00000000	0.06460091
370620	116	0.0015013209	1.00000000	1.00000000	0.06183960
370620	117	0.5588686815	1.00000000	1.00000000	0.08560539
370620	118	0.0007279662	1.00000000	1.00000000	0.07490627
370620	122	0.0002061240	1.00000000	1.00000000	0.07176449
370620	123	0.0211437195	1.00000000	1.00000000	0.06388222
370620	124	0.0014907193	1.00000000	1.00000000	0.06151866
370620	125	0.6819165298	1.00000000	1.00000000	0.06356555
370620	126	0.0021061945	1.00000000	1.00000000	0.05664429
370620	127	0.3955900373	1.00000000	1.00000000	0.08416802
370620	128	0.0010081829	1.00000000	1.00000000	0.07123419
370620	133	0.0000195970	1.00000000	1.00000000	0.10671913
370620	134	0.0000176193	1.00000000	1.00000000	0.07871367
370620	135	0.0340389859	1.00000000	1.00000000	0.05924527
370620	136	0.0006926196	1.00000000	1.00000000	0.05800427
370620	137	0.0187411871	1.00000000	1.00000000	0.08099696
370620	138	0.0003229659	1.00000000	1.00000000	0.07606581
370620	144	0.0000098797	1.00000000	1.00000000	0.07455477
370620	145	0.0016797877	1.00000000	1.00000000	0.05654557
370620	146	0.0453186981	1.00000000	1.00000000	0.06092776
370620	147	0.0008077861	1.00000000	1.00000000	0.07385221
370620	148	0.0192295608	1.00000000	1.00000000	0.07792430
370620	157	0.7280789222	1.00000000	1.00000000	0.07328355
370620	158	0.0014642018	1.00000000	1.00000000	0.06676658
370620	167	0.0014587803	1.00000000	1.00000000	0.06499176
370620	168	0.0324683300	1.00000000	1.00000000	0.06503155
394313	157	0.7280789222	0.111019377	1.0812E-01	0.07328355
394314	127	0.3955900373	0.105384522	1.8923E-01	0.08416802
394315	125	0.6819165298	0.105384522	1.8805E-01	0.06356555
394316	112	0.6603094819	0.105384522	1.7600E-01	0.07005129

Table A.4: The cross-sections, branching fraction, and filter efficiency for the NUHM2 signal samples $m_{1/2} = 500$ GeV.

DSID	Final state	Cross-section [pb]	K-factor/BF	Filter efficiency	Relative uncertainty
370621	111	0.0012897690	1.00000000	1.00000000	0.07308455
370621	112	0.6656504736	1.00000000	1.00000000	0.07047924
370621	113	0.0001361496	1.00000000	1.00000000	0.07047382
370621	114	0.0000378018	1.00000000	1.00000000	0.07036880
370621	115	0.8824882181	1.00000000	1.00000000	0.06538492
370621	116	0.0006132703	1.00000000	1.00000000	0.05826096
370621	117	0.5187808653	1.00000000	1.00000000	0.08546879
370621	118	0.0002849360	1.00000000	1.00000000	0.07563404
370621	122	0.0001627043	1.00000000	1.00000000	0.06980768
370621	123	0.0078958339	1.00000000	1.00000000	0.06365983
370621	124	0.0005370949	1.00000000	1.00000000	0.06338450
370621	125	0.6791453722	1.00000000	1.00000000	0.06375124
370621	126	0.0007771667	1.00000000	1.00000000	0.05779085
370621	127	0.3930396433	1.00000000	1.00000000	0.08337329
370621	128	0.0003583832	1.00000000	1.00000000	0.07532675
370621	133	0.0000068529	1.00000000	1.00000000	0.09776310
370621	134	0.0000060514	1.00000000	1.00000000	0.07178228
370621	135	0.0118585454	1.00000000	1.00000000	0.06459092
370621	136	0.0001672449	1.00000000	1.00000000	0.05977911
370621	137	0.0063210120	1.00000000	1.00000000	0.07773831
370621	138	0.0000738669	1.00000000	1.00000000	0.07600501
370621	144	0.0000050854	1.00000000	1.00000000	0.10988000
370621	145	0.0006099769	1.00000000	1.00000000	0.05679637
370621	146	0.0230198632	1.00000000	1.00000000	0.06402567
370621	147	0.0002805066	1.00000000	1.00000000	0.07646096
370621	148	0.0091676826	1.00000000	1.00000000	0.07848717
370621	157	0.6745140438	1.00000000	1.00000000	0.07398616
370621	158	0.0005268754	1.00000000	1.00000000	0.06482055
370621	167	0.0005263009	1.00000000	1.00000000	0.06458416
370621	168	0.0159949974	1.00000000	1.00000000	0.06360196
394317	157	0.6745140438	0.110994804	9.9998E-02	0.07398616
394318	127	0.3930396433	0.107603552	1.6870E-01	0.08337329
394319	125	0.6791453722	0.107603552	1.6924E-01	0.06375124
394320	112	0.6656504736	0.107603552	1.5353E-01	0.07047924

Table A.5: The cross-sections, branching fraction, and filter efficiency for the NUHM2 signal samples $m_{1/2} = 600$ GeV.

DSID	Final state	Cross-section [pb]	K-factor/BF	Filter efficiency	Relative uncertainty
370622	111	0.0007869897	1.00000000	1.00000000	0.07181679
370622	112	0.6643270342	1.00000000	1.00000000	0.07021531
370622	113	0.0000996207	1.00000000	1.00000000	0.06721434
370622	114	0.0000204490	1.00000000	1.00000000	0.07299332
370622	115	0.8407296201	1.00000000	1.00000000	0.06552209
370622	116	0.0002658841	1.00000000	1.00000000	0.06040295
370622	117	0.4923724748	1.00000000	1.00000000	0.08491961
370622	118	0.0001190742	1.00000000	1.00000000	0.08405305
370622	122	0.0001324452	1.00000000	1.00000000	0.07307817
370622	123	0.0033217150	1.00000000	1.00000000	0.06361965
370622	124	0.0002184464	1.00000000	1.00000000	0.06456221
370622	125	0.6766070496	1.00000000	1.00000000	0.06427279
370622	126	0.0003241413	1.00000000	1.00000000	0.05818056
370622	127	0.3913281838	1.00000000	1.00000000	0.08575382
370622	128	0.0001431279	1.00000000	1.00000000	0.07221632
370622	133	0.0000034045	1.00000000	1.00000000	0.08794933
370622	134	0.0000026928	1.00000000	1.00000000	0.07609993
370622	135	0.0048337927	1.00000000	1.00000000	0.05703733
370622	136	0.0000502367	1.00000000	1.00000000	0.06355969
370622	137	0.0025078220	1.00000000	1.00000000	0.07562175
370622	138	0.0000209783	1.00000000	1.00000000	0.07847390
370622	144	0.0000052666	1.00000000	1.00000000	0.07856700
370622	145	0.0002494848	1.00000000	1.00000000	0.06059516
370622	146	0.0118318988	1.00000000	1.00000000	0.07046938
370622	147	0.0001094560	1.00000000	1.00000000	0.07805891
370622	148	0.0044453542	1.00000000	1.00000000	0.08306247
370622	157	0.6438838471	1.00000000	1.00000000	0.07295880
370622	158	0.0002140543	1.00000000	1.00000000	0.06775447
370622	167	0.0002138494	1.00000000	1.00000000	0.06731630
370622	168	0.0079546496	1.00000000	1.00000000	0.06899943
394321	157	0.6438838471	0.110976399	9.3533E-02	0.07295880
394322	127	0.3913281838	0.109700775	1.5801E-01	0.08575382
394323	125	0.6766070496	0.109700775	1.5871E-01	0.06427279
394324	112	0.6643270342	0.109700775	1.3786E-01	0.07021531

Table A.6: The cross-sections, branching fraction, and filter efficiency for the NUHM2 signal samples $m_{1/2} = 700$ GeV.

DSID	Final state	Cross-section [pb]	K-factor/BF	Filter efficiency	Relative uncertainty
370623	111	0.0005212386	1.00000000	1.00000000	0.07063351
370623	112	0.6598118363	1.00000000	1.00000000	0.06943069
370623	113	0.0000669873	1.00000000	1.00000000	0.06712724
370623	114	0.0000113016	1.00000000	1.00000000	0.07064093
370623	115	0.8098002978	1.00000000	1.00000000	0.06493814
370623	116	0.0001234140	1.00000000	1.00000000	0.06889051
370623	117	0.4737135796	1.00000000	1.00000000	0.08608973
370623	118	0.0000526249	1.00000000	1.00000000	0.07771427
370623	122	0.0001087675	1.00000000	1.00000000	0.07088280
370623	123	0.0015416626	1.00000000	1.00000000	0.06537577
370623	124	0.0000974637	1.00000000	1.00000000	0.06530325
370623	125	0.6748686972	1.00000000	1.00000000	0.06282954
370623	126	0.0001487367	1.00000000	1.00000000	0.06359830
370623	127	0.3906074836	1.00000000	1.00000000	0.08243869
370623	128	0.0000632347	1.00000000	1.00000000	0.07613879
370623	133	0.0000021556	1.00000000	1.00000000	0.08808178
370623	134	0.0000013753	1.00000000	1.00000000	0.08184458
370623	135	0.0022215540	1.00000000	1.00000000	0.05781810
370623	136	0.0000179127	1.00000000	1.00000000	0.06707128
370623	137	0.0011306653	1.00000000	1.00000000	0.07974272
370623	138	0.0000071002	1.00000000	1.00000000	0.07996818
370623	144	0.0000033200	1.00000000	1.00000000	0.08521909
370623	145	0.0001114849	1.00000000	1.00000000	0.06626951
370623	146	0.0064128038	1.00000000	1.00000000	0.07356448
370623	147	0.0000474513	1.00000000	1.00000000	0.07695978
370623	148	0.0023333882	1.00000000	1.00000000	0.08950999
370623	157	0.6240319555	1.00000000	1.00000000	0.07242344
370623	158	0.0000960852	1.00000000	1.00000000	0.06651898
370623	167	0.0000961123	1.00000000	1.00000000	0.06811969
370623	168	0.0042577101	1.00000000	1.00000000	0.07239458
394325	157	0.6240319555	0.1109638923	8.7153E-02	0.07242344
394326	127	0.3906074836	0.1116429166	1.3865E-01	0.08243869
394327	125	0.6748686972	0.1116429166	1.4629E-01	0.06282954
394328	112	0.6598118363	0.1116429166	1.2823E-01	0.06943069

Table A.7: The cross-sections, branching fraction, and filter efficiency for the NUHM2 signal samples $m_{1/2} = 800$ GeV.

| ID	Particles	ID	Particles	ID	Particles	ID	Particles	ID	Particles	ID	Particles
111	$\widetilde{\chi}_1^0\widetilde{\chi}_1^0$	-	-	-	-	-	-	-	-	-	-
112	$\widetilde{\chi}_1^0\widetilde{\chi}_2^0$	122	$\widetilde{\chi}_2^0\widetilde{\chi}_2^0$	-	-	-	-	-	-	-	-
113	$\widetilde{\chi}_1^0\widetilde{\chi}_3^0$	123	$\widetilde{\chi}_2^0\widetilde{\chi}_3^0$	133	$\widetilde{\chi}_3^0\widetilde{\chi}_3^0$	-	-	-	-	-	-
114	$\widetilde{\chi}_1^0\widetilde{\chi}_4^0$	124	$\widetilde{\chi}_2^0\widetilde{\chi}_4^0$	134	$\widetilde{\chi}_3^0\widetilde{\chi}_4^0$	144	$\widetilde{\chi}_4^0\widetilde{\chi}_4^0$	-	-	-	-
115	$\widetilde{\chi}_1^0\widetilde{\chi}_1^+$	125	$\widetilde{\chi}_2^0\widetilde{\chi}_1^+$	135	$\widetilde{\chi}_3^0\widetilde{\chi}_1^+$	145	$\widetilde{\chi}_4^0\widetilde{\chi}_1^+$	-	-	-	-
116	$\widetilde{\chi}_1^0\widetilde{\chi}_2^+$	126	$\widetilde{\chi}_2^0\widetilde{\chi}_2^+$	136	$\widetilde{\chi}_3^0\widetilde{\chi}_2^+$	146	$\widetilde{\chi}_4^0\widetilde{\chi}_2^+$	-	-	-	-
117	$\widetilde{\chi}_1^0\widetilde{\chi}_1^-$	127	$\widetilde{\chi}_2^0\widetilde{\chi}_1^-$	137	$\widetilde{\chi}_3^0\widetilde{\chi}_1^-$	147	$\widetilde{\chi}_4^0\widetilde{\chi}_1^-$	157	$\widetilde{\chi}_1^+\widetilde{\chi}_1^-$	167	$\widetilde{\chi}_2^+\widetilde{\chi}_1^-$
118	$\widetilde{\chi}_1^0\widetilde{\chi}_2^-$	128	$\widetilde{\chi}_2^0\widetilde{\chi}_2^-$	138	$\widetilde{\chi}_3^0\widetilde{\chi}_2^-$	148	$\widetilde{\chi}_4^0\widetilde{\chi}_2^-$	158	$\widetilde{\chi}_1^+\widetilde{\chi}_2^-$	168	$\widetilde{\chi}_2^+\widetilde{\chi}_2^-$

Table A.8: The list of various final states.

APPENDIX B

THE DISTRIBUTIONS

The kinematic distributions for the NUHM2 model with $m_{1/2}$ from 350 GeV to 800 GeV in $1 < \mathrm{SR}\ell\ell\text{-}m_{\ell\ell} < 60$ GeV are shown in Figs. B.1 to B.10.[1] The kinematic distribution comparisons in TRUTH level using the NUHM2 samples with $m_{1/2} = 600$ GeV and the simplified Higgsino samples with $m_{\widetilde{\chi}_2^0} = 170$ GeV, $m_{\widetilde{\chi}_1^0} = 150$ GeV are shown in Figs. B.11 to B.16. The kinematic distributions of NUHM2, simplified Higgsino, and reweighted Higgsino samples in TRUTH level for all NUHM2 mass points are shown in Figs. B.17 to B.41.[2]

---

[1]The distributions for $m_{1/2} = 500$ GeV can be found in Sect. 6.2.3.
[2]The distributions for $m_{1/2} = 700$ GeV can be found in Sect. 8.2.2.
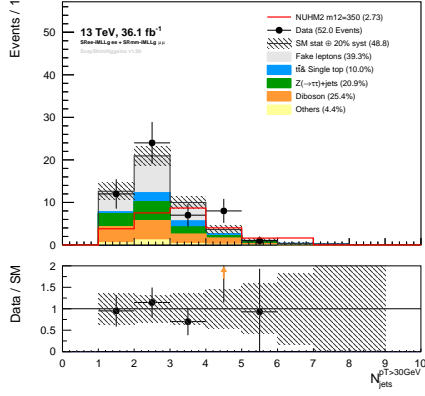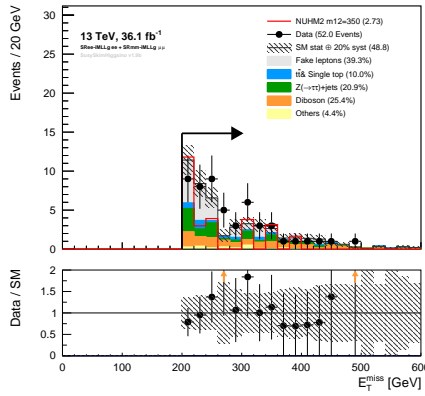
(a) N_{jets}^{30}
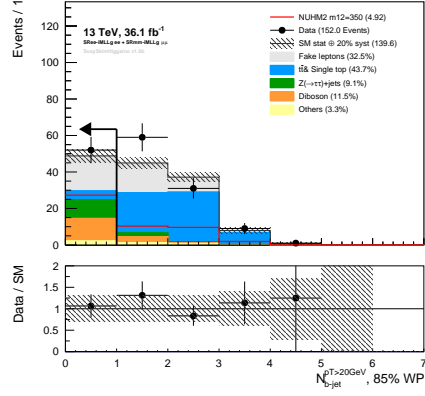
(b) $N_{\text{b-jets}}^{20}$
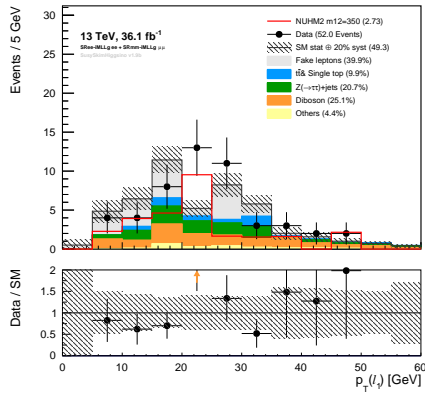
(c) $p_{\text{T}}^{\ell_1}$
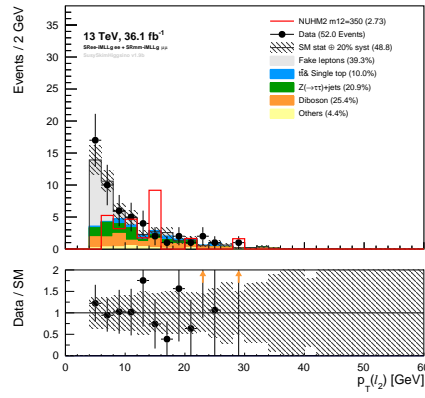
(d) $p_{\text{T}}^{\ell_2}$
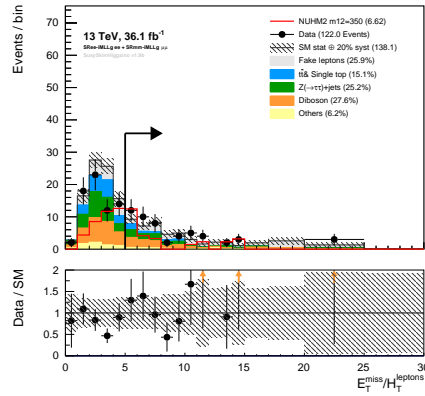
(e) $E_{\text{T}}^{\text{miss}}$

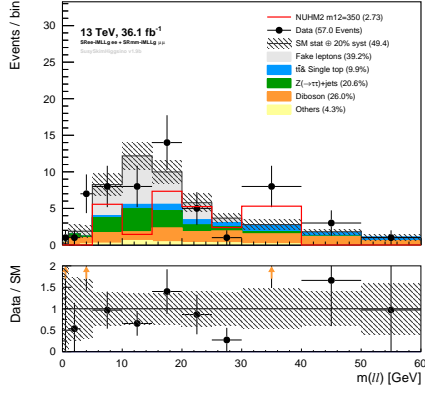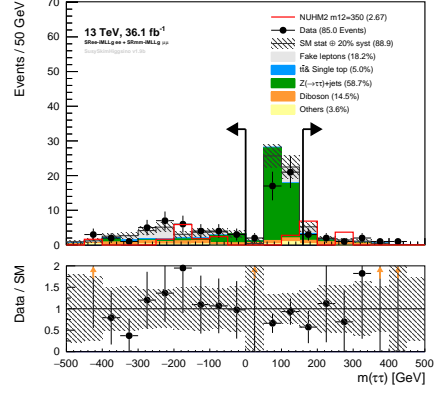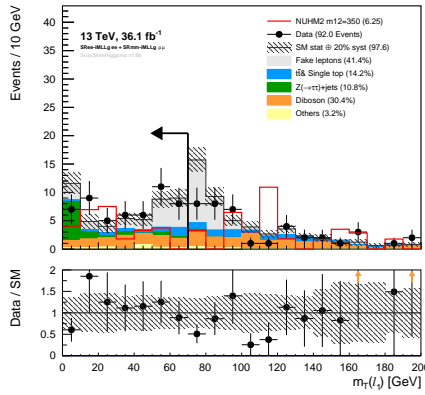**(f)** $E_{\text{T}}^{\text{miss}}/H_{\text{T}}^{\text{leptons}}$

Figure B.1: The '$N-1$' distributions for NUHM2 model with $m_{1/2} = 350$ GeV in SR region 1 <SR$\ell\ell$-$m_{\ell\ell} < 60$ GeV. The NUHM2 distributions are multiplied by 10 but the number of events in the legends are actual values.
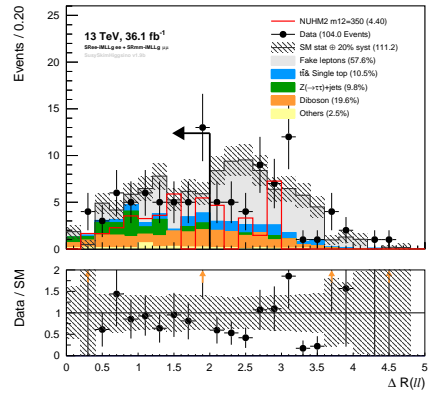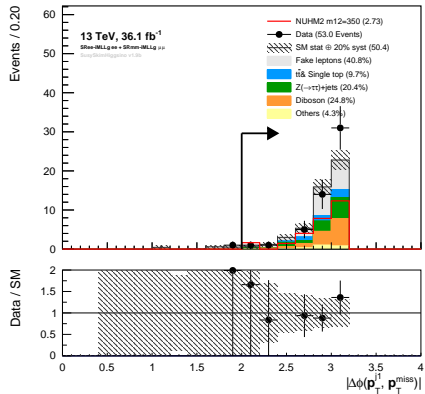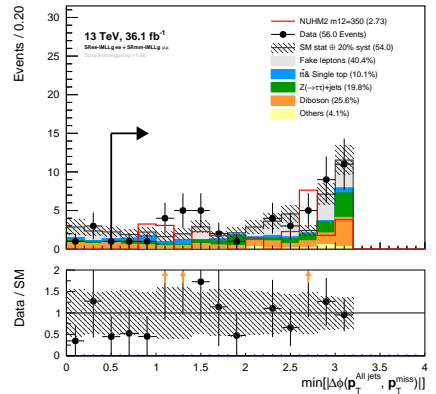
(a) $m_{\ell\ell}$

(b) $m_{\tau\tau}$
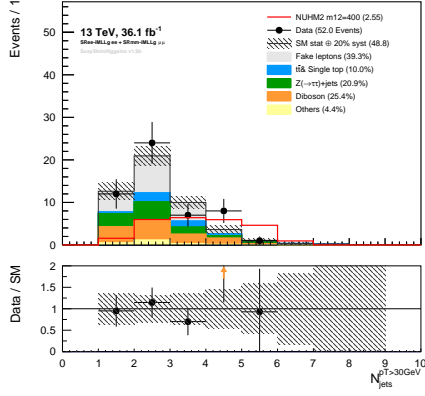
(c) $m_T(\ell_1)$

(d) $\Delta R_{\ell\ell}$

(e) $|\Delta\phi(\mathbf{p}_T^{j_1}, \mathbf{p}_T^{\mathrm{miss}})|$
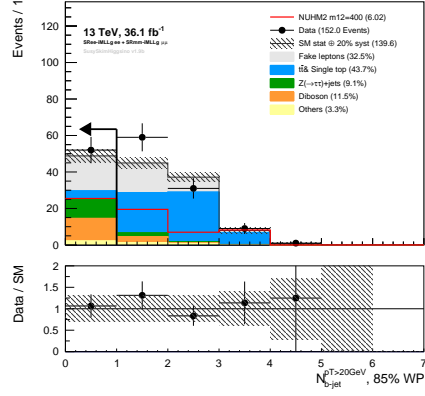
(f) $\min[|\Delta\phi(\mathbf{p}_T^{\mathrm{All\ jets}}, \mathbf{p}_T^{\mathrm{miss}})|]$

Figure B.2: The '$N-1$' distributions for NUHM2 model with $m_{1/2} = 350$ GeV in SR region 1 $<$SR$\ell\ell$-$m_{\ell\ell} < 60$ GeV. The NUHM2 distributions are multiplied by 10 but the number of events in the legends are actual values.

144

(a) N_{jets}^{30}

(b) $N_{\text{b-jets}}^{20}$

(c) $p_{\text{T}}^{\ell_1}$

(d) $p_{\text{T}}^{\ell_2}$

(e) $E_{\text{T}}^{\text{miss}}$

(f) $E_{\text{T}}^{\text{miss}}/H_{\text{T}}^{\text{leptons}}$

Figure B.3: The '$N-1$' distributions for NUHM2 model with $m_{1/2} = 400$ GeV in SR region 1 $<$SR$\ell\ell$-$m_{\ell\ell} < 60$ GeV. The NUHM2 distributions are multiplied by 10 but the number of events in the legends are actual values.

145

(a) $m_{\ell\ell}$

(b) $m_{\tau\tau}$

(c) $m_T(\ell_1)$

(d) $\Delta R_{\ell\ell}$

(e) $|\Delta\phi(\mathbf{p}_T^{j_1}, \mathbf{p}_T^{\mathrm{miss}})|$
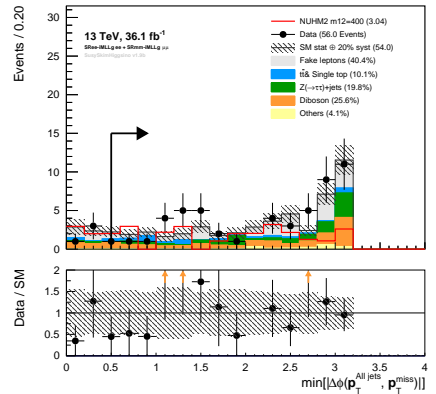
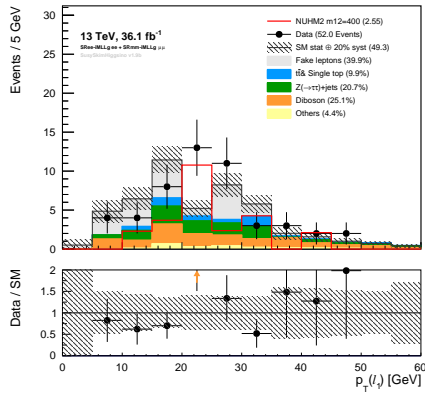**(f)** $\min[|\Delta\phi(\mathbf{p}_T^{\mathrm{All\ jets}}, \mathbf{p}_T^{\mathrm{miss}})|]$

Figure B.4: The '$N-1$' distributions for NUHM2 model with $m_{1/2} = 400$ GeV in SR region 1 <SR$\ell\ell$-$m_{\ell\ell}$ < 60 GeV. The NUHM2 distributions are multiplied by 10 but the number of events in the legends are actual values.
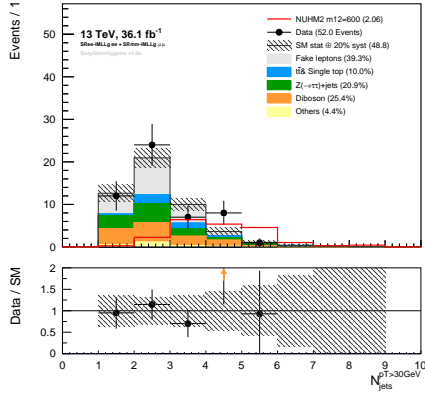
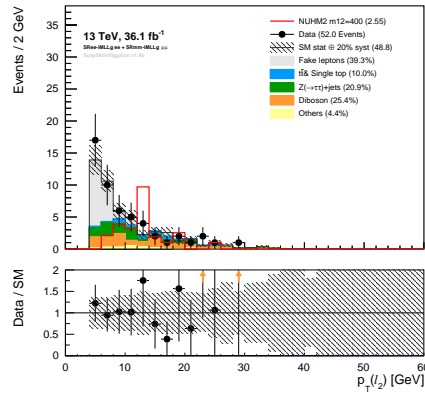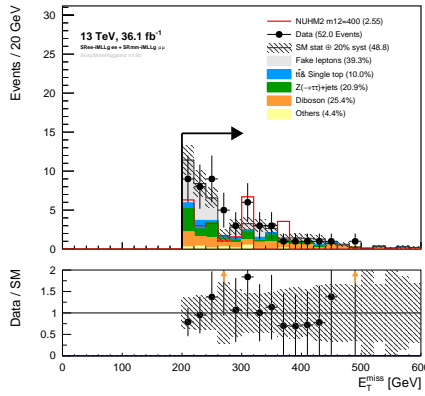**(a)** N_{jets}^{30}

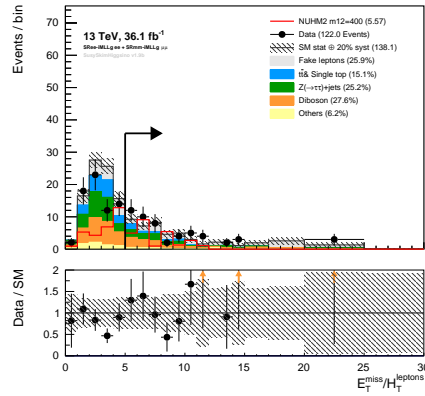**(b)** $N_{\text{b-jets}}^{20}$

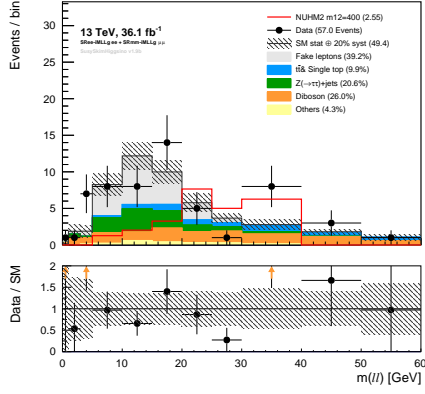**(c)** $p_T^{\ell_1}$
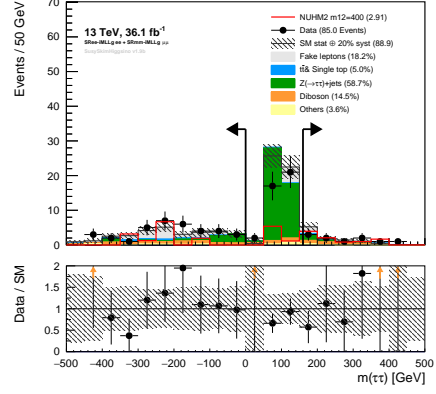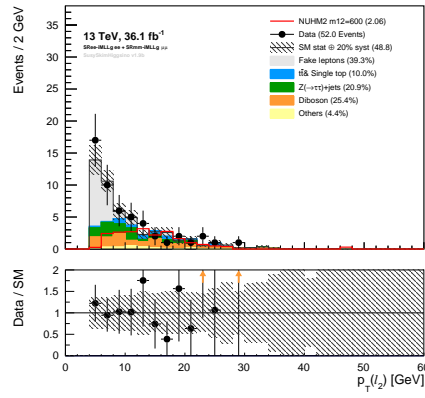
(d) $p_T^{\ell_2}$
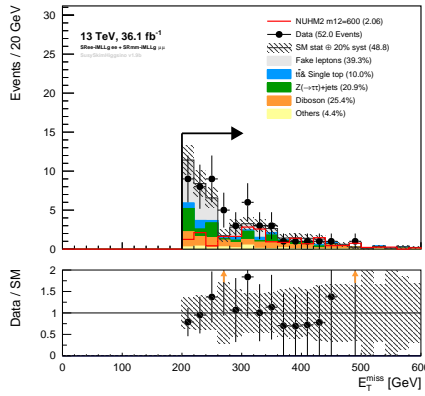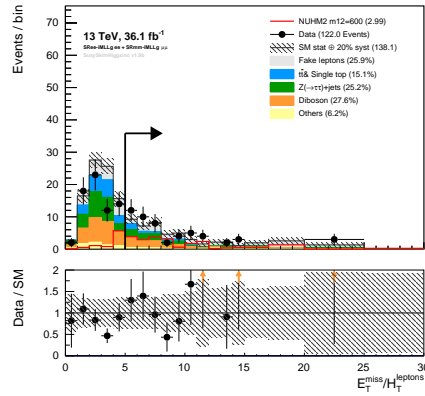
(e) E_T^{miss}

(f) $E_T^{\text{miss}}/H_T^{\text{leptons}}$

Figure B.5: The '$N-1$' distributions for NUHM2 model with $m_{1/2} = 600$ GeV in SR region $1 <$SR$\ell\ell$-$m_{\ell\ell} < 60$ GeV. The NUHM2 distributions are multiplied by 10 but the number of events in the legends are actual values.

(a) $m_{\ell\ell}$

(b) $m_{\tau\tau}$

(c) $m_T(\ell_1)$

(d) $\Delta R_{\ell\ell}$
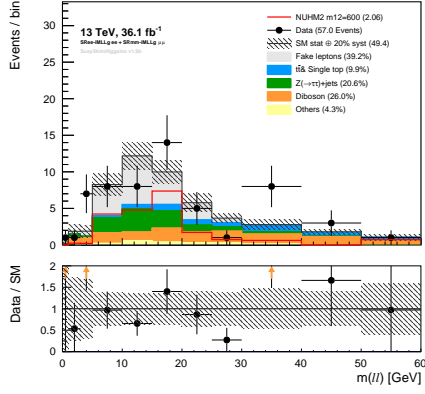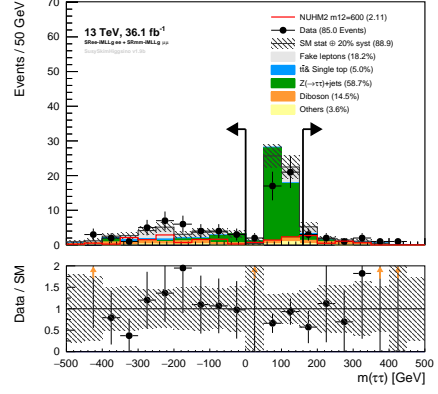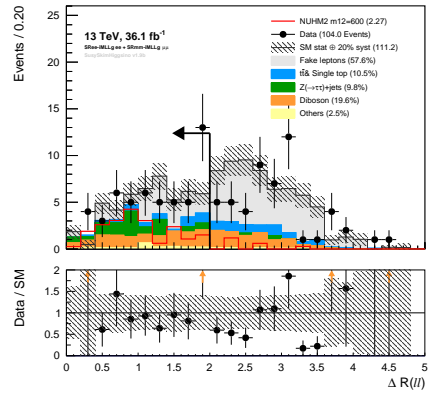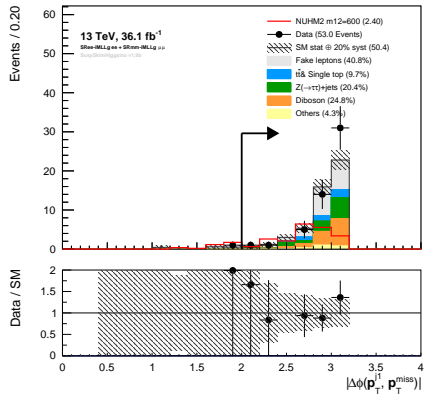
(e) $|\Delta\phi(\mathbf{p}_T^{j_1}, \mathbf{p}_T^{\text{miss}})|$
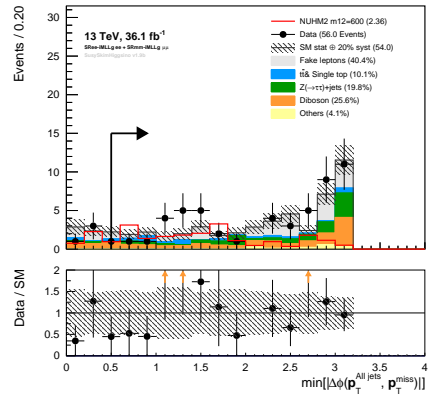
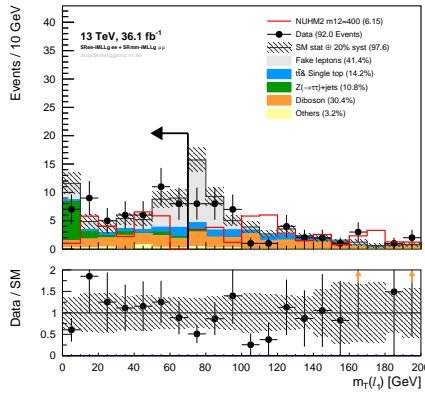**(f)** $\min[|\Delta\phi(\mathbf{p}_T^{\text{All jets}}, \mathbf{p}_T^{\text{miss}})|]$

Figure B.6: The '$N-1$' distributions for NUHM2 model with $m_{1/2} = 600$ GeV in SR region $1 <$SR$\ell\ell$-$m_{\ell\ell} < 60$ GeV. The NUHM2 distributions are multiplied by 10 but the number of events in the legends are actual values.
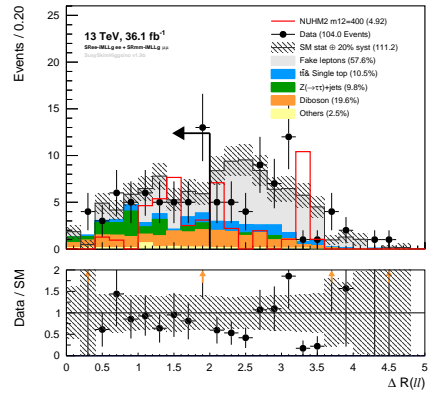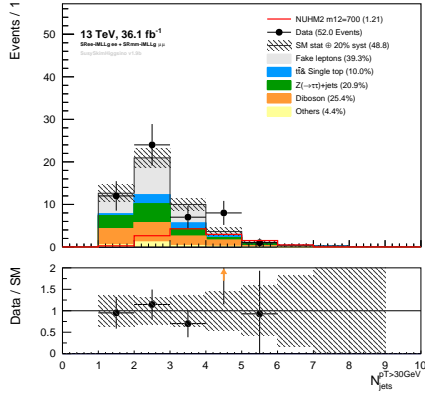
(a) N_{jets}^{30}
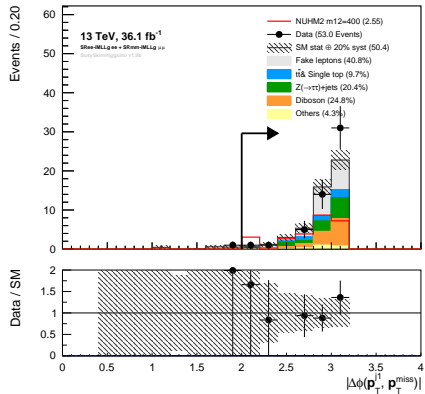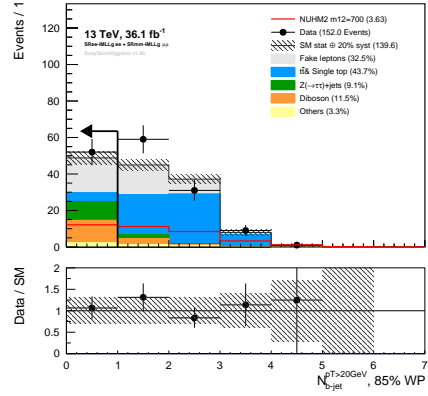
(b) $N_{\text{b-jets}}^{20}$
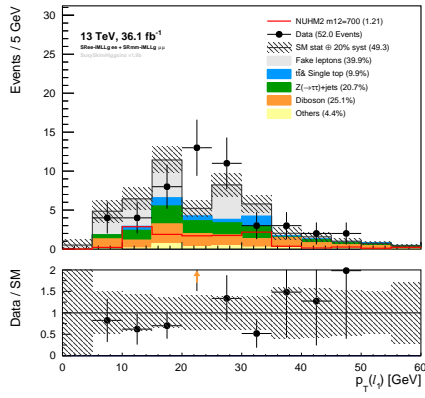
(c) $p_T^{\ell_1}$
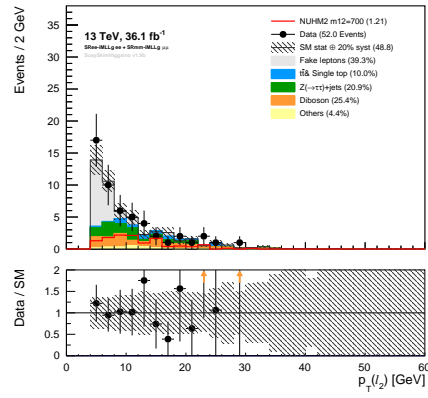
(d) $p_T^{\ell_2}$
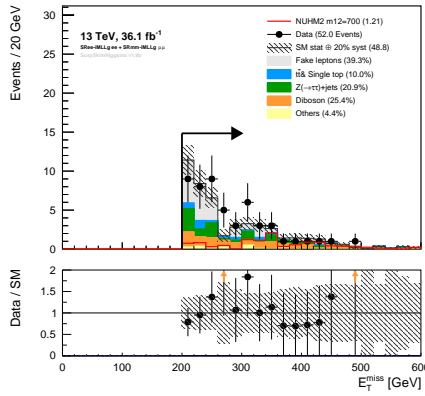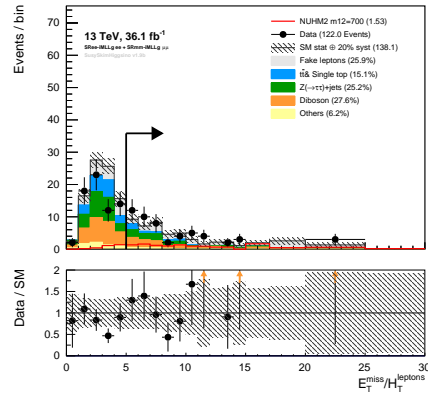
(e) E_T^{miss}

(f) $E_T^{\text{miss}}/H_T^{\text{leptons}}$

Figure B.7: The '$N-1$' distributions for NUHM2 model with $m_{1/2} = 700$ GeV in SR region 1 $<$SR$\ell\ell$-$m_{\ell\ell} < 60$ GeV. The NUHM2 distributions are multiplied by 10 but the number of events in the legends are actual values.

149

(a) $m_{\ell\ell}$

(b) $m_{\tau\tau}$

(c) $m_T(\ell_1)$

(d) $\Delta R_{\ell\ell}$
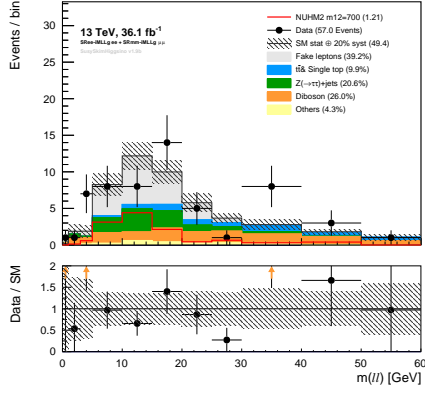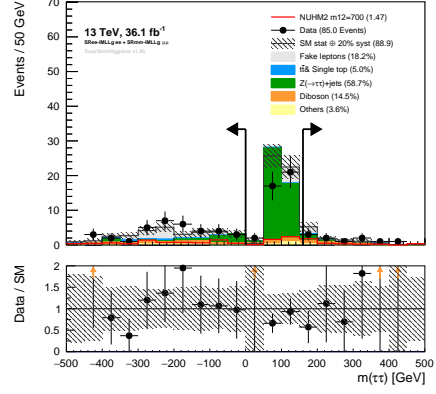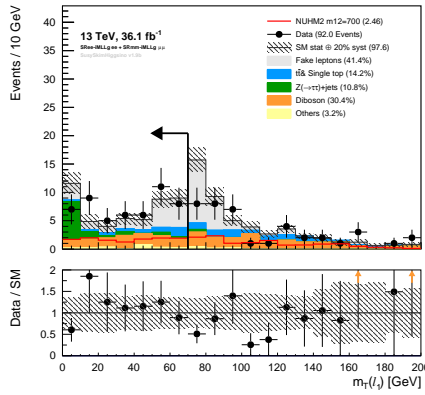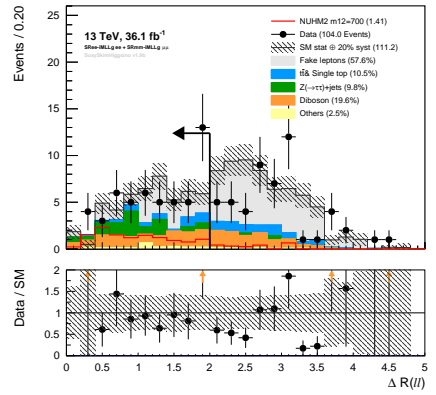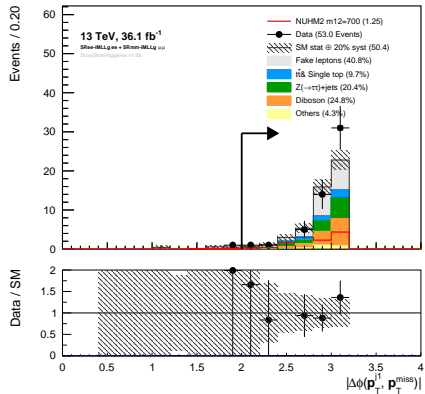
(e) $|\Delta\phi(\mathbf{p}_T^{j_1}, \mathbf{p}_T^{\mathrm{miss}})|$
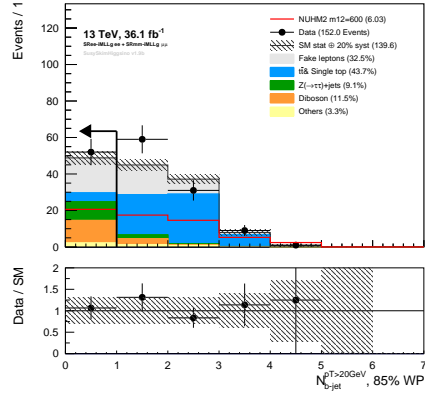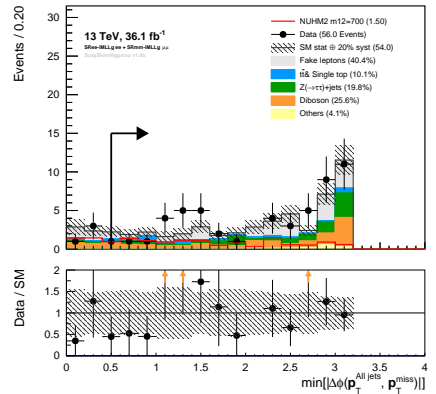
(f) $\min[|\Delta\phi(\mathbf{p}_T^{\mathrm{All\ jets}}, \mathbf{p}_T^{\mathrm{miss}})|]$
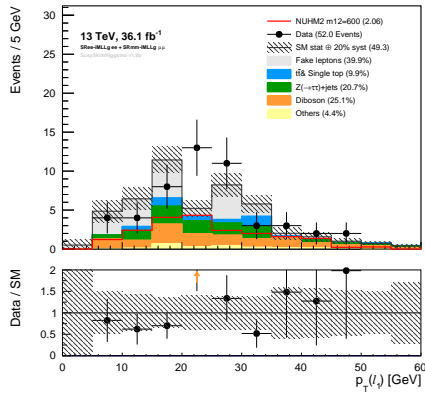
Figure B.8: The '$N-1$' distributions for NUHM2 model with $m_{1/2} = 700$ GeV in SR region 1 $<$SR$\ell\ell$-$m_{\ell\ell} < 60$ GeV. The NUHM2 distributions are multiplied by 10 but the number of events in the legends are actual values.
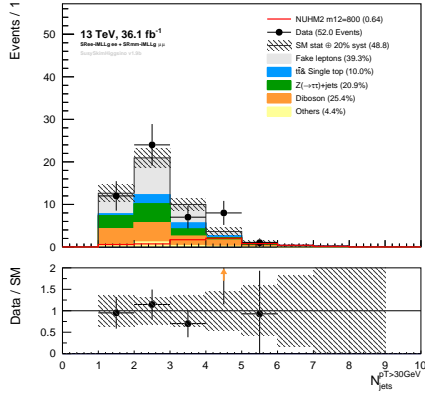
(a) N_{jets}^{30}
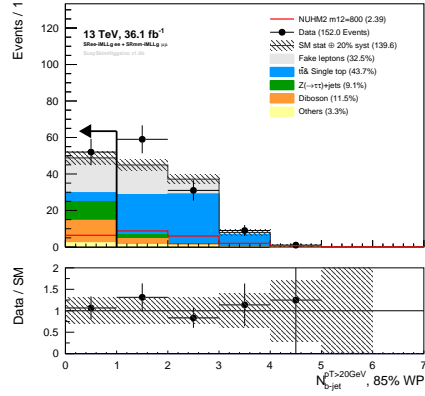
(b) $N_{\mathrm{b-jets}}^{20}$
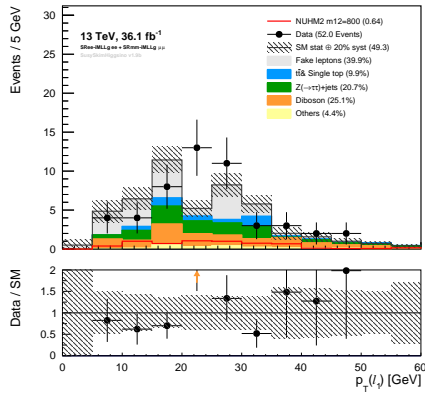
(c) $p_{\mathrm{T}}^{\ell_1}$
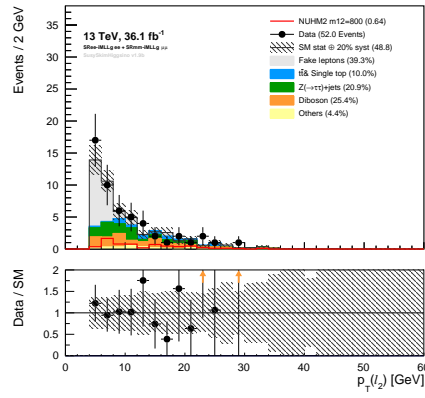
(d) $p_{\mathrm{T}}^{\ell_2}$
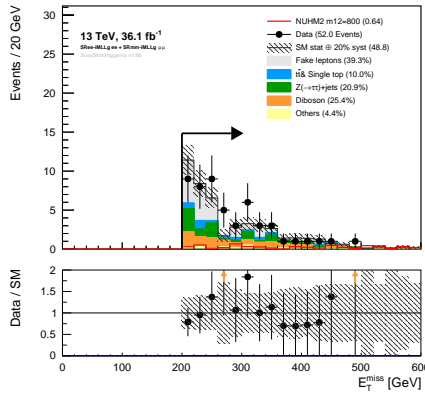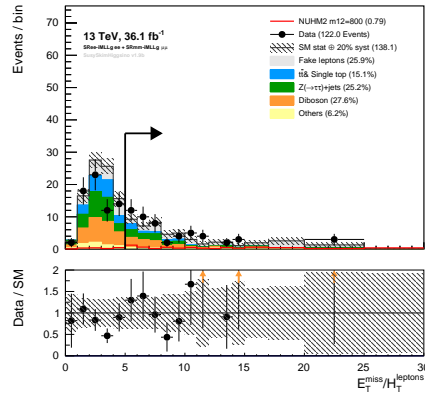
(e) $E_{\mathrm{T}}^{\mathrm{miss}}$

(f) $E_{\mathrm{T}}^{\mathrm{miss}}/H_{\mathrm{T}}^{\mathrm{leptons}}$

Figure B.9: The '$N-1$' distributions for NUHM2 model with $m_{1/2} = 800$ GeV in SR region 1 $<$SR$\ell\ell$-$m_{\ell\ell} < 60$ GeV. The NUHM2 distributions are multiplied by 10 but the number of events in the legends are actual values.

(a) $m_{\ell\ell}$

(b) $m_{\tau\tau}$

(c) $m_T(\ell_1)$

(d) $\Delta R_{\ell\ell}$
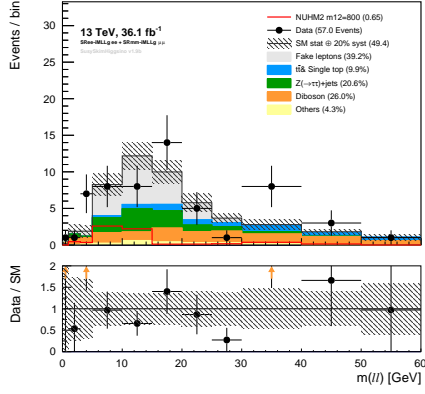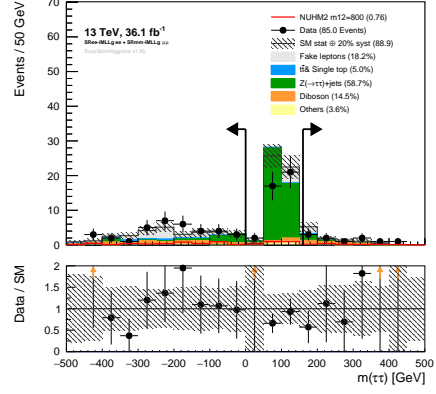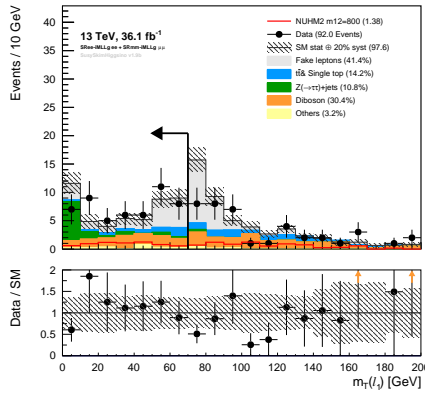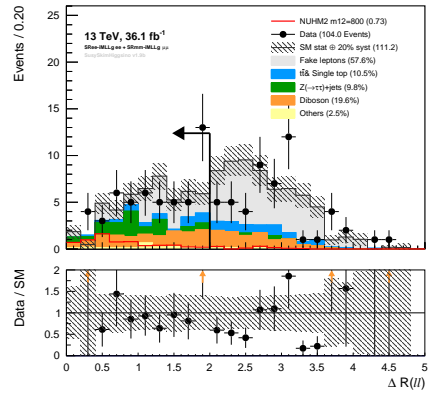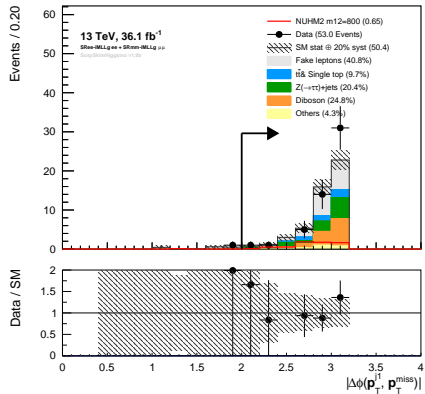
(e) $|\Delta\phi(\mathbf{p}_T^{j_1}, \mathbf{p}_T^{\mathrm{miss}})|$
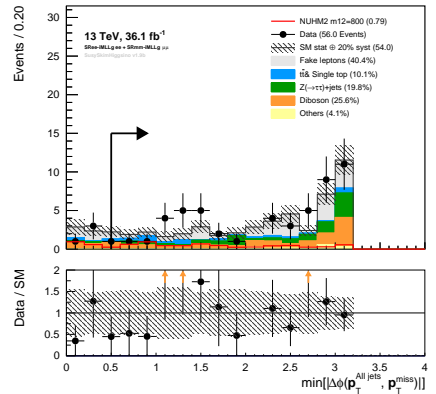
(f) $\min[|\Delta\phi(\mathbf{p}_T^{\mathrm{All\ jets}}, \mathbf{p}_T^{\mathrm{miss}})|]$
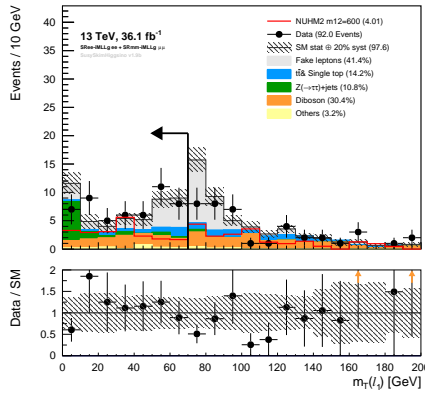
Figure B.10: The '$N-1$' distributions for NUHM2 model with $m_{1/2} = 800$ GeV in SR region $1 <$SR$\ell\ell$-$m_{\ell\ell} < 60$ GeV. The NUHM2 distributions are multiplied by 10 but the number of events in the legends are actual values.
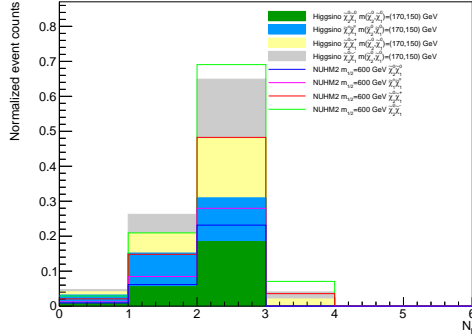
**(a)** Baseline leptons multiplicities
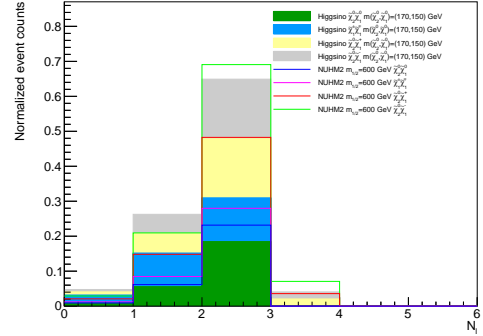
(b) Signal leptons multiplicities
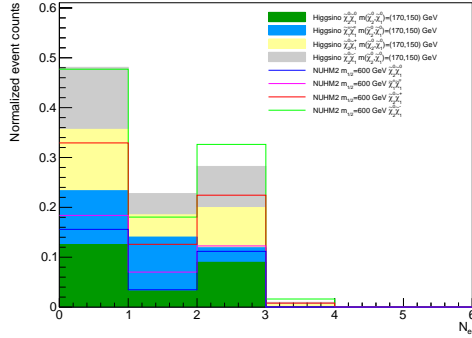
(c) Signal electrons multiplicities
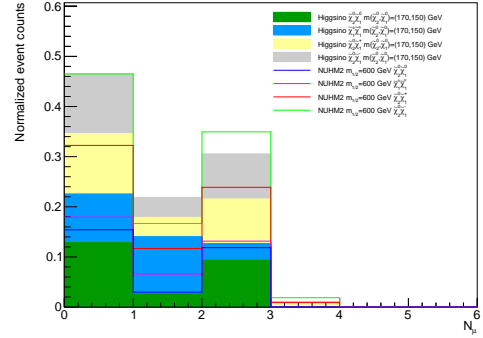
(d) Signal muons multiplicities

Figure B.11: The lepton multiplicity distributions. The lepton multiplicity of NUHM2 with $m_{1/2} = 600$ GeV are compared to the simplified Higgsino model with $m_{\widetilde{\chi}_2^0} = 170$ GeV and $m_{\widetilde{\chi}_1^0} = 150$ GeV. Four different production channels, $\widetilde{\chi}_2^0\widetilde{\chi}_1^0$, $\widetilde{\chi}_2^0\widetilde{\chi}_1^+$, $\widetilde{\chi}_2^0\widetilde{\chi}_1^-$, and $\widetilde{\chi}_1^\pm\widetilde{\chi}_1^\mp$, for the NUHM2 and the simplified Higgsino model are considered. The distributions of four productions are combined and normalized to equal area.
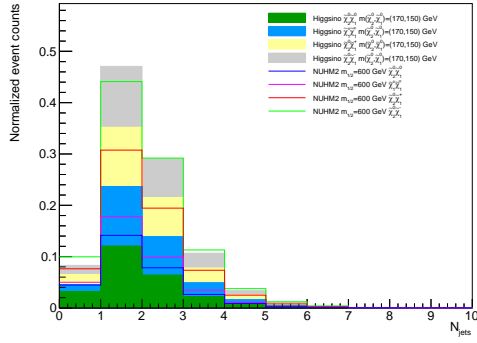
(a) Jets multiplicity
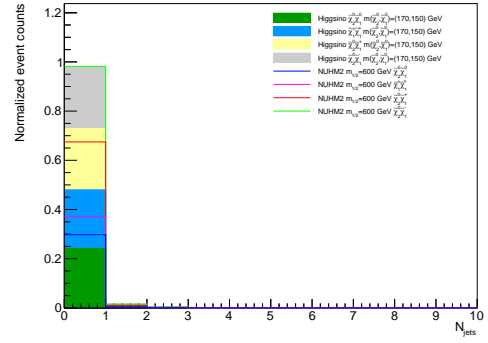
(b) b-jets multiplicity
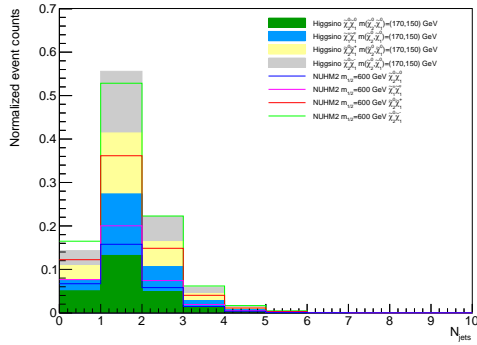
(c) Signal jets multiplicity with $p_{\mathrm{T}} >$ 25 GeV
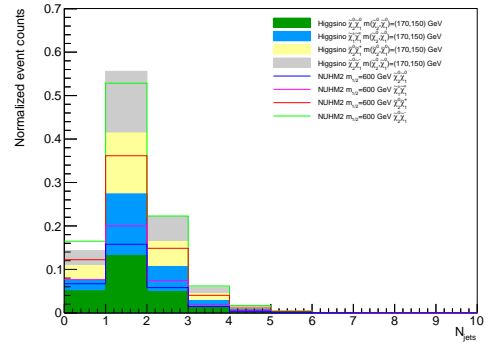
(d) Signal jets multiplicity with $p_{\mathrm{T}} >$ 30 GeV

Figure B.12: The jets multiplicity distributions. The jet multiplicity of NUHM2 with $m_{1/2} = 600$ GeV are compared to the simplified Higgsino model with $m_{\tilde{\chi}_2^0} = 170$ GeV and $m_{\tilde{\chi}_1^0} = 150$ GeV. The top left plot includes the forward jets and the bottom two plots use the signal jets with $p_{\mathrm{T}} > 25$ GeV and $p_{\mathrm{T}} > 30$ GeV, respectively. Four different production channels, $\tilde{\chi}_2^0\tilde{\chi}_1^0$, $\tilde{\chi}_2^0\tilde{\chi}_1^+$, $\tilde{\chi}_2^0\tilde{\chi}_1^-$, and $\tilde{\chi}_1^{\pm}\tilde{\chi}_1^{\mp}$, for the NUHM2 and the simplified Higgsino model are considered. The distributions of four productions are combined and normalized to equal area.
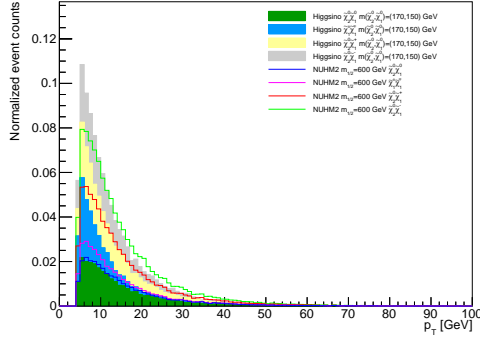
(a) Signal electrons p_{T}
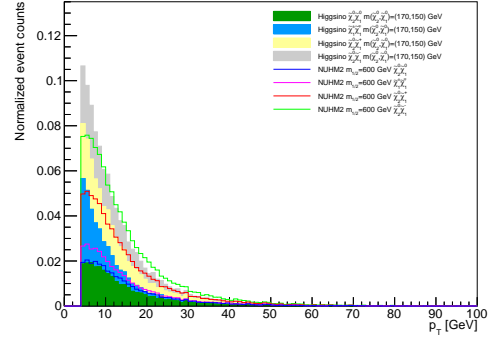
(b) Signal muons p_{T}
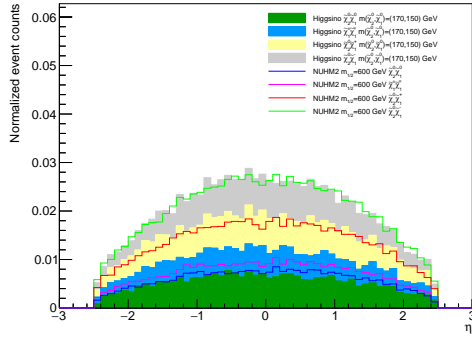
(c) Signal electrons η
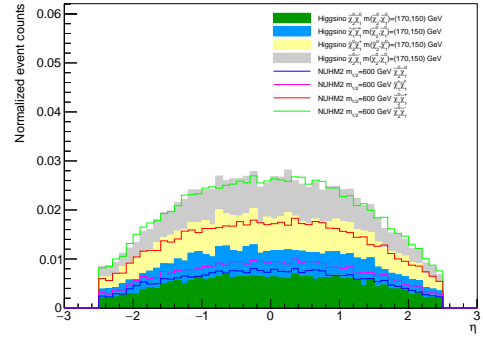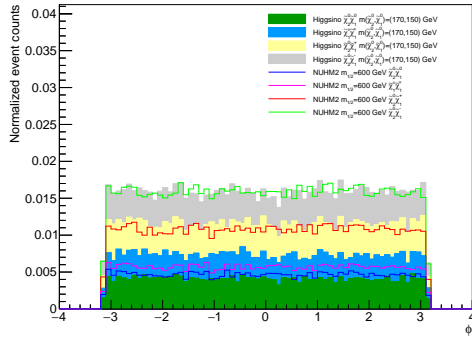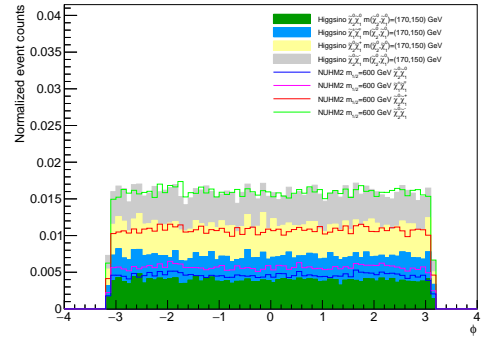
(d) Signal muons η

(e) Signal electrons ϕ

(f) Signal muons ϕ

Figure B.13: The p_{T}, η, and ϕ distributions for the NUHM2 with $m_{1/2} = 600$ GeV and the simplified Higgsino model with $m_{\widetilde{\chi}_2^0} = 170$ GeV and $m_{\widetilde{\chi}_1^0} = 150$ GeV. The signal electrons p_{T}, η, and ϕ distributions are on the left column and the signal muons distributions are on the right. Four different production channels, $\widetilde{\chi}_2^0 \widetilde{\chi}_1^0$, $\widetilde{\chi}_2^0 \widetilde{\chi}_1^+$, $\widetilde{\chi}_2^0 \widetilde{\chi}_1^-$, and $\widetilde{\chi}_1^{\pm} \widetilde{\chi}_1^{\mp}$, for the NUHM2 and the simplified Higgsino model are considered. The distributions of four productions are combined and normalized to equal area.

155
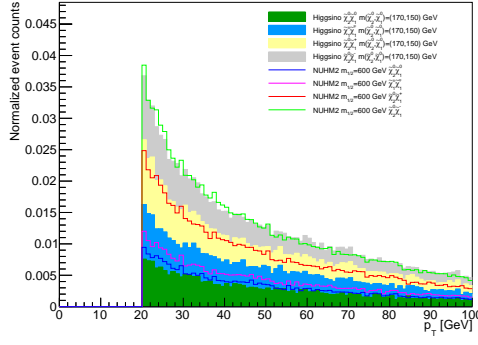
(a) The signal jets p_T.
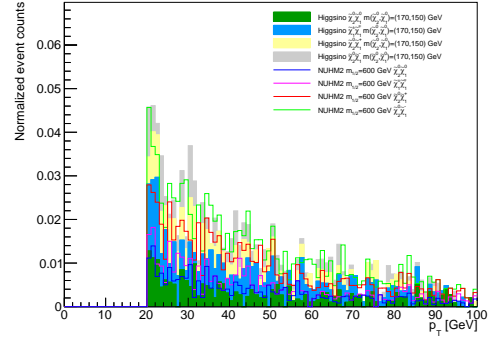
(b) The signal b-jets p_T.
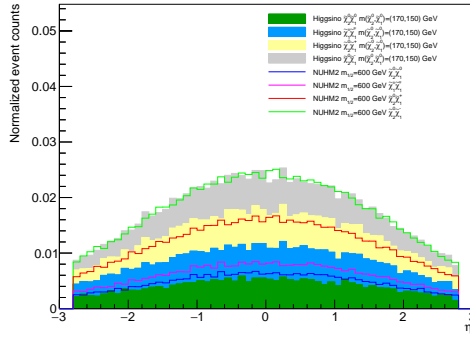
(c) The signal jets η.
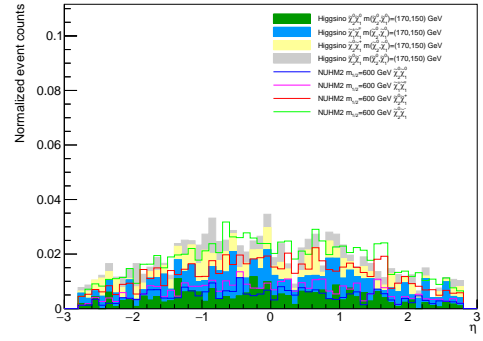
(d) The signal b-jets η.
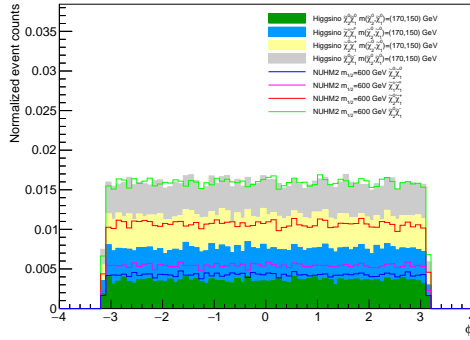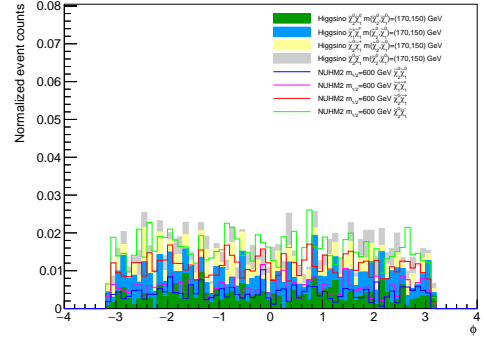
(e) The signal jets ϕ.

(f) The signal b-jets ϕ.

Figure B.14: The signal jets and the signal b-jets p_T, η, and ϕ distributions for the NUHM2 with $m_{1/2} = 600$ GeV and the simplified Higgsino model with $m_{\widetilde{\chi}_2^0} = 170$ GeV and $m_{\widetilde{\chi}_1^0} = 150$ GeV. Four different production channels, $\widetilde{\chi}_2^0\widetilde{\chi}_1^0$, $\widetilde{\chi}_2^0\widetilde{\chi}_1^+$, $\widetilde{\chi}_2^0\widetilde{\chi}_1^-$, and $\widetilde{\chi}_1^\pm\widetilde{\chi}_1^\mp$, for the NUHM2 and the simplified Higgsino model are considered. The distributions of four productions are combined and normalized to equal area.

(a) $m_{\ell\ell}$

(b) $m_{\tau\tau}$

(c) m_T
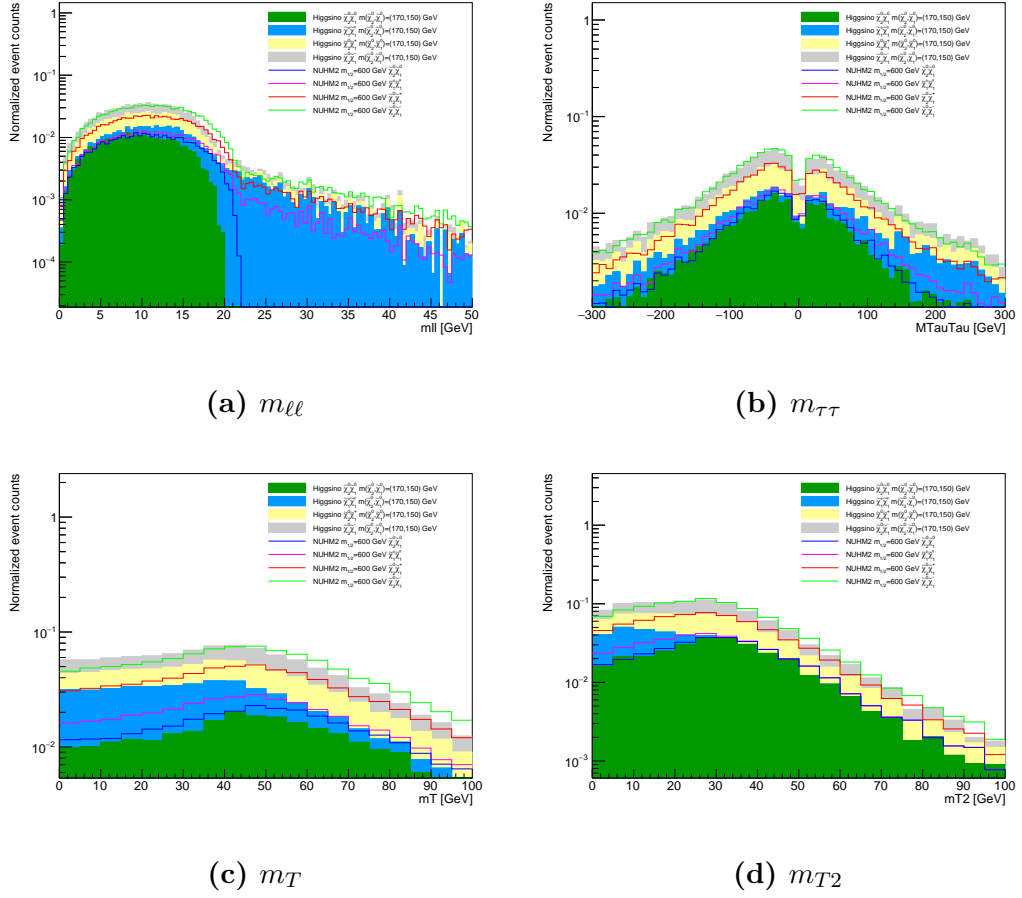
(d) m_{T2}

Figure B.15: The invariant mass $m_{\ell\ell}$ and $m_{\tau\tau}$ distributions and the transverse mass m_{T} and m_{T2} distributions. The first two leading baseline leptons are used to calculate the $m_{\ell\ell}$ which contains a hump and a tail region. The $\widetilde{\chi}_2^0\widetilde{\chi}_1^0$ contributes to the hump only and the tail is contributed by the decay products containing the chargino $\widetilde{\chi}_1^\pm$. The Eq. (6.6) is used to calculate the di-tau invariant mass $m_{\tau\tau}$. The first or first two leading signal leptons and $E_{\mathrm{T}}^{\mathrm{miss}}$ are used to evaluate the transverse mass m_{T} and m_{T2}, respectively. Four different production channels, $\widetilde{\chi}_2^0\widetilde{\chi}_1^0$, $\widetilde{\chi}_2^0\widetilde{\chi}_1^+$, $\widetilde{\chi}_2^0\widetilde{\chi}_1^-$, and $\widetilde{\chi}_1^\pm\widetilde{\chi}_1^\mp$, for the NUHM2 and the simplified Higgsino model are considered. The distributions of four productions are combined and normalized to equal area.
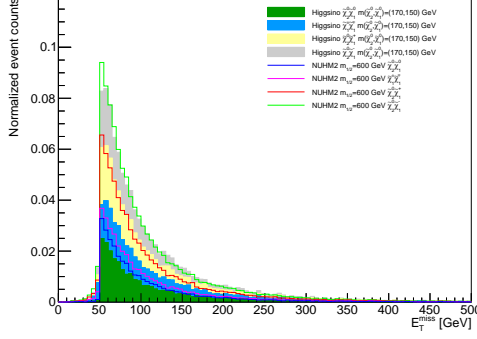
(a) $E_{\mathrm{T}}^{\mathrm{miss}}$
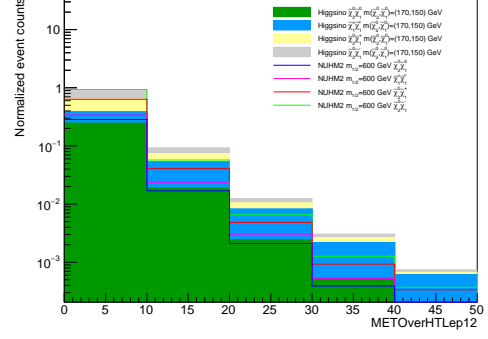
(b) $E_{\mathrm{T}}^{\mathrm{miss}}/H_{\mathrm{T}}^{\mathrm{lepton}}$
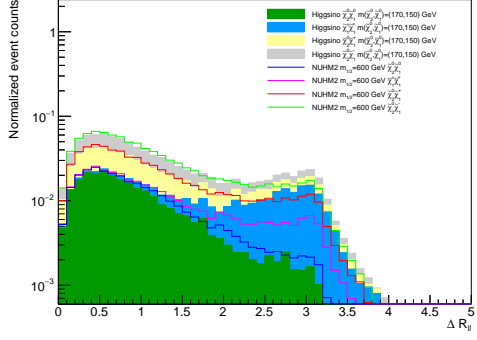
(c) $\Delta R(\ell_1, \ell_2)$
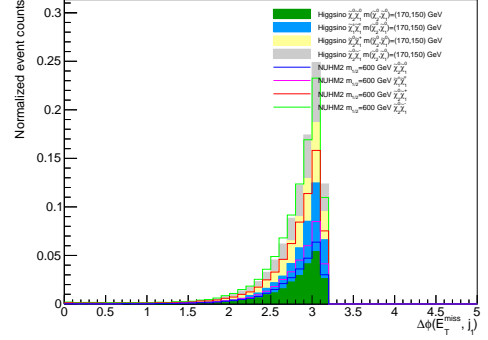
(d) $\Delta\phi(E_{\mathrm{T}}^{\mathrm{miss}}, j_1)$

Figure B.16: The $E_{\mathrm{T}}^{\mathrm{miss}}$, $E_{\mathrm{T}}^{\mathrm{miss}}/H_{\mathrm{T}}^{\mathrm{lepton}}$, $\Delta R(\ell_1, \ell_2)$, and $\Delta\phi(E_{\mathrm{T}}^{\mathrm{miss}}, j_1)$ distributions. The $H_{\mathrm{T}}^{\mathrm{lepton}}$ is the scalar sum of the first two leading baseline leptons p_{T} only. The distance $\Delta R(\ell_1, \ell_2)$ is calculated by the first two leading baseline leptons and the $\Delta\phi(E_{\mathrm{T}}^{\mathrm{miss}}, j_1)$ uses $E_{\mathrm{T}}^{\mathrm{miss}}$ and first leading signal jet. Four different production channels, $\widetilde{\chi}_2^0\widetilde{\chi}_1^0$, $\widetilde{\chi}_2^0\widetilde{\chi}_1^+$, $\widetilde{\chi}_2^0\widetilde{\chi}_1^-$, and $\widetilde{\chi}_1^\pm\widetilde{\chi}_1^\mp$, for the NUHM2 and the simplified Higgsino model are considered. The distributions of four productions are combined and normalized to equal area.
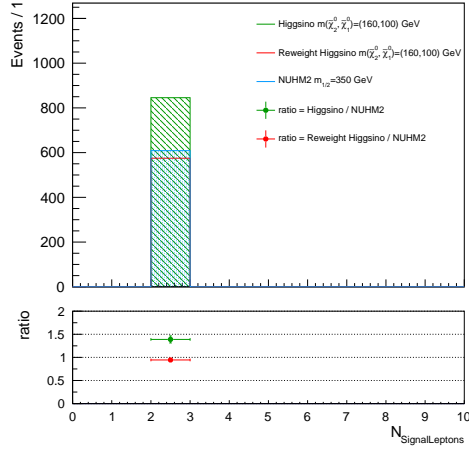
(a) Signal lepton multiplicity
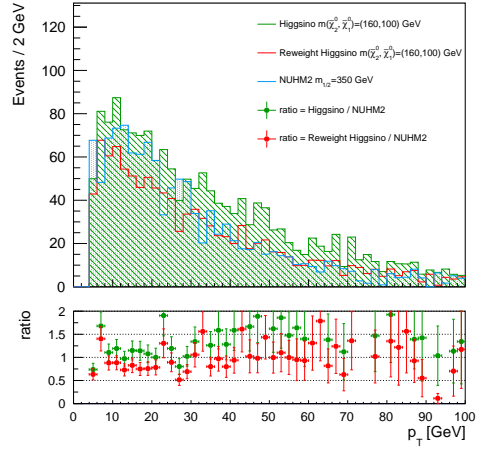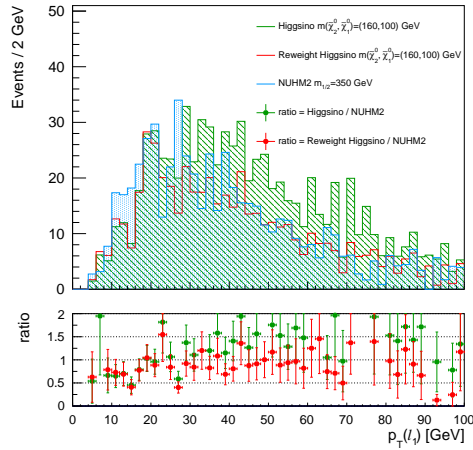
(b) Signal lepton p_T
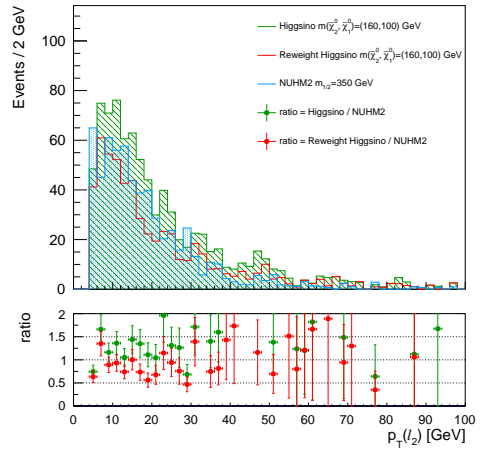
(c) Leading lepton p_T

(d) Subleading lepton p_T

Figure B.17: The distributions for signal lepton multiplicity, all signal leptons p_T, the leading lepton p_T, and the subleading lepton p_T. The NUHM2 signal sample uses $m_{1/2} = 350$ GeV and the Higgsino signal sample uses $m_{\tilde{\chi}_2^0} = 160$ and $m_{\tilde{\chi}_1^0} = 100$ GeV. The reweighted Higgsino sample is shown in red line. The lower pad shows the ratio between NUHM2 and Higgsino (or reweighted Higgsino) distributions.
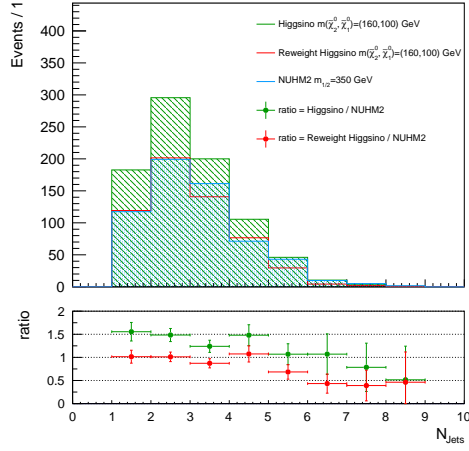
(a) Jet multiplicity
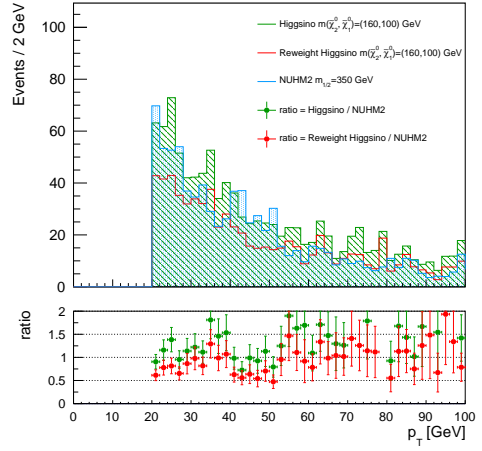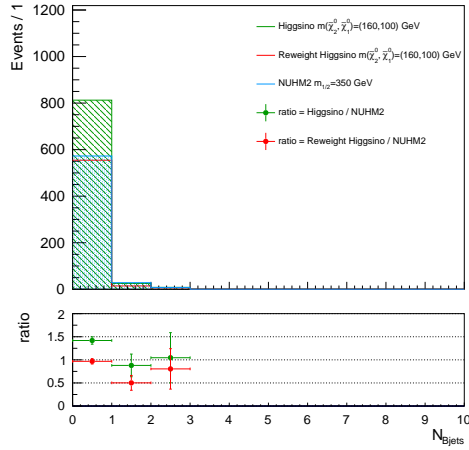
(b) Jet p_T

(c) b-jets multiplicity
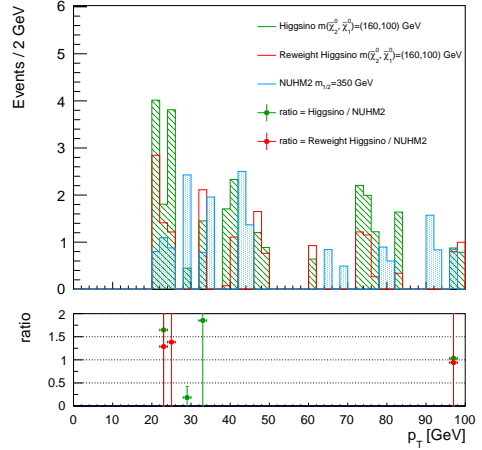
(d) b-jets p_T

Figure B.18: The distributions for jet multiplicity, jet p_T, b-jets multiplicity, and b-jet p_T. The NUHM2 signal sample uses $m_{1/2} = 350$ GeV and the Higgsino signal sample uses $m_{\tilde{\chi}_2^0} = 160$ and $m_{\tilde{\chi}_1^0} = 100$ GeV. The reweighted Higgsino sample is shown in red line. The lower pad shows the ratio between NUHM2 and Higgsino (or reweighted Higgsino) distributions.

(a) $E_{\mathrm{T}}^{\mathrm{miss}}$

(b) $E_{\mathrm{T}}^{\mathrm{miss}}/H_{\mathrm{T}}^{\mathrm{leptons}}$

(c) $m_{\ell\ell}$

(d) $m_{\tau\tau}$
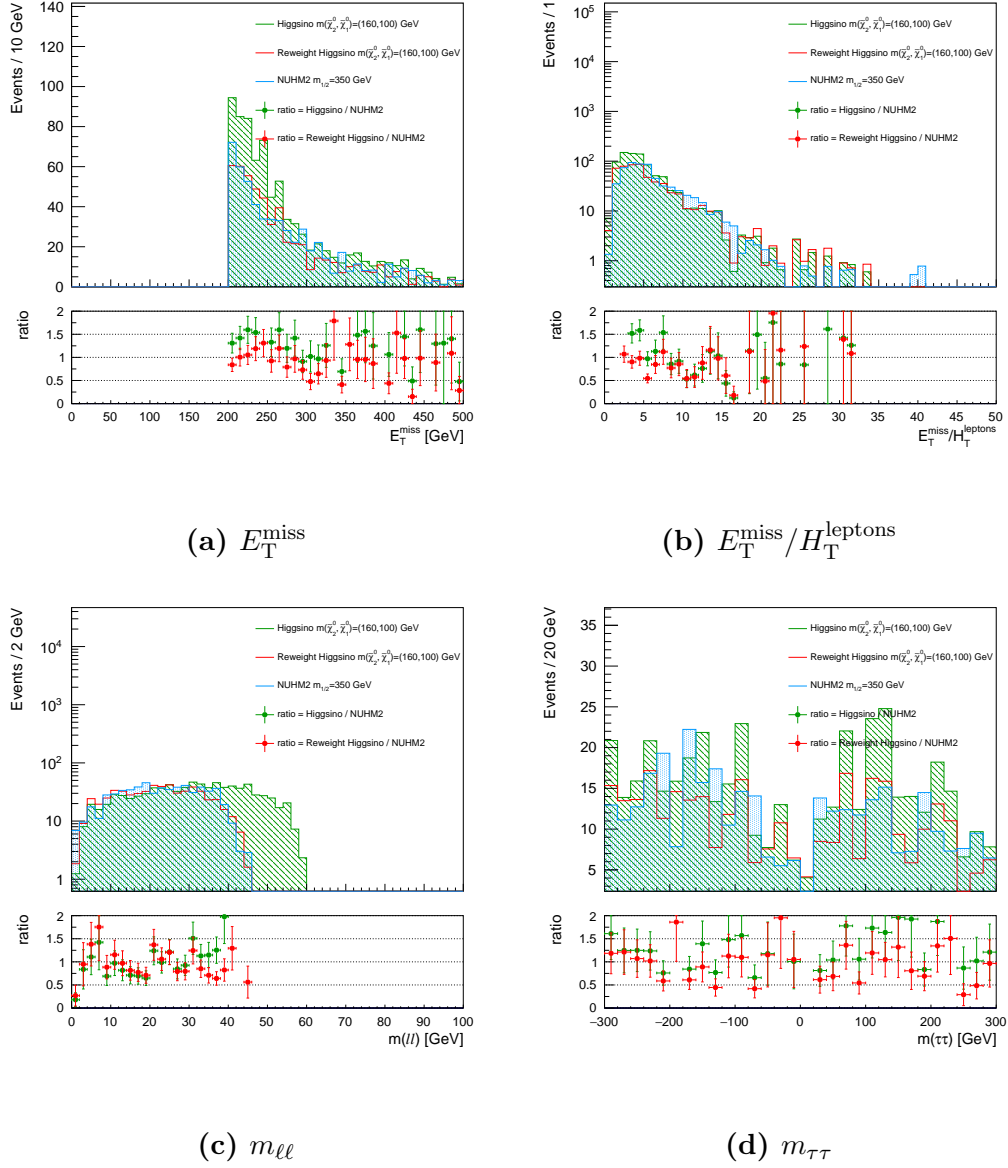
Figure B.19: The distributions for $E_{\mathrm{T}}^{\mathrm{miss}}$, $E_{\mathrm{T}}^{\mathrm{miss}}/H_{\mathrm{T}}^{\mathrm{leptons}}$, $m_{\ell\ell}$, and $m_{\tau\tau}$. The NUHM2 signal sample uses $m_{1/2} = 350$ GeV and the Higgsino signal sample uses $m_{\widetilde{\chi}_2^0} = 160$ and $m_{\widetilde{\chi}_1^0} = 100$ GeV. The reweighted Higgsino sample is shown in red line. The lower pad shows the ratio between NUHM2 and Higgsino (or reweighted Higgsino) distributions.

161

(a) m_{T}

(b) m_{T2}
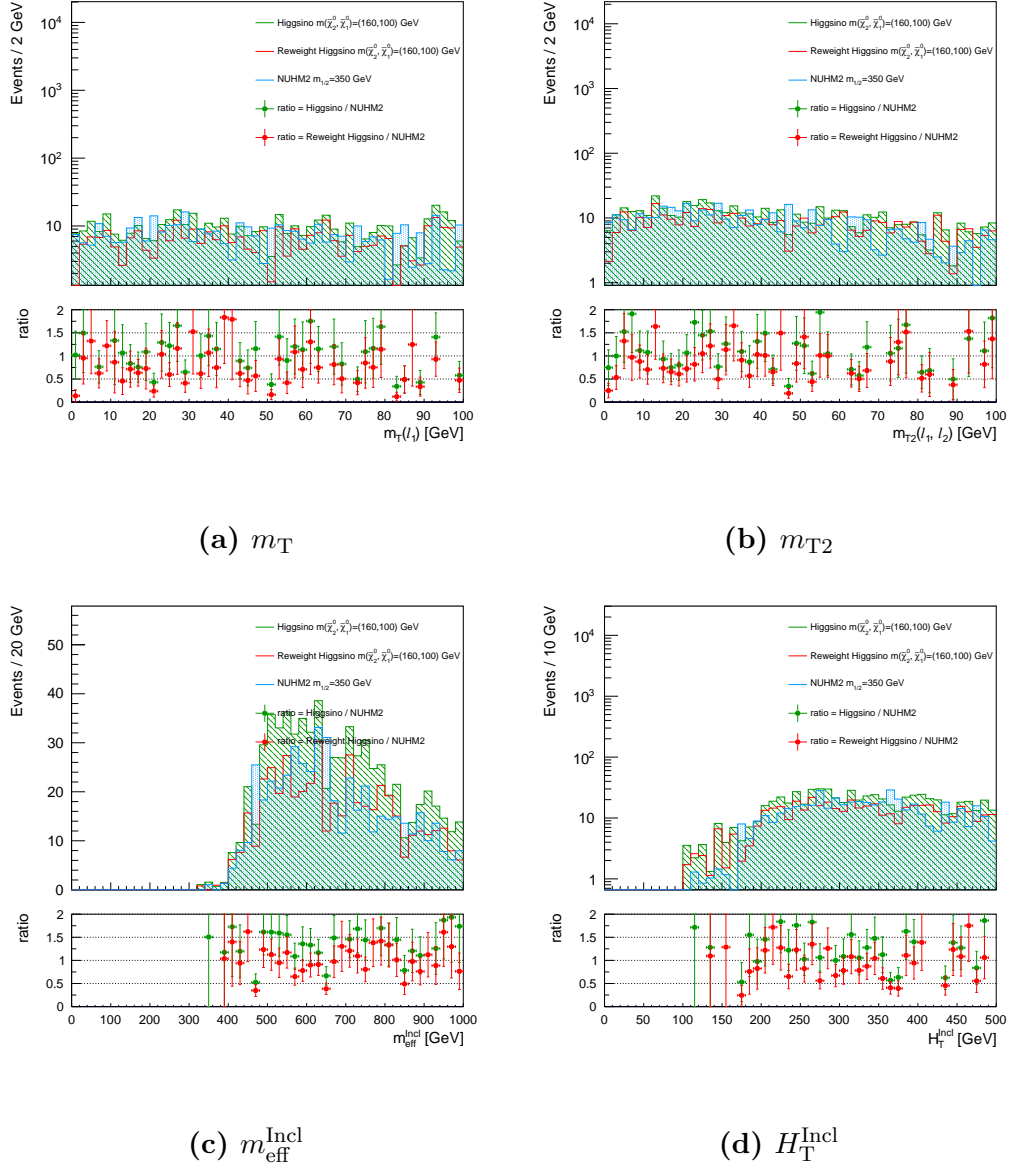
(c) $m_{\mathrm{eff}}^{\mathrm{Incl}}$

(d) $H_{\mathrm{T}}^{\mathrm{Incl}}$

Figure B.20: The distributions for m_{T}, m_{T2}, $m_{\mathrm{eff}}^{\mathrm{Incl}}$, $H_{\mathrm{T}}^{\mathrm{Incl}}$. The NUHM2 signal sample uses $m_{1/2} = 350$ GeV and the Higgsino signal sample uses $m_{\widetilde{\chi}_2^0} = 160$ and $m_{\widetilde{\chi}_1^0} = 100$ GeV. The reweighted Higgsino sample is shown in red line. The lower pad shows the ratio between NUHM2 and Higgsino (or reweighted Higgsino) distributions.

(a) $\Delta R_{\ell\ell}$ **(b)** $\Delta\phi(\mathbf{p}_T^{j1}, \mathbf{p}_T^{miss})$

Figure B.21: The distributions for $\Delta R_{\ell\ell}$ and $\Delta\phi(\mathbf{p}_T^{j1}, \mathbf{p}_T^{miss})$. The NUHM2 signal sample uses $m_{1/2} = 350$ GeV and the Higgsino signal sample uses $m_{\widetilde{\chi}_2^0} = 160$ and $m_{\widetilde{\chi}_1^0} = 100$ GeV. The reweighted Higgsino sample is shown in red line. The lower pad shows the ratio between NUHM2 and Higgsino (or reweighted Higgsino) distributions.

(a) Signal lepton multiplicity
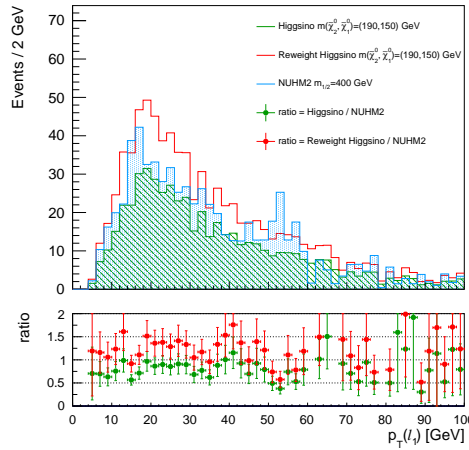
(b) Signal lepton p_T
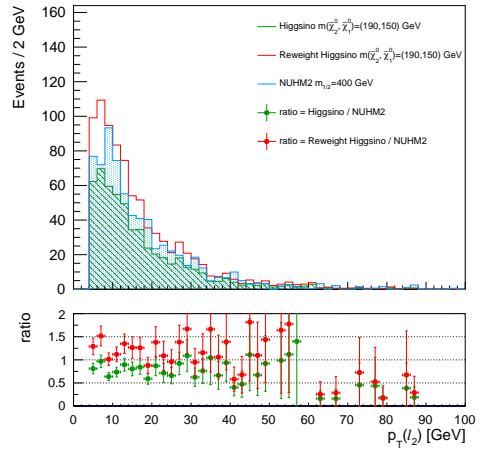
(c) Leading lepton p_T

(d) Subleading lepton p_T

Figure B.22: The distributions for signal lepton multiplicity, all signal leptons p_T, the leading lepton p_T, and the subleading lepton p_T. The NUHM2 signal sample uses $m_{1/2} = 400$ GeV and the Higgsino signal sample uses $m_{\widetilde{\chi}_2^0} = 190$ and $m_{\widetilde{\chi}_1^0} = 150$ GeV. The reweighted Higgsino sample is shown in red line. The lower pad shows the ratio between NUHM2 and Higgsino (or reweighted Higgsino) distributions.
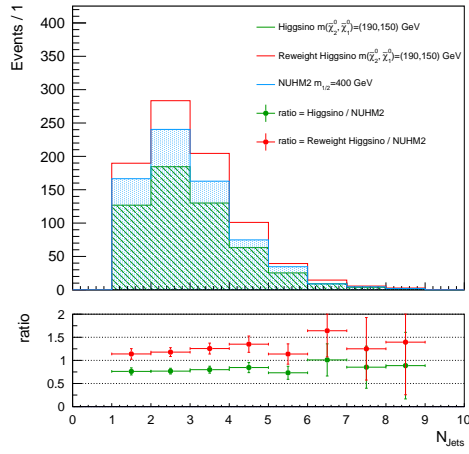
(a) Jet multiplicity
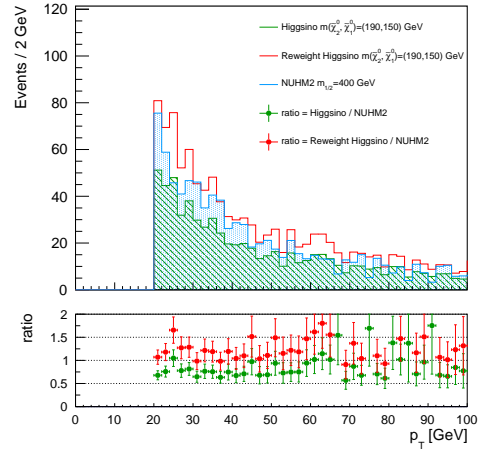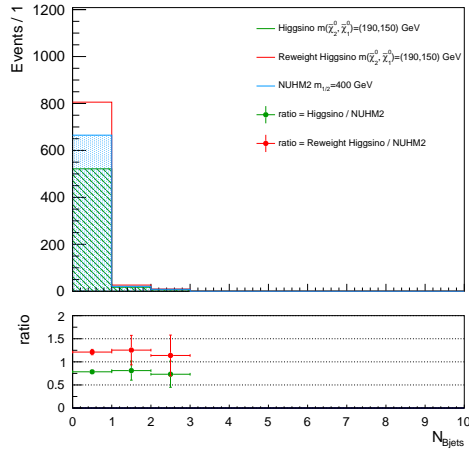
(b) Jet p_T

(c) b-jets multiplicity
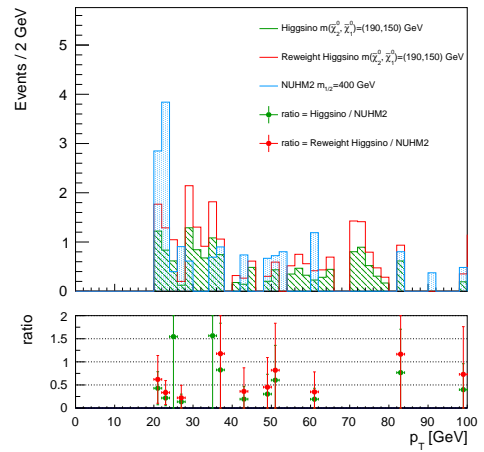
(d) b-jets p_T

Figure B.23: The distributions for jet multiplicity, jet p_T, b-jets multiplicity, and b-jet p_T. The NUHM2 signal sample uses $m_{1/2} = 400$ GeV and the Higgsino signal sample uses $m_{\widetilde{\chi}_2^0} = 190$ and $m_{\widetilde{\chi}_1^0} = 150$ GeV. The reweighted Higgsino sample is shown in red line. The lower pad shows the ratio between NUHM2 and Higgsino (or reweighted Higgsino) distributions.
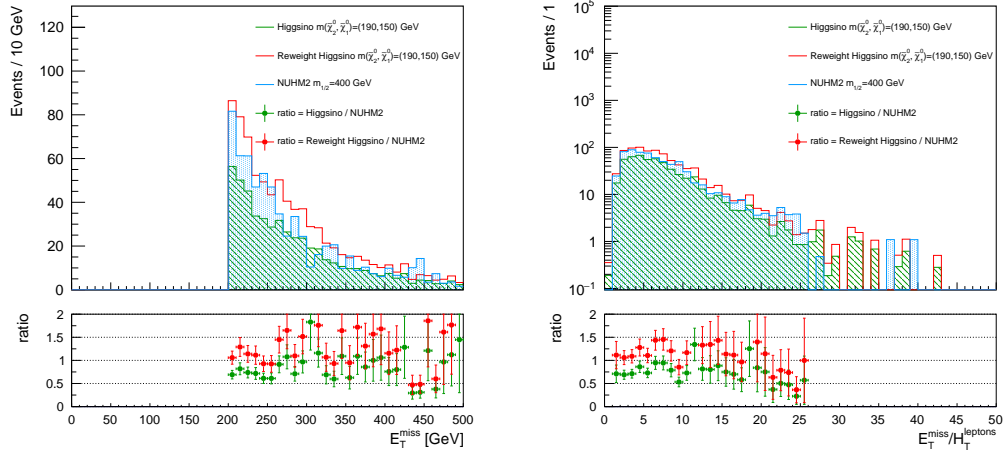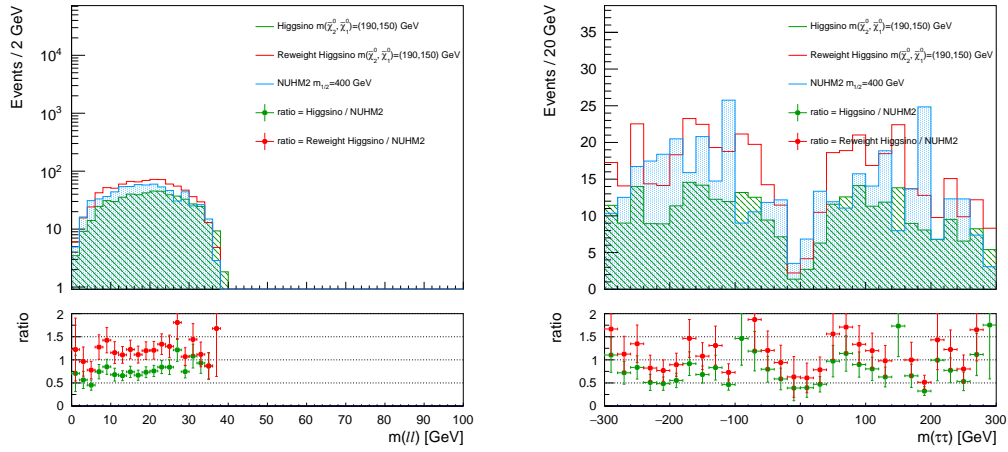
Figure B.24: The distributions for E_T^{miss}, $E_T^{miss}/H_T^{leptons}$, $m_{\ell\ell}$, and $m_{\tau\tau}$. The NUHM2 signal sample uses $m_{1/2} = 400$ GeV and the Higgsino signal sample uses $m_{\widetilde{\chi}_2^0} = 190$ and $m_{\widetilde{\chi}_1^0} = 150$ GeV. The reweighted Higgsino sample is shown in red line. The lower pad shows the ratio between NUHM2 and Higgsino (or reweighted Higgsino) distributions.

(a) m_T

(b) m_{T2}
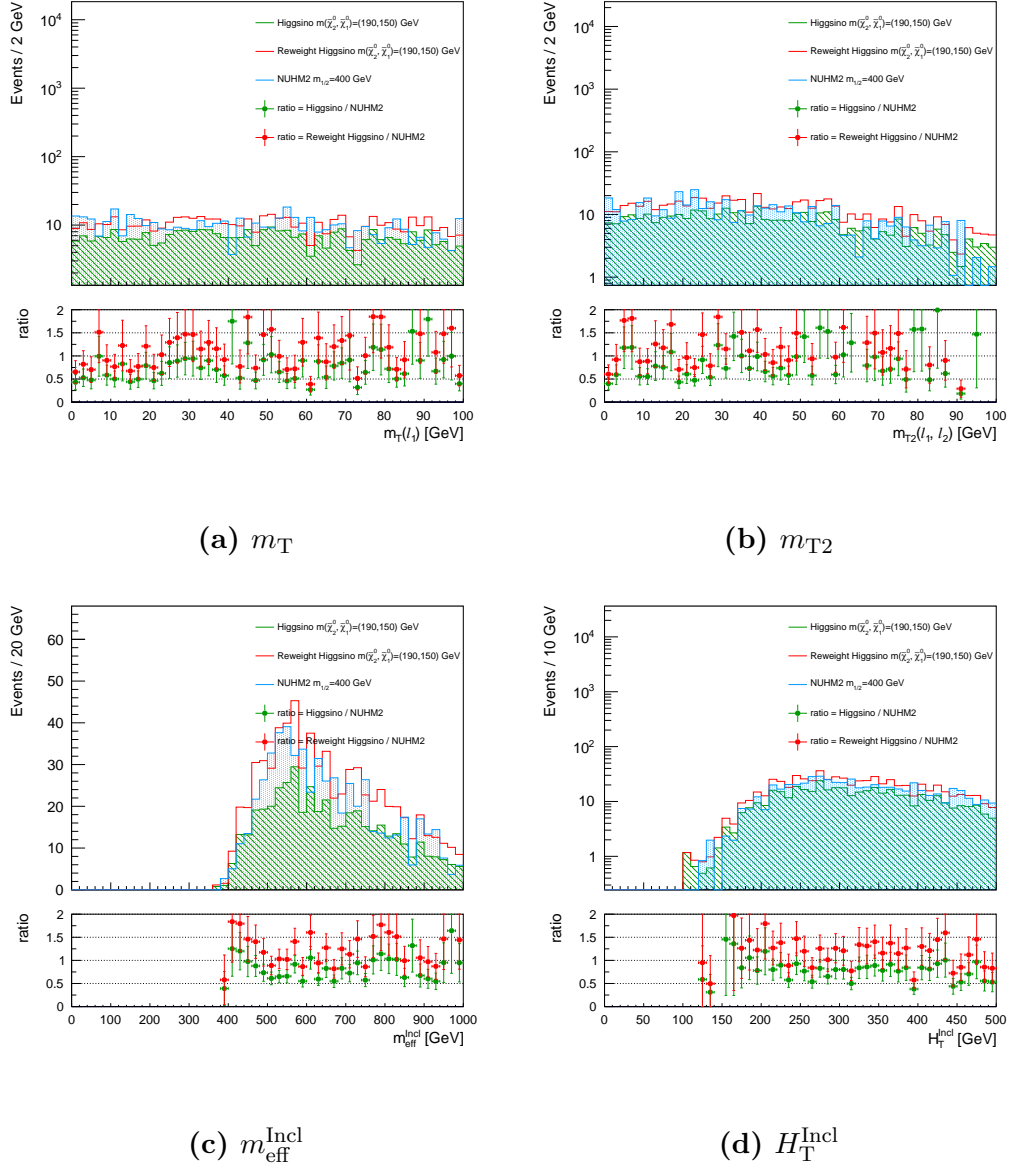
(c) $m_{\text{eff}}^{\text{Incl}}$

(d) H_T^{Incl}

Figure B.25: The distributions for m_T, m_{T2}, $m_{\text{eff}}^{\text{Incl}}$, H_T^{Incl}. The NUHM2 signal sample uses $m_{1/2} = 400$ GeV and the Higgsino signal sample uses $m_{\widetilde{\chi}_2^0} = 190$ and $m_{\widetilde{\chi}_1^0} = 150$ GeV. The reweighted Higgsino sample is shown in red line. The lower pad shows the ratio between NUHM2 and Higgsino (or reweighted Higgsino) distributions.
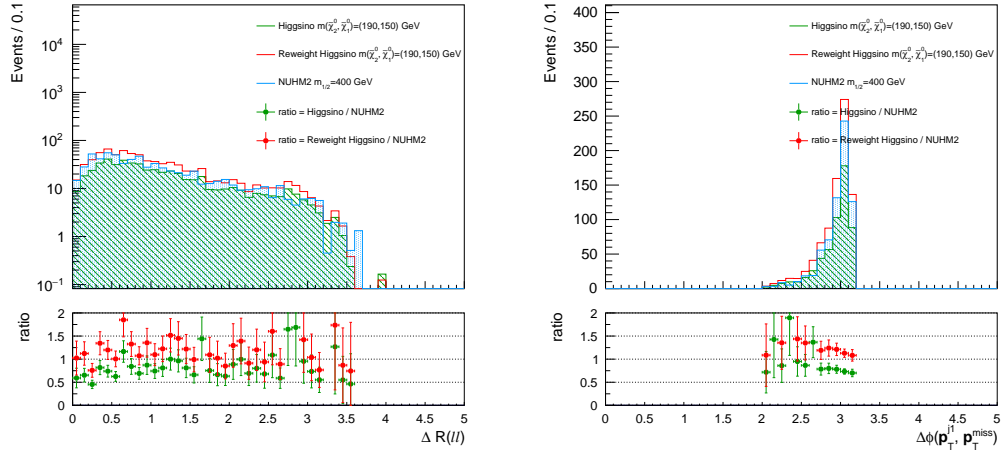
(a) $\Delta R_{\ell\ell}$ **(b)** $\Delta\phi(\mathbf{p}_{\mathrm{T}}^{\mathrm{j1}}, \mathbf{p}_{\mathrm{T}}^{\mathrm{miss}})$

Figure B.26: The distributions for $\Delta R_{\ell\ell}$ and $\Delta\phi(\mathbf{p}_{\mathrm{T}}^{\mathrm{j1}}, \mathbf{p}_{\mathrm{T}}^{\mathrm{miss}})$. The NUHM2 signal sample uses $m_{1/2} = 400$ GeV and the Higgsino signal sample uses $m_{\widetilde{\chi}_2^0} = 190$ and $m_{\widetilde{\chi}_1^0} = 150$ GeV. The reweighted Higgsino sample is shown in red line. The lower pad shows the ratio between NUHM2 and Higgsino (or reweighted Higgsino) distributions.
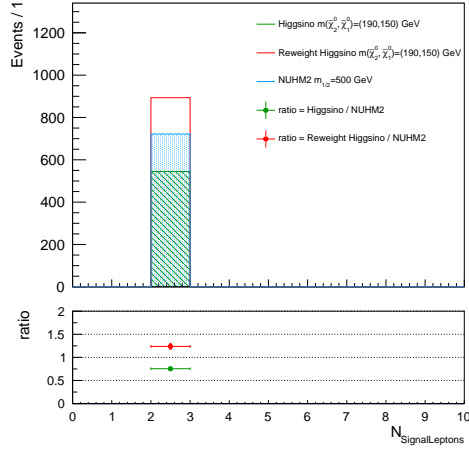
(a) Signal lepton multiplicity
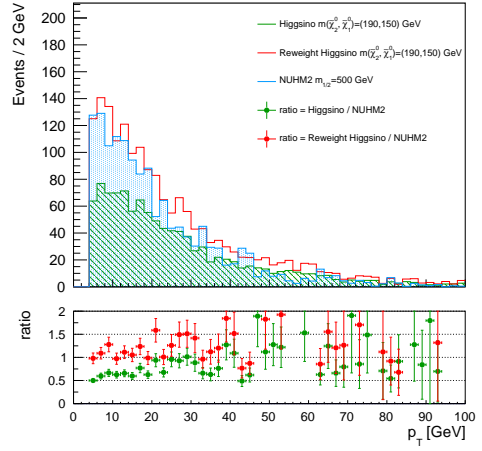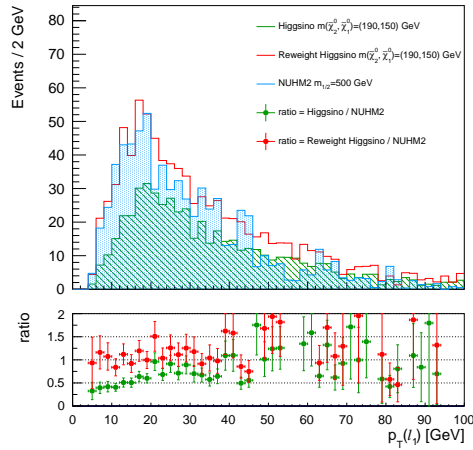
(b) Signal lepton p_T
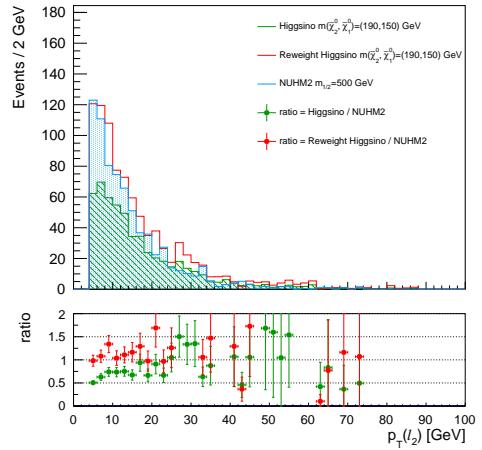
(c) Leading lepton p_T

(d) Subleading lepton p_T

Figure B.27: The distributions for signal lepton multiplicity, all signal leptons p_T, the leading lepton p_T, and the subleading lepton p_T. The NUHM2 signal sample uses $m_{1/2} = 500$ GeV and the Higgsino signal sample uses $m_{\widetilde{\chi}_2^0} = 190$ and $m_{\widetilde{\chi}_1^0} = 150$ GeV. The reweighted Higgsino sample is shown in red line. The lower pad shows the ratio between NUHM2 and Higgsino (or reweighted Higgsino) distributions.
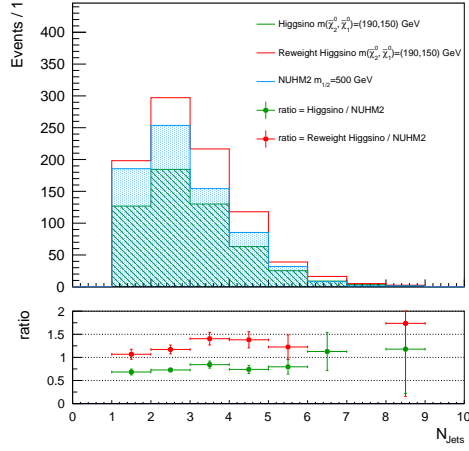
(a) Jet multiplicity
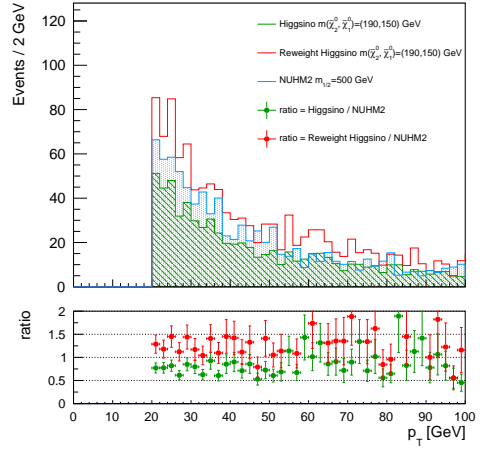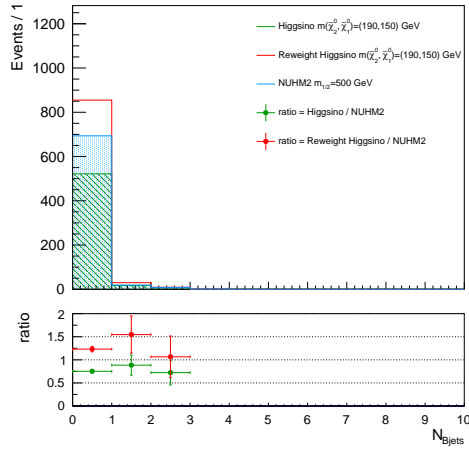
(b) Jet p_T

(c) b-jets multiplicity
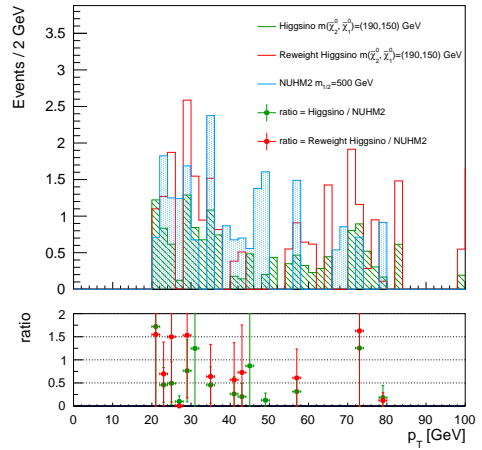
(d) b-jets p_T

Figure B.28: The distributions for jet multiplicity, jet p_T, b-jets multiplicity, and b-jet p_T. The NUHM2 signal sample uses $m_{1/2} = 500$ GeV and the Higgsino signal sample uses $m_{\widetilde{\chi}_2^0} = 190$ and $m_{\widetilde{\chi}_1^0} = 150$ GeV. The reweighted Higgsino sample is shown in red line. The lower pad shows the ratio between NUHM2 and Higgsino (or reweighted Higgsino) distributions.
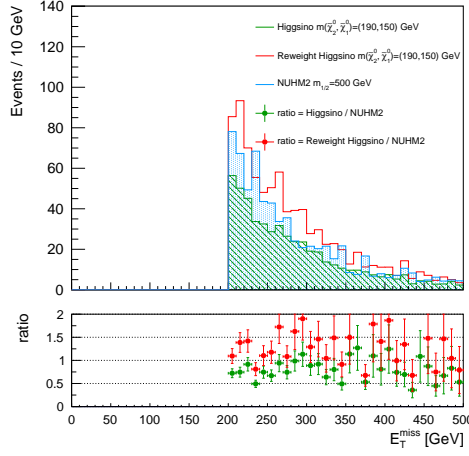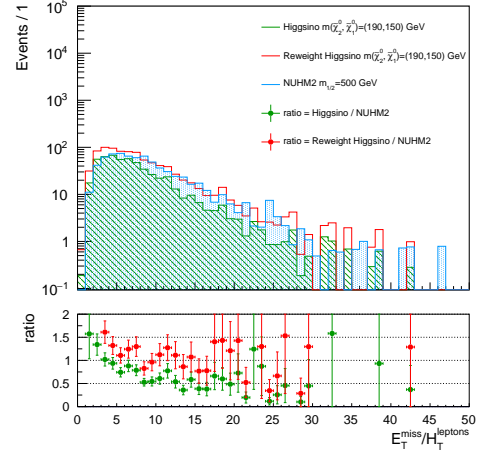
(a) E_T^{miss}
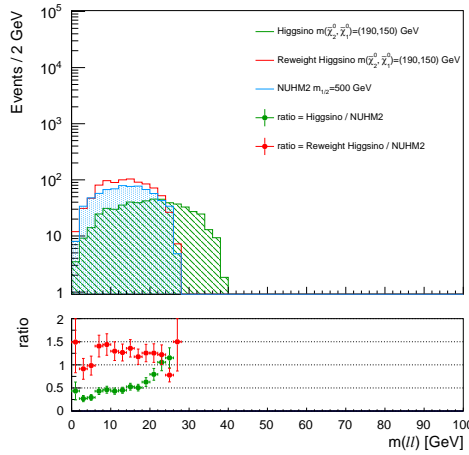
(b) $E_T^{miss}/H_T^{leptons}$

(c) $m_{\ell\ell}$
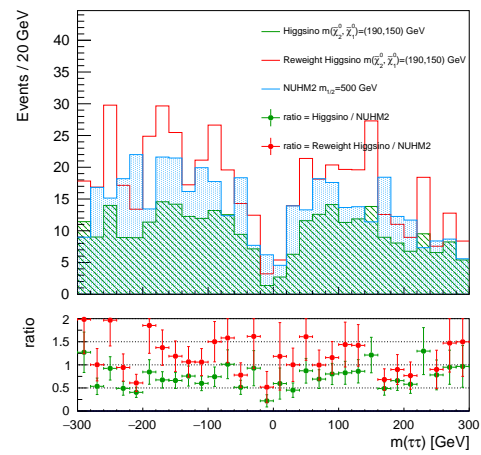
(d) $m_{\tau\tau}$

Figure B.29: The distributions for E_T^{miss}, $E_T^{miss}/H_T^{leptons}$, $m_{\ell\ell}$, and $m_{\tau\tau}$. The NUHM2 signal sample uses $m_{1/2} = 500$ GeV and the Higgsino signal sample uses $m_{\widetilde{\chi}_2^0} = 190$ and $m_{\widetilde{\chi}_1^0} = 150$ GeV. The reweighted Higgsino sample is shown in red line. The lower pad shows the ratio between NUHM2 and Higgsino (or reweighted Higgsino) distributions.

(a) m_T

(b) m_{T2}
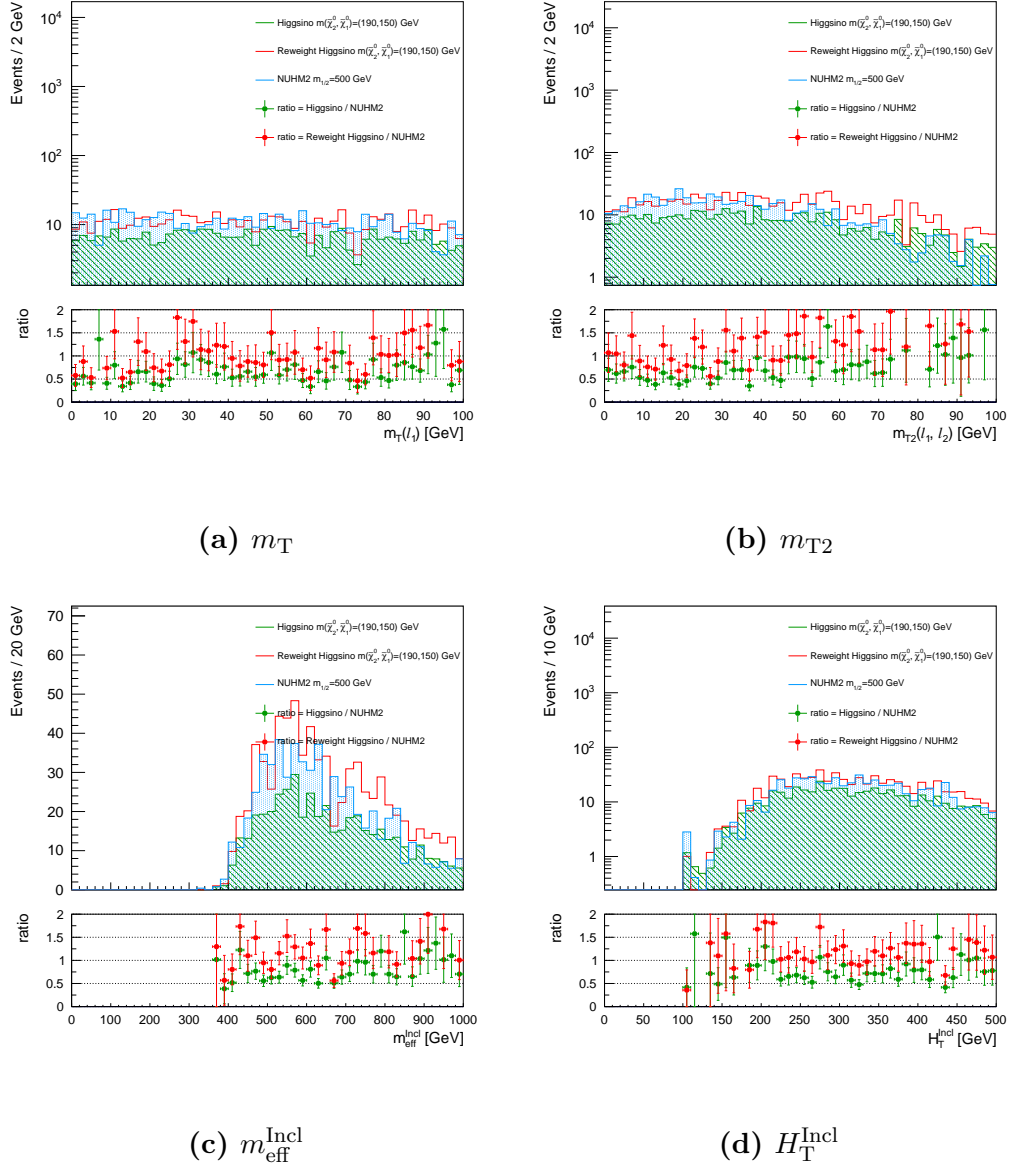
(c) m_{eff}^{Incl}

(d) H_T^{Incl}

Figure B.30: The distributions for m_T, m_{T2}, m_{eff}^{Incl}, H_T^{Incl}. The NUHM2 signal sample uses $m_{1/2} = 500$ GeV and the Higgsino signal sample uses $m_{\widetilde{\chi}_2^0} = 190$ and $m_{\widetilde{\chi}_1^0} = 150$ GeV. The reweighted Higgsino sample is shown in red line. The lower pad shows the ratio between NUHM2 and Higgsino (or reweighted Higgsino) distributions.
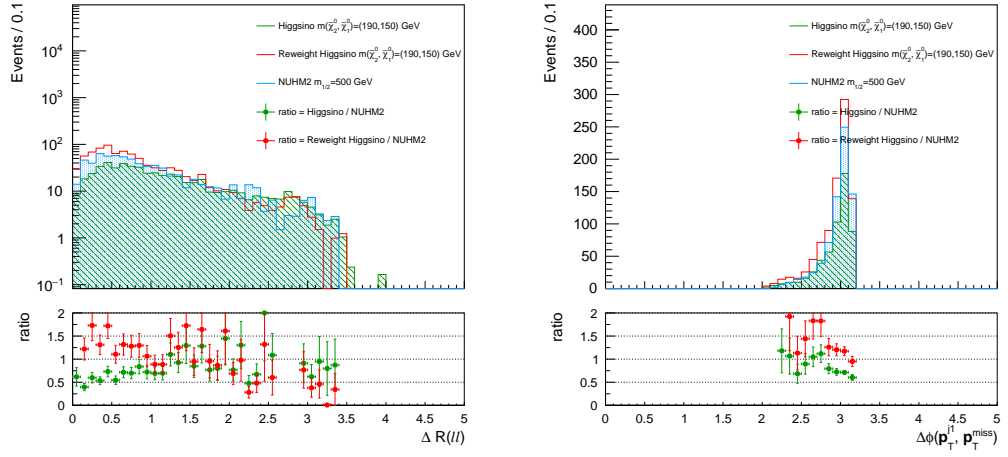
(a) $\Delta R_{\ell\ell}$ **(b)** $\Delta\phi(\mathbf{p}_T^{j1}, \mathbf{p}_T^{miss})$

Figure B.31: The distributions for $\Delta R_{\ell\ell}$ and $\Delta\phi(\mathbf{p}_T^{j1}, \mathbf{p}_T^{miss})$. The NUHM2 signal sample uses $m_{1/2} = 500$ GeV and the Higgsino signal sample uses $m_{\widetilde{\chi}_2^0} = 190$ and $m_{\widetilde{\chi}_1^0} = 150$ GeV. The reweighted Higgsino sample is shown in red line. The lower pad shows the ratio between NUHM2 and Higgsino (or reweighted Higgsino) distributions.

173
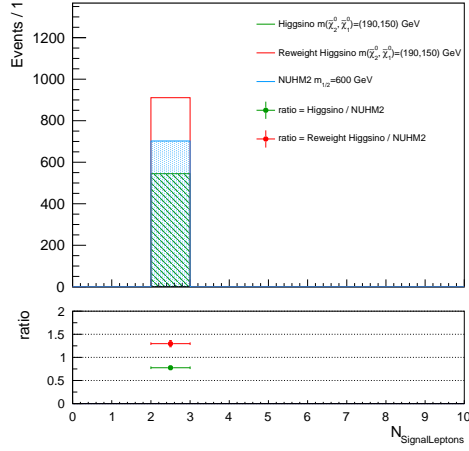
(a) Signal lepton multiplicity
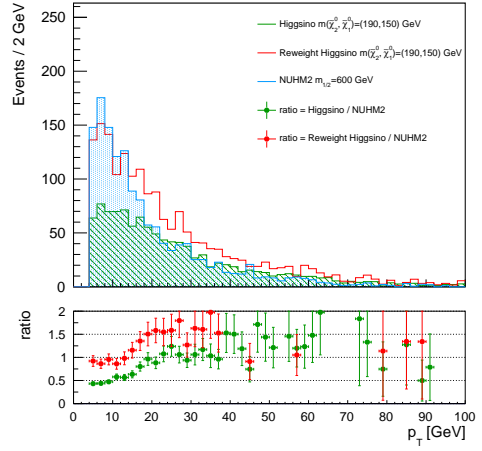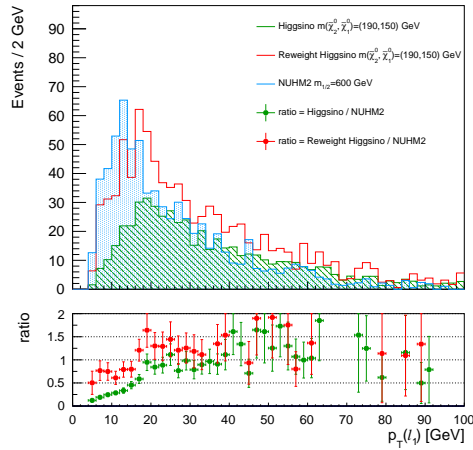
(b) Signal lepton p_T
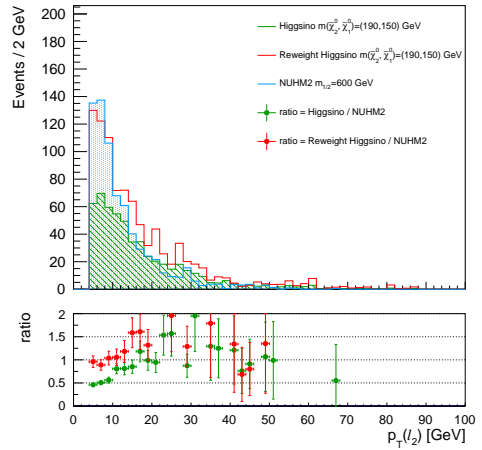
(c) Leading lepton p_T

(d) Subleading lepton p_T

Figure B.32: The distributions for signal lepton multiplicity, all signal leptons p_T, the leading lepton p_T, and the subleading lepton p_T. The NUHM2 signal sample uses $m_{1/2} = 600$ GeV and the Higgsino signal sample uses $m_{\widetilde{\chi}_2^0} = 190$ and $m_{\widetilde{\chi}_1^0} = 150$ GeV. The reweighted Higgsino sample is shown in red line. The lower pad shows the ratio between NUHM2 and Higgsino (or reweighted Higgsino) distributions.
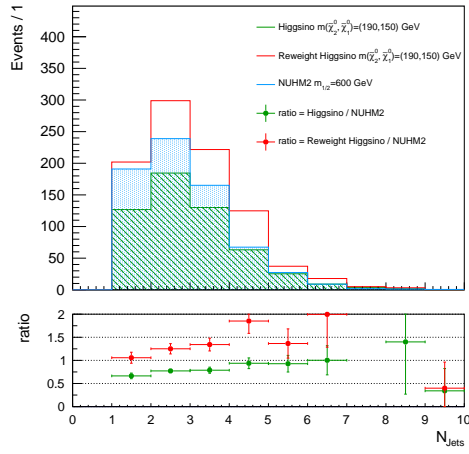
(a) Jet multiplicity
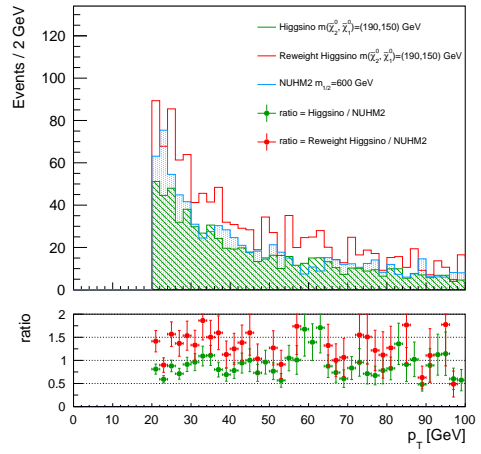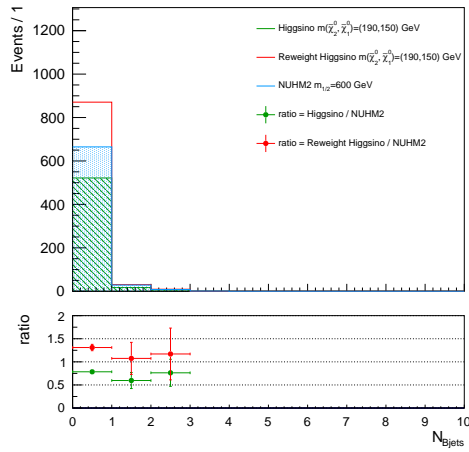
(b) Jet p_T

(c) b-jets multiplicity
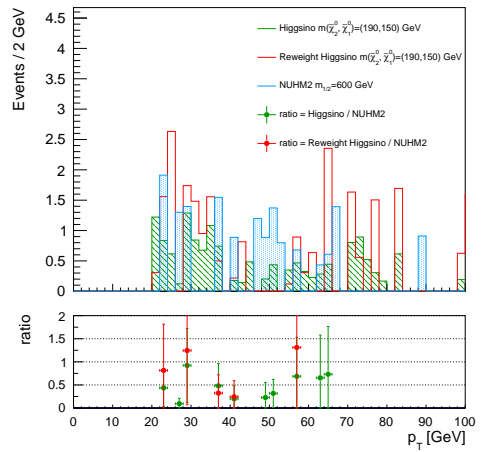
(d) b-jets p_T

Figure B.33: The distributions for jet multiplicity, jet p_T, b-jets multiplicity, and b-jet p_T. The NUHM2 signal sample uses $m_{1/2} = 600$ GeV and the Higgsino signal sample uses $m_{\tilde{\chi}_2^0} = 190$ and $m_{\tilde{\chi}_1^0} = 150$ GeV. The reweighted Higgsino sample is shown in red line. The lower pad shows the ratio between NUHM2 and Higgsino (or reweighted Higgsino) distributions.
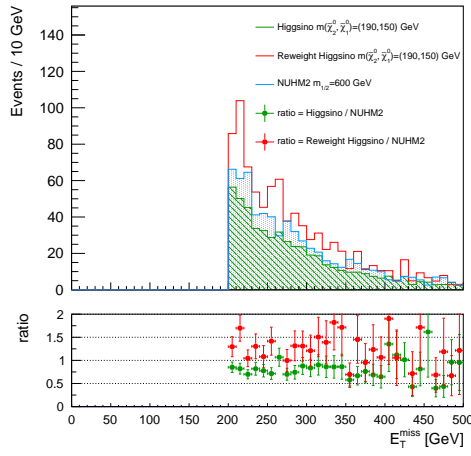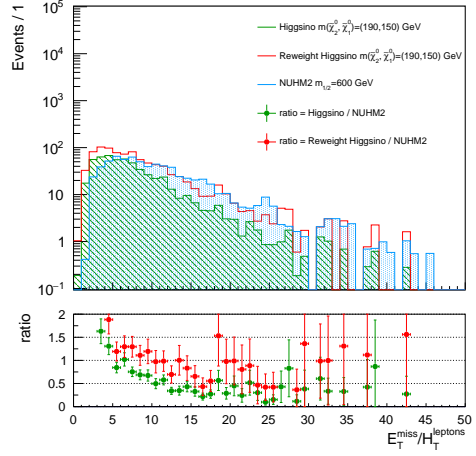
(a) E_T^{miss}
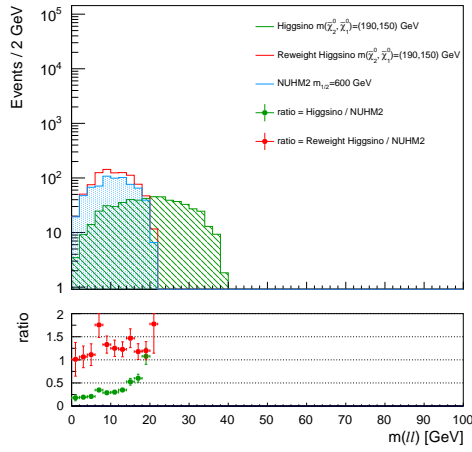
(b) $E_T^{miss}/H_T^{leptons}$

(c) $m_{\ell\ell}$
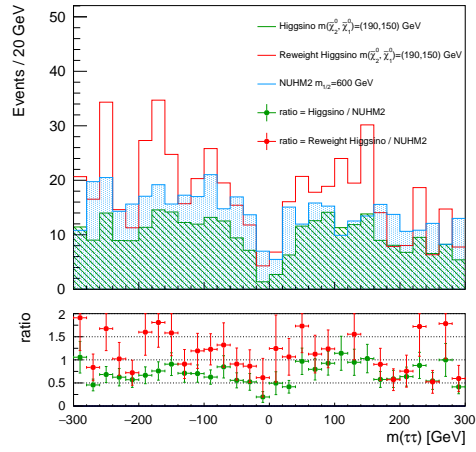
(d) $m_{\tau\tau}$

Figure B.34: The distributions for E_T^{miss}, $E_T^{miss}/H_T^{leptons}$, $m_{\ell\ell}$, and $m_{\tau\tau}$. The NUHM2 signal sample uses $m_{1/2} = 600$ GeV and the Higgsino signal sample uses $m_{\widetilde{\chi}_2^0} = 190$ and $m_{\widetilde{\chi}_1^0} = 150$ GeV. The reweighted Higgsino sample is shown in red line. The lower pad shows the ratio between NUHM2 and Higgsino (or reweighted Higgsino) distributions.

(a) m_T

(b) m_{T2}
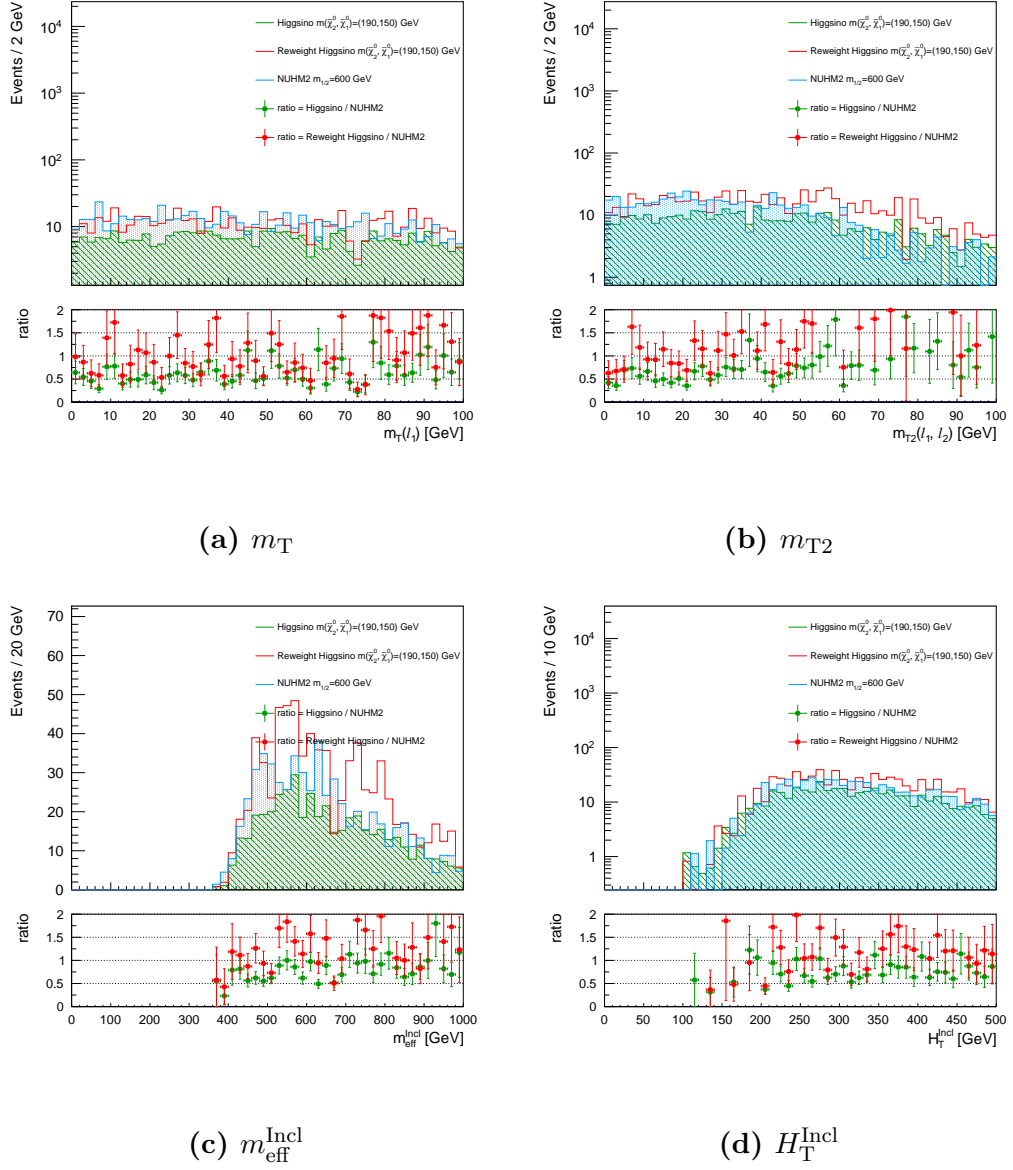
(c) $m_{\text{eff}}^{\text{Incl}}$

(d) H_T^{Incl}

Figure B.35: The distributions for m_T, m_{T2}, $m_{\text{eff}}^{\text{Incl}}$, H_T^{Incl}. The NUHM2 signal sample uses $m_{1/2} = 600$ GeV and the Higgsino signal sample uses $m_{\widetilde{\chi}_2^0} = 190$ and $m_{\widetilde{\chi}_1^0} = 150$ GeV. The reweighted Higgsino sample is shown in red line. The lower pad shows the ratio between NUHM2 and Higgsino (or reweighted Higgsino) distributions.
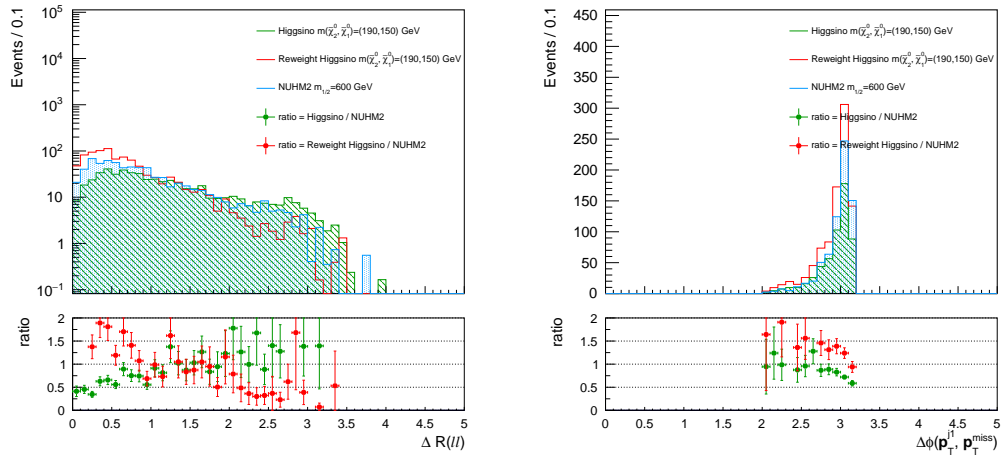
(a) $\Delta R_{\ell\ell}$ **(b)** $\Delta\phi(\mathbf{p}_T^{j1}, \mathbf{p}_T^{miss})$

Figure B.36: The distributions for $\Delta R_{\ell\ell}$ and $\Delta\phi(\mathbf{p}_T^{j1}, \mathbf{p}_T^{miss})$. The NUHM2 signal sample uses $m_{1/2} = 600$ GeV and the Higgsino signal sample uses $m_{\widetilde{\chi}_2^0} = 190$ and $m_{\widetilde{\chi}_1^0} = 150$ GeV. The reweighted Higgsino sample is shown in red line. The lower pad shows the ratio between NUHM2 and Higgsino (or reweighted Higgsino) distributions.
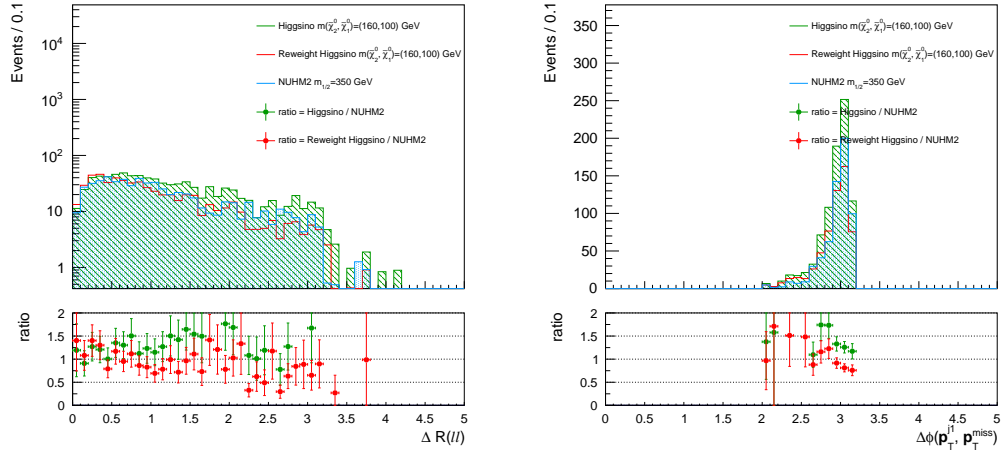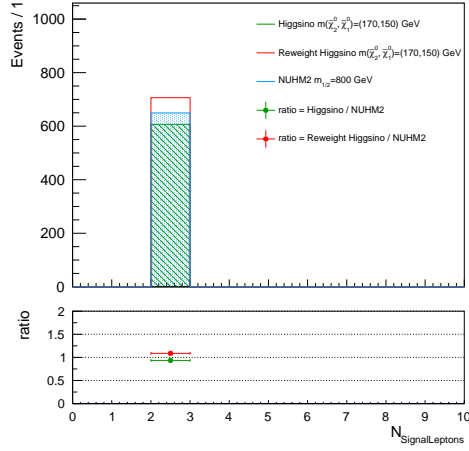
(a) Signal lepton multiplicity
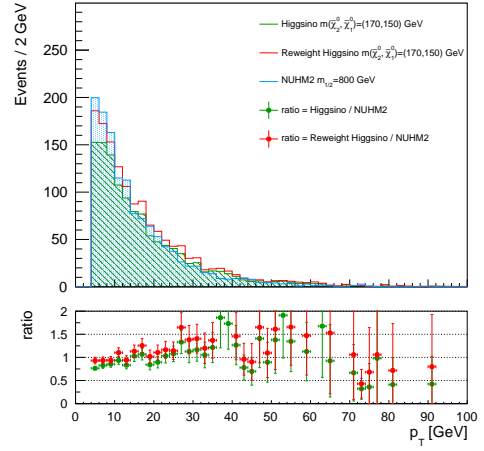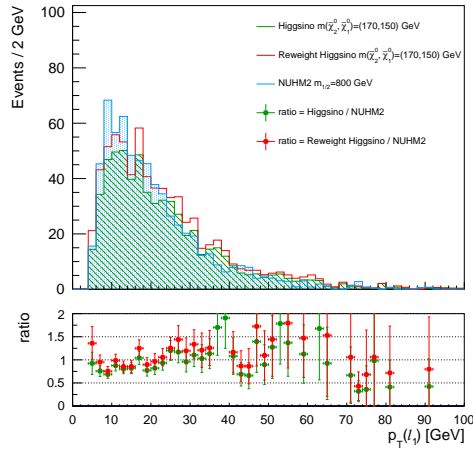
(b) Signal lepton p_T
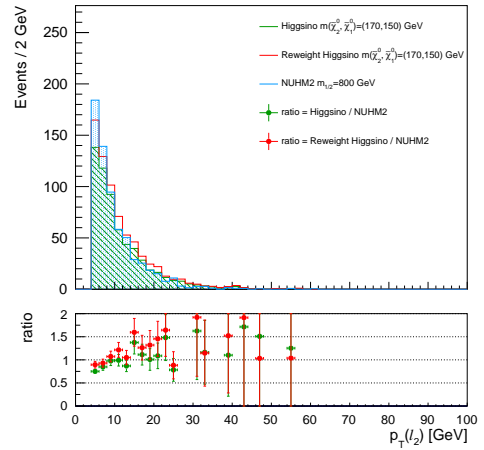
(c) Leading lepton p_T

(d) Subleading lepton p_T

Figure B.37: The distributions for signal lepton multiplicity, all signal leptons p_T, the leading lepton p_T, and the subleading lepton p_T. The NUHM2 signal sample uses $m_{1/2} = 800$ GeV and the Higgsino signal sample uses $m_{\widetilde{\chi}_2^0} = 170$ and $m_{\widetilde{\chi}_1^0} = 150$ GeV. The reweighted Higgsino sample is shown in red line. The lower pad shows the ratio between NUHM2 and Higgsino (or reweighted Higgsino) distributions.
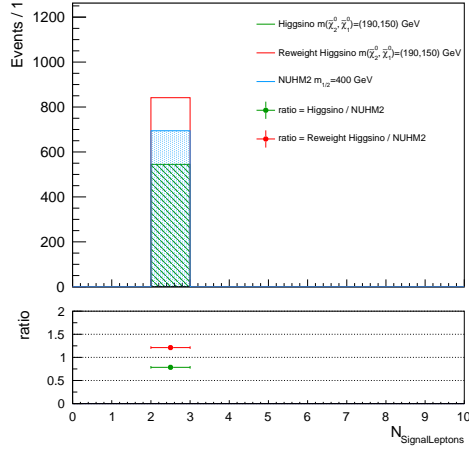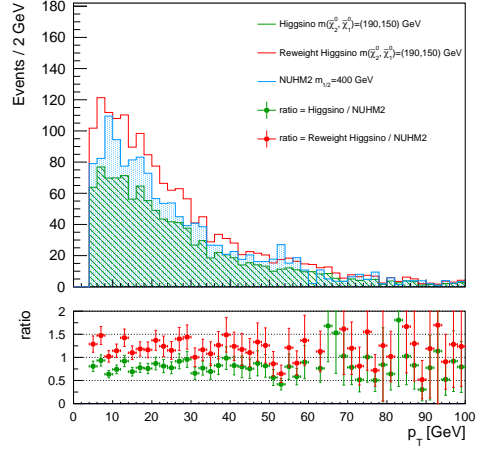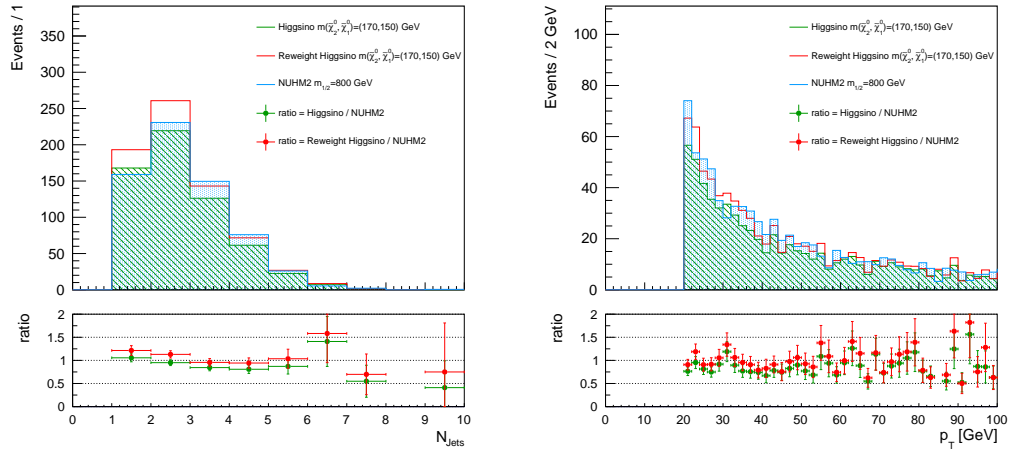
(a) Jet multiplicity
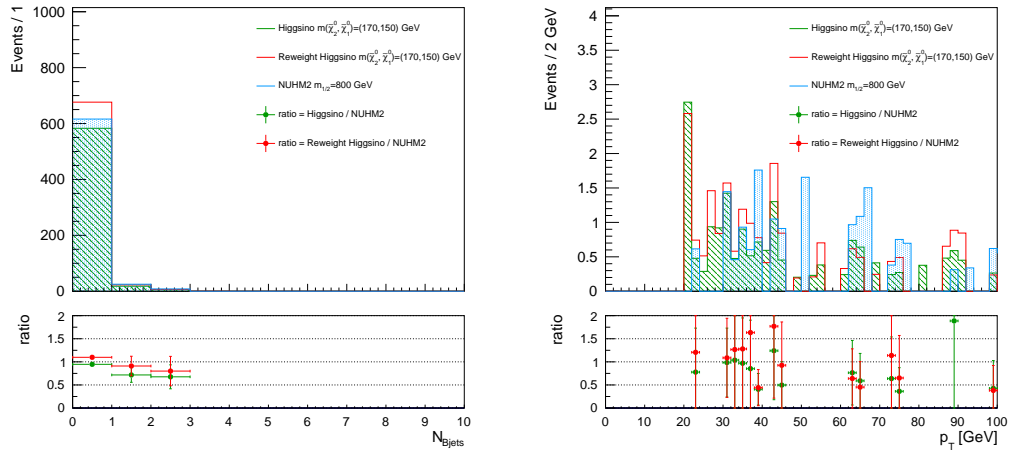
(b) Jet p_T

(c) b-jets multiplicity

(d) b-jets p_T

Figure B.38: The distributions for jet multiplicity, jet p_T, b-jets multiplicity, and b-jet p_T. The NUHM2 signal sample uses $m_{1/2} = 800$ GeV and the Higgsino signal sample uses $m_{\widetilde{\chi}_2^0} = 170$ and $m_{\widetilde{\chi}_1^0} = 150$ GeV. The reweighted Higgsino sample is shown in red line. The lower pad shows the ratio between NUHM2 and Higgsino (or reweighted Higgsino) distributions.
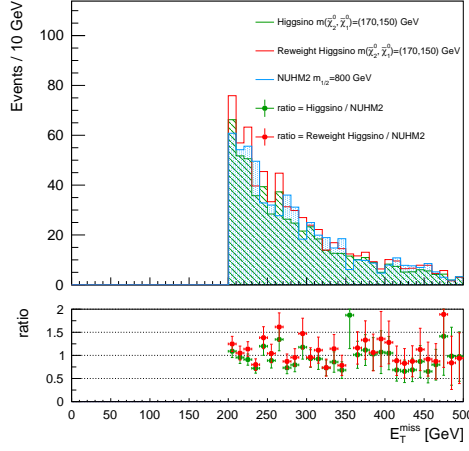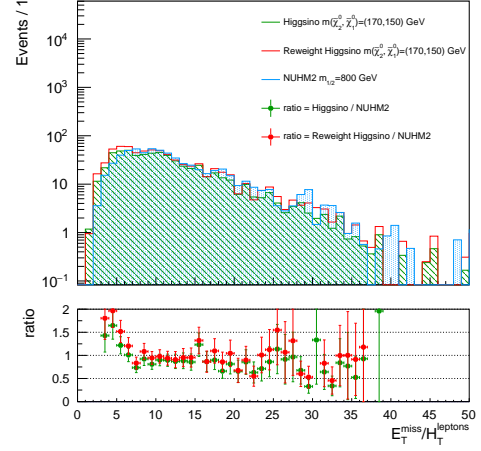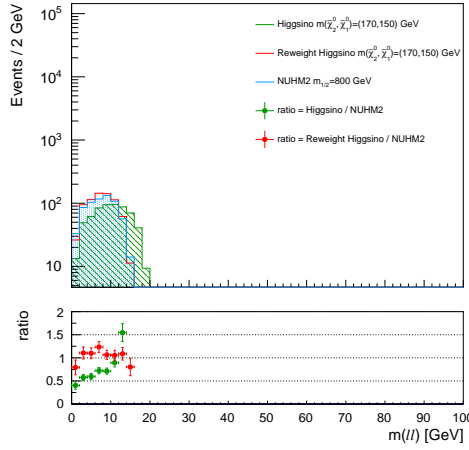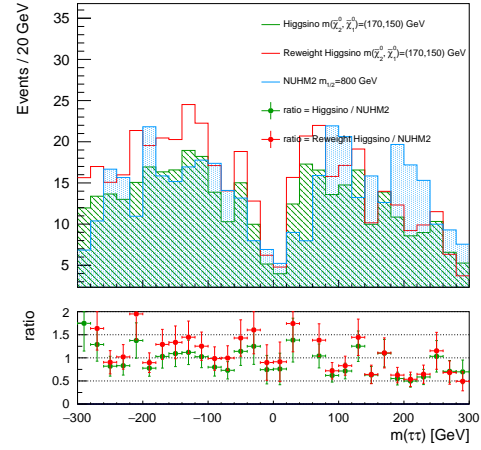
Figure B.39: The distributions for E_T^{miss}, $E_T^{miss}/H_T^{leptons}$, $m_{\ell\ell}$, and $m_{\tau\tau}$. The NUHM2 signal sample uses $m_{1/2} = 800$ GeV and the Higgsino signal sample uses $m_{\widetilde{\chi}_2^0} = 170$ and $m_{\widetilde{\chi}_1^0} = 150$ GeV. The reweighted Higgsino sample is shown in red line. The lower pad shows the ratio between NUHM2 and Higgsino (or reweighted Higgsino) distributions.

(a) m_{T}

(b) m_{T2}
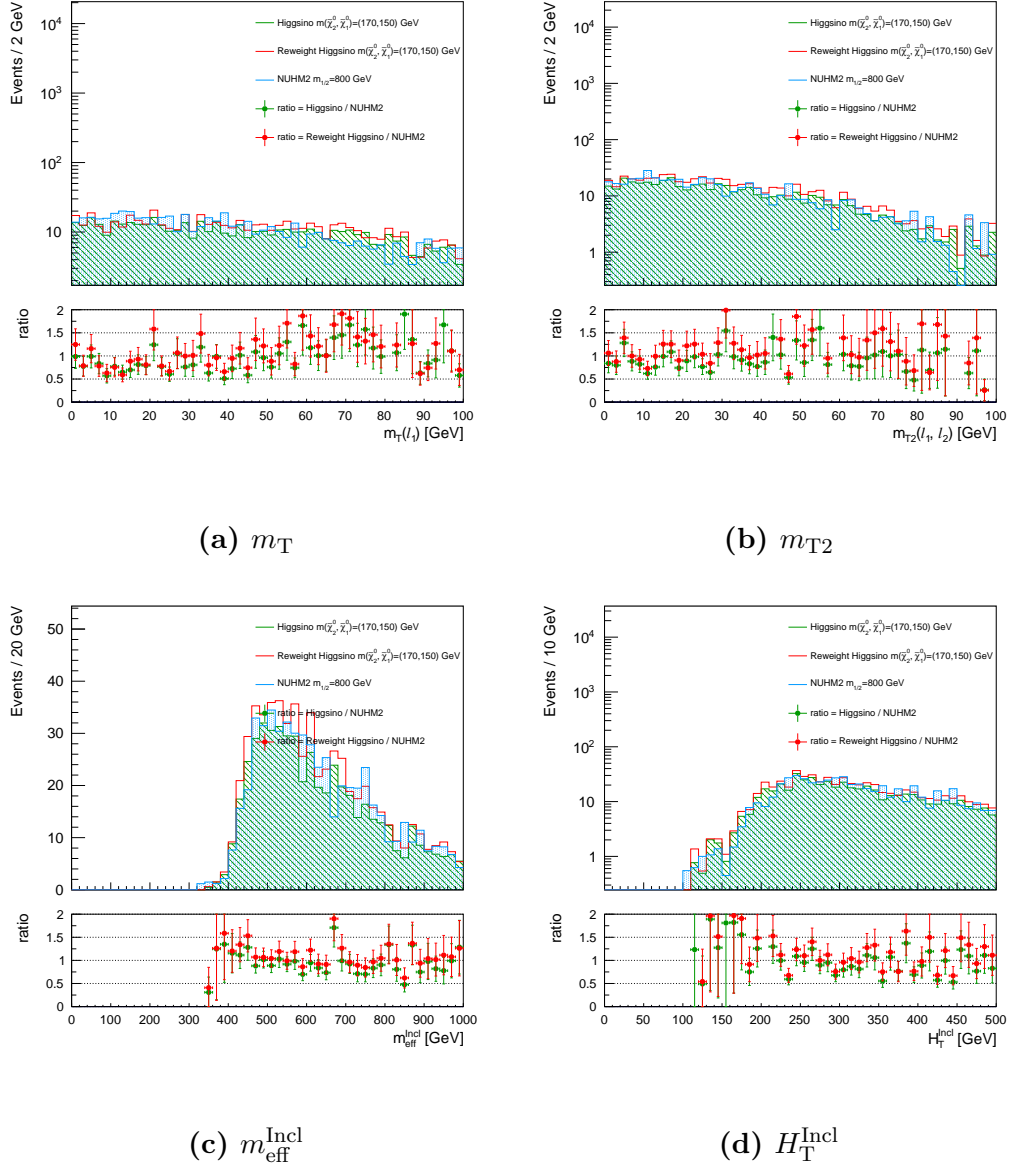
(c) $m_{\mathrm{eff}}^{\mathrm{Incl}}$

(d) $H_{\mathrm{T}}^{\mathrm{Incl}}$

Figure B.40: The distributions for m_{T}, m_{T2}, $m_{\mathrm{eff}}^{\mathrm{Incl}}$, $H_{\mathrm{T}}^{\mathrm{Incl}}$. The NUHM2 signal sample uses $m_{1/2} = 800$ GeV and the Higgsino signal sample uses $m_{\widetilde{\chi}_2^0} = 170$ and $m_{\widetilde{\chi}_1^0} = 150$ GeV. The reweighted Higgsino sample is shown in red line. The lower pad shows the ratio between NUHM2 and Higgsino (or reweighted Higgsino) distributions.

(a) $\Delta R_{\ell\ell}$
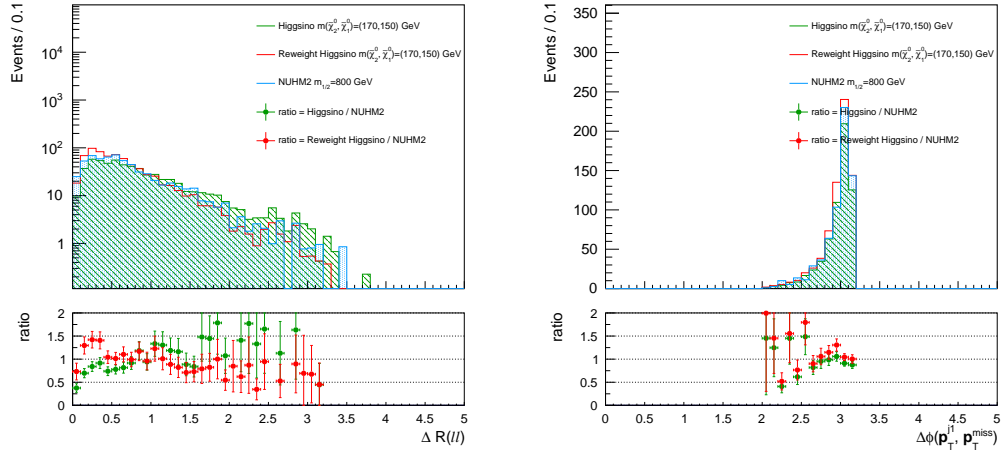
(b) $\Delta\phi(\mathbf{p}_T^{j1}, \mathbf{p}_T^{miss})$

Figure B.41: The distributions for $\Delta R_{\ell\ell}$ and $\Delta\phi(\mathbf{p}_T^{j1}, \mathbf{p}_T^{miss})$. The NUHM2 signal sample uses $m_{1/2} = 800$ GeV and the Higgsino signal sample uses $m_{\widetilde{\chi}_2^0} = 170$ and $m_{\widetilde{\chi}_1^0} = 150$ GeV. The reweighted Higgsino sample is shown in red line. The lower pad shows the ratio between NUHM2 and Higgsino (or reweighted Higgsino) distributions.

APPENDIX C

ELECTRON ISOLATION

Electron reconstruction, identification, and isolation play a crucial role for many ATLAS analyses. Electrons[1] leave tracks in the inner detector and energy deposits in the ECAL. The reconstruction algorithm combines the signals in the calorimeter and the tracks in the inner detector to define electron candidates. Reconstructed candidates are identified as electrons based on a likelihood discrimination which distinguishes the electron candidates from the hadrons, non-prompt electrons originating from photon conversions, and heavy flavor hadron decays. Additionally, electron candidates are required to be isolated to further distinguish the signal and the background objects. Electron efficiency measurements are performed based on the tag-and-probe method using $Z \to ee$ and $J/\psi \to ee$ samples. This chapter briefly describes the basic concept of electron reconstruction and identification and focuses on the electron isolation measurement using the $Z \to ee$ samples only.

C.1   Tag-and-probe method

In order to measure the electron efficiency, the tag-and-probe method and unbiased and clean electron enriched $Z \to ee$ or $J/\psi \to ee$ samples are used. Strict selection criteria are applied on one of the electron candidates (called "tag") together with requirements based on the invariant mass window provide a loose pre-identification

---

[1]The electrons and positrons are referred to as electrons.

of the other electron candidate ("probe"). Only the probe electrons are used in the electron efficiency measurement after subtracting the background. Each valid combination of electron tag-and-probe pairs in the events is considered; therefore, an electron can be the tag in one tag-and-probe pair and the probe in another. There are two background estimation methods using $Z \rightarrow ee$ events: the Z_{mass} and the Z_{iso} methods. The Z_{mass} method constructs background templates by inverting the identification and isolation requirements. The background templates are then normalized using the events in the side band region. The Z_{iso} method constructs a background template by inverting the identification requirements only. The background templates are then normalized to the background dominated upper end of the $E_T^{cone0.3}$ isolation distribution. Figure C.1 shows the background estimations using the Z_{mass} and Z_{iso} methods.
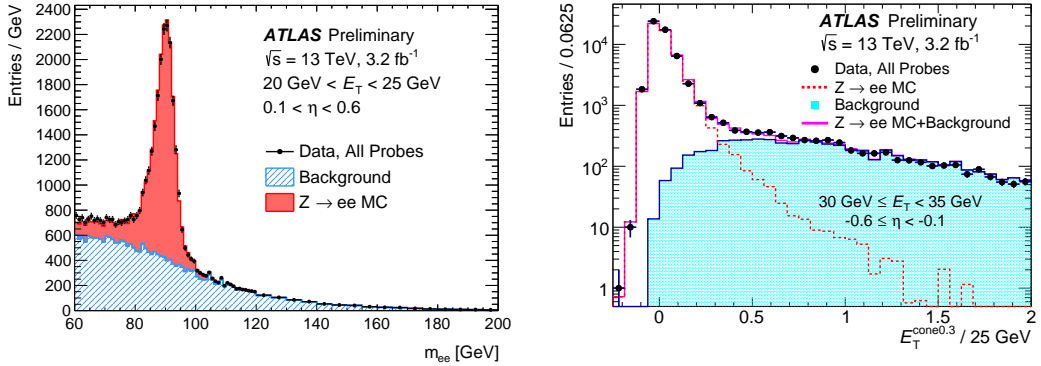
(a) The Z_{mass} method   **(b)** The Z_{iso} method

Figure C.1: Illustration of the background estimations use (a) the Z_{mass} and (b) the Z_{iso} methods [17].

The electrons in J/Ψ samples have prompt and non-prompt components. The prompt electron comes from the prompt production of J/Ψ which comes from the pp collisions and the non-prompt one arises from the non-prompt production of

J/Ψ which comes from b decay. Prompt electrons are expected to be more isolated than the non-prompt ones. By using this distinguishing feature, a tag-and-probe pair can be constructed. There are two background estimation methods: short-τ and τ-fit methods. The short-τ method uses events with short pseudo-proper time to find the prompt electron. The τ-fit method considers the full τ-range to extract the non-prompt electron by fitting the pseudo-proper time distribution. Figure C.2 shows the background estimations using the short-τ and τ-fit methods. In the electron isolation, the $Z \to ee$ samples and Z_{mass} method are used.

(a) The short-τ method
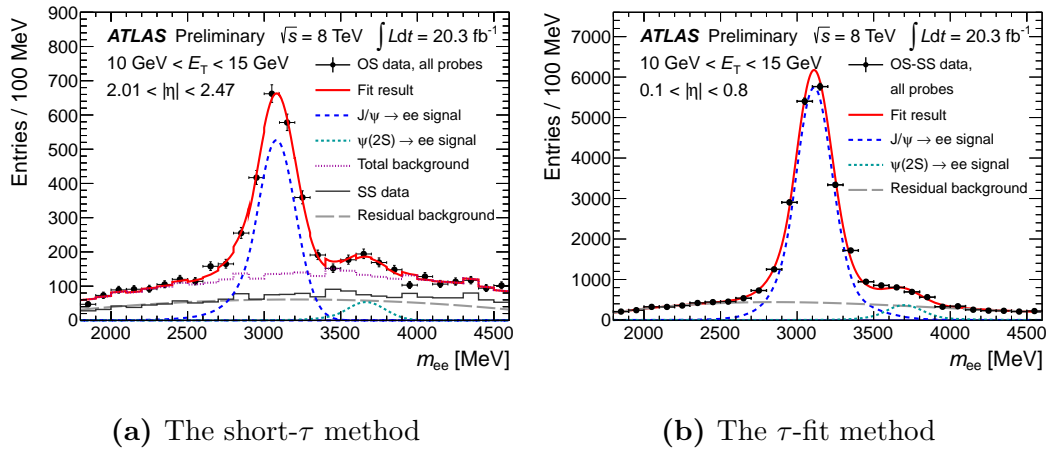
(b) The τ-fit method

Figure C.2: Illustration of the background estimations use (a) the short-τ and (b) the τ-fit methods [18].

C.2 Electron reconstruction and identification

Electron candidates are reconstructed in the central region of the ATLAS detector ($|\eta| < 2.47$) using information from the inner detector and ECAL. Then the electron identification (ID) algorithms are used to distinguish signal or background-like candidates based on multivariate likelihood discriminant. Signal-like electrons should be prompt and isolated. Background-like electrons coming from photon

conversions, hadronic jets misidentification, and heavy flavor decays are non-prompt. The IBL added for Run-2 provides good discrimination between electrons and converted photons. Three electron ID operating points `Tight`, `Medium`, and `Loose` are provided. The `Tight` ID provides the highest background rejection power, the `Loose` has the lowest background rejection power, and `Medium` ID in between. Figure C.3 shows a schematic view of the electron reconstruction and identification. The electron reconstruction and identification efficiencies for 2016 data corresponding 33.9 fb^{-1} are shown in Fig. C.4.
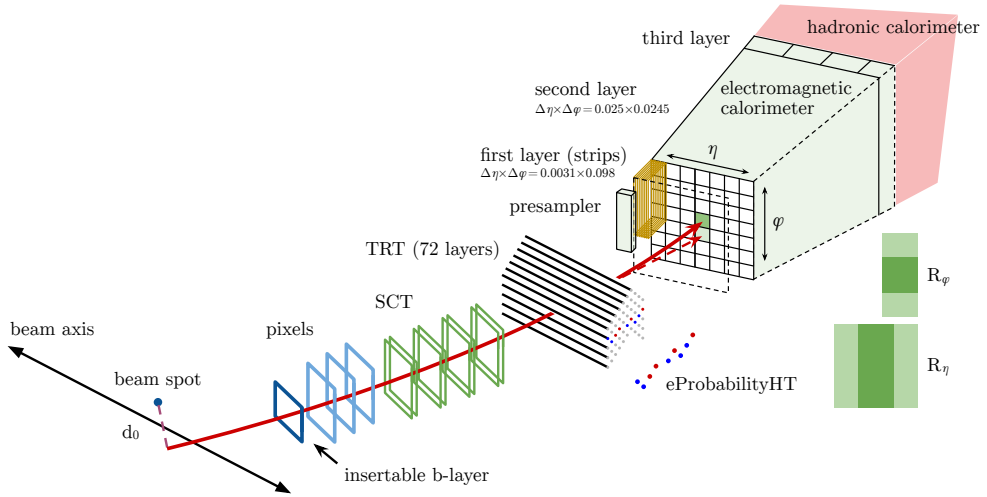
Figure C.3: A schematic view of the electron reconstruction and identification [17].

C.3 Electron isolation

Electrons produced in the LHC pp collisions cover a wide range of $E_{\text{T}}^{\text{miss}}$ from a few GeV to several TeV. Reconstructed electrons suffer large backgrounds from misidentified hadrons, photon conversions, and heavy-flavor decays. In order to further discriminate signal and background, most analyses require electrons to be isolated in addition to the identification criteria. Background electrons are
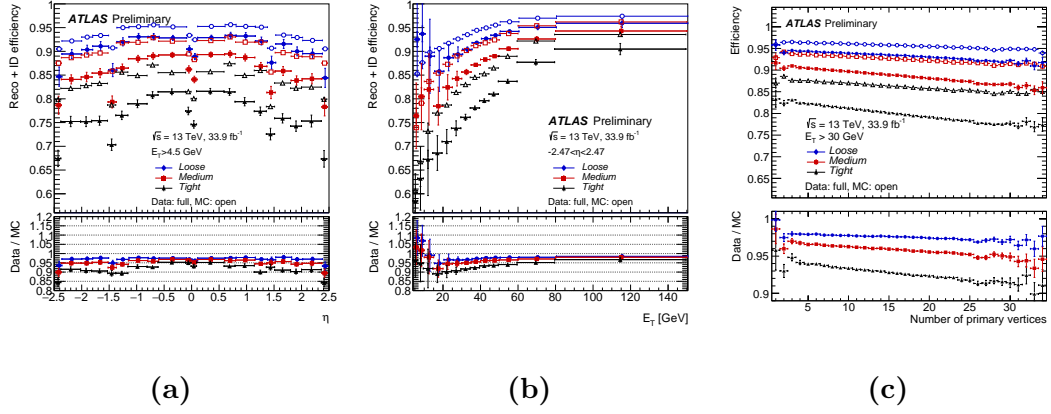
Figure C.4: The electron reconstruction and identification efficiencies as a function of (a) η and (b) E_T^{miss} [19]. The electron identification efficiency as a function of (c) the number of reconstructed primary vertices [20].

produced in association with other objects such as jets, and therefore they have larger values of isolation. However, signal electrons tend to have low values of isolation as they are uncorrelated with other jet activities in the event. The isolation variables quantify the energy deposited in a cone centered around the electron candidates and allow prompt electrons to be disentangled from non-isolated electrons. Hence, electron isolation is a very powerful tool to reject backgrounds. Two discriminating variables have been designed for that purpose: a calorimetric isolation energy $E_T^{\mathrm{cone}\ 0.2}$ and a track isolation $p_T^{\mathrm{varcone}\ 0.2}$. The $E_T^{\mathrm{cone}\ 0.2}$ is defined as the sum of transverse energies of topological clusters [113] within a cone of $\Delta R = 0.2$ around the candidate electron cluster and excluding the contribution in a region $\Delta\eta \times \Delta\phi = 0.125 \times 0.175$ centered around the electron cluster barycenter. Only clusters with positive E_T are considered in the sum. The energy leakage outside the clusters, pileup contributions, and the underlying event activity are corrected. The $p_T^{\mathrm{varcone}\ 0.2}$ is defined as the sum of transverse momenta of all tracks within a cone of $\Delta R = \min(0.2, 10\ \mathrm{GeV}/E_T)$ around the

candidate electron track and originating from the reconstructed primary vertex of the hard collision. The track must satisfy $E_T > 1$ GeV, $|\Delta z_0 \sin\theta| < 3$ mm, and $n_{Si} \geq 7$, $n_{Si}^{hole} \leq 2$, $n_{pixel}^{hole} \leq 1$, and $n_{mod}^{sh} \leq 1$, where n_{Si}^{hole} and n_{pixel}^{hole} are the number of missing hits in the silicon and pixel detector respectively and n_{mod}^{sh} is the number of hits in the silicon detector assigned to more than one track. The distributions of $E_T^{cone\ 0.2}$ and $p_T^{varcone\ 0.2}$ are shown in Fig. C.5.

(a) $E_T^{cone\ 0.2}$ (b) $p_T^{varcone\ 0.2}$
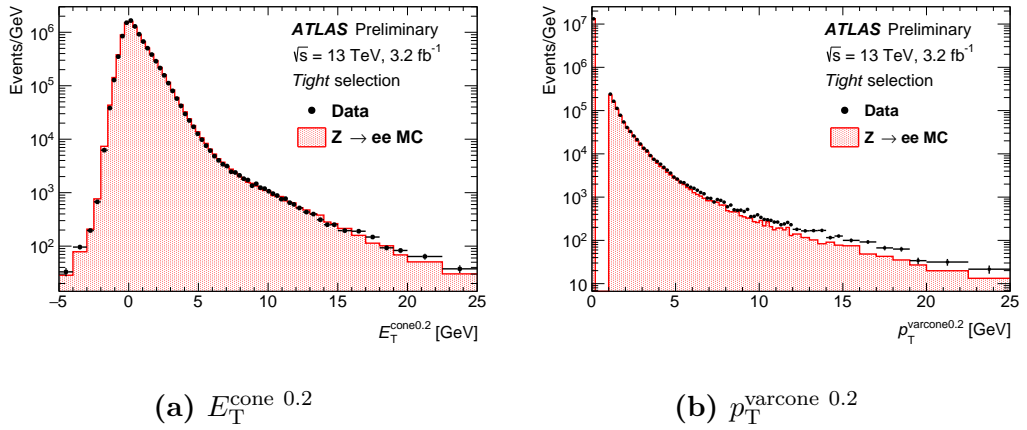
Figure C.5: The (a) $E_T^{cone\ 0.2}$ and (b) $p_T^{varcone\ 0.2}$ distributions [17]. The negative tail of $E_T^{cone\ 0.2}$ originates from the correction for pileup and the underlying event activity. No background subtraction is applied in the plots, so a slight discrepancy is observed in the region at large $E_T^{cone\ 0.2}$ and $p_T^{varcone\ 0.2}$ values where the background dominates.

Table C.1 lists the electron isolation working points, which are various selection requirements on the $E_T^{cone\ 0.2}$ and $p_T^{varcone\ 0.2}$, to select isolated electron candidates. The `Tight`, `Loose`, `LooseTrackOnly`, `Gradient`, and `GradientLoose` are the efficiency targeted working points. By applying various requirements, the isolation efficiency ϵ_{iso} can be obtained. The `FixedCutTightTrackOnly`, `FixedCutTight`, and `FixedCutLoose` are the fixed requirement working points. The upper thresh-

olds on the isolation variables are constant. The fixed requirement working points are used in analyses with low E_T electrons and require high background rejection.

Working point	Calorimeter isolation	Track isolation	Combined isolation
Tight	96%	99%	95%
Loose	99%	99%	99%
LooseTrackOnly	-	99%	99%
Gradient	$(0.1143 \times E_\mathrm{T} + 92.14)$ %	$(0.1143 \times E_\mathrm{T} + 92.14)$ %	90%/99% at 25/60 GeV
GradientLoose	$(0.057 \times E_\mathrm{T} + 95.57)$ %	$(0.057 \times E_\mathrm{T} + 95.57)$ %	95%/99% at 25/60 GeV
FixedCutTightTrackOnly	-	$p_\mathrm{T}^{\mathrm{varcone}\ 0.2}/p_\mathrm{T} < 0.06$	-
FixedCutTight	$E_\mathrm{T}^{\mathrm{cone}\ 0.2}/p_\mathrm{T} < 0.06$	$p_\mathrm{T}^{\mathrm{varcone}\ 0.2}/p_\mathrm{T} < 0.06$	-
FixedCutLoose	$E_\mathrm{T}^{\mathrm{cone}\ 0.2}/p_\mathrm{T} < 0.2$	$p_\mathrm{T}^{\mathrm{varcone}\ 0.2}/p_\mathrm{T} < 0.15$	-

Table C.1: The definitions of the electron isolation working points. The numbers in the table represent the target efficiencies for the target working points. For Gradient, GradientLoose, and fixed requirement working points, the E_T and p_T are in GeV.

C.4   The electron isolation efficiency

The probe electron candidates with $E_\mathrm{T} > 7$ GeV are used in the electron isolation efficiency measurement. The tag-and-probe method with $Z \rightarrow ee$ events are used for the efficiency measurement and the Z_{mass} method is used to estimate background. The isolation efficiency is defined as

$$\epsilon_{iso} = \frac{N_{\mathrm{identification} \cap \mathrm{isolation}}}{N_{\mathrm{identification}}} \quad . \tag{C.1}$$

The efficiencies are measured for all isolation working points listed in Table C.1 with respect to three likelihood identifications `TightLLH`, `MediumLLH`, and `LooseLLH`. The electron isolation efficiencies depend on the transverse energy E_T and pseudo-rapidity η. Fig C.6 shows the electron isolation efficiencies for the fixedCutLoose

working point and data-to-MC ratios as a function of the transverse energy E_{T} and pseudorapidity η, respectively. Larger discrepancies between data and MC are observed for $E_{\mathrm{T}} < 20$ GeV and good agreement is found when $E_{\mathrm{T}} > 20$ GeV. Good agreement is also observed as a function of η with slightly larger discrepancies at the level of 1% in the regions $|\eta| \approx 1.5$.

(a) The transverse energy E_{T} (b) η
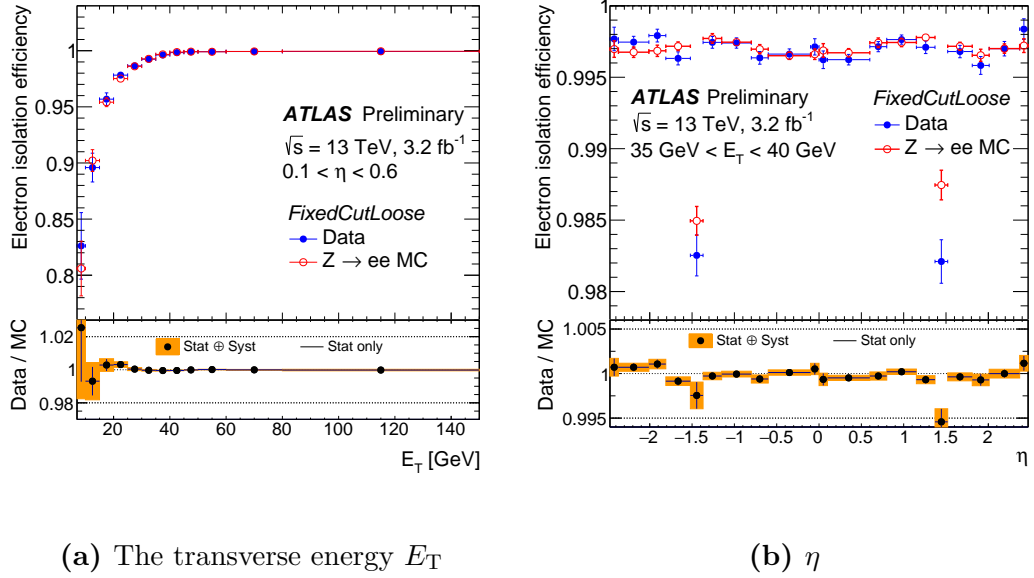
Figure C.6: The electron isolation efficiencies for the fixedCutLoose working point for electrons from $Z \to ee$ as a function of the (a) the transverse energy E_{T} for $0.1 < \eta < 0.6$ and (b) pseudorapidity η for $35 < E_{\mathrm{T}} < 40$ GeV [17]. The electrons are required to fulfill `TightLLH` identification.

APPENDIX D

SAME-SIGN OR THREE LEPTONS AND JETS

The NUHM2 interpretation in the strongly produced SUSY particles search is presented in the paper "Searching for supersymmetry in final states with two same-sign or three leptons and jets using 36 fb^{-1} of $\sqrt{s} = 13$ TeV pp collision data with the ATLAS detector" [114]. This chapter is a complement to the NUHM2 interpretation for the same-sign or three leptons and jets search.

D.1   Monte Carlo event samples and data set

The NUHM2 model involves gluino pair production where gluinos decay into $t\bar{t}\widetilde{\chi}_1^0$ and $t\bar{b}\widetilde{\chi}_1^\pm$ as shown in Fig. D.1.

(a) $\widetilde{g} \to t\bar{t}\widetilde{\chi}_1^0$ **(b)** $\widetilde{g} \to t\bar{b}\widetilde{\chi}_1^\pm \to t\bar{b}W^\pm\widetilde{\chi}_1^0$
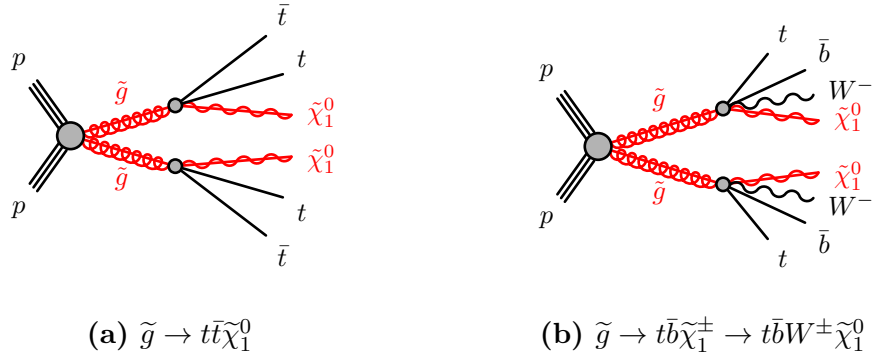
Figure D.1: The Feynman diagrams for the NUHM2 SUSY signal process.

The Monte Carlo (MC) samples are produced to model the SUSY signals and to estimate the SM background. A fast simulation (AFII[1]) based on GEANT4 [89] simulation package is used to generate the NUHM2 signal samples. An ATLAS

---

[1]AFII stands for ATLAS Fast Monte Carlo II.

detector full simulation (FullSim) simulating the detailed properties of the ATLAS detector is used to produce the SM background. The simulated MC events are re-weighted to the observed pileup conditions in the data. Table D.1 shows the event generator, parton shower, cross-section normalization, PDF set [93], and the set of tuned parameters for modeling for all samples. Except those produced by the SHERPA, the EVTGEN v1.2.0 package [95] is used to model the properties of bottom and charm hadron decays for all MC samples.

Signal/Background	Physics process	Event generator	Parton shower	Cross-section normalization	PDF set	Set of tuned parameters
Signal	NUHM2	MG5_aMC@NLO 2.2.3	PYTHIA 8.186	NLO+NLL	NNPDF2.3LO	A14
$t\bar{t} + X$ background	$t\bar{t}W, t\bar{t}Z/\gamma^*$	MG5_aMC@NLO 2.2.2	PYTHIA 8.186	NLO	NNPDF2.3LO	A14
	$t\bar{t}H$	MG5_aMC@NLO 2.3.2	PYTHIA 8.186	NLO	NNPDF2.3LO	A14
	$4t$	MG5_aMC@NLO 2.2.2	PYTHIA 8.186	NLO	NNPDF2.3LO	A14
Diboson background	ZZ, WZ	SHERPA 2.2.1	SHERPA 2.2.1	NLO	NNPDF2.3LO	SHERPA default
	Other (inc. $W^{\pm}W^{\pm}$)	SHERPA 2.1.1	SHERPA 2.1.1	NLO	CT10	SHERPA default
Rare background	$t\bar{t}WW, t\bar{t}WZ$	MG5_aMC@NLO 2.2.2	PYTHIA 8.186	NLO	NNPDF2.3LO	A14
	$tZ, tWZ, tt\bar{t}$	MG5_aMC@NLO 2.2.2	PYTHIA 8.186	LO	NNPDF2.3LO	A14
	WH, ZH	MG5_aMC@NLO 2.2.2	PYTHIA 8.186	NLO	NNPDF2.3LO	A14
	Triboson	SHERPA 2.1.1	SHERPA 2.1.1	NLO	CT10	SHERPA default

Table D.1: The simulated NUHM2 SUSY signal and SM background MC samples. The event generator, parton shower, cross-section normalization, PDF set, and the set of tuned parameters for each samples are shown. The $t\bar{t}WW$, $t\bar{t}WZ$, tZ, tWZ, $tt\bar{t}$, WH, ZH and triboson background samples are labeled in the "rare" because they contribute a very small amount to the signal region.

The data samples are required to satisfy the following good runs list (GRLs) as recommended by the ATLAS collaboration:

- `data15_13TeV.periodAllYear_DetStatus-v79-repro20-02_`
  `DQDefects-00-02-02_PHYS_StandardGRL_All_Good_25ns.xml`

- `data16_13TeV.periodAllYear_DetStatus-v83-pro20-15_`

DQDefects-00-02-04_PHYS_StandardGRL_All_Good_25ns.xml

The integrated luminosities corresponding to these datasets are respectively 3.21 fb^{-1} for 2015 and 32.86 fb^{-1} for 2016. The combined luminosity uncertainty for 2015 and 2016 is 3.2%.

D.2 Event reconstruction and signal region selection

Events are selected using the trigger strategy shown in Table D.2. The definition of objects used in this analysis are based on the recommendations by Combined Performance groups and are summarized in Table D.3.

Year	$E_{\mathrm{T}}^{\mathrm{miss}}$ requirement	triggers
2015	$E_{\mathrm{T}}^{\mathrm{miss}} < 250$ GeV	HLT_2e12_lhloose_L12EM10VH ∪ HLT_e17_lhloose_mu14 ∪ HLT_mu18_mu8noL1
	$E_{\mathrm{T}}^{\mathrm{miss}} > 250$ GeV	HLT_2e12_lhloose_L12EM10VH ∪ HLT_e17_lhloose_mu14 ∪ HLT_mu18_mu8noL1 ∪ HLT_xe70
2016	$E_{\mathrm{T}}^{\mathrm{miss}} < 250$ GeV	HLT_2e17_lhvloose_nod0 ∪ HLT_e17_lhloose_nod0_mu14 ∪ HLT_mu22_mu8noL1
	$E_{\mathrm{T}}^{\mathrm{miss}} > 250$ GeV	HLT_2e17_lhvloose_nod0 ∪ HLT_e17_lhloose_nod0_mu14 ∪ HLT_mu22_mu8noL1 ∪ HLT_xe100_mht_L1XE50 ∪ HLT_xe110_mht_L1XE50

Table D.2: The trigger strategy used in the same-sign or three leptons and jets analysis.

The objects are divided into two categories: preselected and signal objects where signal objects are a subset of preselected objects. Unless otherwise stated, the recommendations implemented in SUSYTools-00-08-58 and AnalysisBase 2.4.29 are used for all the objects. The overlaps between the different objects are applied after the object identification depending on the distance $\Delta R \equiv \sqrt{(\Delta y)^2 + (\Delta \phi)^2}$. For the electron case, the jet is discarded if the $\Delta R(e, \mathrm{jet}) < 0.2$ unless the jet is a b-tagged jet, in which case the electron is removed. For the muon case, if the jet has less than three associated tracks, then the muon is retained and the jet is discarded. The remaining lepton is removed if the lepton

Property	Preselected object	Signal object
Electrons		
Kinematic	$p_{\mathrm{T}} > 10$ GeV, $|\eta_{\mathrm{clus}}| < 2.47$, exclude $1.37 < |\eta_{\mathrm{clus}}| < 1.52$	$p_{\mathrm{T}} > 10$ GeV, $|\eta_{\mathrm{track}}| < 2$
Identification	`LooseAndBLayerLLH`	`MediumLLH`
Isolation	-	$p_{\mathrm{T}}^{\mathrm{varcone}\ 0.2}/p_{\mathrm{T}} < 0.06$ $E_{\mathrm{T}}^{\mathrm{topocone}\ 0.2}/p_{\mathrm{T}} < 0.06$
Impact parameter	$|d_0/\sigma(d_0)| < 5$	$|d_0/\sigma(d_0)| < 5$, $|z_0 \sin\theta| < 0.5$ mm
Muons		
Kinematic	$p_{\mathrm{T}} > 10$ GeV, $|\eta| < 2.5$	$p_{\mathrm{T}} > 10$ GeV, $|\eta| < 2.5$
Identification	`Medium`	`Medium`
Isolation	-	$p_{\mathrm{T}}^{\mathrm{varcone}\ 0.3}/p_{\mathrm{T}} < 0.06$
Impact parameter	-	$|d_0/\sigma(d_0)| < 3$, $|z_0 \sin\theta| < 0.5$ mm
Jets		
Kinematic	$p_{\mathrm{T}} > 20$ GeV, $|\eta| < 2.8$	
Clustering	Anti-k_t $R = 0.4$ `EMTopo`	
Pileup mitigation	reject $p_{\mathrm{T}} < 60$ GeV $\cap$ $|\eta| < 2.4$ $\cap$ JVT < 0.59	after overlap removal
b-tagging	$p_{\mathrm{T}} > 20$ GeV, $|\eta| < 2.5$, `MV2c10` > 0.8244 (70% efficiency)	

Table D.3: Summary of object definitions used in the same-sign or three leptons and jets analysis.

is in a cone $\Delta R = \min(0.4, 0.1 + 9.6~\text{GeV}/p_\text{T}(\ell))$ of a jet. Events are selected if there are at least two signal leptons with $p_\text{T} > 20$ GeV and two signal leptons must have the same electric charge. Events are removed if they contain any jet not satisfying the jet requirement listed in the Table D.3. The signal region is defined in Table D.4 to maximize the sensitivity of the NUHM2 model. The m_eff in the Table D.4 is the scalar sum of the signal leptons p_T, jets p_T and the E_T^miss.

Signal Region	$N_\text{lepton}^\text{signal}$	$N_{b-\text{jets}}$	N_jets	p_T^jet [GeV]	m_eff [GeV]	$E_\text{T}^\text{miss}/m_\text{eff}$
NUHM2	$\geq$ 2SS	≥ 2	≥ 6	> 25	> 1800	> 0.15

Table D.4: The signal region definition for the NUHM2 model.

Because the Z+jets background is important for the NUHM2 model, events are vetoed if the invariant mass of two same-sign electrons is close to the Z mass. Table D.5 shows the cutflow yields table for the NUHM2 signal with $m_{1/2}$ ranging from 300 to 800 GeV.

D.3   Background estimation and systematic uncertainties

The irreducible background are events with two same-sign or at least three prompt leptons. The main sources of the irreducible background are the diboson VV events and $t\bar{t}V$ events. The contributions of the irreducible background are estimated using the MC samples and validated with dedicated validation regions (VRs). Table D.6 lists the definitions of the VRs.

The reducible background are events including electrons with mismeasured charge and fake or non-prompt leptons. The electrons with mismeasured charge, called charge-flip, mainly come from $t\bar{t}$ production. The charge-flip probability

196

Selection criteria	$m_{1/2}$ [GeV]						
	300	350	400	500	600	700	800
All events before derivations (DerivationStat Weights)	47000	49000	50000	50000	50000	49000	49000
All events in derivation/ntuple	23540	25323	25746	25442	24970	23649	22057
GRL (apply on data only)	23540	25323	25746	25442	24970	23649	22057
Primary vertex	23540	25323	25746	25442	24970	23649	22057
Trigger	19223	21824	22882	23523	23607	22942	21459
Global flags (apply on data only)	19223	21824	22882	23523	23607	22942	21459
Bad muon veto	19220	21818	22876	23518	23598	22923	21449
≥ 1 jet passes jet overlap removal	19220	21818	22876	23518	23598	22923	21449
Bad jet veto	18946	21592	22630	23267	23380	22699	21243
$N_{\text{jets}}^{\text{signal}} \geq 1$	18946	21592	22630	23267	23380	22699	21243
Cosmic muons veto	18718	21283	22346	22904	22987	22315	20880
$N_{\text{lepton}}^{\text{baseline}} \geq 2$ with $p_{\text{T}} > 10$ GeV	8439	9363	9411	9415	8890	8687	7908
$N_{\text{lepton}}^{\text{signal}} \geq 2$ with $p_{\text{T}} > 20$ GeV	4891	5497	5640	5706	5281	4994	4594
Same-sign	2357	2693	2839	2693	2480	2245	2152
Electron-electron channel							
Channel separation, same-sign electron-electron	508	585	558	504	508	430	438
Trigger matching	504	579	557	497	501	430	438
$N_{b-\text{jet}} \geq 1$ with $p_{\text{T}} > 20$ GeV	488	558	545	484	489	409	422
4 jets with $p_{\text{T}} > 50$ GeV	461	523	516	464	471	383	397
$E_{\text{T}}^{\text{miss}} > 125$ GeV	374	459	460	427	451	372	387
Electron-muon channel							
Channel separation, same-sign electron-muon	1105	1330	1414	1346	1208	1111	1058
Trigger matching	1066	1296	1381	1329	1201	1102	1051
$N_{b-\text{jet}} \geq 1$ with $p_{\text{T}} > 20$ GeV	1046	1269	1328	1295	1157	1057	1010
4 jets with $p_{\text{T}} > 50$ GeV	980	1182	1260	1246	1101	1013	971
$E_{\text{T}}^{\text{miss}} > 125$ GeV	799	1040	1135	1176	1060	988	956
Muon-muon channel							
Channel separation, same-sign muon-muon	744	778	867	843	764	704	656
Trigger matching	741	772	861	843	763	704	655
$N_{b-\text{jet}} \geq 1$ with $p_{\text{T}} > 20$ GeV	711	754	842	813	736	679	623
4 jets with $p_{\text{T}} > 50$ GeV	667	703	808	778	711	639	590
$E_{\text{T}}^{\text{miss}} > 125$ GeV	547	613	709	719	678	621	583

Table D.5: The cutflow yields table for the NUHM2 signal with $m_{1/2}$ ranging from 300 to 800 GeV. The number of events in the table are the raw events.

Validation Region	$N_{\text{leptons}}^{\text{signal}}$	$N_{b-\text{jets}}$	N_{jets}	$p_{\text{T}}^{\text{jet}}$ [GeV]	$E_{\text{T}}^{\text{miss}}$ [GeV]	m_{eff} [GeV]	other
$t\bar{t}W$	$= 2SS$	≥ 1	$\geq 4(e^{\pm}e^{\pm}, e^{\pm}\mu^{\pm})$ $\geq 3(\mu^{\pm}\mu^{\pm})$	> 40 > 25	> 45	> 550	$p_{\text{T}}^{\ell_2} > 40$ GeV $\sum p_{\text{T}}^{b-\text{jet}}/\sum p_{\text{T}}^{\text{jet}} > 0.25$
$t\bar{t}Z$	≥ 3 ≥ 1 SFOS pair	≥ 1	≥ 3	> 35	—	> 450	$81 < m_{\text{SFOS}} < 101$ GeV
WZ+4j WZ+5j	$= 3$	$= 0$	≥ 4 ≥ 5	> 25	—	> 450	$E_{\text{T}}^{\text{miss}}/\sum p_{\text{T}}^{\ell} < 0.7$
$W^{\pm}W^{\pm}jj$	$= 2SS$	$= 0$	≥ 2	> 50	> 55	> 650	veto $81 < m_{e^{\pm}e^{\pm}} < 101$ GeV $p_{\text{T}}^{\ell_2} > 30$ GeV $\Delta R_{\eta}(\ell_{1,2}, j) > 0.7$ $\Delta R_{\eta}(\ell_1, \ell_2) > 1.3$

Table D.6: The definitions of the validation regions for the irreducible background. The b-jets are required to have $p_{\text{T}} > 20$ GeV. The ℓ_1, ℓ_2 represent the leading and sub-leading leptons. The SFOS means the same-flavor opposite sign lepton.

is measured using a likelihood fit to the $Z/\gamma^* \to ee$ data sample with events in 10 GeV Z mass window. Fake or non-prompt leptons mainly come from hadron misidentified as leptons, photon conversions, and leptons from pion or kaon decays. Two data-driven methods, matrix method [115] and MC template method [115, 116], are used to estimate the fake or non-prompt lepton background. The contributions of the reducible background in the signal region are estimated using data-driven methods and validated by the validation regions.

The various systematic uncertainties related to the background, such as the fake or non-prompt leptons using two different methods, the electron charge-flip probability, diboson background, are considered. The theoretical modeling and the cross-section calculation uncertainties are also assigned. The number of estimated background events and the observed data in the validation regions after considering the statistic and systematic uncertainties are listed in Table D.7.

Validation Region	$t\bar{t}W$	$t\bar{t}Z$	WZ+4j	WZ+5j	$W^{\pm}W^{\pm}jj$
$t\bar{t}V$					
$t\bar{t}Z/\gamma^*$	6.2 ± 0.9	123 ± 17	17.8 ± 3.5	10.1 ± 2.3	1.06 ± 0.22
$t\bar{t}W$	19.0 ± 2.9	1.71 ± 0.27	1.30 ± 0.32	0.45 ± 0.14	4.1 ± 0.8
$t\bar{t}H$	5.8 ± 1.2	3.6 ± 1.8	1.8 ± 0.6	0.96 ± 0.34	0.69 ± 0.14
$4t$	1.02 ± 0.22	0.27 ± 0.14	0.04 ± 0.02	0.03 ± 0.02	0.03 ± 0.02
VV					
$W^{\pm}W^{\pm}$	0.5 ± 0.4	—	—	—	26 ± 14
WZ	1.4 ± 0.8	29 ± 17	200 ± 110	70 ± 40	27 ± 14
ZZ	0.04 ± 0.03	5.5 ± 3.1	22 ± 12	9 ± 5	0.53 ± 0.3
Rare	2.2 ± 0.5	26 ± 13	7.3 ± 2.1	3.0 ± 1.0	1.8 ± 0.5
Fake or non-prompt leptons	18 ± 16	22 ± 14	49 ± 31	17 ± 12	13 ± 10
Charge-flip electrons	3.4 ± 0.5	—	—	—	1.74 ± 0.22
Total SM background	57 ± 16	212 ± 35	300 ± 130	110 ± 50	77 ± 31
Observed events in data	71	209	257	106	99

Table D.7: The number of estimated background events and the observed data in the validation regions. The uncertainties include the statistical and systematic uncertainties.

D.4 NUHM2 interpretation and conclusion

Table D.8 shows the number of observed data events and the expected background in the signal region. The number of observed data events and the expected back-

	Number of events
$t\bar{t}W$ and $t\bar{t}Z/\gamma^*$	0.44 ± 0.14
$t\bar{t}H$	0.10 ± 0.06
$4t$	0.18 ± 0.09
VV	0.04 ± 0.02
Rare	0.15 ± 0.09
Fake or non-prompt leptons	0.15 ± 0.15
Charge-flip electrons	0.02 ± 0.01
Total SM background	1.08 ± 0.32
Observed in data	0
$S_{\mathrm{obs}}^{95\%\mathrm{CL}}$	3.6
$S_{\mathrm{exp}}^{95\%\mathrm{CL}}$	$3.9_{-0.4}^{+1.4}$
p_0	0.91

Table D.8: The number of estimated background events and the observed data in the signal regions. The uncertainties include the statistical and systematic uncertainties. The 95% confidence level (CL) upper limits $S_{\mathrm{obs}}^{95\%\mathrm{CL}}$ and $S_{\mathrm{exp}}^{95\%\mathrm{CL}}$ are shown. The p-value (p_0) shows the probability to observe a deviation from the number of expected background events as large as the one in the data.

ground are consistent within the uncertainties. Because no significant deviation from the SM prediction is observed, the exclusion limit with 95% CL on the cross-section as a function of $m_{1/2}$ in the NUHM2 model is calculated and shown

in Fig D.2. The $m_{1/2} < 650$ GeV region is excluded.
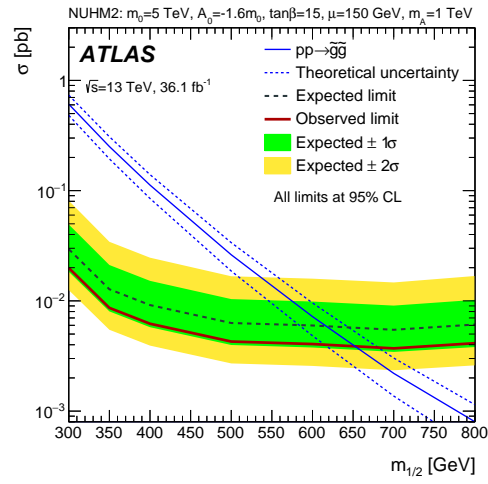
Figure D.2: The upper limit of the cross-section as a function of $m_{1/2}$ in the NUHM2 model. The green and yellow bands around the expected limit are the $\pm 1\sigma$ and $\pm 2\sigma$ variations, respectively.

APPENDIX E

REAL LEPTON EFFICIENCY

This appendix presents more details on the measurement of the data-driven real lepton efficiency using the Z tag-and-probe method.

E.1   The Z tag-and-probe method

The Z tag-and-probe method is used to extract the leptons from data and measure the real lepton efficiency. The selected events are required to have at least two baseline leptons. The lepton candidates with $p_\mathrm{T} > 25$ GeV and satisfying all the signal lepton requirements are categorized into *tag leptons*. The lepton candidates passing baseline lepton requirements can be classified as *probe leptons*. In order to form a tag-and-probe pair, the two selected leptons have to carry the same flavor and opposite charge. The invariant mass of the tag-and-probe pair system should satisfy the Z boson mass window $80 < m_{\ell\ell} < 100$ GeV. All possible combinations of the tag-and-probe pairs are considered to avoid any bias and to increase the statistics. For the $Z \to ee$ decay, an additional $|\eta| < 2$ requirement is applied on the tag and probe leptons. However, no additional requirement is applied for the $Z \to \mu\mu$ decay. The tag lepton is used to select the probe lepton only and the probe lepton is used for the real efficiency measurements. In this study, the tag and probe leptons are required to match the lepton triggers listed in Table E.1.

Figure E.1 shows the data-to-MC comparison of the tag-and-probe pair invariant mass distributions which indicate the need of subtracting the background

Trigger	lepton	2015	2016
Single lepton trigger	electron	e24_lhmedium_iloose_L1EM20VH	e26_lhtight_nod0_ivarloose
	muon	mu20_iloose_L1MU15	mu26_ivarmedium
Dilepton trigger	electron	2e12_lhloose_L12EM10VH	2e17_lhvloose_nod0
	muon	mu18_mu8noL1	mu22_mu8noL1

Table E.1: The list of single lepton and dilepton triggers used for the real lepton efficiency measurements. The dilepton triggers are used for studying the systematic uncertainties causing by the trigger.

especially for the probe electron with $p_\mathrm{T} < 20$ GeV. A background template method, which is similar to the one used by the e/γ performance group for their efficiency measurements [117], is used to estimate the background contamination from the low p_T electrons. No background subtraction is performed on the signal leptons because the background contamination is found to be negligible. However, the background contamination in the baseline probe leptons needs to be subtracted. The real lepton efficiency is obtained by the following equation

$$\epsilon = \frac{N_\mathrm{signal}}{N_\mathrm{baseline} - N_\mathrm{baseline}^{bkg}} \tag{E.1}$$

where N_signal is the number of probe leptons passing the signal requirements, N_baseline is the number of probe leptons passing the baseline requirements, and $N_\mathrm{baseline}^{bkg}$ is the estimated background contamination in the baseline probe leptons.

E.2 Background subtraction

The background template method is used to evaluate the background contamination on data. By inverting the calorimeter and track isolations, requesting the electron object to fail the medium LH identification, the background sample en-
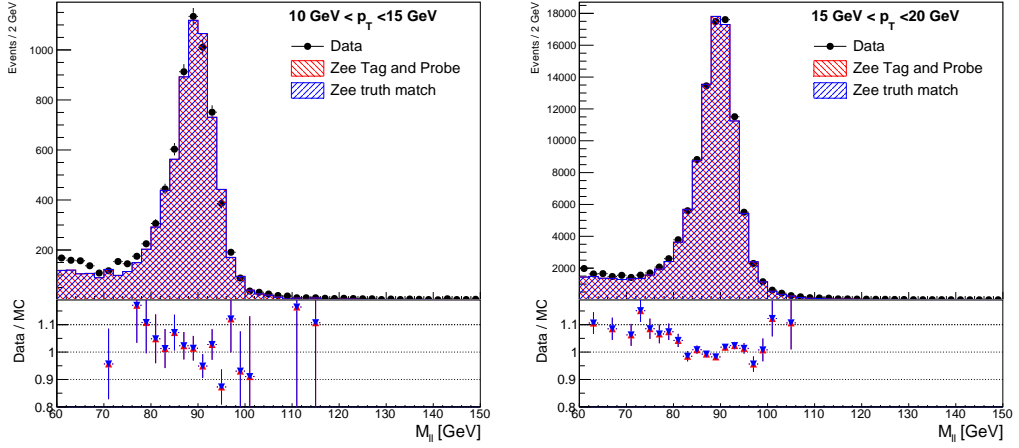
(a) The m_{ee} distribution with $10 < p_T <$ 15 GeV.

(b) The m_{ee} distribution with $15 < p_T <$ 20 GeV.
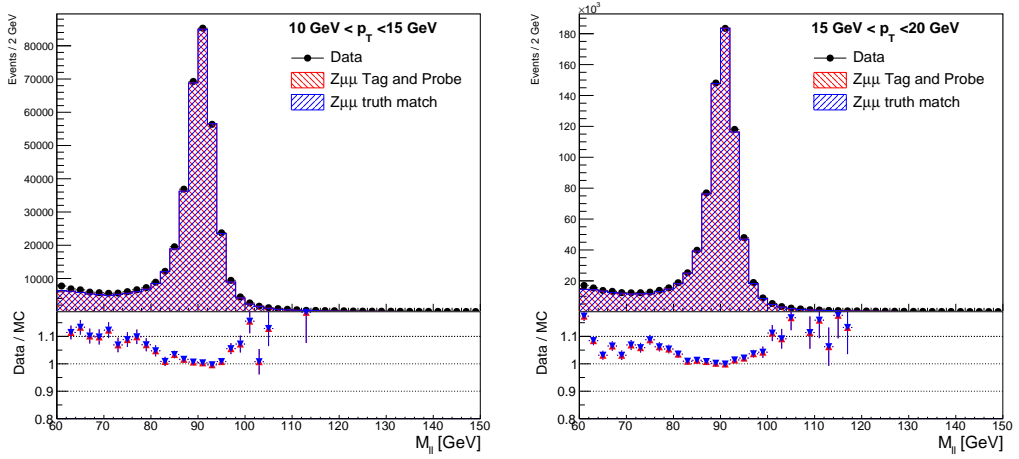
(c) The $m_{\mu\mu}$ distribution with $10 < p_T <$ 15 GeV.

(d) The $m_{\mu\mu}$ distribution with $15 < p_T <$ 20 GeV.

Figure E.1: The invariant mass distributions of the tag-and-probe pair computed using $Z + jets$ MC and 2015 + 2016 data. The red color stands for the Z tag-and-probe events, the blue color represents the Z truth matched events, and the black dots are data. The MC distributions are scaled to the data using a Gaussian fit of the Z mass peak $85 < m_{\ell\ell} < 95$ GeV.

riched template can be obtained. Three background templates are considered for the systematic study. The definitions of the background template are summarized in Table E.2.

cut	variation 1 template	baseline template	variation 2 template
Identification	-	fail medium LH	fail medium LH
Calorimeter isolation	$E_\mathrm{T}^{topocone20}/p_\mathrm{T} > 6\%$	$E_\mathrm{T}^{topocone20}/p_\mathrm{T} > 15\%$	$E_\mathrm{T}^{topocone20}/p_\mathrm{T} > 20\%$
Track isolation	$p_\mathrm{T}^{varcone20}/p_\mathrm{T} > 6\%$	$E_\mathrm{T}^{topocone20}/p_\mathrm{T} > 8\%$	$E_\mathrm{T}^{topocone20}/p_\mathrm{T} > 15\%$

Table E.2: The definition of the background templates for estimating the background contamination associated with the Z tag-and-probe method. The baseline template is used to estimate the background contamination. The variation 1 template has looser requirements and the variation 2 template has tighter requirements. They are used to assess the systematic caused by the background contamination.

Figure E.2 shows the m_{ee} distributions of the background template. The invariant mass distribution of the template events (m_{ee}^template) is then used to estimate the amount of background in $80 < m_{\ell\ell} < 100$ GeV region. In order to estimate the correct of background events, the $120 < m_{ee} < 150$ GeV region is used to normalize the background template because a smaller prompt electron contribution is expected in this region. Equation E.2 shows the estimation of the number of background events in the tail region using the baseline electrons.

$$N_{bkg}^\mathrm{tail} = N_\mathrm{baseline}^\mathrm{tail} - N_\mathrm{MC,prompt}^\mathrm{tail} \qquad (E.2)$$

where $N_\mathrm{baseline}^\mathrm{tail}$ can be obtained by integrating the baseline m_{ee} distribution in the tail region and $N_\mathrm{MC,prompt}^\mathrm{tail}$ is the prompt electron contamination which is estimated by integrating the m_{ee} distribution in the tail region using the $Z \to ee$
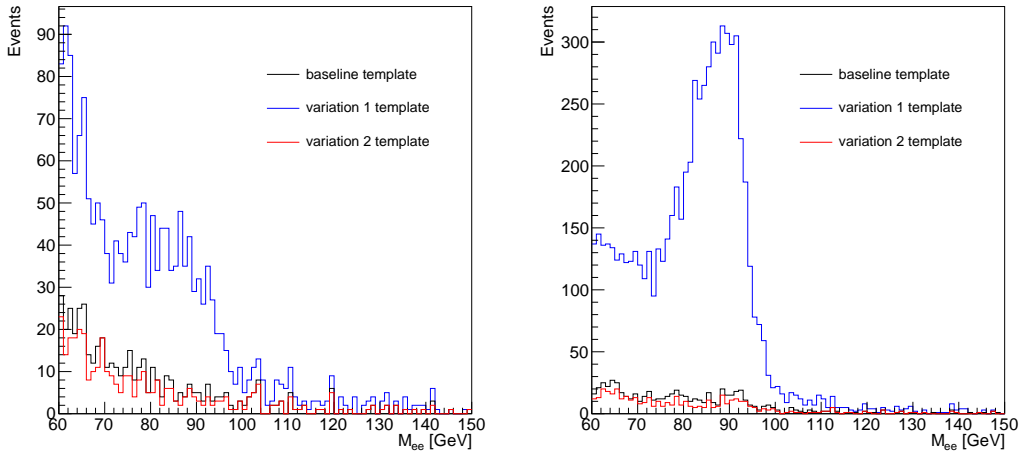
(a) Probe electrons with $10 < p_{\mathrm{T}} <$ 15 GeV.

(b) Probe electrons with $15 < p_{\mathrm{T}} <$ 20 GeV.

Figure E.2: The m_{ee} distributions for the baseline, variation 1 and variation 2 background templates. The m_{ee} distributions are computed using the probe electrons with different p_{T} as indicated in the caption of plots. The variation 1 template has looser calorimeter and track isolation requirements and the baseline and the variation 2 templates have tighter selection criteria. So a peak can be seen in the Z mass region in variation 1 template but not in the baseline and variation 2 templates.

MC simulation. Because the baseline electron selection criteria already provides a relatively high purity of prompt electrons, the background template suffers from low statistics in the tail region. The template is fitted in region $60 < m_{ee}^{\mathrm{template}} < 120$ GeV using an exponential function to avoid any bias in the normalization factor due to statistical fluctuations. However, the $80 < m_{ee}^{\mathrm{template}} < 100$ GeV is excluded to minimize the prompt lepton contamination arising from $Z \to ee$ decays. The fit is mostly driven by the $60 < m_{ee}^{\mathrm{template}} < 80$ GeV due to the low statistics in the tail. After fitting is performed, the template in the tail region $N_{\mathrm{template}}^{\mathrm{tail}}$ is normalized to the background in the tail N_{bkg}^{tail} to get the correct

estimated number of background events. The baseline m_{ee} distributions before and after applying the background subtraction using the background template are shown in Fig. E.3.

The data after performing the background subtraction, the MC simulation samples, the background template distributions, and the fitting results are also shown. The simulated m_{ee} distribution of $Z \rightarrow ee$ MC are normalized to the data, which background subtraction has been performed, using a Gaussian fit in Z peak region $85 < m_{ee} < 95$ GeV. After performing the background subtraction, the data and MC have good agreement within the statistical uncertainties.

Then, the background contamination in the Z mass region $80 < m_{ee} < 100$ GeV is calculated using

$$N_{bkg}^{80 < m_{ee} < 100 \text{ GeV}} = \int_{80}^{100} N_{\text{template}} \, dm_{ee} \cdot \frac{N_{bkg}^{\text{tail}}}{N_{\text{template}}^{\text{tail}}} \tag{E.3}$$

Table E.3 summarize the background estimations in different p_{T} and $|\eta|$ regions.

	$0 < |\eta| < 0.8$	$0.8 < |\eta| < 1.37$	$1.52 < |\eta| < 2.0$
$10 < p_{\mathrm{T}} < 15$ GeV	4.04%	2.10%	3.17%
$15 < p_{\mathrm{T}} < 20$ GeV	0.44%	0.58%	0.76%

Table E.3: The estimated background contamination in in different p_{T} and $|\eta|$ regions. The p_{T} and $|\eta|$ binnings correspond to the one used for the final measurements.

The largest improvements are observed in the lowest p_{T} bin ($10 < p_{\mathrm{T}} < 15$ GeV) where a sizable background contamination is subtracted. The background contamination is relatively small in the second lowest p_{T} bin ($15 < p_{\mathrm{T}} < 20$ GeV)
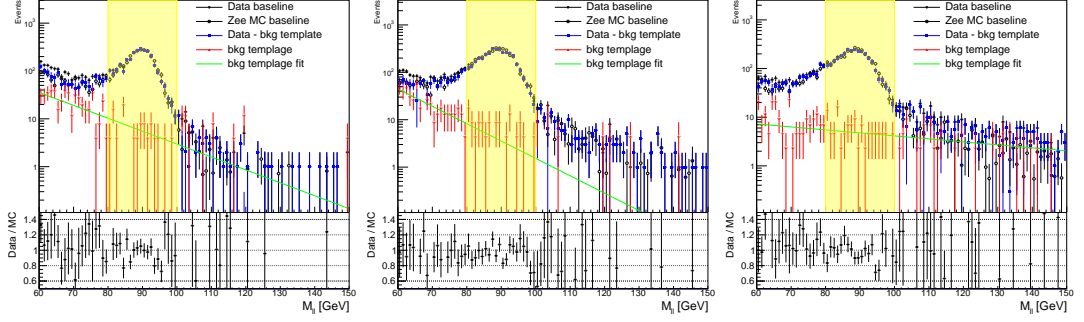
(a) $10 < p_{\mathrm{T}} < 15$ GeV

$0 < |\eta| < 0.8$

(b) $10 < p_{\mathrm{T}} < 15$ GeV

$0.8 < |\eta| < 1.37$

(c) $10 < p_{\mathrm{T}} < 15$ GeV

$1.52 < |\eta| < 2.0$

(d) $15 < p_{\mathrm{T}} < 20$ GeV

$0 < |\eta| < 0.8$
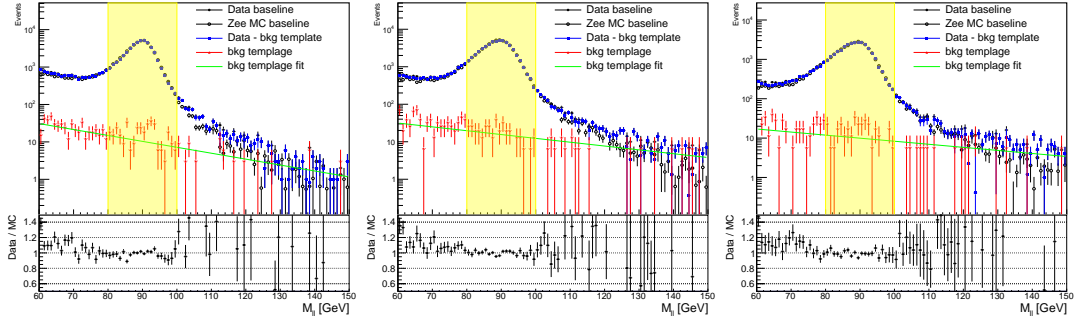
(e) $15 < p_{\mathrm{T}} < 20$ GeV

$0.8 < |\eta| < 1.37$

(f) $15 < p_{\mathrm{T}} < 20$ GeV

$1.52 < |\eta| < 2.0$

Figure E.3: Illustration of the background subtraction procedure. The full black dots and blue squares are the m_{ee} distributions for data before and after performing the background subtraction, respectively. The m_{ee} distribution for $Z \to ee$ MC, which is labeled by the open black circles, is normalized to the data after the background subtraction using a Gaussian fit of $85 < m_{ee} < 95$ GeV. The lower panels show the data-to-MC ratio where the background subtraction has been applied on data. The background templates and their respective fitting results are indicated by the red triangles and green lines, respectively.

providing the evidence that high purity of prompt leptons can be obtained using Z tag-and-probe method. Table E.4 shows the real electron efficiencies before and after performing the background subtraction.

	background subtraction	$0 < |\eta| < 0.8$	$0.8 < |\eta| < 1.37$	$1.52 < |\eta| < 2.0$
$10 < p_{\mathrm{T}} < 15$ GeV	before	57.4 ± 0.9	66.6 ± 0.8	53.2 ± 0.9
	after	59.9 ± 1.9	68.0 ± 1.8	55.0 ± 1.7
$15 < p_{\mathrm{T}} < 20$ GeV	before	64.5 ± 0.2	69.4 ± 0.2	62.0 ± 0.3
	after	64.8 ± 0.5	69.8 ± 0.5	62.5 ± 0.6

Table E.4: The real electron efficiencies before and after performing the background subtraction in different p_{T} and $|\eta|$ regions are shown in percentage.

E.3 Cut efficiencies

Figure E.4 shows the efficiencies associated to each signal cut with respect to baseline definitions. The prompt electron efficiency increases with p_{T} from $\sim$62% to $\sim$98% and the efficiency losses are dominated by the calorimeter isolation. The calorimeter isolation cut efficiency increases with p_{T} from $\sim$ 69% to $\sim$98%. The loose to medium likelihood (LH) cut efficiency increases from $\sim$92% to $\sim$96% in the $10 < p_{\mathrm{T}} < 30$ GeV then reaches a plateau when $30 < p_{\mathrm{T}} < 50$ GeV and increases again to $\sim$98% when $p_{\mathrm{T}} > 60$ GeV. The track isolation cut efficiency increases from $\sim$89% at low p_{T} to $\sim$100% when $p_{\mathrm{T}} > 60$ GeV. The longitudinal impact parameter cut efficiency increases from $\sim$98% at low p_{T} to $\sim$100% when $p_{\mathrm{T}} > 15$ GeV. The cut efficiencies for muon are much higher than the electron case because the same muon identification is used for the baseline and the signal muon definitions. The associated efficiencies computed using $Z \to \mu\mu$ events increase

from ∼80% for $10 < p_T < 15$ GeV to ∼98% when $p_T > 50$ GeV. The dominant contribution is the track isolation cut efficiency which increases from ∼82% to 98% when $p_T > 50$ GeV. The transverse and longitudinal impact parameter cut efficiencies are ∼99% and 100%, respectively. For the electron case, the transverse impact parameter cut is already applied at the baseline level

(a) Electron   **(b)** Muon
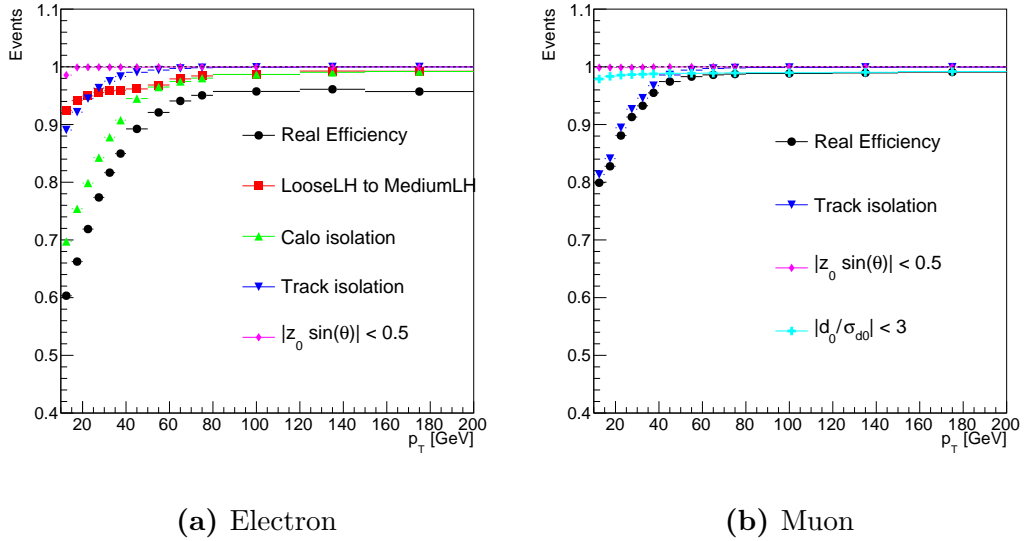
Figure E.4: Cut efficiencies of the signal electron and muon definition as a function of p_T. The total real electron and muon efficiencies are presented by black points. The loose to medium likelihood cut efficiency is presented by red squares. The calorimeter and track isolation cut efficiencies are presented by green triangles and blue triangles, respectively. The longitudinal and transverse impact parameters cut efficiencies are presented by magenta diamonds and cyan crosses, respectively.

E.4   Real lepton efficiencies

The real lepton efficiencies as a function of p_T and $|\eta|$ are shown in Fig E.5 where the background subtraction has been applied on the electron case in

$10 < p_T < 15$ GeV and $15 < p_T < 20$ GeV. The uncertainties are the quadratic sum of the statistical uncertainties and the measurement systematic uncertainties. The 3 $|\eta|$ binnings for the electron case are driven by the geometry of ECAL. The crack region, $1.37 < |\eta| < 1.52$, is removed from the real electron efficiency study. It is expected that the electron efficiencies in $1.52 < |\eta| < 2.01$ are lower because the electron identification is better in the central region of the ECAL.

(a) Electron   (b) Muon
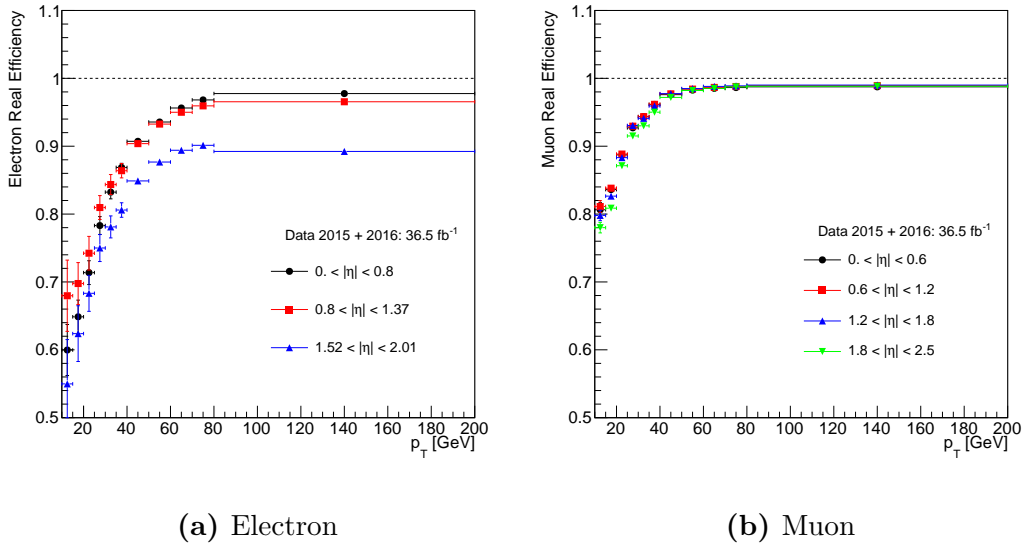
Figure E.5: The real lepton efficiencies as a function of p_T and $|\eta|$ measured using the Z tag-and-probe method. For the real electron efficiencies measurement, the $|\eta|$ binning in the creak region is removed. A homogeneous $|\eta|$ binnings are used for the muon case.

E.4.1 Tag-and-probe method and truth matching comparisons

The truth matched information in the $Z \to \ell\ell$ MC samples are used to verify the accuracy of Z tag-and-probe method. Figure E.6 shows the real lepton efficiencies
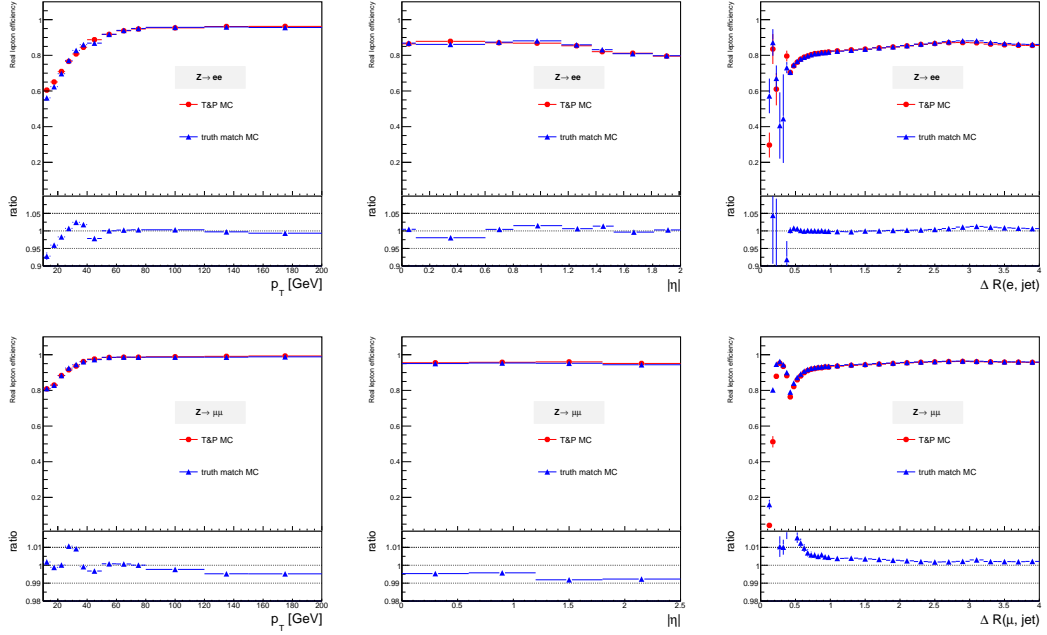
Figure E.6: The real lepton efficiencies computed by Z tag-and-probe method (red dots) and truth matching (blue triangles). The electron cases are on the top row and muon cases are at the bottom row. The three columns from the left to the right are the real lepton efficiencies as a function p_{T}, $|\eta|$, and $\Delta R(\ell, \mathrm{jet})$, respectively. The lower pads show the ratio with respect to the Z tag-and-probe method.

as a function of p_{T}, $|\eta|$, and $\Delta R(\ell, \mathrm{jet})$ using Z tag-and-probe method and truth matching. The associated uncertainties are statistical uncertainties only. For the real electron efficiencies, the largest difference is $\sim$7% in low p_{T} and no differences can be seen when $p_{\mathrm{T}} > 50$ GeV; the largest difference is $\sim$3% in ; the larger differences in $\Delta R(e, \mathrm{jet})$ exist when $\Delta R(e, \mathrm{jet}) < 0.4$. Because the overlap removal has been applied on the baseline electrons, the $\Delta R(e, \mathrm{jet}) < 0.4$ region lacks statistics. For the real muon efficiencies, the differences are less then 1% for p_{T} and $|\eta|$. However, the differences are larger for $\Delta R(\mu, \mathrm{jet}) < 0.4$ also because of the overlap removal. The small differences between two methods indicate the robust of Z tag-and-probe method and the differences may be considered as the

systematic uncertainties.

E.4.2 Data-to-MC comparisons

The real lepton efficiencies calculating by data and $Z \to \ell\ell$ MC samples are compared. All 2015 and 2016 data are considered corresponding to an integrated luminosity of 36.5 fb^{-1}. All the lepton scale factors are applied on the MC samples and the simulation is re-weighted to the pileup observed in data. Figure E.7 shows the real efficiencies as a function of p_T, $|\eta|$ and $\Delta R(\ell, \text{jet})$ using data and $Z \to \ell\ell$ MC samples, respectively. The associated uncertainties are statistical uncertainties only. Good agreement between data and MC can be seen in the p_T and $|\eta|$ plots. Larger differences exist in $\Delta R(\ell, \text{jet})$ plots because of lacking statistics.

E.4.3 Real lepton efficiency versus pileup

The relations between the real lepton efficiencies and the pileup are also studied. The efficiencies computed by 2015 + 2016 data, Z tag-and-probe method and truth matching MC samples are shown in Fig. E.8.

In order to study the efficiencies with different event topologies, the $t\bar{t}$ and $\tilde{g} \to t\bar{t}\widetilde{\chi}_1^0$ MC samples are considered. The real electron efficiencies are $\sim$92% at low $< \mu >$ and decrease when $< \mu >$ increases. The measured real lepton efficiencies using $\tilde{g} \to t\bar{t}\widetilde{\chi}_1^0$ MC sample is lower then the data case. The $t\bar{t}$ and data have similar real electron efficiencies. However, the real muon efficiencies for $t\bar{t}$ is lower than the data because the efficiencies in $p_T < 40$ GeV is lower. If a $p_T > 40$ GeV requirement is applied on the $t\bar{t}$ MC sample, then the efficiencies are agreed with
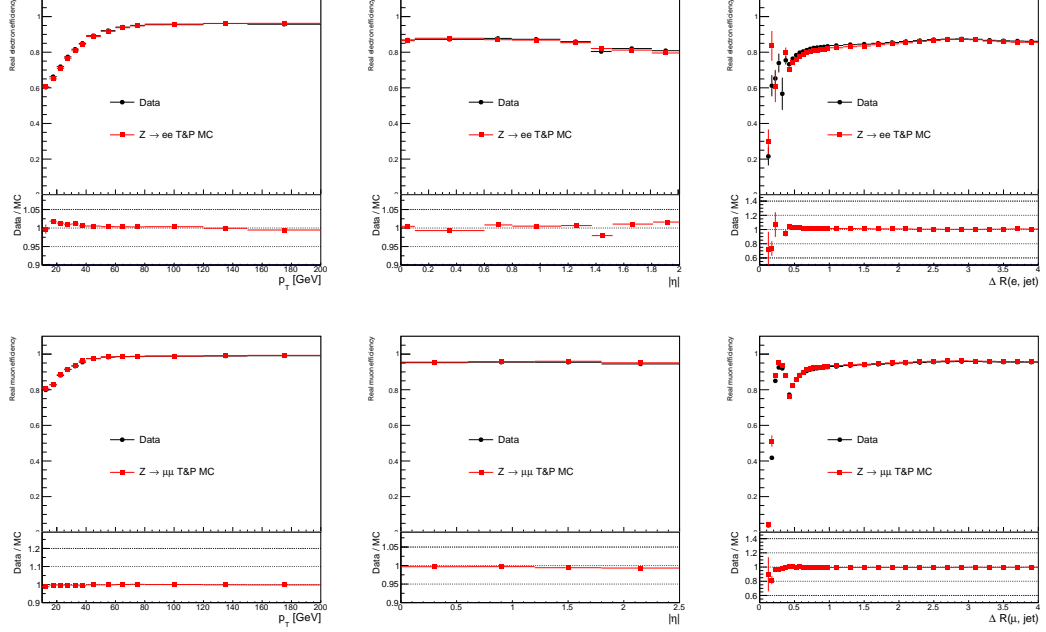
Figure E.7: The real lepton efficiencies measured on 2015 + 2016 data (black dots) and $Z \to \ell\ell$ MC samples (red squares) using the Z tag-and-probe method. The electron cases are on the top row and muon cases are at the bottom row. The three columns from the left to the right are the real lepton efficiencies as a function p_{T}, $|\eta|$, and $\Delta R(\ell, \mathrm{jet})$, respectively. The MC samples have been re-weighted to the pileup observed in data.

data. Figure E.9 shows the measured real electron and muon efficiencies as a function of p_{T} using data, Z tag-and-probe method, truth matching, $t\bar{t}$, and $\tilde{g} \to t\bar{t}\widetilde{\chi}_1^0$ MC samples. The real lepton efficiencies of $t\bar{t}$ process is lower than the data one in $p_{\mathrm{T}} < 40$ GeV region. The real lepton efficiencies of $\tilde{g} \to t\bar{t}\widetilde{\chi}_1^0$ process are lower than data in both electron and muon cases.

(a) Electron   **(b)** Muon
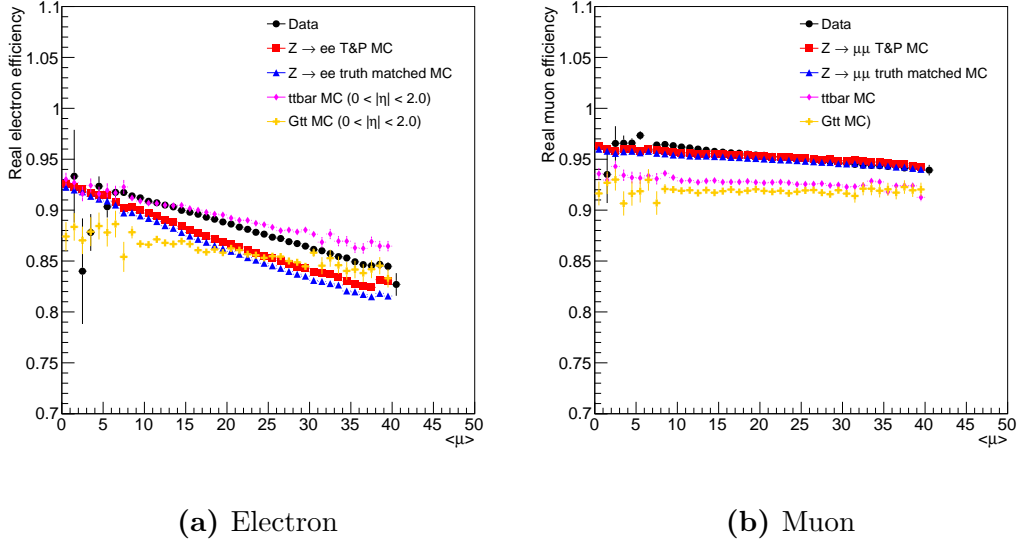
Figure E.8: The real lepton efficiencies as a function of the average interactions per crossing $< \mu >$. The data is presented in black dots, $Z \rightarrow \ell\ell$ tag-and-probe is presented in red squares, the truth matching is presented in blue triangles, the $t\bar{t}$ is presented in magenta diamonds, and $\tilde{g} \rightarrow t\bar{t}\widetilde{\chi}^0_1$ is presented in yellow crosses. The $|\eta| < 2$ requirement has been applied on the $t\bar{t}$ and $\tilde{g} \rightarrow t\bar{t}\widetilde{\chi}^0_1$ MC samples for the electron case.

E.5   Sources of systematic uncertainties

E.5.1   Measurement systematics

The measurement systematic uncertainties of the real lepton efficiency calculated by the Z tag-and-probe method have been studied by varying the background template definitions, the template fitting ranges, and the $m_{\ell\ell}$ windows. The definition of 3 background templates are listed in Table E.2. The additional template fitting ranges are [60 –70] ∪ [100 –120] GeV and [65 –75] ∪ [100 –120] GeV. The two other $m_{\ell\ell}$ windows considered are $75 < m_{ee} < 105$ GeV and $85 < m_{ee} < 95$ GeV. Therefore, there are 27 variations considered in $p_{\mathrm{T}} < 20$ GeV
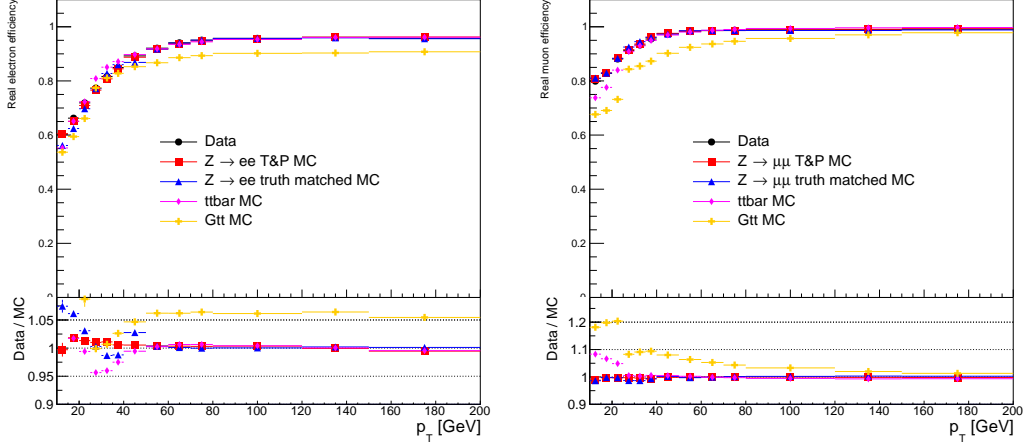
(a) Electron   **(b)** Muon

Figure E.9: The real electron and muon efficiencies as a function of p_T. The data is presented in black dots, $Z \to \ell\ell$ tag-and-probe is presented in red squares, the truth matching is presented in blue triangles, the $t\bar{t}$ is presented in magenta diamonds, and $\tilde{g} \to t\bar{t}\widetilde{\chi}_1^0$ is presented in yellow crosses. The differences in the $p_T < 40$ GeV region come from the different event topologies.

and 3 variations in $p_T > 20$ GeV for the electron case. Because the background subtraction is applied on the electron case only, no background templates and template fitting ranges are considered in the muon case. There are only 3 $m_{\ell\ell}$ window variations considered for the systematic uncertainties of real muon efficiency. Table E.5 and Table E.6 show the measurement uncertainties for the electron and muon cases, respectively.

Since electrons extracted from the $m_{\ell\ell}$ tail region are affected by bremsstrahlung effects, the contribution of the $m_{\ell\ell}$ window variations is larger in the systematic uncertainties. Using larger $m_{\ell\ell}$ window, the lower real electron efficiency we get. In $10 < p_T < 15$ GeV, the contribution comes from the $m_{\ell\ell}$ window variation is $\sim10\%$ whereas the background subtraction one is $\sim6\%$. This result shows the

	Electrons (measurement)		
$\lvert\eta\rvert$	[0, 0.8]	[0.8, 1.37]	[1.52, 2.0]
$10 < p_\mathrm{T} < 15$ GeV	2.32%(t) / 2.85%(f) / 5.06%(m)	4.84%(t) / 1.99%(f) / 5.66%(m)	5.90%(t) / 0.28%(f) / 10.31%(m)
$15 < p_\mathrm{T} < 20$ GeV	1.39%(t) / 0.00%(f) / 3.55%(m)	2.01%(t) / 0.01%(f) / 3.94%(m)	2.05%(t) / 0.15%(f) / 6.19%(m)
$20 < p_\mathrm{T} < 25$ GeV	2.46%	3.34%	3.88%
$25 < p_\mathrm{T} < 30$ GeV	1.69%	2.17%	2.66%
$30 < p_\mathrm{T} < 35$ GeV	1.19%	1.75%	2.07%
$35 < p_\mathrm{T} < 40$ GeV	0.70%	1.23%	1.32%
$40 < p_\mathrm{T} < 50$ GeV	0.20%	0.30%	0.42%
$50 < p_\mathrm{T} < 60$ GeV	0.15%	0.17%	0.20%
$60 < p_\mathrm{T} < 70$ GeV	0.13%	0.14%	0.21%
$70 < p_\mathrm{T} < 80$ GeV	0.10%	0.17%	0.18%
$80 < p_\mathrm{T} < 120$ GeV	0.12%	0.11%	0.19%
$120 < p_\mathrm{T} < 150$ GeV	0.10%	0.16%	0.06%
$150 < p_\mathrm{T} < 200$ GeV	0.11%	0.03%	0.19%

Table E.5: The systematic uncertainties for real electron efficiencies. For the electron case, the background subtraction is applied on the first two p_T bins ($p_\mathrm{T} < 20$ GeV). There are 3 sources of the systematic uncertainties: varying templates (t), varying fitting ranges (f), and varying $m_{\ell\ell}$ windows (m). When $p_\mathrm{T} > 20$ GeV, only $m_{\ell\ell}$ window variation is considered.

robustness of the background subtraction method.

E.5.2 Trigger bias

The systematic uncertainties originate from different trigger strategies are also studied. The leptons entering in the signal regions are required to fire one of the dilepton triggers. If the event fires the dilepton trigger and the considered lepton is the leading lepton or the subleading lepton, then a trigger matching should be applied before the real lepton efficiency measurement. However, if the event fires the $E_\mathrm{T}^\mathrm{miss}$ trigger or the considered lepton is the third leading lepton,

Muon (measurement)				
$\lvert\eta\rvert$	[0, 0.6]	[0.6, 1.2]	[1.2, 1.8]	[1.8, 2.5]
$10 < p_{\mathrm{T}} < 15$ GeV	1.29%	1.06%	0.96%	0.98%
$15 < p_{\mathrm{T}} < 20$ GeV	0.44%	0.38%	0.56%	0.64%
$20 < p_{\mathrm{T}} < 25$ GeV	0.19%	0.22%	0.38%	0.56%
$25 < p_{\mathrm{T}} < 30$ GeV	0.09%	0.12%	0.22%	0.36%
$30 < p_{\mathrm{T}} < 35$ GeV	0.06%	0.11%	0.23%	0.32%
$35 < p_{\mathrm{T}} < 40$ GeV	0.05%	0.07%	0.13%	0.26%
$40 < p_{\mathrm{T}} < 50$ GeV	0.04%	0.04%	0.05%	0.07%
$50 < p_{\mathrm{T}} < 60$ GeV	0.06%	0.06%	0.09%	0.07%
$60 < p_{\mathrm{T}} < 70$ GeV	0.06%	0.07%	0.08%	0.08%
$70 < p_{\mathrm{T}} < 80$ GeV	0.06%	0.08%	0.11%	0.05%
$80 < p_{\mathrm{T}} < 120$ GeV	0.07%	0.07%	0.12%	0.07%
$120 < p_{\mathrm{T}} < 150$ GeV	0.06%	0.06%	0.15%	0.05%
$150 < p_{\mathrm{T}} < 200$ GeV	0.09%	0.11%	0.15%	0.06%

Table E.6: The systematic uncertainties for real muon efficiencies. Only the $m_{\ell\ell}$ window variation is considered because no background subtraction is applied on the muon case.

then no trigger matching should be applied. The systematics uncertainties of are then assigned as the differences between the nominal values and the values measured with different trigger where the nominal value is obtained using events triggered by the single lepton triggers as listed in Table E.1. In order to provide unbiased probe leptons for the real lepton efficiency measurements, the tag lepton must match single lepton trigger. Moreover, the p_{T} of the two leading leptons must satisfies $p_{\mathrm{T}} > 20$ GeV, the leptons with $p_{\mathrm{T}} < 20$ GeV will never be trigger

matched to the dilepton trigger. Hence, no systematics are assigned in the region $10 < p_T < 20$ GeV. The real electron efficiencies as a function of p_T in 3 $|\eta|$ regions using different trigger strategies are shown in Fig. E.10. The crack region, $1.37 < |\eta| < 1.52$, is removed from the study. The real muon efficiencies as a function of p_T in 4 $|\eta|$ regions using different trigger strategies are shown in Fig. E.11. These plots indicate that the trigger strategy does not affect the real muon efficiency measurement. Table E.7 and Table E.8 show the systematic uncertainties due to the different trigger strategies.

(a) $0 < |\eta| < 0.8$ **(b)** $0.8 < |\eta| < 1.37$ **(c)** $1.52 < |\eta| < 2.01$
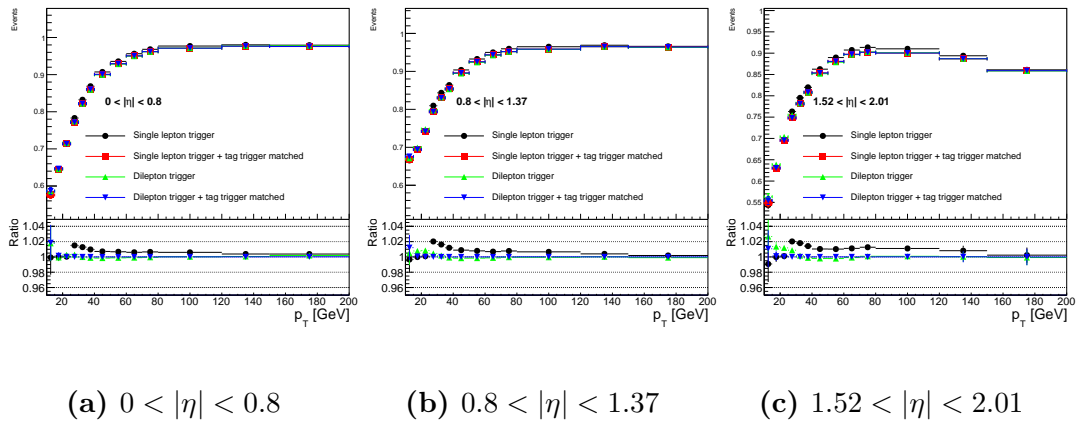
Figure E.10: The real electron efficiencies as a function of p_T in 3 $|\eta|$ regions. Four different trigger strategies are applied. The nominal values are obtained using the single lepton trigger with tag trigger matched. The differences between the nominal values and the values measured using other strategies are assigned as the systematic uncertainties.

E.5.3 Extrapolation to signal regions

Because $Z \to \ell\ell$ events are characterized by well isolated leptons, the leptons presented in the final state are not necessary well isolated using different processes.
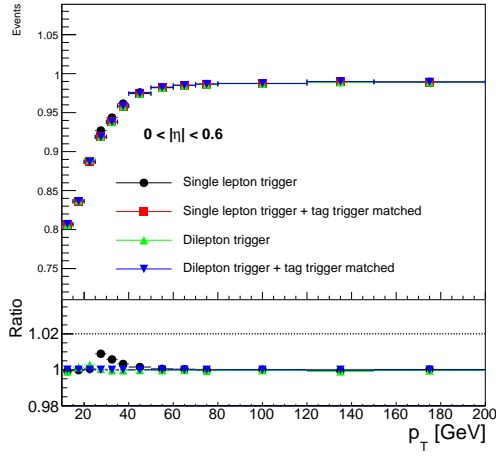
(a) $0 < |\eta| < 0.6$
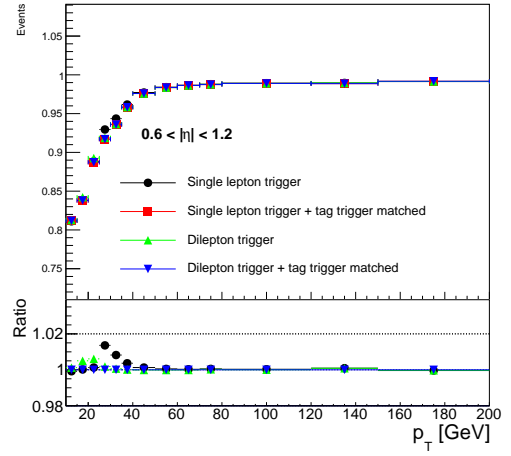
(b) $0.6 < |\eta| < 1.2$
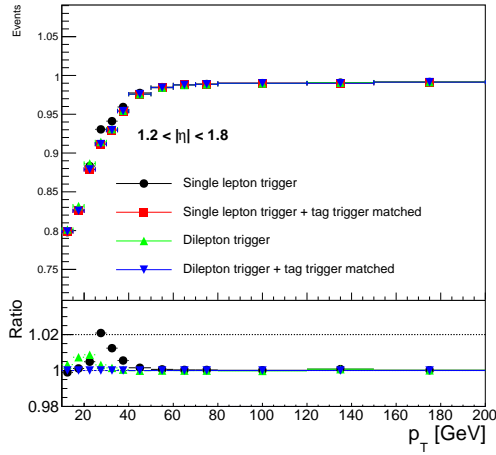
(c) $1.2 < |\eta| < 1.8$
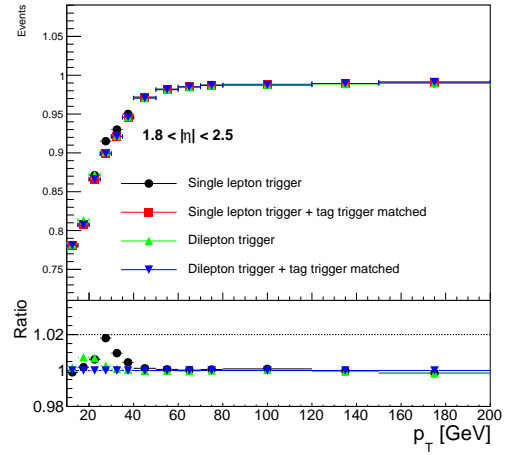
(d) $1.8 < |\eta| < 2.5$

Figure E.11: The real muon efficiencies as a function of p_{T} in 4 $|\eta|$ regions. Four different trigger strategies are applied. The nominal values are obtained using the single lepton trigger with tag trigger matched. The differences between the nominal values and the values measured using other strategies are assigned as the systematic uncertainties.

Electrons (trigger)			
$|\eta|$	[0, 0.8]	[0.8, 1.37]	[1.52, 2.0]
$10 < p_\mathrm{T} < 15$ GeV	2.46%	1.32%	3.02%
$15 < p_\mathrm{T} < 20$ GeV	0.16%	0.78%	1.33%
$20 < p_\mathrm{T} < 25$ GeV	0.29%	0.84%	1.18%
$25 < p_\mathrm{T} < 30$ GeV	1.53%	2.07%	2.20%
$30 < p_\mathrm{T} < 35$ GeV	1.28%	1.63%	1.81%
$35 < p_\mathrm{T} < 40$ GeV	0.98%	1.19%	1.42%
$40 < p_\mathrm{T} < 50$ GeV	0.73%	0.90%	1.05%
$50 < p_\mathrm{T} < 60$ GeV	0.68%	0.81%	1.05%
$60 < p_\mathrm{T} < 70$ GeV	0.61%	0.70%	1.13%
$70 < p_\mathrm{T} < 80$ GeV	0.65%	0.77%	1.27%
$80 < p_\mathrm{T} < 120$ GeV	0.60%	0.66%	1.11%
$120 < p_\mathrm{T} < 120$ GeV	0.38%	0.40%	0.79%
$150 < p_\mathrm{T} < 200$ GeV	0.43%	0.22%	0.25%

Table E.7: The systematic uncertainties for real electron efficiencies due to the different trigger strategies. The uncertainties of each trigger strategy are calculated with respect to the one applied single lepton trigger with tag trigger matched. The total uncertainties are the quadratic sum of the uncertainties of each trigger strategy.

	Muons (trigger)			
$|\eta|$	[0, 0.6]	[0.6, 1.2]	[1.2, 1.8]	[1.8, 2.5]
$10 < p_T < 15$ GeV	0.11%	0.15%	0.34%	0.19%
$15 < p_T < 20$ GeV	0.14%	0.50%	0.75%	0.77%
$20 < p_T < 25$ GeV	0.30%	0.63%	1.01%	0.93%
$25 < p_T < 30$ GeV	0.90%	1.38%	2.12%	1.83%
$30 < p_T < 35$ GeV	0.58%	0.84%	1.27%	0.99%
$35 < p_T < 40$ GeV	0.33%	0.37%	0.57%	0.46%
$40 < p_T < 50$ GeV	0.16%	0.13%	0.16%	0.13%
$50 < p_T < 60$ GeV	0.06%	0.06%	0.07%	0.07%
$60 < p_T < 70$ GeV	0.04%	0.04%	0.04%	0.04%
$70 < p_T < 80$ GeV	0.05%	0.06%	0.04%	0.06%
$80 < p_T < 120$ GeV	0.03%	0.03%	0.03%	0.11%
$120 < p_T < 120$ GeV	0.05%	0.13%	0.10%	0.08%
$150 < p_T < 200$ GeV	0.04%	0.03%	0.02%	0.19%

Table E.8: The systematic uncertainties for real muon efficiencies due to the different trigger strategies. The uncertainties of each trigger strategy are calculated with respect to the one applied single lepton trigger with tag trigger matched. The total uncertainties are the quadratic sum of the uncertainties of each trigger strategy.

The processes other than $Z \to \ell\ell$ might contain many (b-)jets in the SR and with different event topologies. In order to study different event topologies, a SUSY benchmark model $\tilde{g} \to t\bar{t}\widetilde{\chi}_1^0$ is used and $\Delta m = m_{\tilde{g}} - m_{\chi_1^0} > 1$ TeV requirement is applied on the model to selected boosted event. Since one of the main irreducible background, $t\bar{t}V$, has similar event topology, the $t\bar{t}$ samples are also considered. The difference in the real lepton efficiencies between the two processes are assigned as system uncertainties. Figure E.12 shows the kinematic distributions of the baseline leptons for $Z \to \ell\ell$, $\tilde{g} \to t\bar{t}\widetilde{\chi}_1^0$, and $t\bar{t}$ processes.

Figure E.12: The kinematic distributions of the baseline leptons for $Z \to \ell\ell$, $\tilde{g} \to t\bar{t}\widetilde{\chi}_1^0$, and $t\bar{t}$ processes. The top row is the p_{T} distributions and the bottom row is the $|\eta|$ distributions. The electron case is on the left hand side and the muon case is on the right hand side. The $\tilde{g} \to t\bar{t}\widetilde{\chi}_1^0$ process is more boosted and centralized than the $Z \to \ell\ell$ and $t\bar{t}$ processes.

The SUSY process $\tilde{g} \to t\bar{t}\widetilde{\chi}_1^0$ is more boosted and centralized than the $Z \to \ell\ell$ and $t\bar{t}$ processes. Figure E.13 shows the $\Delta R(\ell, \text{jet})$ and the N_{jets} distributions of the baseline leptons for $Z \to \ell\ell$, $\tilde{g} \to t\bar{t}\widetilde{\chi}_1^0$, and $t\bar{t}$ processes. The leptons from

the $Z \to \ell\ell$ processes are not accompanied with a signal jet and the $\Delta R(\ell, \text{jet})$ distribution peak about $\Delta R(\ell, \text{jet}) = 3$. The leptons from the SUSY process $\tilde{g} \to t\bar{t}\tilde{\chi}_1^0$ peak at $\Delta R(\ell, \text{jet}) = 0.5$ and most of the statistics are located in $\Delta R(\ell, \text{jet}) < 1$ region. The $Z \to \ell\ell$ peaks at $N_{\text{jets}} = 4$ and $N_{\text{jets}} = 3$ for the electron and muon case, respectively. The SUSY process $\tilde{g} \to t\bar{t}\tilde{\chi}_1^0$ peaks at $N_{\text{jets}} = 9$. Hence, the leptons produced in the SUSY process are accompanied with many jets and less isolated than the $Z \to \ell\ell$ process. If the isolation requirement is looser, then the associated real lepton efficiencies are larger. This extreme topology enables us to assess a conservative SUSY signal extrapolation systematic uncertainty that should cover all SUSY signal processes considered by the analysis.

Figure E.9 shows the real lepton efficiencies as a function of p_{T} using $Z \to \ell\ell$, $\tilde{g} \to t\bar{t}\tilde{\chi}_1^0$, and $t\bar{t}$ processes and the ratio with respect to the data is shown in the lower panel. The real electron efficiencies are p_{T} dependent when $p_{\text{T}} < 50$ GeV and become stable when $p_{\text{T}} > 50$ GeV. The real electron efficiencies of $\tilde{g} \to t\bar{t}\tilde{\chi}_1^0$ are $\sim 8\%$ lower than the efficiencies of $Z \to ee$. The observed differences in the low p_{T} region are mostly due to the calorimeter isolation and the track isolation requirements. The differences in the real muon efficiencies mainly come from the track isolation and d_0/σ_{d_0} requirements. The average efficiencies of $Z \to \ell\ell$ are computed and the relative efficiency differences are calculated with respect to the average efficiencies. Table E.9 shows the relative efficiency differences as a function of $\Delta R(\ell, jet)$ in p_{T} bins.
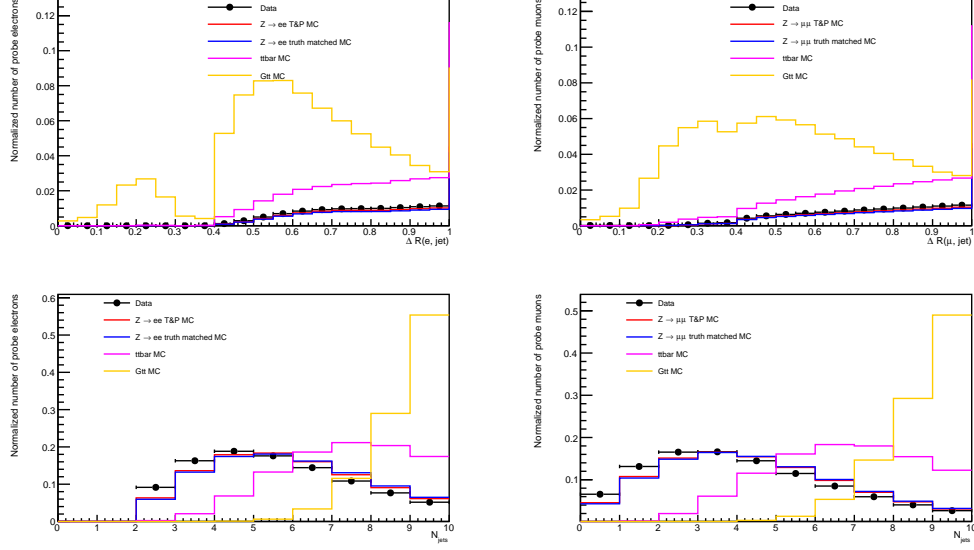
Figure E.13: The $\Delta R(\ell, \text{jet})$ and the N_{jets} distributions of the baseline leptons for $Z \to \ell\ell$, $\tilde{g} \to t\bar{t}\widetilde{\chi}_1^0$, and $t\bar{t}$ processes. The top row is t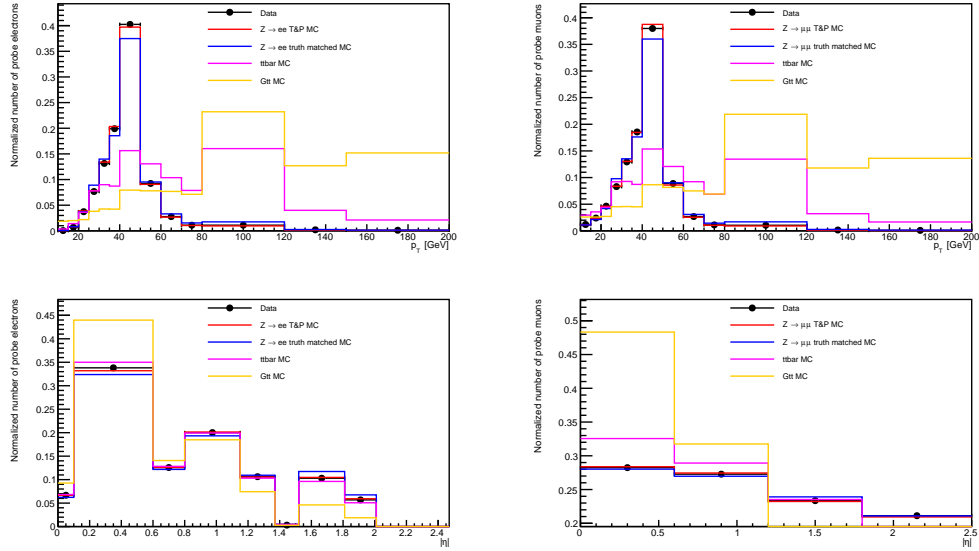he $\Delta R(\ell, \text{jet})$ distributions and the bottom row is the N_{jets} distributions. The electron case is on the left hand side and the muon case is on the right hand side. The statistics of $Z \to \ell\ell$ processes are populated at higher $\Delta R(\ell, \text{jet}) < 1$ region and lower N_{jets} region. The statistics of $\tilde{g} \to t\bar{t}\widetilde{\chi}_1^0$ are located in $\Delta R(\ell, \text{jet}) < 1$ region and higher N_{jets} region.

E.5.4   Final uncertainties

The final uncertainties are the quadratic sum of the statistical uncertainties and the systematic uncertainties. The sources of systematic uncertainty include the measurement uncertainty, the trigger uncertainty, the uncertainty from the differences between Z tag-and-probe method and truth matching, and the uncertainty in the busy environment. Table E.9 shows the uncertainty in the busy environment. The uncertainty in the busy environment is measured as a function of p_{T} and ΔR so it doesn't combine with the other uncertainties which are function of p_{T} and $|\eta|$. Table E.10 and Table E.11 show the final uncertainties for electron

electrons (busy environments)							
$\Delta R(e, \text{jet})$	[0, 0.1]	[0.1, 0.15]	[0.15, 0.2]	[0.2, 0.3]	[0.3, 0.35]	[0.35, 0.4]	[0.4, 0.6]	[0.6, 4]
$10 < p_\text{T} < 20$ GeV	-	-	-	-	-	-	25.31%	6.5%
$20 < p_\text{T} < 30$ GeV	-	-	-	-	-	73.37%	10.21%	0.37%
$30 < p_\text{T} < 40$ GeV	-	-	-	97.71%	48.22%	15.54%	7.29%	0.58%
$40 < p_\text{T} < 50$ GeV	-	-	-	52.81%	22.80%	16.73%	7.68%	1.10%
$50 < p_\text{T} < 60$ GeV	-	-	-	29.96%	21.49%	20.23%	6.99%	2.78%
$60 < p_\text{T} < 80$ GeV	-	-	55.89%	24.31%	17.40%	24.77%	6.20%	2.87%
$80 < p_\text{T} < 150$ GeV	-	57.52%	30.24%	16.45%	12.73%	20.92%	4.44%	2.73%
$150 < p_\text{T} < 200$ GeV	88.54%	40.16%	19.34%	8.45%	14.66%	16.57%	2.57%	1.90%

muons (busy environments)							
$\Delta R(\mu, \text{jet})$	[0, 0.1]	[0.1, 0.15]	[0.15, 0.2]	[0.2, 0.3]	[0.3, 0.35]	[0.35, 0.4]	[0.4, 0.6]	[0.6, 4]
$10 < p_\text{T} < 20$ GeV	-	-	-	-	-	-	33.59%	5.18%
$20 < p_\text{T} < 30$ GeV	-	-	-	-	-	82.34%	22.27%	3.39%
$30 < p_\text{T} < 40$ GeV	-	-	-	98.54%	56.36%	31.89%	14.22%	2.24%
$40 < p_\text{T} < 50$ GeV	-	-	-	53.10%	21.33%	13.90%	6.81%	1.45%
$50 < p_\text{T} < 60$ GeV	-	-	-	24.98%	13.72%	9.62%	3.83%	0.79%
$60 < p_\text{T} < 80$ GeV	-	-	44.41%	13.75%	6.14%	4.76%	2.04%	0.15%
$80 < p_\text{T} < 150$ GeV	-	29.94%	7.14%	3.16%	1.30%	1.04%	0.07%	0.57%
$150 < p_\text{T} < 200$ GeV	82.26%	4.14%	1.02%	0.17%	0.29%	0.62%	1.02%	1.13%

Table E.9: The systematic uncertainties of the real lepton efficiency in busy environment using $\tilde{g} \to t\bar{t}\widetilde{\chi_1^0}$.

and muon real efficiencies, respectively.

Electrons (final uncertainties)			
$\lvert\eta\rvert$	[0, 0.8]	[0.8, 1.37]	[1.52, 2.0]
$10 < p_{\mathrm{T}} < 15$ GeV	0.047	0.063	0.089
$15 < p_{\mathrm{T}} < 20$ GeV	0.027	0.042	0.062
$20 < p_{\mathrm{T}} < 25$ GeV	0.018	0.031	0.041
$25 < p_{\mathrm{T}} < 30$ GeV	0.029	0.024	0.027
$30 < p_{\mathrm{T}} < 35$ GeV	0.023	0.021	0.023
$35 < p_{\mathrm{T}} < 40$ GeV	0.014	0.018	0.018
$40 < p_{\mathrm{T}} < 50$ GeV	0.007	0.010	0.010
$50 < p_{\mathrm{T}} < 60$ GeV	0.008	0.010	0.010
$60 < p_{\mathrm{T}} < 70$ GeV	0.007	0.010	0.010
$70 < p_{\mathrm{T}} < 80$ GeV	0.008	0.011	0.012
$80 < p_{\mathrm{T}} < 120$ GeV	0.010	0.010	0.011
$120 < p_{\mathrm{T}} < 120$ GeV	0.005	0.005	0.011
$150 < p_{\mathrm{T}} < 200$ GeV	0.005	0.003	0.020

Table E.10: The final uncertainties of the real electron efficiencies. The final uncertainties are the quadratic sum of the statistical uncertainties and the systematic uncertainties. The systematic uncertainties include the measurement uncertainty, the trigger uncertainty, the uncertainty comes from the differences between Z tag-and-probe method and truth matching. The uncertainties in the busy environment do not incorporate in the final uncertainties calculation because it is measured as a function of p_{T} and ΔR. The trigger uncertainties are measured using $p_{\mathrm{T}} > 20$ GeV only.

Muons (final uncertainties)				
$|\eta|$	[0, 0.6]	[0.6, 1.2]	[1.2, 1.8]	[1.8, 2.5]
$10 < p_\mathrm{T} < 15$ GeV	0.014	0.010	0.008	0.011
$15 < p_\mathrm{T} < 20$ GeV	0.005	0.006	0.008	0.011
$20 < p_\mathrm{T} < 25$ GeV	0.003	0.006	0.010	0.010
$25 < p_\mathrm{T} < 30$ GeV	0.011	0.015	0.022	0.019
$30 < p_\mathrm{T} < 35$ GeV	0.007	0.009	0.014	0.011
$35 < p_\mathrm{T} < 40$ GeV	0.004	0.004	0.006	0.006
$40 < p_\mathrm{T} < 50$ GeV	0.002	0.001	0.002	0.001
$50 < p_\mathrm{T} < 60$ GeV	0.001	0.001	0.001	0.001
$60 < p_\mathrm{T} < 70$ GeV	0.001	0.001	0.001	0.002
$70 < p_\mathrm{T} < 80$ GeV	0.002	0.001	0.001	0.002
$80 < p_\mathrm{T} < 120$ GeV	0.004	0.002	0.002	0.002
$120 < p_\mathrm{T} < 120$ GeV	0.006	0.005	0.005	0.005
$150 < p_\mathrm{T} < 200$ GeV	0.005	0.005	0.005	0.006

Table E.11: The final uncertainties of the real muon efficiencies. The final uncertainties are the quadratic sum of the statistical uncertainties and the systematic uncertainties. The systematic uncertainties include the measurement uncertainty, the trigger uncertainty, the uncertainty comes from the differences between Z tag-and-probe method and truth matching. The uncertainties in the busy environment do not incorporate in the final uncertainties calculation because it is measured as a function of p_T and ΔR.